TAMPEREEN TEKNILLINEN YLIOPISTO
TAMPERE UNIVERSITY OF TECHNOLOGY

Luis Miguel Castro González

Modelling of Multi-terminal VSC-HVDC Links for Power Flows and Dynamic Simulations of AC/DC Power Networks

Julkaisu 1445 • Publication 1445

Tampere 2016

Tampereen teknillinen yliopisto. Julkaisu 1445
Tampere University of Technology. Publication 1445

Luis Miguel Castro González

Modelling of Multi-terminal VSC-HVDC Links for Power Flows and Dynamic Simulations of AC/DC Power Networks

Thesis for the degree of Doctor of Science in Technology to be presented with due permission for public examination and criticism in Sähkötalo Building, Auditorium S2, at Tampere University of Technology, on the 5th of December 2016, at 12 noon.

Tampereen teknillinen yliopisto - Tampere University of Technology
Tampere 2016

ISBN 978-952-15-3866-7 (printed)
ISBN 978-952-15-3869-8 (PDF)
ISSN 1459-2045

Abstract

Power transmission systems are expanded in order to supply electrical energy to remote users, to strengthen their operational security and reliability and to be able to carry out commercial transactions with neighbouring power grids. Power networks successfully expand, at any time, by incorporating the latest technological developments. A case in point is the current growth of electrical power grids, in terms of both infrastructure and operational complexity, to meet an unprecedented upward trend in global demand for electricity. Today's expansion of the power grid is being supported, more and more, by power electronics, in the form of flexible AC transmission systems and HVDC systems using voltage-sourced converters. The latter option, in particular, has been developing exceedingly rapidly since 1999, when the first commercial VSC-HVDC transmission installation was commissioned; the voltage-sourced converter technology has become the preferred option for transporting electricity when natural barriers are present (e.g. the sea), in Europe and further afield. At least one influential European body has recommended that the next step in the construction of the so-called European super grid, be a meshed HVDC transmission system based on the use of the VSC technology, to facilitate further the massive incorporation of renewable energy sources into the Pan European electrical grid, the harvesting of hydrocarbons that lie in deep sea waters and the energy trading between neighbouring countries.

It is in this context that this thesis contributes new knowledge to the modelling of VSC-based equipment and systems for the assessment of steady-state and transient stability analyses of AC/DC power networks. The STATCOM, the back-to-back VSC-HVDC link, the point-to-point VSC-HVDC link and the multi-terminal VSC-HVDC link, all receive research attention in this work. The new models emanating from this research capture all the key steady-state and dynamic characteristics of the equipment and network. This has required a paradigm shift in which the VSC equipment has been modelled, here-to-fore, assuming that a voltage-sourced converter behaves like an idealised voltage source. In contrast, the models developed in this research resort to an array of basic power systems elements, such as a phase-shifting transformer and an equivalent shunt susceptance, giving rise to a two-port circuit where the AC and DC sides of the VSCs are explicitly represented. The ensuing VSC model is fundamentally different from the voltage source model; it represents, in an aggregated manner, the array of semiconductor switches in the converter and its PWM control. The VSC model was used as the basic building block with which to develop all the VSC-based devices put forward in this thesis. The ultimate device is the multi-terminal VSC-HVDC system, which may comprise an arbitrary number of VSC units commensurate with the number of otherwise independent AC sub-networks and a DC network of an arbitrary topology. The steady-state and dynamic simulations of the AC/DC systems are carried out using a unified frame-of-reference which is amenable to the Newton-Raphson algorithm. This framework accommodates, quite naturally, the set of discretised differential equations arising from the synchronous generators, HVDC and FACTS equipment, and the algebraic equations describing the conventional transmission lines, transformers and loads of the AC sub-networks. The application areas covered in this work are: power-flow studies and dynamic simulations.

Preface

Completion of this doctoral thesis was possible due to the help and support of several people. I would like to express my sincere gratitude to all of them.

The research work presented in this thesis was carried out at the Department of Electrical Engineering (DEE), at Tampere University of Technology (TUT), to which I thank for having accepted me to be part of its vibrant academic atmosphere, first as a visiting student and then as a PhD student.

I am deeply grateful to Prof. Enrique Acha to whom I thank for supervising my thesis, providing me always with his enormous expertise and due guidance throughout my research. I would like to recognize that the years I spent in Finland under his supervision were the most fruitful in terms of my professional growth. I thank him for having facilitated my research in Finland with his unconditional support and friendship. I would like to also thank Prof. Seppo Valkealahti for having accepted me a visiting student when he was the Head of Department of Electrical Engineering.

I am grateful to Prof. Ali Abur and Prof. Neville R. Watson for examining my manuscript and for providing me valuable comments which, undoubtedly, helped improve the quality of this thesis.

The staff of the DEE deserves my regards for providing me with valuable assistance in practical matters of the workplace.

I thank all the colleagues and friends that I encounter by chance in Tampere for their support and friendship, especially thanking Luis Enrique, Carlos, Jorge Paredes, Rodolfo, Angélica, Mafer, Moramay, Viri, Oscar, Kalle, Gabriel, Josmar, Victor, René, Rosa, Gaby, Pancho, Jan Servotte, Nemät Dehghani, Andrii and many others with whom I spent unforgettable moments.

Last but not least, I express my most profound gratitude to my parents, Luis and Guadalupe, and my siblings, Lupita, Victor, Leonardo and Cesar for their all-important encouraging words during the time I spent in Finland.

México City, November 2016

Luis Miguel Castro González

Contents

List of Figures

List of Tables

List of Symbols and Abbreviations

θ , V :	Phase angle and magnitude of nodal voltages
P_g , Q_g :	Generated active and reactive powers
P_{dk} , Q_{dk} :	Active and reactive powers drawn by the load at bus *k*
P_k^{cal} , Q_k^{cal} :	Active and reactive power injections at bus *k*
B_{eq} :	Equivalent shunt susceptance of the converter
C_{dc} :	DC capacitor of the converter
H_c :	Inertia constant of the converter's DC capacitor
E_{dc} :	DC bus voltage
m_a :	Modulation ratio of the converter
ϕ :	Phase-shifting angle of the converter
G_{sw} :	Conductance for computing the switching losses of the converter
R, X :	Series resistance and reactance of the converter
R_{ltc} , X_{ltc} :	Series resistance and reactance of the OLTC transformer
R_f , X_f , B_f :	Resistance, reactance and susceptance of the AC filter of the converter
G_{dc} , R_{dc} :	Conductance and resistance of the DC links
I_{nom} :	Nominal current of the converter
S_{nom} :	Rated apparent power of the converter
AC/DC:	Alternating current/Direct current
EMTS:	Electromagnetic transient simulation
IGBT:	Insulated gate bipolar transistors
$\mathbf{J}$:	Jacobian matrix
HVDC:	High-voltage direct current
OLTC:	On-load tap changer
PWM:	Pulse-width modulation
RMS:	Root mean square
STATCOM:	Static synchronous compensator
SVC:	Static VAR compensator
VSC:	Voltage source converter

1 Introduction

Population growth and its migration to already large metropolitan areas, continue apace. To avoid the collapse of entire megalopolis in various parts of the world, the use of advanced technology has become essential. In particular, technology driven by electricity has enabled large number of people around the globe to reach higher levels of comfort, enabling more sophisticated human activities. All this is coming with a heavy price tag on the use of natural resources, gas emissions into the atmosphere beyond what it is deemed sustainable, toxic waste into the sea, deforestation an open mining of large tracts of land in the quest for metals and hydrocarbons. All this activity is clearly non-sustainable and modern society requires a paradigm shifts so that the new challenges are adequately resolved.

Concerning the remit of this work, electrical power networks have been subjected to a relentless expansion in order to meet the spiralling demand for electricity. This has brought great many challenges to the electricity supply industry as a whole. A case in point is the need to maintain the operational integrity of the system in the face of a large penetration of renewable energy sources and the widespread incorporation of power electronics equipment into the power grid to make it electronically controllable. Most of the so-called renewable energy sources of electricity use primary energy resources that exhibit important degrees of randomness and use power electronics to make them amenable to their incorporation into the power grid. This has led to a more flexible electrical power grid but also one where the operational complexity has increased by a degree. All this comes at a time when large tracts of the electrical power grid have aged and are up for renewal, such as transmission lines, transformers, generators and protection equipment. All this infrastructure is critical to the well-being of an electrical power grid that would be “fit for purpose” to satisfy the users’ expectations for the delivery of high quality electricity at their points of connection. The fulfilment of such high expectations would require the incorporation of cutting-edge technology and operating practises and tools. The aim would be to enable the supply of electrical energy at a reasonable cost, with low power losses in the distribution and bulk power transmission systems, bearing in mind reliability of supply and energy efficiency as the key drivers. In parallel with the

renewal of the critical infrastructure, the development of state-of-the-art models of the emerging electrical equipment, control methods and simulation tools, requires continuous global effort. These present and future developments would provide the theoretical foundations upon which the new, smarter power grids will be built. It is argued in this research work, that power systems simulation tools such as power flows and time-domain simulations would turn out to be the instrumental tools that will assist in the decision-making process at the design, planning and operation stages of future power grids.

The use of power electronic devices to enable a more flexible power grid aimed at achieving higher throughputs and enhancing system stability are high on the agenda in many countries around the globe; specifically, through the use of voltage source converters. The latest innovations in the power electronics field in terms of semiconductor valves, bridges and control strategies are motivating manufacturers to launch new converter designs into the global market, opening the gates to a flurry of new applications. With more power electronics than ever before embedded into the power system, a great deal of both technology and modelling issues are yet to be resolved. In the particular field of power converter modelling, for utility-scale power systems simulations, there has been a very creditable effort. However, it is often said that a voltage-sourced converter (VSC), including its derived family of equipment (e.g., VSC-HVDC), operates according to the basic principles of a controllable voltage source. It is argued here that this may be so only from a superficial standpoint, applicable only to power system studies of limited scope. A deeper analysis of this grid-connected equipment leads to the conclusion that they are very rich in dynamics, whose calculation success cannot always be guaranteed, if the underrepresented idealised voltage source concept is used. Hence, one would need to resort to application tools which model the VSC at the individual valve-level, such as PSCAD-EMTDC, the SimPowerSystems block set within Simulink or, alternatively, the new type of representations put forward in this research; each with their advantages and disadvantages.

This research work advances the topic of grid-connected VSC-based equipment modelling aimed at the steady-state and dynamic simulations of power systems. The modelling of STATCOMs, back-to-back HVDC links, point-to-point HVDC links and multi-terminal HVDC systems are all addressed here. These models have been developed bearing in mind the key operational characteristics of the VSC-based equipment which will impact directly on the operation of the connected power grids. The encapsulation of the equipment's key dynamic effects and efficient numerical solutions of the ensuing models in terms of accuracy and computing times for steady-state and dynamic analyses, have been issues of paramount importance. The family of models of high-voltage, high-power VSC-based equipment which are introduced in this thesis, signify a paradigm shift in the way this equipment has traditionally been modelled with respect to their fundamental frequency, positive-sequence representation of their AC circuits. It ought to be remarked that these models depart from the widely-adopted modelling practice of representing the VSC as idealised

voltage or current sources. It is confirmed in this research work, using credible “what if scenarios” that these lumped models retain the key dynamics characteristics of the equipment by comparing their responses against the switching-based models available in the SimPowerSystems block set of Simulink. The STATCOM and the back-to-back, point-to-point and multi-terminal HVDC systems using VSCs, all received research attention.

1.1 Objectives and scientific contribution

The main objective of this thesis is to advance the fundamental-frequency, positive-sequence modelling, at their AC side, of the STATCOM, back-to-back HVDC link, point-to-point HVDC link and multi-terminal HVDC systems suitable for power systems simulations, with reference to their steady-state and dynamic operating regimes. Furthermore, a new frame-of-reference has been put forward in order to accommodate, in a unified manner, the new models and the positive-sequence model of the AC power network. The steady-state and dynamic models of the STATCOM, two-terminal VSC-HVDC links and multi-terminal VSC-HVDC systems put forward in this thesis represent the most comprehensive RMS-type models available today, to solve AC/DC power systems of realistic size. For instance, as far as this author is aware, there is no commercial package which contains RMS-type transient stability models that possess greater modelling flexibility than the models put forward in this timely piece of research. The same may be said about the models reported in the open literature, which neglect key dynamics and power losses of the VSC and VSC-HVDC equipment, such as switching losses, amplitude modulation indices, etc. Certainly, the dynamics of multi-terminal VSC-HVDC using RMS-type models do not seem to have been tackled anywhere.

In this research work, the AC circuit of the VSC and derived equipment are modelled using the positive-sequence framework and their representation depart from the customary idealised voltage source concept where key operational variables do not find representation. Furthermore, most of the adopted solution approaches found in the open literature are of sequential nature or, at best, quasi-Newton methods. This introduces frailty into their solution approaches. In contrast, the new models take into account the converters’ current-dependent power losses, the explicit representation of the converters’ DC buses, the phase-shifting and scaling nature of the PWM control and the converters’ control strategies that fulfil their operating requirements to conform to the type of pairing AC sub-network, an issue which becomes critical when applied to multi-terminal schemes. The set of algebraic and dynamic equations describing the new models and those of the whole network are solved in a truly unified manner using the Newton-Raphson method for solutions with quadratic convergence. In the case of time-domain solutions, the differential equations are discretised using the implicit trapezoidal method for enhanced numerical stability. This is an elegant, efficient formu-

lation that yields robust numerical solutions and physical insight of the VSC-based equipment for the steady-state and dynamic operating regimes.

The main scientific contributions of this thesis may be summarised as follows:

- Improved fundamental-frequency, positive-sequence representations of voltage-sourced converters for steady-state and dynamic simulations of power systems.
- A method to provide frequency regulation in low-inertia (island) AC grids using point-to-point VSC-HVDC links.
- Comprehensive steady-state and dynamic models of STATCOMs, back-to-back HVDC links, point-to-point HVDC links and multi-terminal HVDC systems bearing in mind their main operational characteristics.
- Development of a generalised frame-of-reference for the unified iterative solution of AC/DC networks. Both steady-state and time-domain simulations are covered.

1.2 List of published papers

***Journal papers*:**

[1] **Luis M. Castro** and Enrique Acha, "A Unified Modeling Approach of Multi-Terminal VSC-HVDC Links for Dynamic Simulations of Large-Scale Power Systems", ***IEEE Transactions on Power Systems***, Vol. 31, pp. 5051-5060, February 2016.

[2] Enrique Acha and **Luis M. Castro**, "A Generalized Frame of Reference for the Incorporation of Multi-Terminal VSC-HVDC Systems in Power Flow Solutions", ***Electric Power Systems Research***, Vol.136, pp. 415-424, July 2016.

[3] **Luis M. Castro** and Enrique Acha, "On the Provision of Frequency Regulation in Low Inertia AC Grids using VSC-HVDC links", ***IEEE Transactions on Smart Grid***, Vol. 7, pp. 2680-2690, November 2015.

[4] **Luis M. Castro**, Enrique Acha, C. R. Fuerte-Esquivel, "A novel VSC-HVDC Link Model for Dynamic Power System Simulations", ***Electric Power Systems Research***, Vol. 126, pp. 111-120, May 2015.

***Conference papers*:**

[5] Enrique Acha and **Luis M. Castro**, "Power Flow Solutions of AC/DC Micro-grid Structures", 19th Power Systems Computation Conference (PSCC'16), Genoa, Italy, 19-24 June 2016.

The author of this thesis had the main responsibility on the development of the dynamic modelling framework of the two-terminal and multi-terminal HVDC links reported in [1], [3] and [4], where the writing of the papers was also carried out by the author. In these publications, Prof. Enrique Acha was responsible for ensuring the quality of the writing process, contributing actively with insightful observations which enabled the realisation of the overall dynamic framework relating to the simulation of HVDC systems. The latter reference was also supported by Prof. C. R. Fuerte-Esquivel who contributed with helpful suggestions which facilitated the incorporation of the control strategy of the HVDC link controlling the DC power flow; his very thoughtful comments helped improve the quality of the paper. Concerning references [2] and [5], Prof. Enrique Acha settled the path for the solution of multi-terminal HVDC systems for power-flow solutions being also responsible for writing up most of the sections included in these papers. The author participated actively in carrying out, developing and implementing in software the modelling framework by himself, something that gave a point of comparison of the obtained results; this was necessary since the power-flow solutions with multi-terminal HVDC systems are used as the starting point in the dynamic simulations of AC/DC power networks. In these two papers, the author wrote the sections relating to the reported study cases.

1.3 Thesis outline

The remainder of this thesis is organised as follows:

Chapter 2 presents the state-of-the-art concerning this topic of research, with emphasis on the early attempts to model VSC-based equipment for both steady-state and dynamic simulations of power systems. It argues the merits of this research work in advancing the modelling of the various power electronics devices put forward in this research, such as the STATCOM, back-to-back and point-to-point HVDC links and multi-terminal HVDC systems.

Chapter 3 addresses the steady-state, positive sequence models of the AC circuit of the STATCOM, back-to-back and point-to-point HVDC links and multi-terminal HVDC systems. Each model is developed based on the power injections concept and solved within the context of a unified power flow formulation using the Newton-Raphson method, where general guidelines for the initialisation of their state variables are provided. The solutions obtained with this frame-of-reference are useful for obtaining the steady-state conditions of the whole network's models, i.e., generators, transmission lines, power transformers and the new VSC-based equipment. The convergent solution represents the equilibrium point with which the follow up dynamic simulations are carried out.

Chapter 4 presents a comprehensive dynamic model of the STATCOM, back-to-back and point-to-point HVDC links and multi-terminal HVDC systems aimed at fundamental-frequency, positive-

sequence dynamic simulations of power systems. These models are developed from first principles, encapsulating the key physical and operational characteristics of the equipment, i.e., each VSC unit is endowed with two degrees of freedom to provide AC voltage control and DC voltage or DC power regulation. The AC nodal voltage regulation is carried out with the amplitude modulation index, the DC voltage control ensures a stable converters operation. In the multi-terminal application, three types of dynamic control strategies are developed to match the specific operational requirements of each converter's pairing AC sub-network. In a similar way to the case of the power flows addressed in Chapter 2, the dynamic modelling and solution approach follows an efficient, unified methodology. The dynamic model of the VSC unit is used as the basic building block with which the various VSC-HVDC models are built. They may include only two VSCs for the case of back-to-back and point-to-point schemes or an arbitrary number of VSCs for cases of multi-terminal systems.

Chapter 5 illustrates the applicability of the newly developed models to carry out power flow solutions and time-domain simulations using popular test power networks. These networks range in size from a few nodes only to a 39-node network. More importantly, to demonstrate that the models yield realistic results concerning both the steady-state and dynamic operating regimes, comparisons of the point-to-point and multi-terminal HVDC systems are carried out against switching-based models, giving a reasonable match between the two types of simulations. However, it is shown that the new models outperform the EMT-type models in terms of the computing time incurred in the simulations by approximately ten times, thus demonstrating their applicability within a context of practical power networks.

Chapter 6 gives the general conclusions of the thesis and provides suggestions for future research work.

2 State-of-the-art of the Thesis

In contrast to earlier reactive power control devices, such as the Static Var Compensator (SVC), voltage source converters afford an excellent under voltage performance, enhancing voltage stability, thus increasing the power system transfer capability. The high performance of VSC stations stems from the fast action of the PWM-driven IGBT (Insulated Gate Bipolar Transistors) valves which enable the power converters to maintain a smooth voltage profile at its connecting node, even in the face of severe disturbances in the power grid. This is so because of its fast VAR supporting function by pure electronic processing of the phase-shifting of the voltage and current waveforms. Both, reduction of the converter switching losses (from 3% in earlier designs to less than 1% in actual converters) and larger operating power ranges up to 2 GW have become the driving force of their implementation on a global scale (ABB, 2014). As a result of its unabated progress, new converter topologies and control algorithms are being developed by commercial vendors in their factories and in research laboratories in Europe and elsewhere. The current drive is in multi-level converters aimed at lowering, even further, its power losses and improving the quality of the AC waveforms with little filtering. It may be argued that the current high level of penetration of power electronics in AC power grids is due to the flexibility and reliability afforded by present day VSC stations using IGBT switches (Gong, 2012; Bauer et al., 2014).

The leading developers of the VSC technology are ABB and Siemens; both use different commercial brands to refer to their own developments relating to VSC-based equipment, i.e., ABB uses the suffix Light® and Siemens uses the suffix Plus®. In both cases, each VSC unit is employed as a building platform to give rise to very important power system components within the family of FACTS devices; among these are the STATCOM, the back-to-back HVDC link, the point-to-point HVDC link, and recently, the concept of DC grids by means of multi-terminal HVDC links. All of them are key enablers for providing reactive power control (Schauder et al., 1997; Dodds et al., 2010), feeding of city centres with high power demand (Jacobson and Asplund, 2006), interconnecting two independent networks (Petersonn and Edris, 2001; Larsson et al., 2001), transmitting power through submarine cables (Ronström et al., 2007), tapping into onshore and offshore wind

power plants (Robinson et al., 2010), harnessing photovoltaic resources into AC power grids (Kjaer et al., 2005), strengthening weak AC systems (Nnachi et al., 2013; Beccuti et al., 2014), voltage and power control in microgrids (Sao and Lehn, 2008; Chung et al., 2010; Rocabert et al., 2012; Eghtedarpour and Farjah, 2014), powering oil and gas rigs that lie in deep waters (Stendius and Jones, 2006; Gilje et al., 2009) and feeding into island networks with no generation of their own (Guo and Zhao, 2010; Zhang et al., 2011). It is in this context that some influential bodies, such as the pan-European electricity market, see as essential that an electricity grid in the North Sea be built (Trötscher et al., 2009). The available options point towards a multi-terminal HVDC system using VSC technology (Vrana et al., 2010). Owing to its great engineering complexity and large investment, a power grid of this nature requires a modular approach to its construction. It is an enterprise where several countries will be contributing technically and financially, just as in its operation (Hertem and Ghandhari, 2010). Plans are well advanced and it may be argued that its construction has already begun as part of the Bard offshore 1 wind park; an 80 5-MW wind turbine development lying 100 km off the German coast. It is argued in (Cole et al., 2011) that some of the advantages of having such an electricity grid in the North Sea would be the tapping of wind parks which might not be feasible since they would require their own cable connection to the shore, as well as the efficient harvesting of fossil fuels in the North Sea.

2.1 Early attempts to modelling VSC-based equipment for power systems simulations

An IGBT-based VSC coupled to an on-load tap-changing (OLTC) transformer is commonly referred to as a STATCOM whose converter is built as a two-level or a modular multi-level inverter operating on a constant DC voltage. It contains capacitors on its DC side whose sole function is to support and stabilise its DC voltage to enable the converter operation. As a result of its VAR generation/absorption by electronic processing of voltage and current waveforms, there is no need for additional capacitor banks and shunt reactors. Indeed, the power network sees the STATCOM as an electronic generator fulfilling the functions of a synchronous condenser but with no inertia of its own, this being the reason why this device is considered as a voltage source behind a reactance in a vast variety of simulation tools of power systems for both the steady-state and dynamic regimes. As a result, the concept of a controllable voltage source behind a coupling impedance has been a popular modelling resource to represent the steady-state fundamental frequency operation of the STATCOM (Acha et al., 2005). This simple model might explain well the operation of the STATCOM from the standpoint of the AC network but its usefulness is very much reduced when the requirement involves the assessment of variables relating to its DC bus. The situation is very much the same when looking at the dynamic regime where the standard approach has also been the use of a controllable voltage source (Cañizares 2000; Faisal et al., 2007; Barrios-Martinez et al., 2009;

Shahgholian et al., 2011; Mahdavian and Shahgholian, 2011; Wang and Crow, 2011). All these modelling approaches use the power flowing into the equivalent voltage source to directly control the DC voltage magnitude – to a greater or lesser extent, the ideal voltage source is treated as the DC bus of the STATCOM. Following this idea, it was shown in (Jabbari et al., 2011) that the STATCOM may be treated as a controllable reactive current source with a time delay response, one where its representation itself hinders the possibility, at best, of calculating the dynamic behaviour of the DC voltage.

Two voltage source converters linked on their corresponding DC side gives rise to multi-purpose applications of power converters. This scheme makes feasible the interconnection of two otherwise independent AC systems which may, or may not, be operating with different electrical frequencies; it is said that this is an asynchronous interconnection of AC systems, whose configuration is commonly referred to as VSC-HVDC link, a well-established application in the arena of high-voltage, high-power electronics. Physically, both VSC stations can be positioned in the same place (referred to as back-to-back connection) or be separated by a DC cable of a certain length (referred to as point-to-point connection). In both cases, the valve switching of the IGBTs driven by PWM controls, at the two VSC stations comprising the high-voltage DC link, permits to regulate dynamically and in an independent manner, both the reactive power injection at either terminal of the AC system and the power flow through the DC link (Latorre et al., 2008). Overall this power electronic device resembles the interconnection of two STATCOMs connected through their DC buses, hence, not surprisingly, the early attempts to modelling VSC-HVDC systems for power systems simulations, resorted to modelling the two VSCs by idealised voltage sources (Zhang, 2004*;* Acha et al., 2005; Ruihua et al., 2005*;* Teeuwsen, 2009). Alternatively, the two converters comprising the VSC-HVDC link have also been represented by equivalent controlled current sources (Cole and Belmans, 2008; Cole and Belmans, 2011), where the currents injected into the AC systems are computed by the existing difference between the complex voltage of the VSC terminals and the AC system bus at which the two conveters of the VSC-HVDC link is embedded. Although it is advantageous to represent each VSC comprising the HVDC link as a controlled voltage source owing to its much reduced complexity, the natural trade-off, when resorting to this modelling approach, will be not having its internal variables readily available, i.e., the DC voltages or the modulation ratio of the converter stations. In an attempt to circumvent the problem of not having available key parameters such as the modulation indices and DC voltages, lossless VSC models, with different control strategies, aimed at modelling two-terminal VSC-based transmission systems for power flows were developed in (Watson and Arrillaga, 2007). Besides the reduced modelling complexity of the VSCs, the employed solution approach to solving power networks including HVDC links was sequential, one where the interconnected AC networks are solved using the Fast Decoupled power-flow method and the DC variables are computed separately through the Newton's method, thus introducing frailty in the overall formulation, from the numerical standpoint. On the other hand, regarding the time-domain solutions of VSC-HVDC links, the concept of dynamic average modelling

has caught the attention of the power system community since it allows the modelling of VSC-HVDC systems in a detailed manner (Chiniforoosh et al., 2010*)*, but with relatively reduced computing time comparing to the time incurred in highly-detailed HVDC models used in electromagnetic-transient (EMT) simulators. In the dynamic average modelling approach, the average value of the output voltage waveform is calculated at each switching interval, a value that changes dynamically depending on the value of the reference waveform. Each power converter comprising the HVDC link is represented by a three-phase controlled voltage source on the AC side and as a controlled current source on the DC side (Moustafa and Filizadeh, 2012*)*. This approach may be time consuming when repetitive simulations studies are required in large-scale power system applications, for instance, in power system expansion planning and in operation planning. The solution time is always an important point to bear in mind and in the dynamic average modelling approach, increasing time steps is always a temptation but caution needs to be exercised when using this method since, as reported in (Moustafa and Filizadeh, 2012*)*, the use of large integration time steps, during the numerical solution of the model, may affect the accuracy of the results.

VSC-HVDC systems are designed to serve in a wide range of power systems applications. Two interconnected AC networks by means of an HVDC link exhibit a natural decoupling in terms of both voltage and frequency. This type of interconnections is primarily aimed at preventing the excursions of oscillations between AC systems, for instance, between a stronger and a weaker AC network. The back-to-back HVDC system linking the USA and Mexican power systems in the Eagle Pass substation and the submarine HVDC link interconnecting the power grids of Finland and Estonia are two examples of this application of the VSC-HVDC technology (Larsson et al., 2001; Ronström et al., 2007). Nevertheless, there are other applications where it is desirable to exert the influence of the strong network upon the weak network through the DC link. Such a situation would arise when power imbalances occur in an AC power network with little or no inertia and fed by a VSC-HVDC link (Guo and Zhao, 2010; Zhang et al., 2011). It should be noticed that in a power network with no inertia, even a very small power imbalance would lead the frequency to experience large rises or drops, depending on the nature of the power imbalance. Furthermore, all AC networks contain a degree of frequency-sensitive loads and VSCs do not possess the ability to strengthen, on their own, the inertial response or to aid the primary frequency control of AC networks. This is a problem demanding research attention because AC networks with poor inertia are likely to become more common (Callavik et al., 2012). Preliminary research progress in the area of frequency support, using HVDC systems, in electrical networks with very low inertia has been made in various fronts, using a range of equipment models and control schemes embedded in software with which simulation studies are carried out (Guo and Zhao, 2010; Zhang et al., 2011; Nnachi et al., 2013*;* Beccuti et al., 2014). For instance, microgrids fed by HVDC links have been a matter of research paying special attention to grid-forming, grid-feeding and grid-supporting topologies (Rocabert et al., 2012). The power control performance in AC microgrids, with their strong impact on frequency, are receiving far greater research attention because these types of grids are

likely to become cost-effective solutions for the interconnection of distributed generators in power systems (Sao and Lehn, 2008; Chung et al., 2010; Eghtedarpour and Farjah, 2014). In this particular application of the VSC-HVDC link, the under-representation of the converters as ideal voltage sources may cause, as in the case of the HVDC link interconnecting two power systems possessing each frequency-regulation equipment, the relevant phenomena that occur in the HVDC link not to be captured (Ruihua et al., 2005; Teeuwsen, 2009). As an attempt to overcome the underrepresented VSCs, switching-based models of the VSC-HVDC link together with three-phase AC power networks have been widely used to investigate the very timely subject of frequency support in low-inertia electrical networks (Guo and Zhao, 2010). However, the simulation studies associated with this approach are time consuming and therefore the AC networks used in such studies have been very contrived and, hence, poorly represented in terms of their actual size. To accelerate the solutions, the so-called dynamic average models have come into play since they enable a detailed representation of the power converters with moderate solution times (Chiniforoosh et al., 2010). As stated earlier, this solution may still incur large computing times, especially in applications of HVDCs providing frequency support to low-inertia grids, one that implicates mid-term to long-term dynamic simulation studies (simulation times of 5 seconds and more), since these are the time scales involved in most frequency oscillations phenomena present in power systems.

Point-to-point HVDC designs have advanced in the direction of multi-terminal VSC-HVDC systems which are currently at the frontier of VSC-based technology developments. The super DC grid which is being constructed in the North Sea is perhaps the most ambitious engineering project that will be built over the next few years (Vrana et al., 2010; Hertem and Ghandhari, 2010; Orths et al., 2012). Its operation will require skilful electrical engineers with suitable tools to deal with an array of technical problems that may emerge from its daily operation. Research interest in multi-terminal VSC-HVDC systems is relatively new; power systems' application tools are being upgraded to incorporate multi-terminal VSC-HVDC models to the conventional formulations of power flows and transient stability in order to conduct system-wide studies. For instance, to obtain the steady-state operating point of electrical networks, power-flow studies are carried out using sequential and quasi-unified solutions of the AC/DC networks formed by multi-terminal HVDC systems (Chen et al., 2005; Beerten et al., 2010; Ye et al., 2011; Baradar and Ghandhari, 2013, Wang and Barnes, 2014). In general terms, both methods compute the state variables of the AC sub-networks through a conventional power-flow algorithm, whilst a sub-problem is formulated for calculating the state variables of the DC network, something that is carried out at each iteration of the power-flow solution, until a convergence tolerance is reached. This sequential approach is attractive because it is straightforward to implement it in existing power flow programs, but caution has to be exercised because it might yield, at best, a non-quadratic convergence in Newton-based power-flow algorithms (Smed et al., 1991; Fuerte-Esquivel and Acha, 1997). In the context of dynamic studies of multi-terminal HVDC systems, a similar situation arises. Conducting holistic dynamic analyses of resultant AC/DC networks is not an easy task due to the size and complexity of

such large systems, although creditable efforts have been made (Cole et al., 2010; Chaudhuri et al., 2011; Peralta et al., 2012; Adam et al., 2013; Shen et al., 2014; Van der Meer et al., 2015). The simulation of innumerable scenarios is an inevitable requirement in power system dynamic analysis, hence, multi-terminal HVDC models which depart from a detailed EMT-type representation have been recently proposed aiming at reducing the computing time of the simulations (Peralta et al., 2012; Van der Meer et al., 2015), this being a major concern in practical networks. Not surprisingly, existing approaches use contrived, idealised voltage or current sources to represent each VSC station comprising the multi-terminal scheme, a fact that leads to executing additional calculations to adjust the power flow control in selected VSC stations (Adam et al., 2013) or solving the AC sub-networks and the DC network in a separated manner (Cole et al., 2010), thus introducing frailty in the formulation.

2.2 Advances in the state-of-the-art modelling of VSC-based equipment for power systems simulations

The field of high-voltage, high-power electronics is evolving rapidly, in a certain sense, thanks to the incentives and encouragements by governments and civil associations to employ cleaner energies as a platform for the development of future societies. Such is the case of the energy-harvesting and integration of a great amount of renewable resources into the power systems, or simply, the power exchange between neighbouring countries to avoid the use of fossil fuel-based power plants. Although this has brought about a relatively higher penetration of VSC-based equipment, there has been limited progress in terms of developing realistic models for system-wide studies. It may be argued that representative models of the network have traditionally been the cornerstone of planners and analysts of power systems because counting on suitable models and simulation tools enable them to anticipate operational problems that may emerge from the daily operation of power networks. In this sense, models of STATCOMs, back-to-back and point-to-point VSC-HVDC links and multi-terminal VSC-HVDC systems aimed at utility-scale electrical systems are also of major concern for power systems analysts.

The use of these VSC-based power devices has been on the increase in recent years. Paradoxically, the standard practice in their modelling approach has not fundamentally changed in the sense that reduced models are being used in order to facilitate, for instance, their implementation in existing power system simulation tools. On the contrary, if highly detailed models are employed, such as those found in EMT-type simulation packages, then excessive simulation times may be incurred; this is a fact that would impair their applicability in large power networks. Overall, this summarises the motivation of this thesis where the emphasis is placed on the investigation of a novel VSC model which may be used, with due extensions, as a modelling platform to represent

the STATCOM and any possible configuration of VSC-HVDC links including the so-called multi-terminal arrangement with arbitrary DC network topologies.

The whole family of models of VSC-based devices, developed in this thesis, represents a paradigm shift in the way voltage source converters are modelled and in the manner they are solved through a unified frame-of-reference for both power flow simulations and positive-sequence dynamic simulations. At first, the developed VSC itself contrasts with those in current use, departing from the controllable voltage source concept so far used to represent the converter. It rather uses a compound of a phase-shifting transformer and an equivalent shunt admittance to represent the phase-shifting and scaling nature of the PWM control, respectively, resulting in a far superior modelling flexibility when it comes to representing the AC and DC sides of the converter. The AC terminal of the power converter combines quite easily with the model of the interfacing load-tap changing transformer to make up the full VSC station found in STATCOMs or VSC-HVDC links. Given that the DC bus of the converter is explicitly represented, any basic circuit element may be attached to it, something that is particularly advantageous when setting up multi-terminal schemes where one or various DC transmission lines may connect to the DC node of the converter. All these facts result in a straightforward computation of the internal state variables of the VSCs, including the DC circuit, facilitating also the inclusion of conduction losses and switching losses.

Building up on this VSC model, carrying out the implementation of back-to-back and point-to-point VSC-HVDC models is not a difficult task; it only requires bearing in mind the operating features of this equipment. The four degrees of freedom found in actual VSC-HVDC installations, characterised by having simultaneous voltage support at its two AC terminals, DC voltage control at the inverter converter and regulated DC power at the rectifier converter, can be inherited to these models subjected to their particular application, i.e., to provide a constant power flow regulation through the DC link or to exert frequency regulation to low-inertia AC networks. Despite the pursued application, the grid-oriented VSC-HVDC models, developed in this thesis, encapsulate the essential steady-state and dynamic characteristics of the AC networks, the load-tap changing transformers, the power electronic converters and the DC transmission line, where the ensuing dynamic model is solved at only a fraction of the time than that required by highly-detailed, switching-based models. For instance, the four degrees of freedom together with a communication channel between the two converter stations are exploited to investigate the viability of exerting frequency control in low-inertia AC grids fed by a VSC-HVDC link, whose application lies in the realm of the mid-term to long-term power system dynamics involving several seconds of simulation, with the inverter station seen to act as a power electronic source capable of controlling the voltage magnitude and phase angle at its AC bus, hence, effectively acting as the slack bus of the AC grid with near-zero inertia.

With regards to the modelling of multi-terminal schemes, any converter might play the role of either a rectifier or inverter; this is so because the power may flow in a bidirectional fashion, i.e., from the DC grid to the AC network or vice versa, according to the prevailing operating conditions. In this context, the enhanced representation of the VSC model permits to make due provisions for three types of converters and their control strategies: the slack VSC whose aim is to control the DC voltage, the scheduled-power VSC that controls the power transfer and the passive VSC which is connected to AC networks that have no load/frequency control equipment. This gives rise to a comprehensive formulation, not found in other approaches, which is straightforwardly expandable to build up a model that comprises a number of VSC units which is commensurate with the number of AC sub-networks. More importantly, any type of AC/DC system, which is represented within this framework, will not omit the calculation of important variables of the VSCs, as is the case of the modulation ratio in other methods (Cole et al., 2010; Adam et al., 2013; Shen et al., 2014).

The overall steady-state and dynamic models of the new range of power electronic devices presented in this thesis are developed in an all-encompassing frame-of-reference based on the concept of power injections, where the non-linear algebraic equations of the power system, synchronous generators, STATCOMs, back-to-back and point-to-point VSC-HVDC links and multi-terminal VSC-HVDC links including its DC network are linearised around a base operating point and combined together with the discretised differential equations arising from the controls of the various equipment being modelled, for unified iterative solutions using the Newton-Raphson method. One such iterative solution is valid for a given point in time and its rate of convergence is quadratic. Moreover, the differential equations are discretised using the implicit trapezoidal method for enhanced numerical stability. This is a time-domain solution where the emphasis is placed on the dynamic models of the VSC-based equipment which is comprehensive, quite elegant and yields physical insight. It should be remarked that the new models put forward are not switching-based models (EMT-type models), such as those used in commercial packages as PSCAD and SIMULINK where the PWM pattern is fully emulated together with the switching action of each converter's IGBT valve. Rather, this model follows the standard way of representing electrical equipment and their controls in large-scale electrical power system modelling and simulations (Stagg and El-Abiad, 1968) – they are said to be lumped-type models. These models take the approach of representing one full period of the fundamental frequency waveform by a phasor corresponding to the base waveform's frequency. Lumped-type models are used in a number of industry-grade commercial packages, such as PowerWorld and PSS®E. In this formulation, the Jacobian matrix of the entire system becomes available, at any point in time, opening a window of applications for many other power systems studies, such as eigenvalue tracking, dynamic sensitivity analysis and evaluation of dynamic stability indices, although these analyses are not addressed in this thesis.

3 Modelling of VSC-based equipment for power flows

The power electronics equipment that emerged from the FACTS initiative (Hingorani and Gyugyi, 1999) has a common purpose: to alleviate one or more operational problems at key locations of the power grid. A case in point is the use of VSC-based FACTS controllers such as the STATCOM and VSC-HVDC systems. This technology is designed to regulate the reactive power at its point of connection with the grid, in response to both fast and slow network voltage variations. Its good performance arises from the fast action of the PWM-driven IGBT valves which enable the VSCs to maintain a smooth voltage profile at its connecting node, even in the face of severe disturbances in the power grid.

This chapter presents enhanced models of the STATCOM, back-to-back, pointo-to-point and multi-terminal VSC-HVDC links suitable for the steady-state operating regime of power grids. In the new models, the VSC itself is represented as a phase-shifting transformer; one where its primary and secondary sides yield quite naturally to the AC and DC sides of the power converter, respectively. Hence, the VSC model and by extension those of the STATCOM, two-terminal and multi-terminal VSC-HVDC links, take into account in aggregated form, the phase-shifting and scaling nature of the PWM control. Furthermore, the AC terminal of the VSC combines quite easily with the model of the interfacing load tap-changing transformer whereas the explicit representation of its DC side permits to connect, if required, to DC transmission lines or any other basic power system elements to its DC bus. Therefore, the modelling approach adopted for the STATCOM and VSC-HVDC systems is incremental in nature, whose frame-of-reference accomodates quite naturally any number of AC/DC networks generated by an arbitrary number of VSC converters.

3.1 Voltage source converter model

The combination of a voltage source converter and a load-tap changing transformer, as shown in Figure 3.1(a), is usually termed STATCOM. The AC terminal of the VSC is connected to the secondary winding of the OLTC transformer which plays the role of an interface between the power converter and the AC power grid, adding a further degree of voltage magnitude controllability. Physically, the VSC is built as a two-level or a multi-level converter that uses an array of self-commutating power electronic switches driven by PWM control. On its DC side, the VSC employs a capacitor bank of relatively small rating whose sole function is to support and stabilise the voltage at its DC bus to enable the converter operation. The converter keeps the capacitor charged to the required voltage level by making its output voltage lag the AC system voltage by a small angle (Hingorani and Gyugyi, 1999). The DC capacitor of value C_{dc} is shown quite prominently in Figure 3.1(a). It should be mentioned that C_{dc} is not responsible per se for the actual VAR generation process and certainly not at all for the VAR absorption process. Instead the VAR generation/absorption process is carried out by the PWM control to satisfy operating requirements. Such an electronic processing of the voltage and current waveforms may be well characterised, from the fundamental frequency representation standpoint, by an equivalent susceptance which can be either capacitive or inductive to conform to operating conditions.

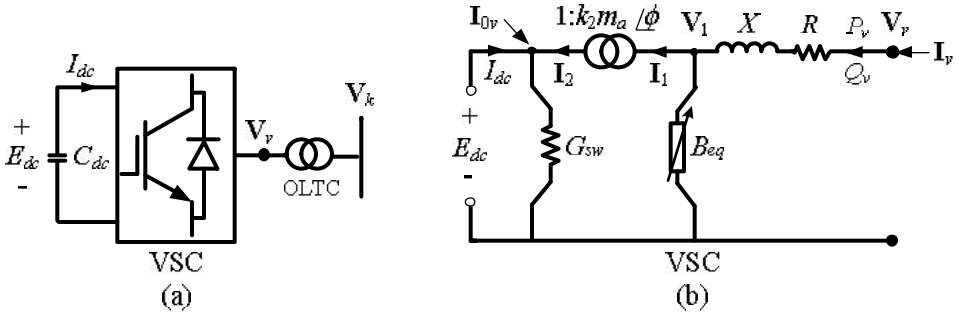

Figure 3.1 (a)STATCOM schematic representation; (b) VSC steady-state equivalent circuit

The VSC operation at the fundamental frequency may be modelled by means of electric circuit components, as shown in Figure 3.1(b). The electronic processing of the voltage and current waveforms of the VSC is well synthesised by a notional variable susceptance which is resposible for the whole reactive power production in the valve set of the converter. Furthermore, the ideal phase-shifting transformer with complex taps is the key component that enables a dissociation, from the voltage angle standpoint, between the AC voltage $\mathbf{V}_1$ and the DC voltage E_{dc}, resulting in the element that provides the interface AC and DC circuits of the VSC, which follows the ensuing basic voltage relationship (Acha and Kazemtabrizi, 2013).

$$\mathbf{V}_1 = k_2 m_a E_{dc} e^{j\phi} \tag{3.1}$$

where the complex voltage $\mathbf{V}_1$ is the voltage relative to the system phase reference, the tap magnitude m_a of the ideal phase-shifting transformer corresponds to the VSC's amplitude modulation coefficient where the following relationship holds for a two-level, three-phase VSC: $k_2 = \sqrt{3/8}$, the angle ϕ is the phase angle of voltage $\mathbf{V}_1$, and E_{dc} is the DC bus voltage which is a real scalar.

The steady-state VSC model comprises an ideal phase-shifting transformer with complex taps connected in series with an impedance, an equivalent variable shunt susceptance B_{eq} placed on the right-hand side of the transformer and a resistor on its DC side, as seen on Figure 3.1(b). The series reactance X represents the VSC's interface magnetics whereas the series resistor R is associated to the ohmic losses which are proportional to the AC terminal current squared. The switching loss model corresponds to a constant resistance (conductance G_0) ,which under the presence of constant DC voltage and constant load current, would yield constant power loss for a given switching frequency of the PWM converter. Admittedly, the constant resistance characteristic may be inaccurate because although the DC voltage is kept essentially constant, the load current will vary according to the prevailing operating condition. Hence, the shunt resistor (with a conductance value of G_{sw}) produces active power losses to account for the switching action of the PWM converter. This conductance is calculated according to the existing operating conditions and ensures that the switching losses are scaled by the quadratic ratio of the actual terminal current magnitude I_v to the nominal current I_{nom},

$$G_{sw} = G_0 \left(I_v / I_{nom} \right)^2 \tag{3.2}$$

The phase-shifting transformer making up the VSC model plays a crucial role in describing the converter operation; it decouples, angle-wise, the circuits connected at both ends of the transformer. This has the immediate consequence that the AC and DC circuits brought about by the inclusion of one or more VSCs in the power network can be solved by using conventional AC power system applications, such as the AC power flows. It is worth mentioning that the voltage E_{dc} is directly linked to the AC voltage $\mathbf{V}_1$ where only the phase-shifting transformer lies in between. Arguably, both voltages may be seen to be linked to the same connection point, and hence, to the same AC system. This fact is akin to that resulting from the steady-state modelling of idealised power transformers, in per-unit basis, employed in conventional power flow theory where, in a notional manner, the high-voltage and low-voltage sides are separated by a mere connection point. However, in the case of the VSC, its ideal phase-shifting transformer not only links two different voltage levels, but also, these two voltages may be seen to correspond to different current sys-

tems, i.e., alternating current and direct current.

In connection with the two-port VSC steady-state circuit shown in Figure 3.1(b), the voltage and current relationships in the ideal phase-shifting transformer are (Acha and Kazemtabrizi, 2013; Castro et al., 2013):

$$\frac{\mathbf{V}_1}{E_{dc}} = \frac{k_2 m_a \angle \phi}{1} \tag{3.3}$$

$$\frac{k_2 m_a \angle -\phi}{1} = \frac{\mathbf{I}_2}{\mathbf{I}_1} \tag{3.4}$$

The current flowing through the impedance connected between v and 1 is computed using (3.5):

$$\mathbf{I}_v = \mathbf{Y}_1 \left(\mathbf{V}_v - \mathbf{V}_1 \right) = \mathbf{Y}_1 \mathbf{V}_v - k_2 m_a \angle \phi \cdot \mathbf{Y}_1 E_{dc} \tag{3.5}$$

Where $\mathbf{Y}_1 = \left(R + \mathrm{j} X \right)^{-1} = G + \mathrm{j} B$. At the DC bus the relationship (3.6) holds,

$$\mathbf{I}_{0v} = -\mathbf{I}_2 + G_{sw} E_{dc} = -k_2 m_a \angle -\phi \cdot \mathbf{Y}_1 \mathbf{V}_v + k_2^2 m_a^2 \mathbf{Y}_1 E_{dc} + \mathrm{j} B_{eq} k_2^2 m_a^2 E_{dc} + G_{sw} E_{dc} \tag{3.6}$$

Rearranging equations (3.5) and (3.6) yields:

$$\begin{bmatrix} \mathbf{I}_v \\ \mathbf{I}_{0v} \end{bmatrix} = \begin{bmatrix} \mathbf{Y}_1 & -k_2 m_a \angle \phi \cdot \mathbf{Y}_1 \\ -k_2 m_a \angle -\phi \cdot \mathbf{Y}_1 & k_2^2 m_a^2 \left(\mathbf{Y}_1 + \mathrm{j} B_{eq} \right) + G_{sw} \end{bmatrix} \begin{bmatrix} \mathbf{V}_v \\ E_{dc} \end{bmatrix} \tag{3.7}$$

The VSC nodal power flow equations are derived using the definition of complex power $\mathbf{S} = \mathbf{V}\mathbf{I}^*$ and from the nodal current injections (3.7), as shown in (3.8).

$$\begin{bmatrix} \mathbf{S}_v \\ \mathbf{S}_{0v} \end{bmatrix} = \begin{bmatrix} \mathbf{V}_v & 0 \\ 0 & E_{dc} \end{bmatrix} \left\{ \begin{bmatrix} \mathbf{Y}_1 & -k_2 m_a \angle \phi \cdot \mathbf{Y}_1 \\ -k_2 m_a \angle -\phi \cdot \mathbf{Y}_1 & k_2^2 m_a^2 \left(\mathbf{Y}_1 + \mathrm{j} B_{eq} \right) + G_{sw} \end{bmatrix} \begin{bmatrix} \mathbf{V}_v \\ E_{dc} \end{bmatrix} \right\}^* \tag{3.8}$$

Defining the AC terminal voltage in polar coordinates $\mathbf{V}_v = V_v \angle \theta_v$, the active and reactive powers expressions for the powers injected at both ends of the VSC, (3.9)-(3.12), are derived after some arduous algebra.

$$P_v = V_v^2 G - k_2 m_a V_v E_{dc} \left[G \cos(\gamma) + B \sin(\gamma) \right] \tag{3.9}$$

$$Q_v = -V_v^2 B - k_2 m_a V_v E_{dc} \left[G \sin(\gamma) - B \cos(\gamma) \right] \tag{3.10}$$

$$P_{0v} = k_2^2 m_a^2 E_{dc}^2 G - k_2 m_a V_v E_{dc} \left[G \cos(\gamma) - B \sin(\gamma) \right] + E_{dc}^2 G_0 \left(I_v / I_{nom} \right)^2 \tag{3.11}$$

$$Q_{0v} = -k_2^2 m_a^2 E_{dc}^2 B - k_2 m_a V_v E_{dc}\left[-G\sin(\gamma) - B\cos(\gamma)\right] - k_2^2 m_a^2 E_{dc}^2 B_{eq} \tag{3.12}$$

where $\gamma = \theta_v - \phi$ represents the angular aperture between the angle of the converter's AC terminal voltage θ_v and the angle of the phase-shifting transformer ϕ . This angular difference is strongly linked to the active power flowing through the converter. Notice that the expression $k_2^2 m_a^2 E_{dc}^2 B_{eq}$ in (3.12) stands for the VAR generation/absorption process of the converter and that the term $E_{dc}^2 G_0 \left(I_v / I_{nom}\right)^2$ in (3.11) represents the switching power losses of the converter which depends on the terminal current squared (3.13).

$$I_v^2 = \left(G^2 + B^2\right)\left[V_v^2 + k_2^2 m_a^2 E_{dc}^2 - 2k_2 m_a V_v E_{dc}\cos(\gamma)\right] \tag{3.13}$$

3.2 On-load tap-changing transformer model

An on-load tap-changing transformer is a series-connected power system component whose main function is to step up or step down the voltage magnitude at its terminals by controlling the reactive power flowing through it. On-load tap-changing transformers are fitted with connection points along the transformer (taps) on the primary or secondary windings enabling the changing of the turns ratio. The tap magnitude regulation at one of the transformer's teminal usually ranges from 0.9 to 1.1. The power-flow model may be seen as the series-connection of the short-circuit impedance, $\mathbf{Z}_{ltc} = R_{ltc} + \mathrm{j}X_{ltc}$, representing the per-unit transfomer and an ideal transformer with taps ratio $T_v{:}1$, assuming that: (i) all the impedance together with the tap-changers are located on the primary side, and (ii) the impact of the magnetising branch is neglected (Acha et al., 2005). Figure 3.2(a) depicts a simplified single-phase steady-state representation of the OLTC transfomer for power flows, assuming that the total short-circuit impedance is located on the primary side. The schematic representation of the power-flow model for the OLTC transformer when the tap is in off-nominal position is shown in Fig. 3.2(b).

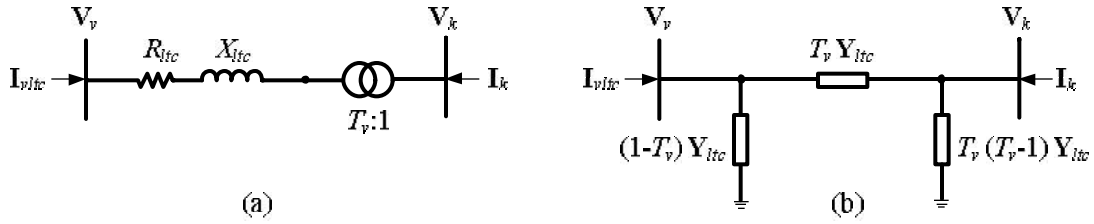

Figure 3.2 Simplified representation of the power-flow model for the OLTC transformer; (a) Tap in nominal position, (b) Tap in off-nominal position

where $\mathbf{Y}_{ltc} = \mathbf{Z}_{ltc}^{-1} = G_{ltc} + \mathrm{j}B_{ltc}$. Considering the situation where the OLTC transformer operates with its tap in off-nominal position, the expressions of the nodal current injections, at both ends of the OLTC transformer, are those shown in (3.14).

$$\begin{bmatrix} \mathbf{I}_{vltc} \\ \mathbf{I}_{kltc} \end{bmatrix} = \begin{bmatrix} \mathbf{Y}_{ltc} & -T_v \mathbf{Y}_{ltc} \\ -T_v \mathbf{Y}_{ltc} & T_v^2 \mathbf{Y}_{ltc} \end{bmatrix} \begin{bmatrix} \mathbf{V}_v \\ \mathbf{V}_k \end{bmatrix} \tag{3.14}$$

After some arduous algebra, the nodal power flow equations at both ends of the OLTC transformer are arrived at (3.15)-(3.18).

$$P_{vltc} = V_v^2 G_{ltc} - T_v V_v V_k \left[G_{ltc} \cos\left(\theta_v - \theta_k\right) + B_{ltc} \sin\left(\theta_v - \theta_k\right) \right] \tag{3.15}$$

$$Q_{vltc} = -V_v^2 B_{ltc} - T_v V_v V_k \left[G_{ltc} \sin\left(\theta_v - \theta_k\right) - B_{ltc} \cos\left(\theta_v - \theta_k\right) \right] \tag{3.16}$$

$$P_{kltc} = T_v^2 V_k^2 G_{ltc} - T_v V_k V_v \left[G_{ltc} \cos\left(\theta_v - \theta_k\right) + B_{ltc} \sin\left(\theta_v - \theta_k\right) \right] \tag{3.17}$$

$$Q_{kltc} = -T_v^2 V_k^2 B_{ltc} - T_v V_k V_v \left[G_{ltc} \sin\left(\theta_v - \theta_k\right) - B_{ltc} \cos\left(\theta_v - \theta_k\right) \right] \tag{3.18}$$

3.3 STATCOM model

The numerical solution of both the VSC model and the OLTC transformer model acting together as a STATCOM requires defining the mismatch power terms and state variables. A mismatch power is the difference between the net injected power and the calculated power at a given bus. Assuming that the STATCOM is connected at node k of the system, the set of mismatch equations that must be solved to obtain the steady-state equilibrium point is given by (3.19)-(3.24) (Acha and Kazemtabrizi, 2013; Castro et al., 2013).

$$\Delta P_k = -P_{kltc} - P_{dk} - P_k^{cal} \tag{3.19}$$

$$\Delta Q_k = -Q_{kltc} - Q_{dk} - Q_k^{cal} \tag{3.20}$$

$$\Delta P_v = -P_v - P_{dv} - P_{vltc} \tag{3.21}$$

$$\Delta Q_v = -Q_v - Q_{dv} - Q_{vltc} \tag{3.22}$$

$$\Delta Q_{0v} = -Q_{0v} \tag{3.23}$$

$$\Delta P_{0v} = -P_{0v} \tag{3.24}$$

where, for the sake of generality P_{dv}, P_{dk} and Q_{dv}, Q_{dk} represent the active and reactive powers

drawn by a load connected at bus v or k, respectively, and P_k^{cal} and Q_k^{cal} stand for the powers leaving the node k towards the rest of the power network. They are given by expressions (3.25)-(3.26).

$$P_k^{cal} = V_k^2 G_{kk} + V_k \sum_{m \in k} V_m \left[G_{km} \cos\left(\theta_k - \theta_m\right) + B_{km} \sin\left(\theta_k - \theta_m\right) \right] \tag{3.25}$$

$$Q_k^{cal} = -V_k^2 B_{kk} + V_k \sum_{m \in k} V_m \left[G_{km} \sin\left(\theta_k - \theta_m\right) - B_{km} \cos\left(\theta_k - \theta_m\right) \right] \tag{3.26}$$

Since the objective is to regulate the AC voltage magnitudes V_v and V_k at the specified values and, at the same time, to maintain E_{dc} at a constant value, the state variables $\left(\theta_k, T_v, \theta_v, m_a, B_{eq}, \phi\right)$ need to be found by solving (3.19)-(3.24). Hence, if a pre-defined generation and load pattern is gicen, the numerical solution for the STATCOM set of equations may be carried out using the Newton-Raphson method; the set of linearised power mismatch equations given by (3.27) must be assembled and combined with the Jacobian matrix of the whole network, i.e.:

$$\begin{bmatrix} \Delta P_k \\ \Delta Q_k \\ \Delta P_v \\ \Delta Q_v \\ \Delta Q_{0v} \\ \Delta P_{0v} \end{bmatrix}^i = - \begin{bmatrix} \frac{\partial \Delta P_k}{\partial \theta_k} & \frac{\partial \Delta P_k}{\partial T_v} & \frac{\partial \Delta P_k}{\partial \theta_v} & 0 & 0 & 0 \\ \frac{\partial \Delta Q_k}{\partial \theta_k} & \frac{\partial \Delta Q_k}{\partial T_v} & \frac{\partial \Delta Q_k}{\partial \theta_v} & 0 & 0 & 0 \\ \frac{\partial \Delta P_v}{\partial \theta_k} & \frac{\partial \Delta P_v}{\partial T_v} & \frac{\partial \Delta P_v}{\partial \theta_v} & \frac{\partial \Delta P_v}{\partial m_a} & 0 & \frac{\partial \Delta P_v}{\partial \phi} \\ \frac{\partial \Delta Q_v}{\partial \theta_k} & \frac{\partial \Delta Q_v}{\partial T_v} & \frac{\partial \Delta Q_v}{\partial \theta_v} & \frac{\partial \Delta Q_v}{\partial m_a} & 0 & \frac{\partial \Delta Q_v}{\partial \phi} \\ 0 & 0 & \frac{\partial \Delta Q_{0v}}{\partial \theta_v} & \frac{\partial \Delta Q_{0v}}{\partial m_a} & \frac{\partial \Delta Q_{0v}}{\partial B_{eq}} & \frac{\partial \Delta Q_{0v}}{\partial \phi} \\ 0 & 0 & \frac{\partial \Delta P_{0v}}{\partial \theta_v} & \frac{\partial \Delta P_{0v}}{\partial m_a} & 0 & \frac{\partial \Delta P_{0v}}{\partial \phi} \end{bmatrix}^i \begin{bmatrix} \Delta \theta_k \\ \Delta T_v \\ \Delta \theta_v \\ \Delta m_a \\ \Delta B_{eq} \\ \Delta \phi \end{bmatrix}^i \tag{3.27}$$

The state variable increments computed at each iteraion i are used to update the variables after the $i-th$ iteration, as shown in (3.28).

$$\begin{bmatrix} \theta_k \\ T_v \\ \theta_v \\ m_a \\ B_{eq} \\ \phi \end{bmatrix}^{i+1} = \begin{bmatrix} \theta_k \\ T_v \\ \theta_v \\ m_a \\ B_{eq} \\ \phi \end{bmatrix}^i + \begin{bmatrix} \Delta \theta_k \\ \Delta T_v \\ \Delta \theta_v \\ \Delta m_a \\ \Delta B_{eq} \\ \Delta \phi \end{bmatrix}^i \tag{3.28}$$

3.3.1 Checking of the converter's operating limits and nonregulated solutions

The aggregated representation of the power electronic converter and the load tap-changing transformer facilitates the checking of the converter's physical operating limits. This is something that results particularly advantageous since in VSC-based power converters the current flowing through the electronic switches is a crucial limiting factor in their operation. Hence, a terminal current restriction can be advantageously appended to the developed set of equations (3.19)-(3.24). Equation (3.29) shows the restriction that would be active in cases where the magnitude of the terminal current I_v exceeds its nominal value I_{nom}.

$$\Delta I_{\lim} = I_{nom} - I_v \tag{3.29}$$

Therefore, in the event the current of the converter surpasses its maximum allowed current, the new set of state variables $\left(\theta_v, V_v, \phi, B_{eq}, \theta_k, T_v, m_a\right)$ will define the steady-state operating conditions of the VSC. This implies that the AC voltage V_v is not regulated, however the modulation ratio of the VSC continues to be part of the set of state variables whose main aim is to bring the current I_v back to its nominal value. Notice that in this situation the Jacobian matrix of the STATCOM model must be expanded by one dimension.

In addition to the current limit, due attention must be paid to the operating limits of the modulation index $m_a \leq 1$ so as not to incur over-modulation. At the same time, keeping the tap of the OLTC between its design limits $T_{\min} \leq T_v \leq T_{\max}$ will ensure obtaining realistic results. Hence, if no voltage regulation at node v is applied by the converter, the voltage magnitude V_v must replace m_a in the set of variables $\left(\theta_v, V_v, \phi, B_{eq}, \theta_k, T_v\right)$. On the other hand, if no voltage regulation at node k is applied by the OLTC, then the set of variables will be $\left(\theta_v, m_a, \phi, B_{eq}, \theta_k, V_k\right)$, keeping at the same time the tap fixed at its limit. It is worth mentioning that the violation of either the modulation index or the tap of the OLTC does not cause an expansion of the set of equations of the STATCOM as is the case for the violation of the current limit. Also, caution needs to be exercised with the selection of the DC voltage value to prevent the modulation index from being near its maximum limit since numerical issues might emerge in operating scenarios where the STATCOM is delivering its nominal reactive current.

3.3.2 Initialisation of variables

It is well-known that the convergence of Newton's algorithm may face numerical issues if inadequate initial conditions are selected for the state variables. The VSC has three state variables that require initialisation. They are the amplitude modulation ratio, the phase shifting angle and the equivalent shunt susceptance. A good practice is to set m_a and ϕ at 1 and 0, respectively, whilst the susceptance B_{eq} may be also given the initial value of 0. The VSC is assumed to operate within the linear region, whereas the phase-shifting angle is assumed to have no limits. As for the case of the OLTC, it is convenient to initialise its tap T_v at 1.

3.4 High-voltage direct current link

If two VSC stations are linked as shown in Figure 3.3, a VSC-HVDC system is formed and termed point-to-point configuration. In this arrangement of converters, electric power is taken from one point of the AC network, converted to DC in the rectifier station, transmitted through the DC link and then converted back to AC in the inverter station and injected into the receiving AC network. In addition to transmitting power in DC form, this VSC-HVDC system is also capable of supplying/absorbing reactive power at both AC terminals and to provide independent dynamic voltage control. Each converter station comprises an interfacing OLTC transformer where their primary and secondary windings are connected to the high-voltage power grid and to the AC side of the VSC, respectively – this makes each VSC to be shunt-connected with the AC system, just as if they were two STATCOMs. However, the two VSCs are series-connected on their DC sides. If the cable does not exist then this may be assumed to be a cable of zero resistance and the VSC-HVDC configuration is termed back-to-back.

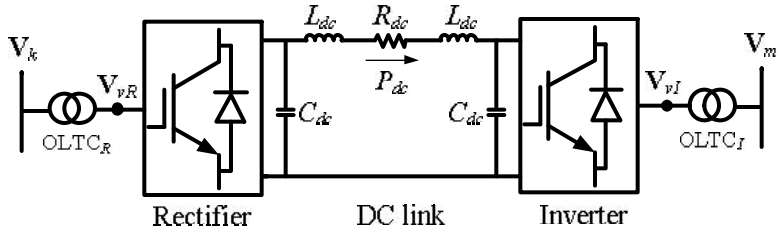

Figure 3.3 VSC-HVDC schematic representation

The VSC-HVDC link system is built with two VSCs coupled back-to-back through a DC cable, where it is a standard practice to operate the DC link with constant voltage. A capacitor bank of value C_{dc} and a smoothing inductor of value L_{dc} are connected at each VSC's DC bus to ensure a

stable and smooth operation of the DC transmission system. The AC voltage magnitudes, V_{vR} and V_{vI}, and phase angles are controlled by modulating the PWM patterns in the VSCs. The change of the PWM pattern takes place in an almost instantaneous basis, resulting in a fast control of both active and reactive powers, with further voltage control attained by means of the OLTCs that interface the power electronic converters to their respective AC networks. The switching of the IGBT valves commanded by the PWM patterns, gives these converters the overall characteristic of a virtual power source which can either inject or draw active and reactive powers independently.

In power system applications, it is necessary to develop suitable positive-sequence models that permit assessment of the steady-state behaviour of the whole system in a fraction of time. Repetitive simulations are often needed to conduct system-wide studies required to ensure the security and reliability of the power network. To that end, steady-state models of VSC-based systems must be tailored in such a way that their major features are captured, enabling not only the estimation of the steady-state operating conditions of all the interconnected AC networks and the HVDC link, but also, with due extensions to the steady-state model, to be applicable to other type of studies such as state estimation, optimal power flows and dynamic simulations of power systems, among others. A suitable VSC-HVDC model for steady-state studies may be developed with particular reference to a certain pursued application. From the point of view of its integration to power networks, different HVDC configurations may emerge. For instance, embedded HVDC links are physically connected to the same meshed synchronous power system – the AC terminal of both the rectifier and inverter share the same electrical reference from the conceptual power flow standpoint. Another case in point is the employment of HVDC systems to interconnect two otherwise independent electrical networks; it is obvious that in such configuration, both VSCs operate and respond to power grids with decoupled electrical references, where even their operating electrical frequencies can be different from each other. Hence, from the power-flow solution point of view, the physical connection configuration of HVDCs into power networks may give rise to a different set of power flow equations and state variables to be computed. However, the basic functions of an HVDC link will remain the same, namely, the control of both DC power flow and AC voltage. A number of regulation options are available for the VSC-HVDC link by making use of the voltage and power regulating capabilities of the two VSCs and the voltage regulating capabilities of the two OLTCs. A common practice is to use the rectifier to regulate power on its DC side and to use the inverter to regulate voltage on its DC side, whereas at the same time both VSC stations exert voltage control at their corresponding AC teminal.

The fundamental voltage relationship of power converters (3.1) is the starting point to linking the AC/DC system formed by the point-to-point VSC-HVDC system and the interconnected AC networks. Figure 3.4 depicts the equivalent circuit of the VSC-HVDC link aimed at its fundamental frequency operation; it may be modelled by employing two of the VSC models shown in Figure 3.1(b). For both the rectifier and inverter stations, the ideal phase shifting transformer with complex

tap decouples, angle-wise, both connecting ends and provides the fundamental AC and DC voltage relationship that exits at each converter station. This implies that a true DC circuit is obtained with the DC voltages, E_{dcR} and E_{dcI}, being the internal state variables of the point-to-point HVDC link (Acha et al., 2013). Also notice that it is assumed that the capacitors and inductors are an open circuit and short circuit, respectively, something that agrees with their steady-state behaviour when they are fed by DC current.

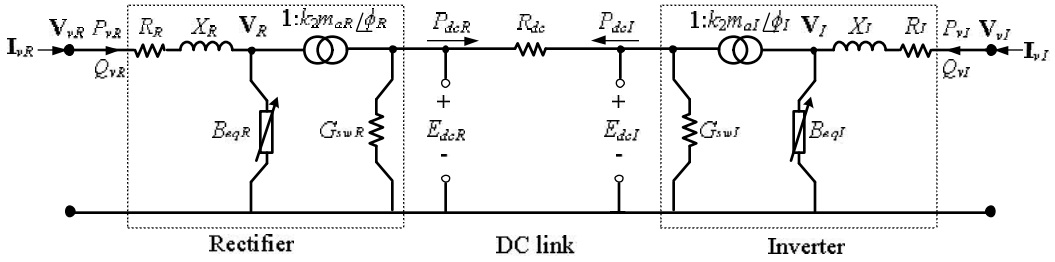

Figure 3.4 Steady-state equivalent circuit of the VSC-HVDC link

Following nearly the same derivation carried out to determine the voltage and current relationships existing for a single VSC station, the two-terminal VSC model is developed. The nodal admittance matrix for the HVDC system is given in (3.30).

$$\begin{bmatrix} \mathbf{I}_{vR} \\ \mathbf{I}_{0vR} \\ \mathbf{I}_{vI} \\ \mathbf{I}_{0vI} \end{bmatrix} = \left\{ \begin{bmatrix} \mathbf{Y}_{AR} & \mathbf{Y}_{BR} & 0 & 0 \\ \mathbf{Y}_{CR} & \mathbf{Y}_{DR} & 0 & 0 \\ 0 & 0 & \mathbf{Y}_{AI} & \mathbf{Y}_{BI} \\ 0 & 0 & \mathbf{Y}_{CI} & \mathbf{Y}_{DI} \end{bmatrix} + \begin{bmatrix} 0 & 0 & 0 & 0 \\ 0 & G_{dc} & 0 & -G_{dc} \\ 0 & 0 & 0 & 0 \\ 0 & -G_{dc} & 0 & G_{dc} \end{bmatrix} \right\} \begin{bmatrix} \mathbf{V}_{vR} \\ E_{dcR} \\ \mathbf{V}_{vI} \\ E_{dcI} \end{bmatrix} \tag{3.30}$$

where $G_{dc} = R_{dc}^{-1}$. The structure of (3.30) carries two matrix terms whose individual entries correspond to the nodal admittance matrices of both the rectifier and inverter stations and the admittance matrix of the DC transmission line, as shown in equations (3.31)-(3.32).

$$\begin{aligned} \mathbf{Y}_{AR} &= \mathbf{Y}_{1R} \\ \mathbf{Y}_{BR} &= -k_2 m_{aR} \angle \phi_R \cdot \mathbf{Y}_{1R} \\ \mathbf{Y}_{CR} &= -k_2 m_{aR} \angle -\phi_R \cdot \mathbf{Y}_{1R} \\ \mathbf{Y}_{DR} &= k_2^2 m_{aR}^2 \left(\mathbf{Y}_{1R} + \mathrm{j} B_{eqR} \right) + G_{swR} \end{aligned} \tag{3.31}$$

$$\begin{aligned} \mathbf{Y}_{AI} &= \mathbf{Y}_{1I} \\ \mathbf{Y}_{BI} &= -k_2 m_{aI} \angle \phi_I \cdot \mathbf{Y}_{1I} \\ \mathbf{Y}_{CI} &= -k_2 m_{aI} \angle -\phi_I \cdot \mathbf{Y}_{1I} \\ \mathbf{Y}_{DI} &= k_2^2 m_{aI}^2 \left(\mathbf{Y}_{1I} + \mathrm{j} B_{eqI} \right) + G_{swI} \end{aligned} \tag{3.32}$$

The nodal complex power equations of the HVDC are derived by multiplying the nodal voltages by the conjugate of the nodal currents, as shown in (3.33).

$$\begin{bmatrix} \mathbf{S}_{vR} \\ \mathbf{S}_{0vR} \\ \mathbf{S}_{vI} \\ \mathbf{S}_{0vI} \end{bmatrix} = \begin{bmatrix} \mathbf{V}_{vR} & 0 & 0 & 0 \\ 0 & E_{dcR} & 0 & 0 \\ 0 & 0 & \mathbf{V}_{vI} & 0 \\ 0 & 0 & 0 & E_{dcI} \end{bmatrix} \left\{ \begin{bmatrix} \mathbf{Y}_{\mathbf{A}R} & \mathbf{Y}_{\mathbf{B}R} & 0 & 0 \\ \mathbf{Y}_{CR} & \mathbf{Y}_{\mathbf{D}R} & 0 & 0 \\ 0 & 0 & \mathbf{Y}_{\mathbf{A}I} & \mathbf{Y}_{\mathbf{B}I} \\ 0 & 0 & \mathbf{Y}_{CI} & \mathbf{Y}_{\mathbf{D}I} \end{bmatrix} + \begin{bmatrix} 0 & 0 & 0 & 0 \\ 0 & G_{dc} & 0 & -G_{dc} \\ 0 & 0 & 0 & 0 \\ 0 & -G_{dc} & 0 & G_{dc} \end{bmatrix} \right\}^* \begin{bmatrix} \mathbf{V}_{vR} \\ E_{dcR} \\ \mathbf{V}_{vI} \\ E_{dcI} \end{bmatrix}^* \tag{3.33}$$

The nodal voltages at the AC buses are defined in polar coordinates as $\mathbf{V}_{vR} = V_{vR} \angle \theta_{vR}$ and $\mathbf{V}_{vI} = V_{vI} \angle \theta_{vI}$. Equations (3.34)-(3.41) are the nodal active and reactive powers expressions of the HVDC which are obtained after some complex number algebra and separating into real and imaginary parts.

$$P_{vR} = V_{vR}^2 G_R - k_2 m_{aR} V_{vR} E_{dcR} \left[G_R \cos(\gamma_R) + B_R \sin(\gamma_R) \right] \tag{3.34}$$

$$Q_{vR} = -V_{vR}^2 B_R - k_2 m_{aR} V_{vR} E_{dcR} \left[G_R \sin(\gamma_R) - B_R \cos(\gamma_R) \right] \tag{3.35}$$

$$P_{0vR} = k_2^2 m_{aR}^2 E_{dcR}^2 G_R - k_2 m_{aR} V_{vR} E_{dcR} \left[G_R \cos(\gamma_R) - B_R \sin(\gamma_R) \right] + E_{dcR}^2 G_{0R} \left(I_{vR} / I_{nom} \right)^2 \tag{3.36}$$

$$Q_{0vR} = -k_2^2 m_{aR}^2 E_{dcR}^2 B_R - k_2 m_{aR} V_{vR} E_{dcR} \left[-G_R \sin(\gamma_R) - B_R \cos(\gamma_R) \right] - k_2^2 m_{aR}^2 E_{dcR}^2 B_{eqR} \tag{3.37}$$

$$P_{vI} = V_{vI}^2 G_I - k_2 m_{aI} V_{vI} E_{dcI} \left[G_I \cos(\gamma_I) + B_I \sin(\gamma_I) \right] \tag{3.38}$$

$$Q_{vI} = -V_{vI}^2 B_I - k_2 m_{aI} V_{vI} E_{dcI} \left[G_I \sin(\gamma_I) - B_I \cos(\gamma_I) \right] \tag{3.39}$$

$$P_{0vI} = k_2^2 m_{aI}^2 E_{dcI}^2 G_I - k_2 m_{aI} V_{vI} E_{dcI} \left[G_I \cos(\gamma_I) - B_I \sin(\gamma_I) \right] + E_{dcI}^2 G_{0I} \left(I_{vI} / I_{nom} \right)^2 \tag{3.40}$$

$$Q_{0vI} = -k_2^2 m_{aI}^2 E_{dcI}^2 B_I - k_2 m_{aI} V_{vI} E_{dcI} \left[-G_I \sin(\gamma_I) - B_I \cos(\gamma_I) \right] - k_2^2 m_{aI}^2 E_{dcI}^2 B_{eqI} \tag{3.41}$$

where the angular aperture between the angles of each corresponding AC terminal voltage and phase-shifting transformer are given by $\gamma_R = \theta_{vR} - \phi_R$ and $\gamma_I = \theta_{vI} - \phi_I$, for the rectifier and inverter stations, respectively. The DC power expressions (3.42)-(3.43) conclude the overall steady-state power flow equations of the HVDC model, where P_{dcR} stands for the power flowing from the DC bus of the rectifier towards the DC bus of the inverter and P_{dcI} is the power flowing in the opposite direction through the DC transmission cable.

$$P_{dcR} = \left(E_{dcR}^2 - E_{dcR} E_{dcI} \right) G_{dc} \tag{3.42}$$

$$P_{dcI} = \left(E_{dcI}^2 - E_{dcI} E_{dcR} \right) G_{dc} \tag{3.43}$$

The current expressions (3.44)-(3.45) at both the sending and receiving ends of the HVDC link are needed to prevent the VSCs from exceeding its physical operating limits, as explained in section 3.3.1.

$$I_{vR}^2 = \left(G_R^2 + B_R^2\right)\left[V_{vR}^2 + k_2^2 m_{aR}^2 E_{dcR}^2 - 2k_2 m_{aR} V_{vR} E_{dcR} \cos\left(\gamma_R\right)\right] \tag{3.44}$$

$$I_{vI}^2 = \left(G_I^2 + B_I^2\right)\left[V_{vI}^2 + k_2^2 m_{aI}^2 E_{dcI}^2 - 2k_2 m_{aI} V_{vI} E_{dcI} \cos\left(\gamma_I\right)\right] \tag{3.45}$$

3.4.1 Point-to-point HVDC link model with DC power regulation capabilities

The solution of the nonlinear VSC-HVDC nodal power equations may be carried out for a predefined set of generation and load pattern. In AC networks the slack generator provides the angular reference to all nodes of the system; it also supplies as much active and reactive powers as needed for balancing the power flows of the network considering the given system generation and load – this implies that the slack generator copes with the power losses of the whole power system. An HVDC system linking two otherwise independent AC power networks requires synchronous generation, and more precisely a slack bus at each AC system, in order to make the DC power flow control possible. This is so because power losses cannot be known a priori in the system fed by the inverter. On the other hand, in the case of an embedded HVDC link, the meshed power network would require only one slack generator as usual. The standard practice of controlling the DC power flow to a scheduled value with the rectifier and the DC voltage at its nominal value with the inverter is followed in the developed steady-state VSC-HVDC model.

The mismatch equations arising from the difference between the net power and the calculated power, at buses vR, vI and DC buses of the VSC-HVDC system, are used to determine the steady-state equilibrium point of both the power networks and the HVDC system itself. The set of equations (3.46)-(3.57) include the power expressions of the associated power transformers with OLTCs; they must be solved together with the overall mismatch power flow equations arising from the interconnected AC networks for a unified, iterative solution (Castro and Acha, 2015a).

$$\Delta P_k = -P_{kltc} - P_{dk} - P_k^{cal} \tag{3.46}$$

$$\Delta Q_k = -Q_{kltc} - Q_{dk} - Q_k^{cal} \tag{3.47}$$

$$\Delta P_{vR} = -P_{vR} - P_{dvR} - P_{vRltc} \tag{3.48}$$

$$\Delta Q_{vR} = -Q_{vR} - Q_{dvR} - Q_{vRltc} \tag{3.49}$$

$$\Delta Q_{0vR} = -Q_{0vR} \tag{3.50}$$

$$\Delta P_{0vR} = -\left(P_{0vR} + P_{dcR}\right) \tag{3.51}$$

$$\Delta P_m = -P_{mltc} - P_{dm} - P_m^{cal} \tag{3.52}$$

$$\Delta Q_m = -Q_{mltc} - Q_{dm} - Q_m^{cal} \tag{3.53}$$

$$\Delta P_{vI} = -P_{vI} - P_{dvI} - P_{vIltc} \tag{3.54}$$

$$\Delta Q_{vI} = -Q_{vI} - Q_{dvI} - Q_{vIltc} \tag{3.55}$$

$$\Delta Q_{0vI} = -Q_{0vI} \tag{3.56}$$

$$\Delta P_{0vI} = -\left(P_{0vI} + P_{dcI}\right) \tag{3.57}$$

where the powers of the OLTCs $P_{vRltc}, Q_{vRltc}, P_{kltc}, Q_{kltc}, P_{vIltc}, Q_{vIltc}, P_{mltc}, Q_{mltc}$ are computed as shown in Section 3.2 and the powers $P_k^{cal}, Q_k^{cal}, P_m^{cal}, Q_m^{cal}$ are calculated as in (3.25) and (3.26).

In addition to the mismatch equations arising from each VSC station, the constraining branch power equation (3.58) is required to ensure that the power flow leaving the rectifier station P_{0vR} be kept at the scheduled value P_{sch}. Given that the inverter station is chosen to keep the DC link voltage at a constant value, then the additional equation (3.58) also allows the computation of the DC voltage at the rectifier's side E_{dcR}.

$$\Delta P_{sch} = -\left(P_{sch} + P_{0vR}\right) \tag{3.58}$$

Since the objective is to regulate the voltage magnitude at both AC sides of the VSC-HVDC while keeping the DC voltage of the inverter constant, therefore V_{vR}, V_{vI} and E_{dcI} are not part of the set of state variables that need to be computed. The set of linearised HVDC power mismatch equations is given by (3.59); this has to be integrated into the set of linearised mismatch equations of the whole network to compute the equilibrium point through a power-flow solution.

$$\left[\Delta F\right]^i = -\left[\begin{array}{ccc} \mathbf{J_{RR}} & \mathbf{0} & \mathbf{J_{Ra}} \\ \mathbf{0} & \mathbf{J_{II}} & \mathbf{0} \\ \hline \mathbf{J_{aR}} & \mathbf{0} & \dfrac{\partial \Delta P_{0vR}}{\partial E_{dcR}} \end{array}\right]^i \left[\Delta z\right]^i \tag{3.59}$$

where the $\mathbf{0}$ entries are zero-padded matrices of suitable orders; the individual matrices of each VSC station $\mathbf{J_{RR}}$ and $\mathbf{J_{II}}$ together with the vectors containing the derivatives with respect to the DC voltage of the rectifier $\mathbf{J_{aR}}$ and $\mathbf{J_{Ra}}$ are shown in (3.60)-(3.62).

$$\mathbf{J_{RR}}=\begin{bmatrix} \frac{\partial\Delta P_k}{\partial\theta_k} & \frac{\partial\Delta P_k}{\partial T_{vR}} & \frac{\partial\Delta P_k}{\partial\theta_{vR}} & 0 & 0 & 0 \\ \frac{\partial\Delta Q_k}{\partial\theta_k} & \frac{\partial\Delta Q_k}{\partial T_{vR}} & \frac{\partial\Delta Q_k}{\partial\theta_{vR}} & 0 & 0 & 0 \\ \frac{\partial\Delta P_{vR}}{\partial\theta_k} & \frac{\partial\Delta P_{vR}}{\partial T_{vR}} & \frac{\partial\Delta P_{vR}}{\partial\theta_{vR}} & \frac{\partial\Delta P_{vR}}{\partial m_{aR}} & 0 & \frac{\partial\Delta P_{vR}}{\partial\phi_R} \\ \frac{\partial\Delta Q_{vR}}{\partial\theta_k} & \frac{\partial\Delta Q_{vR}}{\partial T_{vR}} & \frac{\partial\Delta Q_{vR}}{\partial\theta_{vR}} & \frac{\partial\Delta Q_{vR}}{\partial m_{aR}} & 0 & \frac{\partial\Delta Q_{vR}}{\partial\phi_R} \\ 0 & 0 & \frac{\partial\Delta Q_{0vR}}{\partial\theta_{vR}} & \frac{\partial\Delta Q_{0vR}}{\partial m_{aR}} & \frac{\partial\Delta Q_{0vR}}{\partial B_{eqR}} & \frac{\partial\Delta Q_{0vR}}{\partial\phi_R} \\ 0 & 0 & \frac{\partial\Delta P_{sch}}{\partial\theta_{vR}} & \frac{\partial\Delta P_{sch}}{\partial m_{aR}} & 0 & \frac{\partial\Delta P_{sch}}{\partial\phi_R} \end{bmatrix} \tag{3.60}$$

$$\mathbf{J_{II}}=\begin{bmatrix} \frac{\partial\Delta P_m}{\partial\theta_m} & \frac{\partial\Delta P_m}{\partial T_{vI}} & \frac{\partial\Delta P_m}{\partial\theta_{vI}} & 0 & 0 & 0 \\ \frac{\partial\Delta Q_m}{\partial\theta_m} & \frac{\partial\Delta Q_m}{\partial T_{vI}} & \frac{\partial\Delta Q_m}{\partial\theta_{vI}} & 0 & 0 & 0 \\ \frac{\partial\Delta P_{vI}}{\partial\theta_m} & \frac{\partial\Delta P_{vI}}{\partial T_{vI1}} & \frac{\partial\Delta P_{vI}}{\partial\theta_{vI}} & \frac{\partial\Delta P_{vI}}{\partial m_{aI}} & 0 & \frac{\partial\Delta P_{vI}}{\partial\phi_I} \\ \frac{\partial\Delta Q_{vI}}{\partial\theta_m} & \frac{\partial\Delta Q_{vI}}{\partial T_{vI}} & \frac{\partial\Delta Q_{vI}}{\partial\theta_{vI}} & \frac{\partial\Delta Q_{vI}}{\partial m_{aI}} & 0 & \frac{\partial\Delta Q_{vI}}{\partial\phi_I} \\ 0 & 0 & \frac{\partial\Delta Q_{0vI}}{\partial\theta_{vI}} & \frac{\partial\Delta Q_{0vI}}{\partial m_{aI}} & \frac{\partial\Delta Q_{0vI1}}{\partial B_{eqI1}} & \frac{\partial\Delta Q_{0vI}}{\partial\phi_I} \\ 0 & 0 & \frac{\partial\Delta P_{0vI}}{\partial\theta_{vI}} & \frac{\partial\Delta P_{0vI}}{\partial m_{aI}} & 0 & \frac{\partial\Delta P_{0vI}}{\partial\phi_I} \end{bmatrix} \tag{3.61}$$

$$\mathbf{J_{aR}}=\begin{bmatrix} 0 & 0 & \frac{\partial\Delta P_{0vR}}{\partial\theta_{vR}} & \frac{\partial\Delta P_{0vR}}{\partial m_{aR}} & 0 & \frac{\partial\Delta P_{0vR}}{\partial\phi_R} \end{bmatrix},\quad \mathbf{J_{Ra}}=\begin{bmatrix} 0 & 0 & \frac{\partial\Delta P_{vR}}{\partial E_{dcR}} & \frac{\partial\Delta Q_{vR}}{\partial E_{dcR}} & \frac{\partial\Delta Q_{0vR}}{\partial E_{dcR}} & \frac{\partial\Delta P_{sch}}{\partial E_{dcR}} \end{bmatrix}^T \tag{3.62}$$

The vectors of mismatches and corrections are shown in (3.63) and (3.64), respectively. The state variables of the VSCs comprising the point-to-point VSC-HVDC link, including the DC voltage E_{dcR}, are updated at each iteration i as (3.65).

$$\left[\Delta F\right]^i=\left[\Delta P_k\ \Delta Q_k\ \Delta P_{vR}\ \Delta Q_{vR}\ \Delta Q_{0vR}\ \Delta P_{sch}\ \Delta P_m\ \Delta Q_m\ \Delta P_{vI}\ \Delta Q_{vI}\ \Delta Q_{0vI}\ \Delta P_{0vI}\ \Delta P_{0vR}\right]^T \tag{3.63}$$

$$\left[\Delta z\right]^i=\left[\Delta\theta_k\ \Delta T_{vR}\ \Delta\theta_{vR}\ \Delta m_{aR}\ \Delta B_{eqR}\ \Delta\phi_R\ \Delta\theta_m\ \Delta T_{vI}\ \Delta\theta_{vI}\ \Delta m_{aI}\ \Delta B_{eqI}\ \Delta\phi_I\ \Delta E_{dcR}\right]^T \tag{3.64}$$

$$\left[z\right]^{i+1}=\left[z\right]^i+\left[\Delta z\right]^i \tag{3.65}$$

Notice that the Jacobian matrices of the VSCs are decoupled but that the overall system of equations is strongly coupled through the constrained branch power (3.58). To guarantee that each VSC operates within feasible operating limits, a limit checking of the modulation ratio and terminal current must take place, as shown in Section 3.3.1. Furthermore, to enable good starting conditions for the Newton's algorithm, the same guidelines explained in Section 3.3.2 must be considered.

3.4.2 Point-to-point HVDC link model feeding into a passive network

Two independent AC networks connected using an HVDC link exhibit a natural decoupling in terms of both voltage and frequency and it is said that the two AC power systems are interconnected in an asynchronous manner. These kinds of interconnections are primarily aimed at preventing the excursions of oscillations between AC systems, for instance, between a stronger and a weaker electrical network. Nevertheless, there are other applications where it is desirable to exert the influence of the strong network upon the weak network through the DC link. A case in point is the use of a VSC-HVDC link to feed an island system, e.g. a passive network containing only load. In such situation, the inverter station must play the role of a virtual synchronous generator with power regulation capabilities, providing at the same time the electrical angular reference for the passive network.This means that contrary to the customary control of a fixed amount of power in the DC link, the power injected by the inverter must be one that matches the passive network demand plus its transmission losses.

The power flow application tool must enable the determination of such an equilibrium point which calls for the development of a suitable VSC-HVDC model able to estimate the steady-state operating conditions of all, the AC network coupled to the rectifier, the HVDC link and the passive network together. To such and end, the power balance at each node of the VSC-HVDC system may be achieved by solving the set of equations (3.66)-(3.77). These equations must be added to the set of mismatch power flow equations arising from the interconnected AC networks for a unified solution.

$$\Delta P_k = -P_{kltc} - P_{dk} - P_k^{cal} \tag{3.66}$$

$$\Delta Q_k = -Q_{kltc} - Q_{dk} - Q_k^{cal} \tag{3.67}$$

$$\Delta P_{vR} = -P_{vR} - P_{dvR} - P_{vRltc} \tag{3.68}$$

$$\Delta Q_{vR} = -Q_{vR} - Q_{dvR} - Q_{vRltc} \tag{3.69}$$

$$\Delta Q_{0vR} = -Q_{0vR} \tag{3.70}$$

$$\Delta P_{0vR} = -\left(P_{0vR} + P_{dcR}\right) \tag{3.71}$$

$$\Delta P_m = -P_{mltc} - P_{dm} - P_m^{cal} \tag{3.72}$$

$$\Delta Q_m = -Q_{mltc} - Q_{dm} - Q_m^{cal} \tag{3.73}$$

$$\Delta P_{vI} = -P_{vI} - P_{dvI} - P_{vIltc} \tag{3.74}$$

$$\Delta Q_{vI} = -Q_{vI} - Q_{dvI} - Q_{vIltc} \tag{3.75}$$

$$\Delta Q_{0vI} = -Q_{0vI} \tag{3.76}$$

$$\Delta P_{0vI} = -\left(P_{0vI} + P_{dcI}\right) \tag{3.77}$$

This steady-state VSC-HVDC model has been developed with particular reference to providing the power that the HVDC link must transfer to satisfy the load connected at the inverter end, i.e., the passive network. The inverter provides the angular reference which corresponds to the angle of the inverter's phase-shifting transformer ϕ_I. In this case, the constraining power mismatch equation (3.58) $\Delta P_{sch} = -\left(P_{sch} + P_{0vR}\right)$ is not needed as it is not the objective in this HVDC application; this implies that the DC power through the DC link is not regulated to a specified constant value P_{sch}. Instead, the DC voltage E_{dcR} will be one that enables the HVDC power transfer to meet the power requirements of the passive network (Castro and Acha, 2015b). That said, the linearisation of the mismatch equations is given by (3.78).

$$\left[\Delta F\right]^i = -\left[\begin{array}{cc:c} \mathbf{J_{RR}} & \mathbf{0} & \mathbf{J_{Ra}} \\ \mathbf{0} & \mathbf{J_{II}} & \mathbf{0} \\ \hdashline \mathbf{0} & \mathbf{J_{aI}} & \dfrac{\partial \Delta P_{0vI}}{\partial E_{dcR}} \end{array}\right]^i \left[\Delta z\right]^i \tag{3.78}$$

where $\mathbf{J_{RR}}$ and $\mathbf{J_{II}}$ have been suitably modified as shown in (3.79)-(3.80). Notice that in the last expression appears a different term $\mathbf{J_{aI}}$ to conform to the new set of state variables to be solved, a new set that also alters the vector $\mathbf{J_{Ra}}$ as can be seen in (3.81).

$$\mathbf{J_{RR}}=\begin{bmatrix} \frac{\partial \Delta P_k}{\partial \theta_k} & \frac{\partial \Delta P_k}{\partial T_{vR}} & \frac{\partial \Delta P_k}{\partial \theta_{vR}} & 0 & 0 & 0 \\ \frac{\partial \Delta Q_k}{\partial \theta_k} & \frac{\partial \Delta Q_k}{\partial T_{vR}} & \frac{\partial \Delta Q_k}{\partial \theta_{vR}} & 0 & 0 & 0 \\ \frac{\partial \Delta P_{vR}}{\partial \theta_k} & \frac{\partial \Delta P_{vR}}{\partial T_{vR}} & \frac{\partial \Delta P_{vR}}{\partial \theta_{vR}} & \frac{\partial \Delta P_{vR}}{\partial m_{aR}} & 0 & \frac{\partial \Delta P_{vR}}{\partial \phi_R} \\ \frac{\partial \Delta Q_{vR}}{\partial \theta_k} & \frac{\partial \Delta Q_{vR}}{\partial T_{vR}} & \frac{\partial \Delta Q_{vR}}{\partial \theta_{vR}} & \frac{\partial \Delta Q_{vR}}{\partial m_{aR}} & 0 & \frac{\partial \Delta Q_{vR}}{\partial \phi_R} \\ 0 & 0 & \frac{\partial \Delta Q_{0vR}}{\partial \theta_{vR}} & \frac{\partial \Delta Q_{0vR}}{\partial m_{aR}} & \frac{\partial \Delta Q_{0vR}}{\partial B_{eqR}} & \frac{\partial \Delta Q_{0vR}}{\partial \phi_R} \\ 0 & 0 & \frac{\partial \Delta P_{0vR}}{\partial \theta_{vR}} & \frac{\partial \Delta P_{0vR}}{\partial m_{aR}} & 0 & \frac{\partial \Delta P_{0vR}}{\partial \phi_R} \end{bmatrix} \tag{3.79}$$

$$\mathbf{J_{II}}=\begin{bmatrix} \frac{\partial \Delta P_m}{\partial \theta_m} & \frac{\partial \Delta P_m}{\partial T_{vI}} & \frac{\partial \Delta P_m}{\partial \theta_{vI}} & 0 & 0 \\ \frac{\partial \Delta Q_m}{\partial \theta_m} & \frac{\partial \Delta Q_m}{\partial T_{vI}} & \frac{\partial \Delta Q_m}{\partial \theta_{vI}} & 0 & 0 \\ \frac{\partial \Delta P_{vI}}{\partial \theta_m} & \frac{\partial \Delta P_{vI}}{\partial T_{vI1}} & \frac{\partial \Delta P_{vI}}{\partial \theta_{vI}} & \frac{\partial \Delta P_{vI}}{\partial m_{aI}} & 0 \\ \frac{\partial \Delta Q_{vI}}{\partial \theta_m} & \frac{\partial \Delta Q_{vI}}{\partial T_{vI}} & \frac{\partial \Delta Q_{vI}}{\partial \theta_{vI}} & \frac{\partial \Delta Q_{vI}}{\partial m_{aI}} & 0 \\ 0 & 0 & \frac{\partial \Delta Q_{0vI}}{\partial \theta_{vI}} & \frac{\partial \Delta Q_{0vI}}{\partial m_{aI}} & \frac{\partial \Delta Q_{0vI1}}{\partial B_{eqI1}} \end{bmatrix} \tag{3.80}$$

$$\mathbf{J_{aI}}=\begin{bmatrix} 0 & 0 & \frac{\partial \Delta P_{0vI}}{\partial \theta_{vI}} & \frac{\partial \Delta P_{0vI}}{\partial m_{aI}} & 0 \end{bmatrix}, \quad \mathbf{J_{Ra}}=\begin{bmatrix} 0 & 0 & \frac{\partial \Delta P_{vR}}{\partial E_{dcR}} & \frac{\partial \Delta Q_{vR}}{\partial E_{dcR}} & \frac{\partial \Delta Q_{0vR}}{\partial E_{dcR}} & \frac{\partial \Delta P_{0vR}}{\partial E_{dcR}} \end{bmatrix}^T \tag{3.81}$$

The vector of increments and mismatches carry the form shown in (3.82)-(3.83).

$$\left[\Delta F\right]^i=\left[\Delta P_k \;\; \Delta Q_k \;\; \Delta P_{vR} \;\; \Delta Q_{vR} \;\; \Delta Q_{0vR} \;\; \Delta P_{0vR} \;\; \Delta P_m \;\; \Delta Q_m \;\; \Delta P_{vI} \;\; \Delta Q_{vI} \;\; \Delta Q_{0vI} \;\; \Delta P_{0vI}\right]^T \tag{3.82}$$

$$\left[\Delta z\right]^i=\left[\Delta \theta_k \;\; \Delta T_{vR} \;\; \Delta \theta_{vR} \;\; \Delta m_{aR} \;\; \Delta B_{eqR} \;\; \Delta \phi_R \;\; \Delta \theta_m \;\; \Delta T_{vI} \;\; \Delta \theta_{vI} \;\; \Delta m_{aI} \;\; \Delta B_{eqI} \;\; \Delta E_{dcR}\right]^T \tag{3.83}$$

The phase-shifting angle of the inverter ϕ_I is not part of the set of state variables to be computed through the power-flow solution (3.84), but it is given as an input datum. From the power-flow solution standpoint, the value of the angle ϕ_I will be the angular reference for the passive network, enabling the inverter to supply the power losses for the connected network. The

set of state variables arising from the HVDC link feeding into passive networks are updated at each iteration i as follows:

$$[z]^{i+1} = [z]^{i} + [\Delta z]^{i} \tag{3.84}$$

3.4.3 Back-to-back HVDC model

In the particular case where there is no DC cable but the converter stations are connected back-to-back sharing a common DC bus, simple modifications in the point-to-point HVDC models may be implemented to produce the back-to-back HVDC model. For instance, in the case of the point-to-point HVDC model which interconnects AC systems containing synchronous generation, a simplification of (3.59) reduces to (3.87) to give rise to the back-to-back HVDC model. The DC voltage of the rectifier equals the DC voltage of the inverter $E_{dcR} = E_{dcI}$ and is kept constant, resulting in one less state variable to be calculated through the power-flow solution. The explicit constraining power equation (3.58) is removed from the set of mismatch equations, but equations (3.51) and (3.57) are slightly reformulated, as shown in (3.85) and (3.86), respectively, to endow the back-to-back HVDC model with DC power control capability.

$$\Delta P_{0vR} = -\left(P_{0vR} + P_{sch}\right) \tag{3.85}$$

$$\Delta P_{0vI} = -\left(P_{0vI} - P_{sch}\right) \tag{3.86}$$

$$[\Delta F]^{i} = -\begin{bmatrix} \mathbf{J_{RR}} & \mathbf{0} \\ \mathbf{0} & \mathbf{J_{II}} \end{bmatrix}^{i} [\Delta z]^{i} \tag{3.87}$$

The Jacobian matrix of the rectifier station is modified as seen in (3.88), whereas the one pertaining to the inverter $\mathbf{J_{II}}$ remains the same as in (3.61).

$$\mathbf{J_{RR}}=\begin{bmatrix} \frac{\partial \Delta P_k}{\partial \theta_k} & \frac{\partial \Delta P_k}{\partial T_{vR}} & \frac{\partial \Delta P_k}{\partial \theta_{vR}} & 0 & 0 & 0 \\ \frac{\partial \Delta Q_k}{\partial \theta_k} & \frac{\partial \Delta Q_k}{\partial T_{vR}} & \frac{\partial \Delta Q_k}{\partial \theta_{vR}} & 0 & 0 & 0 \\ \frac{\partial \Delta P_{vR}}{\partial \theta_k} & \frac{\partial \Delta P_{vR}}{\partial T_{vR}} & \frac{\partial \Delta P_{vR}}{\partial \theta_{vR}} & \frac{\partial \Delta P_{vR}}{\partial m_{aR}} & 0 & \frac{\partial \Delta P_{vR}}{\partial \phi_R} \\ \frac{\partial \Delta Q_{vR}}{\partial \theta_k} & \frac{\partial \Delta Q_{vR}}{\partial T_{vR}} & \frac{\partial \Delta Q_{vR}}{\partial \theta_{vR}} & \frac{\partial \Delta Q_{vR}}{\partial m_{aR}} & 0 & \frac{\partial \Delta Q_{vR}}{\partial \phi_R} \\ 0 & 0 & \frac{\partial \Delta Q_{0vR}}{\partial \theta_{vR}} & \frac{\partial \Delta Q_{0vR}}{\partial m_{aR}} & \frac{\partial \Delta Q_{0vR}}{\partial B_{eqR}} & \frac{\partial \Delta Q_{0vR}}{\partial \phi_R} \\ 0 & 0 & \frac{\partial \Delta P_{0vR}}{\partial \theta_{vR}} & \frac{\partial \Delta P_{0vR}}{\partial m_{aR}} & 0 & \frac{\partial \Delta P_{0vR}}{\partial \phi_R} \end{bmatrix} \tag{3.88}$$

The vectors of corrections, mismatches and state variables are expressed in the same manner as in (3.63)-(3.65), but bearing in mind that neither the explicit constraining mismatch equation ΔP_{sch} nor the DC voltage of the rectifier E_{dcR} take part in the steady-state solution of back-to-back HVDC links operating in embeeded form or interconnecting two independent AC networks containing synchronous generation. Similar considerations may be adopted if the aim is to tailor a back-to-back HVDC model to feed into passive networks, something that is a straightforward matter owing to the modularity of the VSC model.

3.5 Multi-terminal VSC-HVDC links

Power transmission using VSC-HVDC links continues its progress unabated. The current high level of penetration of power electronics in AC power grids is due to the flexibility and reliability afforded by present day VSC technology (Gong, 2012; Bauer et al., 2014) where it is often argued that the step forward is the construction of multi-terminal VSC-HVDC systems (Trötscher et al., 2009; Vrana et al., 2010; Hertem and Ghandhari, 2010; Cole et al., 2011). Particularly, a promising application of multi-terminal schemes points towards the tapping into large offshore wind farms that lie in deep waters using long submarine DC power transmission lines, (Li et al., 2014; Yao and Cai, 2015). Arguably, owing to its great engineering complexity, power grids of this nature will require a modular approach to both its construction and analysis. It is in this context that research interest in multi-terminal VSC-HVDC systems is rapidly emerging, resulting in the investigation of new topology arrangements (Cole et al., 2011; Gomis-Bellmunt et al., 2011) and in the upgrading of existing power systems' application tools to incorporate multi-terminal VSC-HVDC models within the conventional formulations of power flows and transient stability in order to conduct system-wide stud-

ies. However, such studies are carried out using sequential and quasi-unified AC and DC power-flow solutions (Chen et al., 2005; Beerten et al., 2010; Ye et al., 2011; Baradar and Ghandhari, 2013, Wang and Barnes, 2014), introducing frailty in their formulations. This has been one of the main motivations of this research work where a new and general frame-of-reference for truly unified, iterative solutions of AC/DC power flows using the Newton-Raphson method is introduced (Acha and Castro, 2016a; Acha and Castro, 2016b).

By way of example, the system in Figure 3.5 represents a multi-terminal VSC-HVDC system with a DC power network, accommodating quite naturally any number of AC/DC sub-networks generated by a number of voltage source converters. Networks AC 1 to AC 4 might represent each very large power systems consisting of a number of transmission lines, loads and generating units, whose integration into a far more complex power grid would be possible thanks to the realisation of a custom-tailored DC power network. Such DC power grid could, in turn, facilitate the aggregation of various types of electrical networks spanning from renewable energy stations to island networks such as low-inertia networks, passive networks, oil and gas platforms, among others.

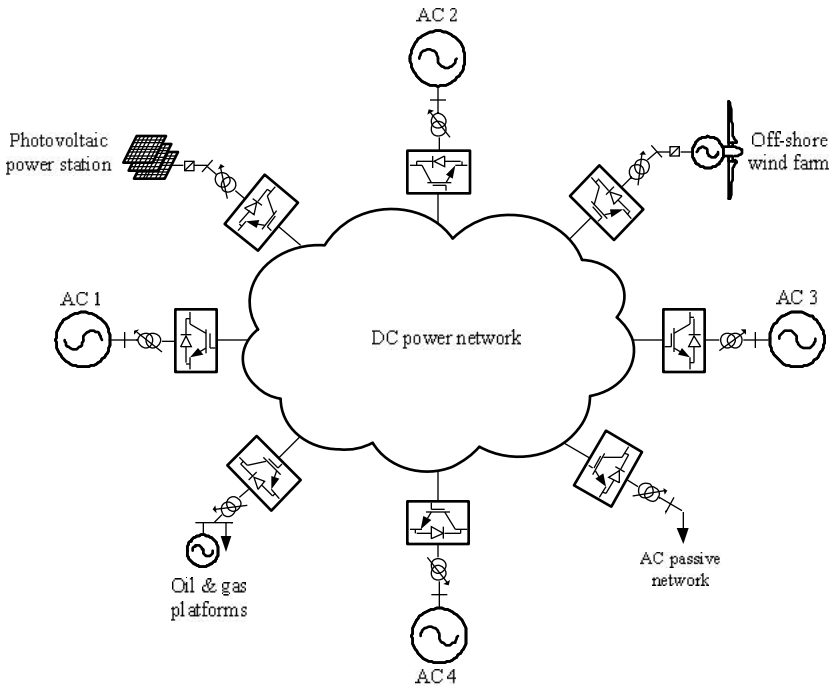

Figure 3.5 Multi-terminal VSC-HVDC system interconnecting power networks of various kinds

The fundamental frequency steady-state operation of the multi-terminal VSC-HVDC scheme, shown in Figure 3.5, may be assessed by building up a model that comprises a number of VSC units which is commensurate with the number of terminals in the HVDC system, suitably accom-

modated in an all-encompassing frame-of-reference. The power flow model of a full VSC station was derived first in Section 3.1 and it is used to build the model of the most basic multi-terminal VSC-HVDC system, which is a three-terminal system. The formulation is then expanded quite naturally to encompass a multi-terminal VSC-HVDC system having any number of converter stations and an arbitrary DC network topology.

3.5.1 Three-terminal VSC-HVDC link model

The adopted modelling approach to formulate the steady-state models of both the STATCOM and the HVDC link is incremental in nature. Building on this modular philosophy, the most basic multi-terminal VSC-HVDC system is developed in this section. This is the three-terminal system shown in Figure 3.6, comprising three power converters; for simplicity of representation, the OLTCs pertaining to the power converters are not shown in Fig 3.6 but they are taken into account, as addressed in Section 3.2. It should be mentioned that unlike back-to-back or point-to-point HVDC links, any converter can play the role of either a rectifier or inverter in a multi-terminal connection of VSCs. This is due to the fact that each converter adapts itself to the power requirements imposed by its pairing AC grid, i.e., the power can flow in both directions, from the DC grid to the AC network or vice versa.

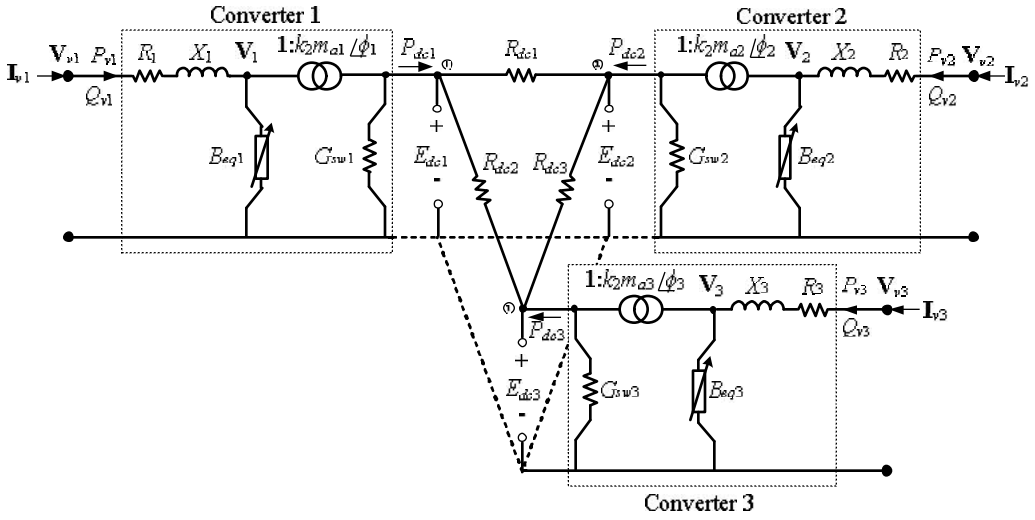

Figure 3.6 Steady-state equivalent circuit of a three-terminal VSC-HVDC link

For simplicity of the developments, the OLTC transformers are not represented in the VSC-HVDC system shown in Figure 3.6. However, their incorporation using (3.14) is quite a straightforward matter. With no loss of generality either, the expressions for a single VSC unit may be used

to represent any of the VSCs in the three-terminal system. The nodal admittance matrix for the three-terminal VSC-HVDC system comprising the three VSCs and the three DC cables is the starting point to furnish the steady-state three-terminal VSC-HVDC link model; this is shown in (3.89).

$$\begin{bmatrix} \mathbf{I}_{v1} \\ \mathbf{I}_{0v1} \\ \mathbf{I}_{v2} \\ \mathbf{I}_{0v2} \\ \mathbf{I}_{v3} \\ \mathbf{I}_{0v3} \end{bmatrix} = \left\{ \begin{bmatrix} \mathbf{Y}_{\mathbf{A}1} & \mathbf{Y}_{\mathbf{B}1} & 0 & 0 & 0 & 0 \\ \mathbf{Y}_{\mathbf{C}1} & \mathbf{Y}_{\mathbf{D}1} & 0 & 0 & 0 & 0 \\ 0 & 0 & \mathbf{Y}_{\mathbf{A}2} & \mathbf{Y}_{\mathbf{B}2} & 0 & 0 \\ 0 & 0 & \mathbf{Y}_{\mathbf{C}2} & \mathbf{Y}_{\mathbf{D}2} & 0 & 0 \\ 0 & 0 & 0 & 0 & \mathbf{Y}_{\mathbf{A}3} & \mathbf{Y}_{\mathbf{B}3} \\ 0 & 0 & 0 & 0 & \mathbf{Y}_{\mathbf{C}3} & \mathbf{Y}_{\mathbf{D}3} \end{bmatrix} + \begin{bmatrix} 0 & 0 & 0 & 0 & 0 & 0 \\ 0 & G_{dc1}+G_{dc2} & 0 & -G_{dc1} & 0 & -G_{dc2} \\ 0 & 0 & 0 & 0 & 0 & 0 \\ 0 & -G_{dc1} & 0 & G_{dc1}+G_{dc3} & 0 & -G_{dc3} \\ 0 & 0 & 0 & 0 & 0 & 0 \\ 0 & -G_{dc2} & 0 & -G_{dc3} & 0 & G_{dc2}+G_{dc3} \end{bmatrix} \right\} \begin{bmatrix} \mathbf{V}_{v1} \\ E_{dc1} \\ \mathbf{V}_{v2} \\ E_{dc2} \\ \mathbf{V}_{v3} \\ E_{dc3} \end{bmatrix} \tag{3.89}$$

The structure of (3.89) comprises two main matrix terms; the former is a block-diagonal matrix whose individual block entries are the nodal admittance matrices of the relevant VSC component having the generic form of (3.8). The latter matrix in (3.89) is in fact the nodal conductance matrix of the three-bus DC circuit, with some zero padding to make it conform to the network's connection of the AC and DC circuits. The voltages E_{dc1}, E_{dc2} and E_{dc3} are the DC voltages at nodes 1, 2 and 3, respectively. The nodal complex power equations are derived by multiplying the nodal voltages by the conjugate of the nodal currents $\mathbf{S} = \mathbf{V}\mathbf{I}^*$. Following some complex algebra, a similar set of power flow equations to that of (3.9)-(3.12) are obtained for the converter stations making up the three-terminal HVDC system: $(P_{v1}, Q_{v1}, P_{0v1}, Q_{0v1})$, $(P_{v2}, Q_{v2}, P_{0v2}, Q_{0v2})$ and $(P_{v3}, Q_{v3}, P_{0v3}, Q_{0v3})$, respectively. Furthermore, the DC power contributions at each node are shown in (3.90)-(3.92), in explicit form.

$$P_{dc1}^{cal} = \left(G_{dc1} + G_{dc2}\right) E_{dc1}^2 - G_{dc1} E_{dc2} - G_{dc2} E_{dc3} \tag{3.90}$$

$$P_{dc2}^{cal} = \left(G_{dc1} + G_{dc3}\right) E_{dc2}^2 - G_{dc1} E_{dc1} - G_{dc3} E_{dc3} \tag{3.91}$$

$$P_{dc3}^{cal} = \left(G_{dc2} + G_{dc3}\right) E_{dc3}^2 - G_{dc2} E_{dc1} - G_{dc3} E_{dc2} \tag{3.92}$$

Classification of VSC types

In a similar manner to the standard classification of types of nodes available in the conventional AC power flow theory, Table 3.1 introduces the types of VSC stations that are required to solve any kind of AC/DC power grid. The classification obeys principles of control and application: (i) the slack converter VSC_{Slack} provides voltage control at its DC terminal and it is linked on its AC side to a network which contains synchronous generation. Another feature of this converter is that it also enables the power equilibrium in the DC network, which means that if there is a load at any of the DC buses, its drawn power will be satisfied through the converter, i.e., the corresponding power will be supplied by its pairing AC network; (ii) the converter of type VSC_{Psch} serves the purpose of

injecting a scheduled power into the DC grid and it is also linked on its AC side to a network with synchronous generation; (iii) the third type of VSC station is the passive converter VSC_{Pass} which is used to interconnect the DC grid with an AC network which contains no synchronous generation of its own, e.g. a passive network. In passive AC power grids, the internal angle of the VSCs, ϕ, provides the angular reference for the network. The specified and calculated VSC variables are given in Table 3.1 for each type of VSC (Acha and Castro, 2016a).

Table 3.1 Types of VSCs and their control variables

Type	Known variables	Unknown variables
VSC_{Slack}	E_{dc}, V_v^{spec}	θ_v, m_a, ϕ, B_{eq}, θ_k, T_v
VSC_{Psch}	P_{sch}, V_v^{spec}	E_{dc}, θ_v, m_a, ϕ, B_{eq}, θ_k, T_v
VSC_{Pass}	ϕ, V_v^{spec}	E_{dc}, θ_v, m_a, B_{eq}, θ_k, T_v

The approach adopted in power flow theory is to determine by iteration, the values of the set of state variables that yields an accurate match between the powers specified at every node and its corresponding nodal power equations, hence, iterations are required because the nodal power equations are expressed as a function of these state variables, which are unknown at the outset of the iterative process. Using the VSCs power flow equations and the DC power contributions (3.90)-(3.92), the nodal mismatch powers incorporating the powers of the associated OLTC transformers, which are connected to nodes k, m and n, take the form of (3.93)-(3.110). In connection with Table 3.1, it is assumed that converter 1 is a converter of type VSC_{Slack}, converter 2 is a converter of type VSC_{Psch} and converter 3 is a converter of type VSC_{Pass}.

$$\Delta P_k = -P_{kltc} - P_{dk} - P_k^{cal} \tag{3.93}$$

$$\Delta Q_k = -Q_{kltc} - Q_{dk} - Q_k^{cal} \tag{3.94}$$

$$\Delta P_{v1} = -P_{v1} - P_{dv1} - P_{v1ltc} \tag{3.95}$$

$$\Delta Q_{v1} = -Q_{v1} - Q_{dv1} - Q_{v1ltc} \tag{3.96}$$

$$\Delta Q_{0v1} = -Q_{0v1} \tag{3.97}$$

$$\Delta P_{0v1} = -\left(P_{0v1} + P_{dc1}^{cal}\right) \tag{3.98}$$

$$\Delta P_m = -P_{mltc} - P_{dm} - P_m^{cal} \tag{3.99}$$

$$\Delta Q_m = -Q_{mltc} - Q_{dm} - Q_m^{cal} \tag{3.100}$$

$$\Delta P_{v2} = -P_{v2} - P_{dv2} - P_{v2ltc} \tag{3.101}$$

$$\Delta Q_{v2} = -Q_{v2} - Q_{dv2} - Q_{v2ltc} \tag{3.102}$$

$$\Delta Q_{0v2} = -Q_{0v2} \tag{3.103}$$

$$\Delta P_{0v2} = -\left(P_{0v2} + P_{dc2}^{cal}\right) \tag{3.104}$$

$$\Delta P_{n} = -P_{nltc} - P_{dn} - P_{n}^{cal} \tag{3.105}$$

$$\Delta Q_{n} = -Q_{nltc} - Q_{dn} - Q_{n}^{cal} \tag{3.106}$$

$$\Delta P_{v3} = -P_{v3} - P_{dv3} - P_{v3ltc} \tag{3.107}$$

$$\Delta Q_{v3} = -Q_{v3} - Q_{dv3} - Q_{v3ltc} \tag{3.108}$$

$$\Delta Q_{0v3} = -Q_{0v3} \tag{3.109}$$

$$\Delta P_{0v3} = -\left(P_{0v3} + P_{dc3}^{cal}\right) \tag{3.110}$$

As in the case of a single VSC unit or a two-terminal VSC arrangement, the reactive power constraining equations (3.97), (3.103) and (3.109) are required for all three converters to prevent the flow of reactive power into the DC grid by virtue that no reactive power exist in the DC grid. Also the expressions (3.98), (3.104) and (3.110) represent the nodal mismatch equations at the DC nodes 1, 2 and 3 of the three-terminal system. Converters of type VSC$_{Psch}$ require each a constraining power equation which for the three-terminal case, and with no loss of generality, takes the form of (3.111) assuming that P_{sch} is the amount of DC power leaving the converter 2 at its DC bus.

$$\Delta P_{sch2} = -\left(P_{sch} + P_{0v2}\right) \tag{3.111}$$

Linearisation of equations (3.93)-(3.111) around a starting operating point, as discussed in Section 3.3.2 for each power converter, enables the calculation of the equilibrium point whose state variables solution conforms to the control of the DC voltage on the slack converter's DC bus, the regulation of power on the DC bus of converter 2 and the regulation of the voltage magnitude at the AC terminal of the three voltage source converters. The relevant system of equations is arranged, using compact notation, in the structure shown in (3.112).

$$\begin{bmatrix} \mathbf{F}_{\mathbf{Slack}} \\ \mathbf{F}_{\mathbf{Psch}} \\ \mathbf{F}_{\mathbf{Pass}} \\ \hline \mathbf{F}_{\mathbf{dc}} \end{bmatrix}^{i} = -\left[\begin{array}{ccc|c} \mathbf{J}_{\mathbf{Slack}} & \mathbf{0} & \mathbf{0} & \mathbf{J}_{\mathbf{Sdc}} \\ \mathbf{0} & \mathbf{J}_{\mathbf{Psch}} & \mathbf{0} & \mathbf{J}_{\mathbf{Psdc}} \\ \mathbf{0} & \mathbf{0} & \mathbf{J}_{\mathbf{Pass}} & \mathbf{J}_{\mathbf{Padc}} \\ \hline \mathbf{0} & \mathbf{J}_{\mathbf{dcPs}} & \mathbf{J}_{\mathbf{dcPa}} & \mathbf{J}_{\mathbf{dc}} \end{array}\right]^{i} \begin{bmatrix} \mathbf{\Delta\Phi}_{\mathbf{Slack}} \\ \mathbf{\Delta\Phi}_{\mathbf{Psch}} \\ \mathbf{\Delta\Phi}_{\mathbf{Pass}} \\ \hline \mathbf{\Delta E}_{\mathbf{dc}} \end{bmatrix}^{i} \tag{3.112}$$

It is noticed that in addition to the matrix entries corresponding to the three VSCs comprising the three-terminal HVDC system, there are matrix entries corresponding to the DC cables and mutual matrix terms between the DC nodes and their respective AC nodes. The matrix contributions from the three VSCs are shown in equations (3.113)-(3.115).

$$\mathbf{J_{Slack}}=\begin{bmatrix} \frac{\partial \Delta P_k}{\partial \theta_k} & \frac{\partial \Delta P_k}{\partial T_{vR}} & \frac{\partial \Delta P_k}{\partial \theta_{v1}} & 0 & 0 & 0 \\ \frac{\partial \Delta Q_k}{\partial \theta_k} & \frac{\partial \Delta Q_k}{\partial T_{vR}} & \frac{\partial \Delta Q_k}{\partial \theta_{v1}} & 0 & 0 & 0 \\ \frac{\partial \Delta P_{v1}}{\partial \theta_k} & \frac{\partial \Delta P_{v1}}{\partial T_{v1}} & \frac{\partial \Delta P_{v1}}{\partial \theta_{v1}} & \frac{\partial \Delta P_{v1}}{\partial m_{a1}} & 0 & \frac{\partial \Delta P_{v1}}{\partial \phi_1} \\ \frac{\partial \Delta Q_{v1}}{\partial \theta_k} & \frac{\partial \Delta Q_{v1}}{\partial T_{v1}} & \frac{\partial \Delta Q_{v1}}{\partial \theta_{v1}} & \frac{\partial \Delta Q_{v1}}{\partial m_{a1}} & 0 & \frac{\partial \Delta Q_{v1}}{\partial \phi_1} \\ 0 & 0 & \frac{\partial \Delta Q_{0v1}}{\partial \theta_{v1}} & \frac{\partial \Delta Q_{0v1}}{\partial m_{a1}} & \frac{\partial \Delta Q_{0v1}}{\partial B_{eq1}} & \frac{\partial \Delta Q_{0v1}}{\partial \phi_1} \\ 0 & 0 & \frac{\partial \Delta P_{0v1}}{\partial \theta_{v1}} & \frac{\partial \Delta P_{0v1}}{\partial m_{a1}} & 0 & \frac{\partial \Delta P_{0v1}}{\partial \phi_1} \end{bmatrix} \tag{3.113}$$

$$\mathbf{J_{Psch}}=\begin{bmatrix} \frac{\partial \Delta P_m}{\partial \theta_m} & \frac{\partial \Delta P_m}{\partial T_{v2}} & \frac{\partial \Delta P_m}{\partial \theta_{v2}} & 0 & 0 & 0 \\ \frac{\partial \Delta Q_m}{\partial \theta_m} & \frac{\partial \Delta Q_m}{\partial T_{v2}} & \frac{\partial \Delta Q_m}{\partial \theta_{v2}} & 0 & 0 & 0 \\ \frac{\partial \Delta P_{v2}}{\partial \theta_m} & \frac{\partial \Delta P_{v2}}{\partial T_{v2}} & \frac{\partial \Delta P_{v2}}{\partial \theta_{v2}} & \frac{\partial \Delta P_{v2}}{\partial m_{a2}} & 0 & \frac{\partial \Delta P_{v2}}{\partial \phi_2} \\ \frac{\partial \Delta Q_{v2}}{\partial \theta_m} & \frac{\partial \Delta Q_{v2}}{\partial T_{v2}} & \frac{\partial \Delta Q_{v2}}{\partial \theta_{v2}} & \frac{\partial \Delta Q_{v2}}{\partial m_{a2}} & 0 & \frac{\partial \Delta Q_{v2}}{\partial \phi_2} \\ 0 & 0 & \frac{\partial \Delta Q_{0v2}}{\partial \theta_{v2}} & \frac{\partial \Delta Q_{0v2}}{\partial m_{a2}} & \frac{\partial \Delta Q_{0v2}}{\partial B_{eq2}} & \frac{\partial \Delta Q_{0v2}}{\partial \phi_2} \\ 0 & 0 & \frac{\partial \Delta P_{sch2}}{\partial \theta_{v2}} & \frac{\partial \Delta P_{sch2}}{\partial m_{a2}} & 0 & \frac{\partial \Delta P_{sch2}}{\partial \phi_2} \end{bmatrix} \tag{3.114}$$

$$\mathbf{J_{Pass}}=\begin{bmatrix} \frac{\partial \Delta P_n}{\partial \theta_n} & \frac{\partial \Delta P_n}{\partial T_{v3}} & \frac{\partial \Delta P_n}{\partial \theta_{v3}} & 0 & 0 \\ \frac{\partial \Delta Q_n}{\partial \theta_n} & \frac{\partial \Delta Q_n}{\partial T_{v3}} & \frac{\partial \Delta Q_n}{\partial \theta_{v3}} & 0 & 0 \\ \frac{\partial \Delta P_{v3}}{\partial \theta_n} & \frac{\partial \Delta P_{v3}}{\partial T_{v3}} & \frac{\partial \Delta P_{v3}}{\partial \theta_{v3}} & \frac{\partial \Delta P_{v3}}{\partial m_{a3}} & 0 \\ \frac{\partial \Delta Q_{v3}}{\partial \theta_n} & \frac{\partial \Delta Q_{v3}}{\partial T_{v3}} & \frac{\partial \Delta Q_{v3}}{\partial \theta_{v3}} & \frac{\partial \Delta Q_{v3}}{\partial m_{a3}} & 0 \\ 0 & 0 & \frac{\partial \Delta Q_{0v3}}{\partial \theta_{v3}} & \frac{\partial \Delta Q_{0v3}}{\partial m_{a3}} & \frac{\partial \Delta Q_{0v3}}{\partial B_{eq3}} \end{bmatrix} \tag{3.115}$$

The mutual terms between the DC nodes and their corresponding AC nodes are shown in equations (3.116)-(3.117).

$$\mathbf{J_{Sdc}}=\begin{bmatrix} 0 & 0 \\ 0 & 0 \\ 0 & 0 \\ 0 & 0 \\ 0 & 0 \\ \dfrac{\partial \Delta P_{0v1}}{\partial E_{dc2}} & \dfrac{\partial \Delta P_{0v1}}{\partial E_{dc3}} \end{bmatrix},\ \mathbf{J_{Psdc}}=\begin{bmatrix} 0 & 0 \\ 0 & 0 \\ \dfrac{\partial \Delta P_{v2}}{\partial E_{dc2}} & 0 \\ \dfrac{\partial \Delta Q_{v2}}{\partial E_{dc2}} & 0 \\ \dfrac{\partial \Delta Q_{0v2}}{\partial E_{dc2}} & 0 \\ \dfrac{\partial \Delta P_{sch2}}{\partial E_{dc2}} & 0 \end{bmatrix},\ \mathbf{J_{Padc}}=\begin{bmatrix} 0 & 0 \\ 0 & 0 \\ 0 & \dfrac{\partial \Delta P_{v3}}{\partial E_{dc3}} \\ 0 & \dfrac{\partial \Delta Q_{v3}}{\partial E_{dc3}} \\ 0 & \dfrac{\partial \Delta Q_{0v3}}{\partial E_{dc3}} \end{bmatrix} \tag{3.116}$$

$$\mathbf{J_{dcPs}}=\begin{bmatrix} 0 & 0 & \dfrac{\partial \Delta P_{0v2}}{\partial \theta_{v2}} & \dfrac{\partial \Delta P_{0v2}}{\partial m_{a2}} & 0 & \dfrac{\partial \Delta P_{0v2}}{\partial \phi_{2}} \\ 0 & 0 & 0 & 0 & 0 & 0 \end{bmatrix},\ \mathbf{J_{dcPa}}=\begin{bmatrix} 0 & 0 & 0 & 0 & 0 \\ 0 & 0 & \dfrac{\partial \Delta P_{0v3}}{\partial \theta_{v3}} & \dfrac{\partial \Delta P_{0v3}}{\partial m_{a3}} & 0 \end{bmatrix} \tag{3.117}$$

The terms corresponding to the DC circuit of the three-terminal HVDC system are given in (3.118).

$$\mathbf{J_{dc}}=\begin{bmatrix} \dfrac{\partial \Delta P_{0v2}}{\partial E_{dc2}} & \dfrac{\partial \Delta P_{0v2}}{\partial E_{dc3}} \\ \dfrac{\partial \Delta P_{0v3}}{\partial E_{dc2}} & \dfrac{\partial \Delta P_{0v3}}{\partial E_{dc3}} \end{bmatrix} \tag{3.118}$$

The power mismatch vectors and the state variables increments for the three VSC units and the DC circuit are given by (3.119)-(3.120).

$$\begin{aligned} \mathbf{F_{Slack}} &= \left[\Delta P_k\ \Delta Q_k\ \Delta P_{v1}\ \Delta Q_{v1}\ \Delta Q_{0v1}\ \Delta P_{0v1}\right]^T \\ \mathbf{F_{Psch}} &= \left[\Delta P_m\ \Delta Q_m\ \Delta P_{v2}\ \Delta Q_{v2}\ \Delta Q_{0v2}\ \Delta P_{sch2}\right]^T \\ \mathbf{F_{Pass}} &= \left[\Delta P_n\ \Delta Q_n\ \Delta P_{v3}\ \Delta Q_{v3}\ \Delta Q_{0v3}\right]^T \\ \mathbf{F_{dc}} &= \left[\Delta P_{0v2}\ \Delta P_{0v3}\right]^T \end{aligned} \tag{3.119}$$

$$\begin{aligned} \mathbf{\Delta\Phi_{Slack}} &= \left[\Delta\theta_k\ \Delta T_{v1}\ \Delta\theta_{v1}\ \Delta m_{a1}\ \Delta B_{eq1}\ \Delta\phi_1\right]^T \\ \mathbf{\Delta\Phi_{Psch}} &= \left[\Delta\theta_m\ \Delta T_{v2}\ \Delta\theta_{v2}\ \Delta m_{a2}\ \Delta B_{eq2}\ \Delta\phi_2\right]^T \\ \mathbf{\Delta\Phi_{Pass}} &= \left[\Delta\theta_n\ \Delta T_{v3}\ \Delta\theta_{v3}\ \Delta m_{a3}\ \Delta B_{eq3}\right]^T \\ \mathbf{\Delta E_{dc}} &= \left[\Delta E_{dc2}\ \Delta E_{dc3}\right]^T \end{aligned} \tag{3.120}$$

Notice that the vector $\mathbf{\Delta E_{dc}}$ contains only DC voltages as state variables. If voltage regulation takes place at any of the DC buses, then the corresponding row and column are deleted from (3.116)-(3.118). It should be remarked that the voltage must be specified in at least one of the

buses of the DC network. Such a node plays the role of reference node in the DC network and in this three-terminal VSC-HVDC example this role has been assigned to the converter station 1 which is VSC_{Slack} type. On the other hand, if no voltage regulation is exerted at the AC bus of either the rectifier or any of the two inverters then suitable changes take place in (3.113)-(3.115). For instance, if no voltage regulation takes place in the AC bus of the slack converter then $\mathbf{J}_{\mathbf{Slack}}$ and $\mathbf{\Delta\Phi}_{\mathbf{Slack}}$ are modified as shown in expression (3.121).

$$\mathbf{J}_{\mathbf{Slack}}=\begin{bmatrix} \frac{\partial\Delta P_k}{\partial\theta_k} & \frac{\partial\Delta P_k}{\partial T_{v1}} & \frac{\partial\Delta P_k}{\partial\theta_{v1}} & 0 & 0 & 0 \\ \frac{\partial\Delta Q_k}{\partial\theta_k} & \frac{\partial\Delta Q_k}{\partial T_{v1}} & \frac{\partial\Delta Q_k}{\partial\theta_{v1}} & 0 & 0 & 0 \\ \frac{\partial\Delta P_{vR}}{\partial\theta_k} & \frac{\partial\Delta P_{v1}}{\partial T_{v1}} & \frac{\partial\Delta P_{v1}}{\partial\theta_{v1}} & \frac{\partial\Delta P_{v1}}{\partial V_{v1}} & 0 & \frac{\partial\Delta P_{v1}}{\partial\phi_1} \\ \frac{\partial\Delta Q_{vR}}{\partial\theta_k} & \frac{\partial\Delta Q_{v1}}{\partial T_{v1}} & \frac{\partial\Delta Q_{v1}}{\partial\theta_{v1}} & \frac{\partial\Delta Q_{v1}}{\partial V_{v1}} & 0 & \frac{\partial\Delta Q_{v1}}{\partial\phi_1} \\ 0 & 0 & \frac{\partial\Delta Q_{0v1}}{\partial\theta_{v1}} & \frac{\partial\Delta Q_{0v1}}{\partial V_{v1}} & \frac{\partial\Delta Q_{0v1}}{\partial B_{eq1}} & \frac{\partial\Delta Q_{0v1}}{\partial\phi_1} \\ 0 & 0 & \frac{\partial\Delta P_{0v1}}{\partial\theta_{v1}} & \frac{\partial\Delta P_{0v1}}{\partial V_{v1}} & 0 & \frac{\partial\Delta P_{0v1}}{\partial\phi_1} \end{bmatrix},\ \mathbf{\Delta\Phi}_{\mathbf{Slack}}=\begin{bmatrix} \Delta\theta_k \\ \Delta T_{v1} \\ \Delta\theta_{v1} \\ \Delta V_{v1} \\ \Delta B_{eq1} \\ \Delta\phi_1 \end{bmatrix} \tag{3.121}$$

Notice that the state variable m_{a1} charged with regulating the AC voltage at node $v1$ becomes a constant parameter. The increments of the converters state variables, calculated at iteration i, are used to update the state variables, as shown in (3.122).

$$\mathbf{\Phi}_{\mathbf{Slack}}^{i+1}=\mathbf{\Phi}_{\mathbf{Slack}}^{i}+\mathbf{\Delta\Phi}_{\mathbf{Slack}}^{i},\quad \mathbf{\Phi}_{\mathbf{Psch}}^{i+1}=\mathbf{\Phi}_{\mathbf{Psch}}^{i}+\mathbf{\Delta\Phi}_{\mathbf{Psch}}^{i},\quad \mathbf{\Phi}_{\mathbf{Pass}}^{i+1}=\mathbf{\Phi}_{\mathbf{Pass}}^{i}+\mathbf{\Delta\Phi}_{\mathbf{Pass}}^{i} \tag{3.122}$$

Similarly, the updating of the DC voltages is carried out as follows:

$$\mathbf{E}_{\mathbf{dc}}^{i+1}=\mathbf{E}_{\mathbf{dc}}^{i}+\mathbf{\Delta E}_{\mathbf{dc}}^{i} \tag{3.123}$$

It should be noticed that when all entries relating to the converter of type VSC_{Pass} (entries with subscripts 3) are removed in (3.112) then the three-terminal VSC-HVDC model reduces neatly to the more particular case of the point-to-point VSC-HVDC link model presented in Section 3.4. It should be remarked that the three-terminal model is general and handles the DC link in explicit form, i.e., it is not solved as an equivalent back-to-back VSC-HVDC system. It is precisely the explicit representation of all the DC nodes in this formulation that enables multi-terminal AC/DC power-flow solutions in a truly unified fashion.

3.5.2 Multi-terminal VSC-HVDC link model

Moving into the multi-terminal direction, expression (3.112) may be extended to represent a VSC-HVDC system with multiple terminals consisting of m VSC$_{Slack}$ type converters, n VSC$_{Psch}$ type converters and r VSC$_{Pass}$ type converters and an arbitrary DC network. Such a general expression takes the form of expression (3.124) (Acha and Castro, 2016a).

$$\begin{bmatrix} \mathbf{F}_{\mathbf{Slack}1} \\ \vdots \\ \mathbf{F}_{\mathbf{Slack}m} \\ \hline \mathbf{F}_{\mathbf{Psch}1} \\ \vdots \\ \mathbf{F}_{\mathbf{Psch}n} \\ \hline \mathbf{F}_{\mathbf{Pass}1} \\ \vdots \\ \mathbf{F}_{\mathbf{Pass}r} \\ \hline \left[\mathbf{F}_{\mathbf{dc}}\right] \end{bmatrix}^{i} = - \left[\begin{array}{ccc|c|c|c} \mathbf{J}_{\mathbf{Slack}1} \cdots \mathbf{0} & & & & & \\ \vdots \ddots \vdots & & \mathbf{0} & & \mathbf{0} & \left[\mathbf{J}_{\mathbf{Sdc}}\right] \\ \mathbf{0} \cdots \mathbf{J}_{\mathbf{Slack}m} & & & & & \\ \hline & \mathbf{J}_{\mathbf{Psch}1} \cdots \mathbf{0} & & & & \\ \mathbf{0} & \vdots \ddots \vdots & & \mathbf{0} & & \left[\mathbf{J}_{\mathbf{Psdc}}\right] \\ & \mathbf{0} \cdots \mathbf{J}_{\mathbf{Psch}n} & & & & \\ \hline & & \mathbf{J}_{\mathbf{Pass}1} \cdots \mathbf{0} & & & \\ \mathbf{0} & \mathbf{0} & \vdots \ddots \vdots & & & \left[\mathbf{J}_{\mathbf{Padc}}\right] \\ & & \mathbf{0} \cdots \mathbf{J}_{\mathbf{Pass}r} & & & \\ \hline \mathbf{0} & \left[\mathbf{J}_{\mathbf{dcPs}}\right] & \left[\mathbf{J}_{\mathbf{dcPa}}\right] & & & \left[\mathbf{J}_{\mathbf{dc}}\right] \end{array}\right]^{i} \begin{bmatrix} \Delta\boldsymbol{\Phi}_{\mathbf{Slack}1} \\ \vdots \\ \Delta\boldsymbol{\Phi}_{\mathbf{Slack}m} \\ \hline \Delta\boldsymbol{\Phi}_{\mathbf{Psch}1} \\ \vdots \\ \Delta\boldsymbol{\Phi}_{\mathbf{Psch}n} \\ \hline \Delta\boldsymbol{\Phi}_{\mathbf{Pass}1} \\ \vdots \\ \Delta\boldsymbol{\Phi}_{\mathbf{Pass}r} \\ \hline \left[\Delta\mathbf{E}_{\mathbf{dc}}\right] \end{bmatrix}^{i} \tag{3.124}$$

As implied from this last equation, there will be as many of these zero-padded vectors as the number of VSC converters there is in the multi-terminal VSC-HVDC system. Caution has to be exercised because vectors having a location of the VSC$_{Slack}$ type converter and DC nodes with a connection to this converter will contain non-zero entries – this situation is well exemplified by the three-terminal case derived in Section 3.5.1. In cases when the converter type is VSC$_{Slack}$, the corresponding vector term would be a zero-padded vector of suitable dimensions and it is removed from (3.124).

In connection with equation (3.124), each one of the mismatch terms $\mathbf{F}$ with subscripts $\mathbf{Slack}$, $\mathbf{Psch}$ and $\mathbf{Pass}$ take the form of vector expressions (3.119) depending on the type of converter it is, namely, VSC$_{Slack}$, VSC$_{Psch}$ or VSC$_{Pass}$. Likewise, the vectors of incremental state variables $\Delta\boldsymbol{\Phi}$ take the form of vectors (3.120). By the same token, matrices $\mathbf{J}$ take the form of (3.113)-(3.115). The vectors and matrices of higher dimensionality that appear in (3.124) have the structure shown in (3.125)-(3.128).

$$\left[\mathbf{J}_{\mathbf{Sdc}}\right] = \begin{bmatrix} \begin{bmatrix} \mathbf{0} \\ \mathbf{J}'_{\mathbf{Sdc}1} \end{bmatrix} \\ \vdots \\ \begin{bmatrix} \mathbf{0} \\ \mathbf{J}'_{\mathbf{Sdc}m} \end{bmatrix} \end{bmatrix} \tag{3.125}$$

$$\left[\mathbf{J}_{\mathbf{Psdc}}\right]=\begin{bmatrix}\mathbf{J}'_{\mathbf{Psdc}1} & \cdots & \mathbf{0} & \mathbf{0} & \cdots & \mathbf{0}\\ \vdots & \ddots & \vdots & \vdots & \ddots & \vdots\\ \mathbf{0} & \cdots & \mathbf{J}'_{\mathbf{Psdc}n} & \mathbf{0} & \cdots & \mathbf{0}\end{bmatrix} \tag{3.126}$$

$$\left[\mathbf{J}_{\mathbf{Padc}}\right]=\begin{bmatrix}\mathbf{0} & \cdots & \mathbf{0} & \mathbf{J}'_{\mathbf{Padc}1} & \cdots & \mathbf{0}\\ \vdots & \ddots & \vdots & \vdots & \ddots & \vdots\\ \mathbf{0} & \cdots & \mathbf{0} & \mathbf{0} & \cdots & \mathbf{J}'_{\mathbf{Padc}r}\end{bmatrix} \tag{3.127}$$

$$\left[\mathbf{J}_{\mathbf{dcPs}}\right]=\begin{bmatrix}\mathbf{J}'_{\mathbf{dcPs}1} & \cdots & \mathbf{0}\\ \vdots & \ddots & \vdots\\ \mathbf{0} & \cdots & \mathbf{J}'_{\mathbf{dcPs}n}\\ \hline \mathbf{0} & \cdots & \mathbf{0}\\ \vdots & \ddots & \vdots\\ \mathbf{0} & \cdots & \mathbf{0}\end{bmatrix},\quad \left[\mathbf{J}_{\mathbf{dcPa}}\right]=\begin{bmatrix}\mathbf{0} & \cdots & \mathbf{0}\\ \vdots & \ddots & \vdots\\ \mathbf{0} & \cdots & \mathbf{0}\\ \hline \mathbf{J}'_{\mathbf{dcPa}1} & \cdots & \mathbf{0}\\ \vdots & \ddots & \vdots\\ \mathbf{0} & \cdots & \mathbf{J}'_{\mathbf{dcPa}n}\end{bmatrix} \tag{3.128}$$

The various entries in (3.125)-(3.128) are vectors with the generic j–th terms given in (3.129)-(3.133), depending on the type of the converter j, with $k=1,...,m$, $k=m+1,...,m+n$ and $k=m+n+1,...,n_{vsc}$ for the converters VSC*Slack*, VSC*Psch* and VSC*Pass*, respectively, where n_{dc} is the total number of DC nodes and n_{vsc} is the total number of converter units making up the multi-terminal arrangement:

$$\mathbf{J}'_{\mathbf{Sdc}j}=\begin{bmatrix}\dfrac{\partial\Delta P_{0vk}}{\partial E_{dc\,m+1}} & \dfrac{\partial\Delta P_{0vk}}{\partial E_{dc\,m+2}} & \cdots & \dfrac{\partial\Delta P_{0vk}}{\partial E_{dc\,n_{dc}-1}} & \dfrac{\partial\Delta P_{0vk}}{\partial E_{dc\,n_{dc}}}\end{bmatrix} \tag{3.129}$$

$$\mathbf{J}'_{\mathbf{Psdc}j}=\begin{bmatrix}0 & 0 & \dfrac{\partial\Delta P_{vk}}{\partial E_{dck}} & \dfrac{\partial\Delta Q_{vk}}{\partial E_{dck}} & \dfrac{\partial\Delta Q_{0vk}}{\partial E_{dck}} & \dfrac{\partial\Delta P_{schk}}{\partial E_{dck}}\end{bmatrix}^T \tag{3.130}$$

$$\mathbf{J}'_{\mathbf{Padc}j}=\begin{bmatrix}0 & 0 & \dfrac{\partial\Delta P_{vk}}{\partial E_{dck}} & \dfrac{\partial\Delta Q_{vk}}{\partial E_{dck}} & \dfrac{\partial\Delta Q_{0vk}}{\partial E_{dck}}\end{bmatrix}^T \tag{3.131}$$

$$\mathbf{J}'_{\mathbf{dcPs}j}=\begin{bmatrix}0 & 0 & \dfrac{\partial\Delta P_{0vk}}{\partial\theta_{vk}} & \dfrac{\partial\Delta P_{0vk}}{\partial m_{ak}} & 0 & \dfrac{\partial\Delta P_{0vk}}{\partial\phi_{k}}\end{bmatrix} \tag{3.132}$$

$$\mathbf{J}'_{\mathbf{dcPa}j}=\begin{bmatrix}0 & 0 & \dfrac{\partial\Delta P_{0vk}}{\partial\theta_{vk}} & \dfrac{\partial\Delta P_{0vk}}{\partial m_{ak}} & 0\end{bmatrix} \tag{3.133}$$

The Jacobian matrix of the DC network takes the general form given by (3.134).

$$\left[\mathbf{J}_{\mathbf{dc}}\right]=\begin{bmatrix}J_{m+1,m+1} & \cdots & J_{m+1,n_{dc}}\\ \vdots & \ddots & \vdots\\ J_{n_{dc},m+1} & \cdots & J_{n_{dc},n_{dc}}\end{bmatrix} \tag{3.134}$$

with the row and column corresponding to the VSC$_{Slack}$ type converters being removed from (3.134). The remaining terms, corresponding to the DC side of the network, in the general expression (3.124), are shown in equations (3.135)-(3.136).

$$\left[\mathbf{F_{dc}}\right] = \begin{bmatrix} \Delta P_{0vm+1} & \Delta P_{0vm+2} & \cdots & \Delta P_{0vn_{dc}-1} & \Delta P_{0vn_{dc}} \end{bmatrix}^T \tag{3.135}$$

$$\left[\mathbf{\Delta E_{dc}}\right] = \begin{bmatrix} E_{dcm+1} & E_{dcm+2} & \cdots & E_{dcn_{dc}-1} & E_{dcn_{dc}} \end{bmatrix}^T \tag{3.136}$$

where the entries corresponding to the VSC$_{Slack}$ type converters are removed from (3.135) and (3.136). As it turns out, the generalised reference frame is highly sparse and the use of standard sparsity techniques plays a useful role in actual software implementations. In the particular case when there is no DC network but all the converter stations in the multi-terminal VSC-HVDC system are connected back-to-back, sharing a common DC bus, then a simplification of (3.124) reduces to (3.137).

$$\begin{bmatrix} \mathbf{F}_{\mathbf{Slack}1} \\ \vdots \\ \mathbf{F}_{\mathbf{Slack}m} \\ \hline \mathbf{F}_{\mathbf{Psch}1} \\ \vdots \\ \mathbf{F}_{\mathbf{Psch}n} \\ \hline \mathbf{F}_{\mathbf{Pass}1} \\ \vdots \\ \mathbf{F}_{\mathbf{Pass}r} \end{bmatrix}^i = - \left[\begin{array}{ccc|ccc|ccc} \mathbf{J}_{\mathbf{Slack}1} & \cdots & \mathbf{0} & & & & & & \\ \vdots & \ddots & \vdots & & \mathbf{0} & & & \mathbf{0} & \\ \mathbf{0} & \cdots & \mathbf{J}_{\mathbf{Slack}m} & & & & & & \\ \hline & & & \mathbf{J}_{\mathbf{Psch}1} & \cdots & \mathbf{0} & & & \\ & \mathbf{0} & & \vdots & \ddots & \vdots & & \mathbf{0} & \\ & & & \mathbf{0} & \cdots & \mathbf{J}_{\mathbf{Psch}n} & & & \\ \hline & & & & & & \mathbf{J}_{\mathbf{Pass}1} & \cdots & \mathbf{0} \\ & \mathbf{0} & & & \mathbf{0} & & \vdots & \ddots & \vdots \\ & & & & & & \mathbf{0} & \cdots & \mathbf{J}_{\mathbf{Pass}r} \end{array}\right]^i \begin{bmatrix} \mathbf{\Delta\Phi}_{\mathbf{Slack}1} \\ \vdots \\ \mathbf{\Delta\Phi}_{\mathbf{Slack}m} \\ \hline \mathbf{\Delta\Phi}_{\mathbf{Psch}1} \\ \vdots \\ \mathbf{\Delta\Phi}_{\mathbf{Psch}n} \\ \hline \mathbf{\Delta\Phi}_{\mathbf{Pass}1} \\ \vdots \\ \mathbf{\Delta\Phi}_{\mathbf{Pass}r} \end{bmatrix}^i \tag{3.137}$$

Notice that the Jacobian matrix is decoupled but that the overall system of equations remains tightly coupled through the constrained branch powers (3.111) which make up the m VSC$_{Slack}$ type converters, n VSC$_{Psch}$ type converters and r VSC$_{Pass}$ type converters in (3.137).

3.5.3 Unified solutions of AC/DC networks

Since the multi-terminal VSC-HVDC system is used to interconnect a number of otherwise independent networks, the linearised form of the overall electric power system equations at a given iteration i, is given by (3.138) (Acha and Castro, 2016a; Acha and Castro, 2016b).

$$\underbrace{\begin{pmatrix} \mathbf{F}_{AC} \\ \hdashline \mathbf{F}_{Slack} \\ \vdots \\ \hdashline \mathbf{F}_{Psch} \\ \vdots \\ \hdashline \mathbf{F}_{Pass} \\ \vdots \\ \hdashline \mathbf{F}_{dc} \end{pmatrix}^{i}}_{\mathbf{F}^{i}_{AC/DC}} = - \begin{pmatrix} \\ \mathbf{J}_{AC/DC} \\ \\ \end{pmatrix}^{i} \underbrace{\begin{pmatrix} \Delta\boldsymbol{\Psi}_{AC} \\ \hdashline \Delta\boldsymbol{\Phi}_{Slack} \\ \vdots \\ \hdashline \Delta\boldsymbol{\Phi}_{Psch} \\ \vdots \\ \hdashline \Delta\boldsymbol{\Phi}_{Pass} \\ \vdots \\ \hdashline \Delta\mathbf{E}_{dc} \end{pmatrix}^{i}}_{\Delta\boldsymbol{\Psi}^{i}_{AC/DC}} \tag{3.138}$$

where $\mathbf{J}_{AC/DC}$ accommodates the first order partial derivatives of all the mismatches of the AC networks $\mathbf{F}_{AC}$, the voltage source converters $\mathbf{F}_{Slack}$, $\mathbf{F}_{Psch}$ and $\mathbf{F}_{Pass}$, and the DC network $\mathbf{F}_{dc}$, with respect to all the state variables involved. The mismatches relating to any FACTS device that may exist in any of the AC power grids would be included in $\mathbf{F}_{AC}$. Correspondingly, $\Delta\boldsymbol{\Psi}_{AC}$ is a vector that accommodates all the state variables of the AC networks, such as the phase angles and magnitudes of the AC voltages, including those pertaining to any FACTS device. It should be remarked that the manner in which the VSCs of the multi-terminal VSC-HVDC system are modelled and assembled in an all-encompassing frame-of-reference, gives rise to a simultaneous, unified solution of the AC/DC system, as shown in Figure 3.7. This is a holistic approach in which the AC systems of arbitrary configurations are connected to the high-voltage side of each OLTC transformer; in turn, the DC side of each pairing VSC is linked to a DC system that has an arbitrary connection.

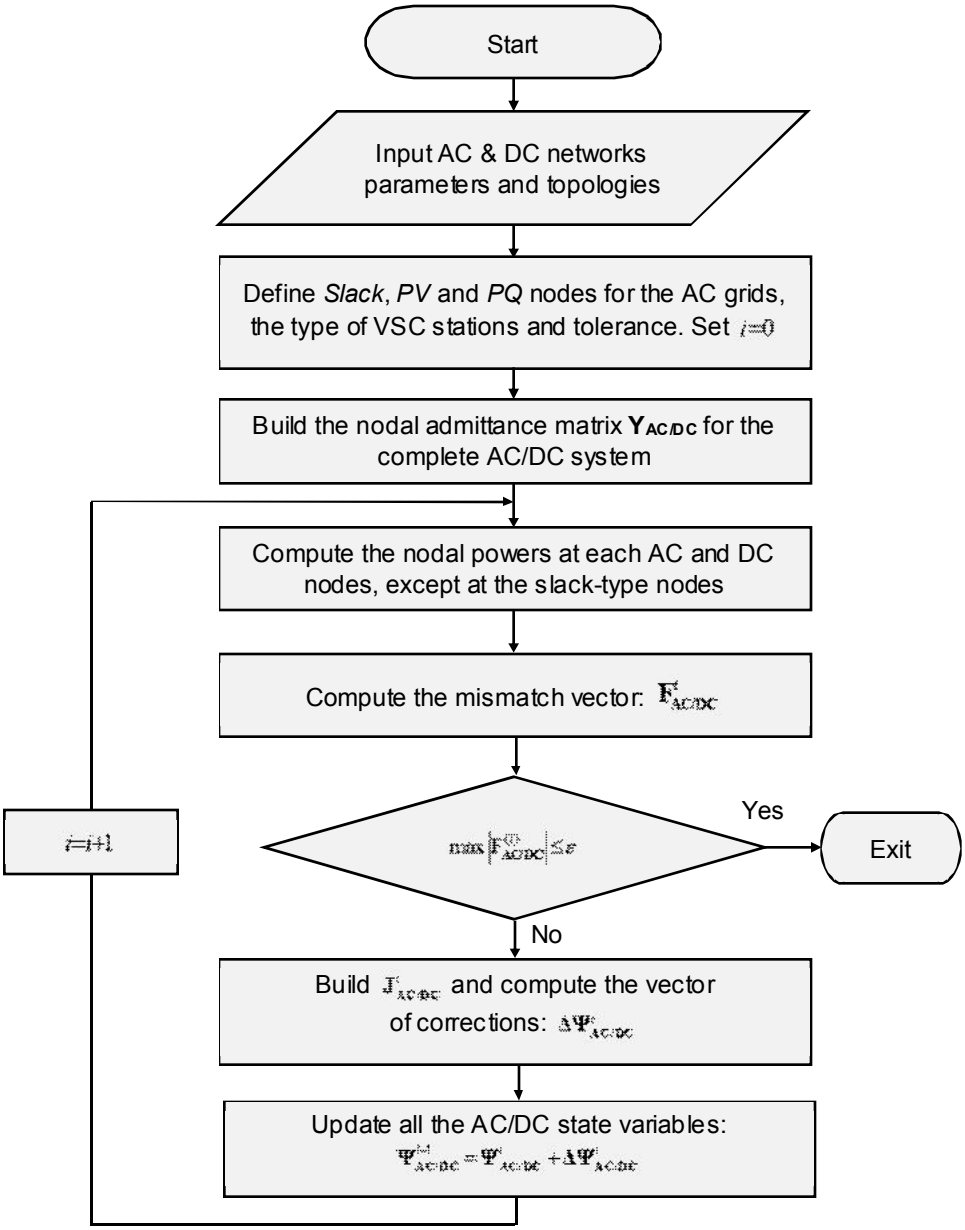

Figure 3.7 Flow diagram of a true unified solution of the multi-terminal VSC-HVDC system

3.6 Conclusions

This Chapter has introduced new models of the STATCOM, back-to-back and point-to-point VSC-HVDC links, and multi-terminal HVDC systems for steady-state analysis of power systems, i.e., the models haven numerically solved within the context of power flows. The central component of such

devices is the VSC which, in contrast to the converter's treatment as customary controllable voltage and current sources in earlier models, the introduced positive-sequence VSC model rather uses a compound of a phase-shifting transformer and equivalent shunt admittance with which key control properties of PWM-based converters may be linked, where the conduction losses and the switching losses of the converters are also captured in the model.

The modular representation of the VSC facilitates, for instance, the creation of all-encompassing models of the back-to-back and point-to-point VSC-HVDC links, models that retain characteristics that conform well to actual VSC-HVDC links, i.e., the models possess four degrees of freedom by exerting voltage control at its two AC terminals and at its DC bus whereas simultaneously regulating the transmitted power through the DC link. Furthermore, this Chapter presented a particular application of point-to-point HVDC links feeding into AC passive networks, i.e., electrical networks with no synchronous generation of their own; the inverter takes the responsibility of a slack generator providing both the electrical angular reference and the active power required to match the load plus the power losses in the passive network. This new power flow model has been developed as the basis of a VSC-HVDC link dynamic model aimed at providing frequency support to low-inertia AC networks, an application that is presented in the next Chapter.

Moving into the multi-terminal direction, a generalised frame-of-reference for the unified power-flow solution of AC power systems and multi-terminal VSC-HVDC systems has been presented in this Chapter. The new frame-of-reference is a linearised representation of the whole AC and DC power networks around a base operating point enabling its iterative solution using the Newton-Raphson method, retaining its well-proven characteristics of convergence towards the solution. As in the case of the STATCOM and two-terminal HVDC link models, the basic building block is a nodal transfer admittance representing the fundamental frequency operation of a balanced three-phase VSC. It should be highlighted that this model of multi-terminal schemes does not limit the size of the AC sub-networks nor the number of VSC units or the topology of the DC grid, thus converting it into a far-reaching formulation in terms of its applicability to practical power systems.

4 Modelling of VSC-based equipment for dynamic simulations

The interest in DC-based transmission systems has been long associated with the need for transferring electrical energy over very long distances, which led to the development of CSC-based transmission systems, the predecessor technology of VSC-based installations. Other challenges inherent to the operation of power systems, such as the interconnection of weak or passive AC systems as well as the desire for more voltage and power controllability, have also motivated the construction of VSC-based transmission systems. The operation of today's power networks is becoming more complex due to the use of HVDC-type controllers to enable a smoother operation of the network; the need to balance the large power deviations in important tie lines resorting to only power regulation using conventional synchronous generators does not seem as effective as it was in the past. The problem is intensified if intermittent electrical energy sources lie nearby key transmission paths. A host of undesirable phenomena may result in those tie lines such as reverse power flows. The installation of FACTS-type power flow controlling devices seems to offer a realistic solution to resolve such problems and to enable the transmission of larger amounts of electrical energy between control areas without endangering the stability of the interconnected networks; VSC-HVDC systems have become the preferred technically, and more cost-effective option for renewable energy applications, particularly for off-shore wind farms.

There are still many technical challenges that are awaiting solution concerning the technology of VSC-based equipment, particularly in the area of multi-level converter topologies. But concerning the power system itself, the application areas of power electronics are already well identified. Moreover, the key principle remains largely untouched: generation, transmission and distribution facilities must operate in a co-ordinated fashion to guarantee that at any given time, loads are served with a high quality of service. Arguably, electric power systems are amongst one of the most complex dynamic systems ever built, something that requires the intervention of skilful engineers. Power systems analysts ought to be able to assess in advance the various issues that may emerge when the network undergoes drastic changes as it will be the case when new

equipment is added into the transmission system such as STATCOMs, back-to-back, point-to-point and multi-terminal HVDC links. Accordingly, research effort is required to develop reliable and comprehensive VSC models with which to evaluate the dynamic impact of these devices in the network prior to its installation. At the design stage, simulation studies of credible disturbances will reveal how the new equipment will perform and impact the network. Careful consideration needs to be given to the control systems of the power converters: the effectiveness of the voltage and power control strategies, to counteract a wide range of perturbations in the electrical networks, must be beyond doubt.

This chapter addresses the dynamic modelling of STATCOMs, back-to-back, point-to-point and multi-terminal VSC-HVDC links aimed at conducting power systems simulations. The basic VSC dynamic model is incremental in nature whose derivation is carried out to conform to its particular pairing AC network and application. For instance, in the case of multi-terminal VSC-HVDC links, three VSC dynamic models are introduced - the slack converter whose aim is to control its DC voltage, the scheduled-power converter which injects a scheduled amount of power and the passive converter which is connected to an AC network with no frequency control equipment. Disregarding its application as STATCOM or any configuration of HVDC links, each VSC unit makes provisions for the phase reactor, AC filter, DC capacitor, DC smoothing inductor and OLTC transformer, thus giving rise to comprehensive dynamic models. This situation is very much the same with regards to their overall formulation and numerical solution, the modelling is carried out in a unified time-domain framework underpinned by the trapezoidal and Newton methods with which the positive-sequence dynamic solution of the various VSC-based devices is carried out.

4.1 STATCOM model for dynamic simulations

Figure 4.1 shows a schematic representation of the STATCOM and its control variables. The voltage source converter, whose AC terminal is connected to the low-voltage side of the OLTC transformer, is charged with the control of the AC voltage magnitude V_v. The VSC station uses a DC capacitor, one that plays an important role in the dynamics of the converter. In the steady-state regime, its voltage is kept constant at the nominal value E_{dcnom} and the current in the capacitor becomes zero, $i_c=0$, something that can be inferred from the expression of the capacitor current (4.1) in which the derivative of the voltage with respect to time is zero. During the dynamic regime, however, failures on the AC network are reflected in the DC link voltage, pushing the capacitor to a charging/discharging stage.

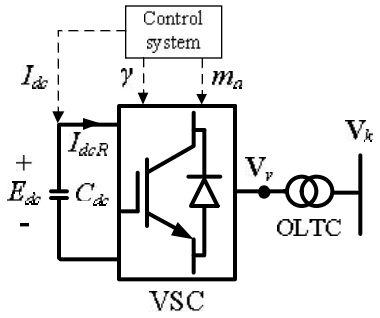

Figure 4.1 Schematic diagram of the STATCOM and its control variables

The VSC dynamics are accurately captured if the dynamics in the DC capacitor are suitably represented when it is exposed to changes in the current flowing through it. The computation of the voltage oscillations at the DC bus requires the determination of both the current injected at the DC bus I_{dcR} (4.2) and the capacitor current $i_c = -I_{dcR} - I_{dc}$.

$$i_c = C_{dc} \frac{dE_{dc}}{dt} \tag{4.1}$$

$$I_{dcR} = \frac{P_{0v}}{E_{dc}} \tag{4.2}$$

where P_{0v} is the nodal power injected at the DC bus (3.11), previously derived in Section 3.1. Therefore, the expression (4.3) serves the purpose of calculating the DC voltage dynamics of the STATCOM (Castro et al., 2013).

$$\frac{dE_{dc}}{dt} = \frac{-I_{dcR} - I_{dc}}{C_{dc}} \tag{4.3}$$

where I_{dc} is the selected control variable acting upon the DC voltage. This last mathematical expression permits the calculation of the DC voltage dynamics in the voltage source converter. At this point, paying attention to the value of the capacitor C_{dc} is necessary as it plays a crucial role when attaining the DC voltage dynamics. Its value is estimated according to the energy stored in the capacitor: $W_c = \frac{1}{2} C_{dc} E_{dc}^2$. Arguably, the electrostatic energy stored in the capacitor bears a resemblance with the kinetic energy of the rotating electrical machinery, where this energy can be further related to the inertia constant that impacts the motion equation of a certain rotating machine. Following the same reasoning, the electrostatic energy stored in the DC capacitor can be associated with an equivalent inertia constant H_c [s] as $W_c = H_c S_{nom}$, where S_{nom} would correspond to the rated apparent power of the VSC. This time constant may be taken to be approximately

$H_c = \omega_s^{-1}$ by drawing a parallel between the converter and a bank of thyristor-switched capacitors of the same rating; however, it is recommended that $H_c \geq 5ms$ so as to avoid numerical instabilities (de Oliveira, 2000). Hence, the value of the capacitor is computed as in (4.4).

$$C_{dc} = \frac{2S_{nom}H_c}{E_{dc}^2} \tag{4.4}$$

The stability of the DC voltage ensures a smooth operation of the STATCOM; the voltage control at the DC side of the VSC is carried out through the regulation of the DC current entering or leaving the converter, I_{dc}. The implementation of the DC voltage controller is shown in Figure 4.2 (Castro et al., 2013), in which the error between the actual voltage E_{dc} and E_{dcnom} is processed through a PI controller to obtain new values of the DC current I_{dc} at every time-step. Hence, the DC voltage dynamics is basically determined by the gains K_{pe} and K_{ie}.

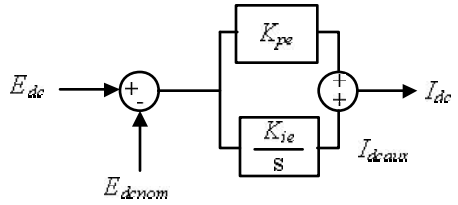

Figure 4.2 DC voltage controller of the VSC

The equations arising from the block diagram corresponding to the DC voltage controller are shown in (4.5)-(4.6).

$$\frac{dI_{dcaux}}{dt} = K_{ie}\left(E_{dc} - E_{dcnom}\right) \tag{4.5}$$

$$I_{dc} = K_{pe}\left(E_{dc} - E_{dcnom}\right) + I_{dcaux} \tag{4.6}$$

The converter keeps the capacitor charged to the required voltage level by making its output voltage lag the AC system voltage by a small angle (Hingorani and Gyugyi, 1999). This angular difference is computed as $\gamma = \theta_v - \phi$, where ϕ is the angle of the phase-shifting transformer and θ_v represents the angle of the AC terminal voltage of the VSC. During the dynamic regime, the power balance on the DC side of the converter is achieved by suitable control of the angle γ. The PI controller designed to meet such a purpose is shown in Figure 4.3 (Castro et al., 2013).

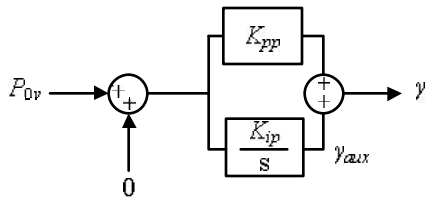

Figure 4.3 DC power controller for the DC side of the VSC

where the 0 entry of the sum block of the PI regulator signifies that there is no external power injection at the DC bus. The differential equations that represent the dynamic behaviour of this power controller are given by (4.7)-(4.8).

$$\frac{d\gamma_{aux}}{dt} = K_{ip} P_{0v} \tag{4.7}$$

$$\gamma = K_{pp} P_{0v} + \gamma_{aux} \tag{4.8}$$

The modulation index is responsible for keeping the AC terminal voltage magnitude at the desired value; to such an end, the AC-bus voltage controller depicted in Figure 4.4 is employed (Castro et al., 2013). This is a first-order controller which yields small changes in the modulation index dma by comparing the actual voltage V_v and the scheduled AC voltage V_v^{spec}. The new value of the modulation index increases or decreases according to the operating requirements conditions. The differential equation for the AC voltage controller is shown in (4.9).

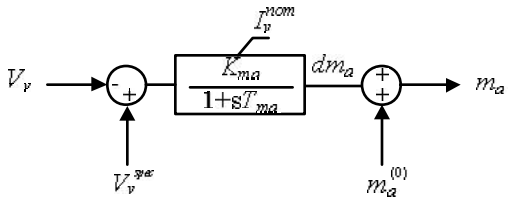

Figure 4.4 AC-bus voltage controller of the VSC

$$\frac{d(dm_a)}{dt} = \frac{K_{ma}\left(V_v^{spec} - V_v\right) - dm_a}{T_{ma}} \tag{4.9}$$

To guarantee that the VSC operates within its operating limits, a limit checking of the terminal current, previously derived in (3.13), must take place $I_v \le I_v^{nom}$. Hence, the overall dynamics of the VSC are well captured by equations (4.3)-(4.9).

The STATCOM differential equations representing the DC voltage dynamics, the DC current controller and the AC voltage controller are discretised as shown in (4.10)-(4.13).

$$F_{E_{dc}} = E_{dc(t-\Delta t)} + 0.5\Delta t \dot{E}_{dc(t-\Delta t)} - \left(E_{dc(t)} - 0.5\Delta t \dot{E}_{dc(t)}\right) \tag{4.10}$$

$$F_{I_{dcaux}} = I_{dcaux(t-\Delta t)} + 0.5\Delta t \dot{I}_{dcaux(t-\Delta t)} - \left(I_{dcaux(t)} - 0.5\Delta t \dot{I}_{dcaux(t)}\right) \tag{4.11}$$

$$F_{\gamma_{aux}} = \gamma_{aux(t-\Delta t)} + 0.5\Delta t \dot{\gamma}_{aux(t-\Delta t)} - \left(\gamma_{aux(t)} - 0.5\Delta t \dot{\gamma}_{aux(t)}\right) \tag{4.12}$$

$$F_{dm_a} = dm_{a(t-\Delta t)} + 0.5\Delta t d\dot{m}_{a(t-\Delta t)} - \left(dm_{a(t)} - 0.5\Delta t d\dot{m}_{a(t)}\right) \tag{4.13}$$

where

$$\dot{E}_{dc(t)} = C_{dc}^{-1}\left(-I_{dcR(t)} - I_{dc(t)}\right) \tag{4.14}$$

$$\dot{E}_{dc(t-\Delta t)} = C_{dc}^{-1}\left(-I_{dcR(t-\Delta t)} - I_{dc(t-\Delta t)}\right) \tag{4.15}$$

$$\dot{I}_{dcaux(t)} = K_{ie}\left(E_{dc(t)} - E_{dcnom}\right) \tag{4.16}$$

$$\dot{I}_{dcaux(t-\Delta t)} = K_{ie}\left(E_{dc(t-\Delta t)} - E_{dcnom}\right) \tag{4.17}$$

$$\dot{\gamma}_{aux(t)} = K_{ip} P_{0v(t)} \tag{4.18}$$

$$\dot{\gamma}_{aux(t-\Delta t)} = K_{ip} P_{0v(t-\Delta t)} \tag{4.19}$$

$$d\dot{m}_{a(t)} = T_{ma}^{-1}\left[K_{ma}\left(V_v^{spec} - V_{v(t)}\right) - dm_{a(t)}\right] \tag{4.20}$$

$$d\dot{m}_{a(t-\Delta t)} = T_{ma}^{-1}\left[K_{ma}\left(V_v^{spec} - V_{v(t-\Delta t)}\right) - dm_{a(t-\Delta t)}\right] \tag{4.21}$$

The discretised differential equations of the VSC are appended to those corresponding to the active and reactive power balances of the power network at the AC terminal of the VSC and the high-voltage side of the OLTC transformer. These equations were derived in Section 3.3 but for the sake of completeness they are reproduced in equations (4.22)-(4.25).

$$\Delta P_k = -P_{kltc} - P_{dk} - P_k^{cal} \tag{4.22}$$

$$\Delta Q_k = -Q_{kltc} - Q_{dk} - Q_k^{cal} \tag{4.23}$$

$$\Delta P_v = -P_v - P_{dv} - P_{vltc} \tag{4.24}$$

$$\Delta Q_v = -Q_v - Q_{dv} - Q_{vltc} \tag{4.25}$$

Equations (4.10)-(4.13) and (4.22)-(4.25) make up the necessary set of equations that must be solved together with the equations of the whole network including synchronous generators and their controls to carry out dynamic simulations of power systems containing STATCOM devices. To solve such non-linear set of equations, the Newton-Raphson method is employed for reliable

dynamic simulations. Hence, in connection with Figure 4.1 where the STATCOM is assumed to be connected at bus k of the power system, the linearised matrix equation (4.26), around a base operating point, provides the computing framework with which the time-domain solutions are performed (Castro et al., 2013).

$$\begin{bmatrix} \Delta P_k \\ \Delta Q_k \\ \Delta P_v \\ \Delta Q_v \\ \hline F_{E_{dc}} \\ F_{I_{dcaux}} \\ F_{\gamma_{aux}} \\ F_{dm_a} \end{bmatrix}^i = -\left[\begin{array}{c|c} \mathbf{J}_{11} & \mathbf{J}_{12} \\ \hline \mathbf{J}_{21} & \mathbf{J}_{22} \end{array}\right]^i \begin{bmatrix} \Delta\theta_k \\ \Delta V_k \\ \Delta\theta_v \\ \Delta V_v \\ \hline \Delta E_{dc} \\ \Delta I_{dcaux} \\ \Delta\gamma_{aux} \\ \Delta dm_a \end{bmatrix}^i \tag{4.26}$$

where $\mathbf{J}_{11}$ comprises the first-order partial derivatives of the nodal active and reactive power mismatches with respect to the voltage angle and voltage magnitude of the AC-side voltages, i.e., both the AC terminal of the VSC and the high-voltage side of the OLTC transformer. Likewise, $\mathbf{J}_{12}$ contains the partial derivatives arising from the nodal active and reactive powers with respect to the state variables of the converter. The matrix $\mathbf{J}_{21}$ consists of partial derivatives of the VSC discretised differential equations with respect to AC voltages. Lastly, $\mathbf{J}_{22}$ is a matrix that accommodates the first-order partial derivatives of the VSC discretised differential equations with respect to its own control variables. These matrices are shown in (4.27)-(4.28).

$$\mathbf{J}_{11} = \begin{bmatrix} \frac{\partial\Delta P_k}{\partial\theta_k} & \frac{\partial\Delta P_k}{\partial V_k} & \frac{\partial\Delta P_k}{\partial\theta_v} & \frac{\partial\Delta P_k}{\partial V_v} \\ \frac{\partial\Delta Q_k}{\partial\theta_k} & \frac{\partial\Delta Q_k}{\partial V_k} & \frac{\partial\Delta Q_k}{\partial\theta_v} & \frac{\partial\Delta Q_k}{\partial V_v} \\ \frac{\partial\Delta P_v}{\partial\theta_k} & \frac{\partial\Delta P_v}{\partial V_k} & \frac{\partial\Delta P_v}{\partial\theta_v} & \frac{\partial\Delta P_v}{\partial V_v} \\ \frac{\partial\Delta Q_v}{\partial\theta_k} & \frac{\partial\Delta Q_v}{\partial V_k} & \frac{\partial\Delta Q_v}{\partial\theta_v} & \frac{\partial\Delta Q_v}{\partial V_v} \end{bmatrix}, \quad \mathbf{J}_{12} = \begin{bmatrix} 0 & 0 & 0 & 0 \\ 0 & 0 & 0 & 0 \\ \frac{\partial\Delta P_v}{\partial E_{dc}} & 0 & 0 & \frac{\partial\Delta P_v}{\partial dm_a} \\ \frac{\partial\Delta Q_v}{\partial E_{dc}} & 0 & 0 & \frac{\partial\Delta Q_v}{\partial dm_a} \end{bmatrix} \tag{4.27}$$

$$\mathbf{J}_{21} = \begin{bmatrix} 0 & 0 & \frac{\partial F_{E_{dc}}}{\partial\theta_v} & \frac{\partial F_{E_{dc}}}{\partial V_v} \\ 0 & 0 & 0 & 0 \\ 0 & 0 & \frac{\partial F_{\gamma_{aux}}}{\partial\theta_v} & \frac{\partial F_{\gamma_{aux}}}{\partial V_v} \\ 0 & 0 & \frac{\partial F_{dm_a}}{\partial\theta_v} & \frac{\partial F_{dm_a}}{\partial V_v} \end{bmatrix}, \quad \mathbf{J}_{22} = \begin{bmatrix} \frac{\partial F_{E_{dc}}}{\partial E_{dc}} & 0 & 0 & \frac{\partial F_{E_{dc}}}{\partial dm_a} \\ \frac{\partial F_{I_{dcaux}}}{\partial E_{dc}} & \frac{\partial F_{I_{dcaux}}}{\partial I_{dcaux}} & 0 & 0 \\ \frac{\partial F_{\gamma_{aux}}}{\partial E_{dc}} & 0 & \frac{\partial F_{\gamma_{aux}}}{\partial\gamma_{aux}} & \frac{\partial F_{\gamma_{aux}}}{\partial dm_a} \\ 0 & 0 & 0 & \frac{\partial F_{dm_a}}{\partial dm_a} \end{bmatrix} \tag{4.28}$$

It is worth recalling that a dynamic simulation requires as its main input the steady-state initial conditions of the dynamic system to be solved. This steady-state equilibrium point is computed in advance using the power flow model that has been addressed in Section 3.3, thus ensuring a reliable dynamic solution.

Considerations for the OLTC transformer during the dynamic operating regime

The adopted modelling approach calculates together the state variables of the VSC station and that of the OLTC transformer through the power-flow solution, as presented in Chapter 3. However, during the dynamic operating regime the time constants involved in the tap controllers of the OLTC transformer are large in comparison with the very rapid time responses afforded by a VSC station. Therefore, from now on in this chapter and with no loss of applicability, the OLTC transformer dynamics are omitted, keeping the tap values furnished by the power-flow solution as constant parameters during the dynamic state. Indeed, the long-term impact that the operation of the OLTC transformer might have on the dynamic performance of the newly developed VSC-based equipment models could also be assessed (if the control loop of the OLTC taps is considered), however, this lies outside the main focus of the research carried out in this thesis.

4.2 VSC-HVDC models for dynamic simulations

Steady-state and dynamic operating regimes are both fields that need to be covered to the satisfaction of the planners and operators of utility-scale power networks, therefore power systems-oriented VSC-HVDC models ought to be created bearing in mind its main operational features. In power system simulations, the tendency has been to keep the HVDC models as simple as possible owing to stringent requirements in terms of simulation time, memory, lack of data, etc., but today more than never before, all these facts shift to the background as technology progresses in many fronts. Some existing VSC-HVDC models are represented with idealised voltage sources owing to its much reduced complexity sacrificing the acquisition of important data since its internal variables may not be readily available. In the arena of modelling and simulation of VSC-HVDC systems, more realistic behaviours may be captured if one is willing to depart from those reduced models.

The assessment of key operational characteristics of the VSCs comprising the HVDC link is achieved if each VSC is modelled with a series of basic electric power system elements, as extensively addressed in Chapter 3, representing the very different features playing a role in both the steady-state and dynamic performances of these AC/DC power electronics devices. This

means that, unlike the earlier positive-sequence models, all the state variables of each VSC become explicit and encapsulate the actual performance of the AC and DC circuits for the dynamic operating regime. Figure 4.5 depicts a schematic representation of the VSC-HVDC link together with its control variables and parameters. The four degrees of freedom found in actual VSC-HVDC installations ought to be encapsulated in practical model developments. These are the simultaneous voltage support on its two AC terminals, DC voltage control at the inverter station and DC power regulation performed by the rectifier station (Castro and Acha, 2015a; Castro and Acha, 2015b).

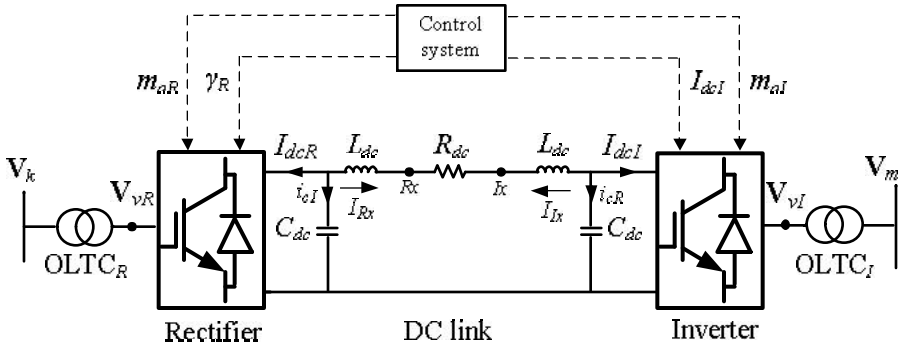

Figure 4.5 Schematic representation of the VSC-HVDC link and its control variables

The dynamics of the capacitors, as in the case of the VSC of the STATCOM, along with that of the inductors play a crucial role in the HVDC link operation when subjected to voltage and power variations in the external AC network. In the point-to-point connection of the VSCs, voltage control must also be exerted on the DC link in order to preserve the stability of the DC transmission system. The inverter station takes on the responsibility of controlling the DC voltage to conform with the standard practice in actual HVDC applications. In connection with Figure 4.5, the following relationships hold at the nodes of the capacitors: $i_{cR}=-I_{dcR}-I_{Rx}$ and $i_{cI}=-I_{dcI}-I_{Ix}$, where i_{cR} and i_{cI} are the capacitors currents, I_{dcR} and I_{dcI} are the currents leaving the DC bus of both the rectifier and the inverter, respectively. Combining these current relationships with those of the well-known capacitor current $i_c=C_{dc}\,dE/dt$ and inductor voltage $E_i=L_{dc}\,dI/dt$, the differential equations (4.29)-(4.30) are obtained. Both enable the calculation of the voltage and current dynamics ocurring in the DC link.

$$\frac{dE_{dcR}}{dt}=\frac{-I_{dcR}-I_{Rx}}{C_{dc}}, \qquad \frac{dI_{Rx}}{dt}=\frac{E_{dcR}-E_{dcRx}}{L_{dc}} \tag{4.29}$$

$$\frac{dE_{dcI}}{dt}=\frac{-I_{dcI}-I_{Ix}}{C_{dc}}, \qquad \frac{dI_{Ix}}{dt}=\frac{E_{dcI}-E_{dcIx}}{L_{dc}} \tag{4.30}$$

where $I_{dcR} = P_{0vR} E_{dcR}^{-1}$ and the power P_{0vR} is given by (3.36). The per-unit value of the capacitance is estimated using (4.4) and an equivalent inertia constant H_c representing the electrostatic energy stored in the capacitor. A similar expression may be derived for the per-unit value of the inductor through an inertia constant that accounts for the electromagnetic energy stored in the inductor; this expression is shown in (4.31).

$$L_{dc} = \frac{2 S_{nom} H_i}{I_{dc}^2} \tag{4.31}$$

where H_i and I_{dc} stand for the fictitious inertia constant and nominal current of the inductor. Arguably, the current balance of the back-to-back converter given by (4.29)-(4.30) is akin to the power balance inside the HVDC link for steady-state operation, when the derivative terms become zero. If the current/power balance is disrupted then voltage variations appear throughout the DC circuit formed by the VSC-based power transmission link. As shown in Figure 4.6, the dynamic control of the DC voltage is carried out using the DC current entering the inverter I_{dcI} as the control variable. The error between the actual voltage E_{dcI} and the reference E_{dcInom} is passed through a PI controller to obtain new values of the DC current of the inverter.

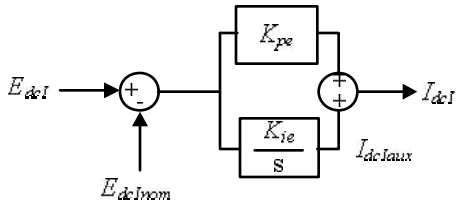

Figure 4.6 DC voltage dynamic controller of the VSC-HVDC link

The differential and algebraic equations arising from the DC voltage dynamic controller are shown in (4.32)-(4.33).

$$\frac{dI_{dcIaux}}{dt} = K_{ie}\left(E_{dcI} - E_{dcInom}\right) \tag{4.32}$$

$$I_{dcI} = K_{pe}\left(E_{dcI} - E_{dcInom}\right) + I_{dcIaux} \tag{4.33}$$

Simultaneously, the rectifier unit must ensure that the active power leaving this station is kept at the scheduled value P_{sch}. From Figure 4.5, it can be inferred that the power entering the inverter is one that results from the power entering the rectifier station minus both the power charging/discharging the rectifier DC capacitor and the power loss incurred in the DC cable (R_{dc}). The DC power flowing from node R_x towards node I_x may be expressed in terms of DC voltages,

as in (4.34).

$$P_{dcR} = \left(E_{dcRx}^2 - E_{dcRx} E_{dcIx} \right) G_{dc} \tag{4.34}$$

Likewise, the power flowing from node I_x towards node R_x through the DC cable may be expressed as in (4.35).

$$P_{dcI} = \left(E_{dcIx}^2 - E_{dcIx} E_{dcRx} \right) G_{dc} \tag{4.35}$$

During the transient period, a disturbance either in the interconnected power networks or in the HVDC link itself would provoke voltage oscillations throughout the DC link. However, when the whole system is back to steady conditions, the above DC power expressions reduce to the powers derived for the steady-state (3.42)-(3.43), where $E_{dcRx} = E_{dcR}$ and $E_{dcIx} = E_{dcI}$, since the current drawn by the capacitors is zero.

If the rectifier is charged with the DC power control, then the regulation of the angular aperture between its phase-shifting angle ϕ_R and the AC voltage angle θ_{vR} must take place. Hence, the desired power exchange between the network and the rectifier P_{sch} is attained by suitably regulating the angle $\gamma_R = \theta_{vR} - \phi_R$. Unlike the objective of the power controller of the STATCOM, shown in Figure 4.3, the pursued power balance on the DC side will be now given by the following expression: $P_{0vR} + P_{sch} = 0$, as inferred from Figure 4.7 (Castro and Acha, 2015a).

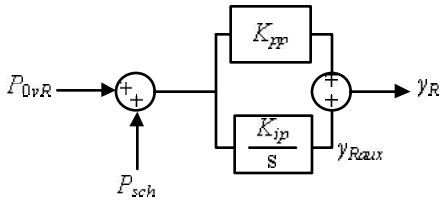

Figure 4.7 DC-power controller of the VSC-HVDC link model

The equations that enable the calculation of the dynamic behaviour of the DC power transmission are expressed as shown in (4.36)-(4.37).

$$\frac{d\gamma_{Raux}}{dt} = K_{ip} \left(P_{sch} + P_{0vR} \right) \tag{4.36}$$

$$\gamma_R = K_{pp} \left(P_{sch} + P_{0vR} \right) + \gamma_{Raux} \tag{4.37}$$

On the other hand, the two VSC stations give rise to two control loops aimed at attaining AC

voltage magnitude control at both ends of the VSC-HVDC system. The modulation indices m_{aI} and m_{aR} are responsible for controlling the AC voltage magnitudes at the receiving and sending ends of the VSC-HVDC link, all this in accordance with the scheduled values V_{vI}^{spec} and V_{vR}^{spec}, respectively. To that end, the first-order control blocks shown in Figure 4.8 are designed to provide AC voltage control. Therefore the modulation indices m_{aI} and m_{aR} are readjusted at every time step according to the difference between the scheduled voltage magnitudes and the actual voltage at the nodes where the converters are connected to: V_{vI} and V_{vR}.

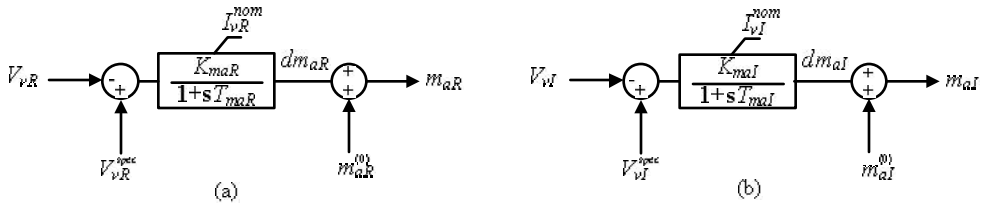

Figure 4.8 AC-bus voltage controllers: (a) rectifier station and (b) inverter station

The differential equations for the AC-bus voltage controllers are given by (4.38)-(4.39).

$$\frac{d\left(dm_{aR}\right)}{dt}=\frac{K_{maR}\left(V_{vR}^{spec}-V_{vR}\right)-dm_{aR}}{T_{maR}} \tag{4.38}$$

$$\frac{d\left(dm_{aI}\right)}{dt}=\frac{K_{maI}\left(V_{vI}^{spec}-V_{vI}\right)-dm_{aI}}{T_{maI}} \tag{4.39}$$

4.2.1 VSC-HVDC dynamic model with DC power regulation capabilities

The differential equations arising from the controllers of the VSC-HVDC link model are discretised and arranged in a suitable form, as shown in (4.40)-(4.47), to facilitate their accommodation in the expanded Jacobian matrix (Castro and Acha, 2015a). They are,

$$F_{E_{dcR}}=E_{dcR(t-\Delta t)}+0.5\Delta t\dot{E}_{dcR(t-\Delta t)}-\left(E_{dcR(t)}-0.5\Delta t\dot{E}_{dcR(t)}\right) \tag{4.40}$$

$$F_{E_{dcI}}=E_{dcI(t-\Delta t)}+0.5\Delta t\dot{E}_{dcI(t-\Delta t)}-\left(E_{dcI(t)}-0.5\Delta t\dot{E}_{dcI(t)}\right) \tag{4.41}$$

$$F_{I_{Rx}}=I_{Rx(t-\Delta t)}+0.5\Delta t\,\dot{I}_{Rx(t-\Delta t)}-\left(I_{Rx(t)}-0.5\Delta t\,\dot{I}_{Rx(t)}\right) \tag{4.42}$$

$$F_{I_{Ix}}=I_{Ix(t-\Delta t)}+0.5\Delta t\,\dot{I}_{Ix(t-\Delta t)}-\left(I_{Ix(t)}-0.5\Delta t\,\dot{I}_{Ix(t)}\right) \tag{4.43}$$

$$F_{I_{dcIaux}} = I_{dcIaux(t-\Delta t)} + 0.5\Delta t \dot{I}_{dcIaux(t-\Delta t)} - \left(I_{dcIaux(t)} - 0.5\Delta t \dot{I}_{dcIaux(t)} \right) \tag{4.44}$$

$$F_{\gamma_{Raux}} = \gamma_{Raux(t-\Delta t)} + 0.5\Delta t \dot{\gamma}_{Raux(t-\Delta t)} - \left(\gamma_{Raux(t)} - 0.5\Delta t \dot{\gamma}_{Raux(t)} \right) \tag{4.45}$$

$$F_{dm_{aR}} = dm_{aR(t-\Delta t)} + 0.5\Delta t d\dot{m}_{aR(t-\Delta t)} - \left(dm_{aR(t)} - 0.5\Delta t d\dot{m}_{aR(t)} \right) \tag{4.46}$$

$$F_{dm_{aI}} = dm_{aI(t-\Delta t)} + 0.5\Delta t d\dot{m}_{aI(t-\Delta t)} - \left(dm_{aI(t)} - 0.5\Delta t d\dot{m}_{aI(t)} \right) \tag{4.47}$$

where

$$\dot{E}_{dcI(t)} = C_{dc}^{-1} \left(-I_{dcI(t)} - I_{Ix(t)} \right) \tag{4.48}$$

$$\dot{E}_{dcI(t-\Delta t)} = C_{dc}^{-1} \left(-I_{dcI(t-\Delta t)} - I_{Ix(t-\Delta t)} \right) \tag{4.49}$$

$$\dot{E}_{dcR(t)} = C_{dc}^{-1} \left(-I_{dcR(t)} - I_{Rx(t)} \right) \tag{4.50}$$

$$\dot{E}_{dcR(t-\Delta t)} = C_{dc}^{-1} \left(-I_{dcR(t-\Delta t)} - I_{Rx(t-\Delta t)} \right) \tag{4.51}$$

$$\dot{I}_{Rx(t)} = L_{dc}^{-1} \left(E_{dcR(t)} - E_{dcRx(t)} \right) \tag{4.52}$$

$$\dot{I}_{Rx(t-\Delta t)} = L_{dc}^{-1} \left(E_{dcR(t-\Delta t)} - E_{dcRx(t-\Delta t)} \right) \tag{4.53}$$

$$\dot{I}_{Ix(t)} = L_{dc}^{-1} \left(E_{dcI(t)} - E_{dcIx(t)} \right) \tag{4.54}$$

$$\dot{I}_{Ix(t-\Delta t)} = L_{dc}^{-1} \left(E_{dcI(t-\Delta t)} - E_{dcIx(t-\Delta t)} \right) \tag{4.55}$$

$$\dot{I}_{dcIaux(t)} = K_{ie} \left(E_{dcI(t)} - E_{dcInom} \right) \tag{4.56}$$

$$\dot{I}_{dcIaux(t-\Delta t)} = K_{ie} \left(E_{dcI(t-\Delta t)} - E_{dcInom} \right) \tag{4.57}$$

$$\dot{\gamma}_{Raux(t)} = K_{ip} \left(P_{sch} + P_{0vR(t)} \right) \tag{4.58}$$

$$\dot{\gamma}_{Raux(t-\Delta t)} = K_{ip} \left(P_{sch} + P_{0vR(t-\Delta t)} \right) \tag{4.59}$$

$$d\dot{m}_{aR(t)} = T_{maR}^{-1} \left[K_{maR} \left(V_{vR}^{spec} - V_{vR(t)} \right) - dm_{aR(t)} \right] \tag{4.60}$$

$$d\dot{m}_{aR(t-\Delta t)} = T_{maR}^{-1} \left[K_{maR} \left(V_{vR}^{spec} - V_{vR(t-\Delta t)} \right) - dm_{aR(t-\Delta t)} \right] \tag{4.61}$$

$$d\dot{m}_{aI(t)} = T_{maI}^{-1} \left[K_{maI} \left(V_{vI}^{spec} - V_{vI(t)} \right) - dm_{aI(t)} \right] \tag{4.62}$$

$$d\dot{m}_{aI(t-\Delta t)} = T_{maI}^{-1} \left[K_{maI} \left(V_{vI}^{spec} - V_{vI(t-\Delta t)} \right) - dm_{aI(t-\Delta t)} \right] \tag{4.63}$$

The expressions (4.40)-(4.63) govern the dynamic behaviour of the VSC-HVDC model. The first five differential equations capture the DC voltage and current performance of the DC link when the energy balance is disrupted owing to an external failure in the AC network. Likewise, the equation involving the angular aperture γ_R (4.45) deals with the planned power transfer in the DC link. Lastly, the expressions given in (4.46)-(4.47) enable the computation of the new values of the

modulation indices with which the AC voltage set points are achieved. In order to associate the VSC-HVDC control variables with the state variables of the entire network, the algebraic power mismatch equations (4.64)-(4.71) must be used. However, completion of the model for dynamic simulation purposes calls for determining the power balance equations at the internal DC nodes R_x, I_x and $0I$, whose expressions are given in (4.72)-(4.74).

$$\Delta P_k = -P_{kltc} - P_{dk} - P_k^{cal} \tag{4.64}$$

$$\Delta Q_k = -Q_{kltc} - Q_{dk} - Q_k^{cal} \tag{4.65}$$

$$\Delta P_{vR} = -P_{vR} - P_{dvR} - P_{vRltc} \tag{4.66}$$

$$\Delta Q_{vR} = -Q_{vR} - Q_{dvR} - Q_{vRltc} \tag{4.67}$$

$$\Delta P_m = -P_{mltc} - P_{dm} - P_m^{cal} \tag{4.68}$$

$$\Delta Q_m = -Q_{mltc} - Q_{dm} - Q_m^{cal} \tag{4.69}$$

$$\Delta P_{vI} = -P_{vI} - P_{dvI} - P_{vIltc} \tag{4.70}$$

$$\Delta Q_{vI} = -Q_{vI} - Q_{dvI} - Q_{vIltc} \tag{4.71}$$

$$\Delta P_{Rx} = E_{dcRx} I_{Rx} - P_{dcR} \tag{4.72}$$

$$\Delta P_{Ix} = E_{dcIx} I_{Ix} - P_{dcI} \tag{4.73}$$

$$\Delta P_{0vI} = E_{dcI} I_{dcI} - P_{0vI} \tag{4.74}$$

The active and reactive powers taking part in the above power mistmaches were derived in Section 3.4. Equations (4.40)-(4.47) and (4.64)-(4.74) constitute the set of mismatch equations that must be assembled together with the equations of the whole network, synchronous generators and their corresponding controllers, for a unified solution approach. The linearised form of the VSC-HVDC mathematical model is given by (4.75).

$$\begin{bmatrix} \mathbf{F_R} \\ \mathbf{F_I} \\ \mathbf{F_{dc}} \end{bmatrix}^i = -\left[\begin{array}{cc|c} \begin{bmatrix} \mathbf{J_{RR1}} \\ \mathbf{J_{RR2}} \end{bmatrix} & \mathbf{0} & \mathbf{J_{Rdc}} \\ \mathbf{0} & \begin{bmatrix} \mathbf{J_{II1}} \\ \mathbf{J_{II2}} \end{bmatrix} & \mathbf{J_{Idc}} \\ \hline \mathbf{J_{dcR}} & \mathbf{0} & \mathbf{J_{dc}} \end{array}\right]^i \begin{bmatrix} \mathbf{\Delta\Phi_R} \\ \mathbf{\Delta\Phi_I} \\ \mathbf{\Delta\Phi_{dc}} \end{bmatrix}^i \tag{4.75}$$

where $\mathbf{J_{Rdc}} = \begin{bmatrix} \mathbf{0} \, \mathbf{J'_{Rdc}} \, \mathbf{0} \end{bmatrix}$, $\mathbf{J_{Idc}} = \begin{bmatrix} \mathbf{0} \, \mathbf{J'_{Idc}} \, \mathbf{0} \end{bmatrix}$ and $\mathbf{J_{dcR}} = \begin{bmatrix} \mathbf{0} \, \mathbf{J'_{dcR}} \, \mathbf{0} \end{bmatrix}^T$. Matrix $\mathbf{J_{RR1}}$ accommodates the derivative terms of the AC power mismatches arising from the rectifier with respect to both the AC state variables (voltages and angles at nodes k and vR) and the control variables of the rectifier,

namely, γ_{Raux} and dm_{aR}, whereas $\mathbf{J}_{\mathbf{RR2}}$ contains the first-order partial derivatives of the discretised differential equations emerging from the two controllers of the rectifier with respect to AC state variables and control variables; they are shown explicitly in (4.76) and (4.77), respectively. The partial derivatives of the discretised differential equation corresponding to the DC voltage of the rectifier's capacitor with respect to its corresponding AC state variables and control variables are located in matrix $\mathbf{J}_{\mathbf{dcR}}$, whilst matrix $\mathbf{J}_{\mathbf{Rdc}}$ comprises the terms emerging from deriving both the AC power mismatches and the discretised differential equations representing the dynamics of the controllers of the rectifier station with respect to the DC voltage of both capacitors; they are shown in expanded form in (4.78).

$$\mathbf{J}_{\mathbf{RR1}} = \begin{bmatrix} \frac{\partial \Delta P_k}{\partial \theta_k} & \frac{\partial \Delta P_k}{\partial V_k} & \frac{\partial \Delta P_k}{\partial \theta_{vR}} & \frac{\partial \Delta P_k}{\partial V_{vR}} & 0 & 0 \\ \frac{\partial \Delta Q_k}{\partial \theta_k} & \frac{\partial \Delta Q_k}{\partial V_k} & \frac{\partial \Delta Q_k}{\partial \theta_{vR}} & \frac{\partial \Delta Q_k}{\partial V_{vR}} & 0 & 0 \\ \frac{\partial \Delta P_{vR}}{\partial \theta_k} & \frac{\partial \Delta P_{vR}}{\partial V_k} & \frac{\partial \Delta P_{vR}}{\partial \theta_{vR}} & \frac{\partial \Delta P_{vR}}{\partial V_{vR}} & 0 & \frac{\partial \Delta P_{vR}}{\partial dm_{aR}} \\ \frac{\partial \Delta Q_{vR}}{\partial \theta_k} & \frac{\partial \Delta Q_{vR}}{\partial V_k} & \frac{\partial \Delta Q_{vR}}{\partial \theta_{vR}} & \frac{\partial \Delta Q_{vR}}{\partial V_{vR}} & 0 & \frac{\partial \Delta Q_{vR}}{\partial dm_{aR}} \end{bmatrix} \tag{4.76}$$

$$\mathbf{J}_{\mathbf{RR2}} = \begin{bmatrix} 0 & 0 & 0 & \frac{\partial F_{\gamma_{Raux}}}{\partial V_{vR}} & \frac{\partial F_{\gamma_{Raux}}}{\partial \gamma_{Raux}} & \frac{\partial F_{\gamma_{Raux}}}{\partial dm_{aR}} \\ 0 & 0 & 0 & \frac{\partial F_{dm_{aR}}}{\partial V_{vR}} & 0 & \frac{\partial F_{dm_{aR}}}{\partial dm_{aR}} \end{bmatrix} \tag{4.77}$$

$$\mathbf{J}'_{\mathbf{dcR}} = \begin{bmatrix} 0 & 0 & 0 & \frac{\partial F_{E_{dcR}}}{\partial V_{vR}} & 0 & \frac{\partial F_{E_{dcR}}}{\partial dm_{aR}} \end{bmatrix}, \quad \mathbf{J}'_{\mathbf{Rdc}} = \begin{bmatrix} 0 & 0 & \frac{\partial \Delta P_{vR}}{\partial E_{dcR}} & \frac{\partial \Delta Q_{vR}}{\partial E_{dcR}} & \frac{\partial F_{\gamma_{Raux}}}{\partial E_{dcR}} & 0 \end{bmatrix}^T \tag{4.78}$$

A similar arrangement to that of the derivatives of the rectifier station model is also obtained for that corresponding to the inverter station, as seen from (4.79)-(4.80). However, notice that all matrices have been suitably expanded to incorporate the phase-shifting angle of the inverter ϕ_I as a state variable together with its power mismatch equation ΔP_{0vI}, something that is not required in the rectifier model.

$$\mathbf{J}_{\mathbf{II1}} = \begin{bmatrix} \frac{\partial \Delta P_m}{\partial \theta_m} & \frac{\partial \Delta P_m}{\partial V_k} & \frac{\partial \Delta P_m}{\partial \theta_{vI}} & \frac{\partial \Delta P_m}{\partial V_{vI}} & 0 & 0 & 0 \\ \frac{\partial \Delta Q_m}{\partial \theta_m} & \frac{\partial \Delta Q_m}{\partial V_k} & \frac{\partial \Delta Q_m}{\partial \theta_{vI}} & \frac{\partial \Delta Q_m}{\partial V_{vI}} & 0 & 0 & 0 \\ \frac{\partial \Delta P_{vI}}{\partial \theta_m} & \frac{\partial \Delta P_{vI}}{\partial V_k} & \frac{\partial \Delta P_{vI}}{\partial \theta_{vI}} & \frac{\partial \Delta P_{vI}}{\partial V_{vI}} & \frac{\partial \Delta P_{vI}}{\partial \phi_I} & 0 & \frac{\partial \Delta P_{vI}}{\partial dm_{aI}} \\ \frac{\partial \Delta Q_{vI}}{\partial \theta_m} & \frac{\partial \Delta Q_{vI}}{\partial V_k} & \frac{\partial \Delta Q_{vI}}{\partial \theta_{vI}} & \frac{\partial \Delta Q_{vI}}{\partial V_{vI}} & \frac{\partial \Delta Q_{vI}}{\partial \phi_I} & 0 & \frac{\partial \Delta Q_{vI}}{\partial dm_{aI}} \\ 0 & 0 & \frac{\partial \Delta P_{0vI}}{\partial \theta_{vI}} & \frac{\partial \Delta P_{0vI}}{\partial V_{vI}} & \frac{\partial \Delta P_{0vI}}{\partial \phi_I} & 0 & \frac{\partial \Delta P_{0vI}}{\partial dm_{aI}} \end{bmatrix} \tag{4.79}$$

$$\mathbf{J}_{\mathbf{II2}} = \begin{bmatrix} 0 & 0 & 0 & 0 & 0 & \frac{\partial F_{I_{dclaux}}}{\partial I_{dclaux}} & 0 \\ 0 & 0 & 0 & \frac{\partial F_{dm_{aI}}}{\partial V_{vI}} & 0 & 0 & \frac{\partial F_{dm_{aI}}}{\partial dm_{aI}} \end{bmatrix}, \quad \mathbf{J}'_{\mathbf{Idc}} = \begin{bmatrix} 0 & 0 & \frac{\partial \Delta P_{vI}}{\partial E_{dcI}} & \frac{\partial \Delta Q_{vI}}{\partial E_{dcI}} & \frac{\partial \Delta P_{0vI}}{\partial E_{dcI}} & \frac{\partial F_{I_{dclaux}}}{\partial E_{dcI}} & 0 \end{bmatrix}^T \tag{4.80}$$

Completion of the VSC-HVDC model for positive-sequence, time domain simulations requires encompassing all the derivative terms corresponding to the DC circuit of the VSC-based transmission system; the linearisation of the equations arising from the DC voltage and current dynamics of the capacitors and inductors, respectively, together with those pertaining to the power mismatches at both ends of the DC cable are shown in (4.81).

$$\mathbf{J}_{\mathbf{dc}} = \begin{bmatrix} \frac{\partial F_{I_{Rx}}}{\partial I_{Rx}} & 0 & \frac{\partial F_{I_{Rx}}}{\partial E_{dcR}} & 0 & \frac{\partial F_{I_{Rx}}}{\partial E_{dcRx}} & 0 \\ 0 & \frac{\partial F_{I_{Ix}}}{\partial I_{Ix}} & 0 & \frac{\partial F_{I_{Ik}}}{\partial E_{dcI}} & 0 & \frac{\partial F_{I_{Ix}}}{\partial E_{dcIx}} \\ \frac{\partial F_{E_{dcR}}}{\partial I_{Rx}} & 0 & \frac{\partial F_{E_{dcR}}}{\partial E_{dcR}} & 0 & 0 & 0 \\ 0 & \frac{\partial F_{E_{dcI}}}{\partial I_{Ix}} & 0 & \frac{\partial F_{E_{dcI}}}{\partial E_{dcI}} & 0 & 0 \\ \frac{\partial \Delta P_{Rx}}{\partial I_{Rx}} & 0 & 0 & 0 & \frac{\partial \Delta P_{Rx}}{\partial E_{dcRx}} & \frac{\partial \Delta P_{Rx}}{\partial E_{dcIx}} \\ 0 & \frac{\partial \Delta P_{Ix}}{\partial I_{Ix}} & 0 & 0 & \frac{\partial \Delta P_{Ix}}{\partial E_{dcRx}} & \frac{\partial \Delta P_{Ix}}{\partial E_{dcIx}} \end{bmatrix} \tag{4.81}$$

It is worth emphasising that the sparse nature of the overall linearised VSC-HVDC link model for dynamic simulations, as in the case of the steady-state model, is favourable in actual software implementations if sparsity techniques are used. The mismatch powers and their corresponding state and control variables are shown in (4.75) and (4.82)-(4.83), respectively. It is envisaged that the encompassing manner in which the dynamic HVDC model has been developed may give rise to a generalisation of multi-terminal arrangements of conveters for VSC-upgraded power networks.

$$\mathbf{F_R} = \left[\Delta P_k \ \Delta Q_k \ \Delta P_{vR} \ \Delta Q_{vR} \ F_{\gamma_{Raux}} \ F_{dm_{aR}} \right]^T$$
$$\mathbf{F_I} = \left[\Delta P_m \ \Delta Q_m \ \Delta P_{vI} \ \Delta Q_{vI} \ \Delta P_{0vI} \ F_{I_{ddaux}} \ F_{dm_{aI}} \right]^T \quad (4.82)$$
$$\mathbf{F_{dc}} = \left[F_{I_{Rx}} \ F_{I_{Ix}} \ F_{E_{dcR}} \ F_{E_{dcI}} \ \Delta P_{Rx} \ \Delta P_{Ix} \right]^T$$

$$\mathbf{\Delta\Phi_R} = \left[\Delta\theta_k \ \Delta V_k \ \Delta\theta_{vR} \ \Delta V_{vR} \ \Delta\gamma_{Raux} \ \Delta dm_{aR} \right]^T$$
$$\mathbf{\Delta\Phi_I} = \left[\Delta\theta_m \ \Delta V_m \ \Delta\theta_{vI} \ \Delta V_{vI} \ \Delta\phi_I \ \Delta I_{dcIaux} \ \Delta dm_{aI} \right]^T \quad (4.83)$$
$$\mathbf{\Delta\Phi_{dc}} = \left[\Delta I_{Rx} \ \Delta I_{Ix} \ \Delta E_{dcR} \ \Delta E_{dcI} \ \Delta E_{dcRx} \ \Delta E_{dcIx} \right]^T$$

4.2.2 VSC-HVDC dynamic model with frequency regulation capabilities

VSC-HVDC systems are designed to serve in a wide range of power systems applications such as interconnecting AC networks of the same or different frequencies, supplying electrical energy to remote islands and off-shore oil and gas platforms, in-feeding of high load points in city centres and the exporting of the electrical energy from off-shore wind parks. In certain applications, it is desirable to exert some influence upon those relatively small networks, often referred to as low-inertia networks or AC microgrids, through the DC link with the aim of making their operation more stable. Perhaps, power fluctuations is the most severe problem these networks face; they lack inertial and primary frequency response due to the non-existance of power controlling devices such as battery energy storage systems or synchronous generators with speed-governing systems. In fact, these island systems may be built without any type of power generating units, e.g. a passive network consisting of only passive loads. In near-zero inertia electrical networks, even a very small power imbalance would lead the frequency to experience large rises or drops, depending on the nature of the power imbalance. This situation would arise when power imbalances occur in an AC power network with little or no inertia and fed by a VSC-HVDC link because VSC converters do not possess the ability to strengthen, on their own, the inertial response or to aid the primary frequency control of AC networks. In this context, aiming at investigating the feasibility of counting on frequency support in near-zero inertia electrical networks, a VSC-HVDC dynamic model with frequency regulation capabilities is developed. The model ought to be applicable to HVDC links feeding into independent, low-inertia networks.

A frequency deviation in a network arises from a mismatch between the mechanical power and the electrical power in a synchronous machine. These frequency deviations are larger in the smaller synchronous generators owing to their lighter rotating masses. As a matter of fact, the inertia constant of the generator is the parameter that determines the size of the frequency deviation following a power imbalance event. Besides the inertial response exhibited by synchronous generators, most of them are fitted with speed-governing controls to bring about a

degree of power controllability into the generating system, which is said to exert primary-frequency control. At least from the conceptual point of view, a parallel may be drawn between the kinetic energy stored in the rotating mass of a synchronous generator relating to its inertia constant and the electrostatic and electromagnetic energies stored in the capacitors and inductors placed at the DC side of the VSC-based transmission system, respectively, which will also have an inertia constant $H = H_c + H_i$, albeit of a much smaller dimension than the inertia constant of a synchronous machine. Furthermore, the difference between the DC power entering the inverter $E_{dcI} I_{dcI}$ and the power P_{0vI} will give rise to a frequency deviation in the network connected to the inverter. Hence, the angular speed ω_I and the angle ϕ_I of the inverter station are dynamically computed as shown in (7.84)-(7.85) (Castro and Acha, 2015b).

$$\frac{d\omega_I}{dt} = K_\omega \left(E_{dcI} I_{dcI} - P_{0vI} \right) \tag{7.84}$$

$$\frac{d\phi_I}{dt} = \omega_I - 2\pi f_{Inom} \tag{7.85}$$

where $K_\omega = \pi f_{Inom} / H$ and f_{Inom} [Hz] represents the nominal electrical frequency of the island network. Its value may be the same or different from that of the main utility grid connected at the rectifier AC terminal. It should be remarked that the angle ϕ_I as well as the angular speed ω_I become the reference signals for the near-zero inertia network.

Given that the total fictitious inertia of the inverter H is very small (let us say 10 ms), in the event of relatively small power disturbances, big sags or swells in the angular speed would be caused. To prove this point, let us take the case of a low-inertia grid operating at 60 Hz, where the value of K_ω would be around 18.85×10^3; if the power imbalance is in the order of $\Delta P = -1 \times 10^{-3}$ p.u. and there is no power control action after only one second, $\Delta t = 1$ s, then the speed deviation would be: $\Delta\omega \approx K_\omega \cdot \Delta P \cdot \Delta t \approx$ -18.85 rad/s, which in terms of frequency is $f_I \approx 57$ Hz. This would be a critical problem that should not be overlooked when the island network contains frequency-sensitive loads. In these cases, there is a need for implementing a practical solution to mitigate the frequency excursions. An alternative is to import electrical power from the main utility grid through the HVDC link. Hence, in these conditions, the VSC-HVDC model ought to depart from the idea of transmitting a fixed amount of power between two interconnected networks which, so far, has been the main functionality sought from HVDC applications. To this end, the auxiliary control loop shown in Figure 4.9 is designed to enable the VSC-HVDC link to import the power required from the system connected at the rectifier AC terminal to satisfy any power mismatch taking place in the AC island network, with the inverter station acting as a power electronic source with active and reactive power control capabilities. The control loop measures the actual angular speed of the island network, which happens to be the same as ω_I , and compares it with its nominal one,

$\omega_{Inom} = 2\pi f_{Inom}$. The error is processed by a PI controller to adjust the angular aperture between the AC system voltage phase angle θ_{vR} and the phase-shifting angle of the rectifier ϕ_R (Castro and Acha, 2015b).

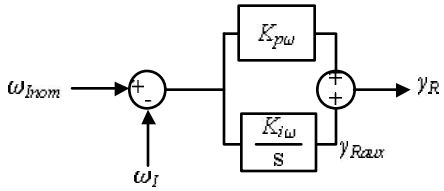

Figure 4.9 Frequency controller of the VSC-HVDC link

It should be remarked that while the aim of the controller shown in Figure 4.7 is to attain a fixed power transfer in the DC link, the target of the VSC-HVDC controller shown in Figure 4.9 is to maintain the electrical frequency of the network connected to the inverter within safe limits by modifying the extracted power from the grid connected to the rectifier AC terminal. This means that the value of the DC power transfer will be one, for instance, that brings the frequency of the island grid back to its nominal steady-state value. The equations that enable the calculation of the dynamic behaviour of the DC power when the inverter station of the HVDC system is acting as a power electronic source with frequency regulation capabilities are expressed as (7.86)-(7.87).

$$\frac{d\gamma_{Raux}}{dt} = K_{i\omega}\left(\omega_{Inom} - \omega_I\right) \tag{7.86}$$

$$\gamma_R = K_{p\omega}\left(\omega_{Inom} - \omega_I\right) + \gamma_{Raux} \tag{7.87}$$

As in the case of the VSC-HVDC model aimed at scheduled DC power regulation presented in Section 4.2.1, the set of power flow equations for the two interconnected AC networks together with the differential-algebraic equations pertaining to the synchronous generators and their controllers, induction machines, etc., as well as the HVDC's algebraic and discretised differential equations, are solved simultaneously using the trapezoidal method and the Newton's algorithm. For the sake of completeness, the overall mismatch expressions that must be solved together with the equations of the whole network, at every integration step Δt , are shown in (4.88)-(4.107) (Castro and Acha, 2015b).

$$\Delta P_k = -P_{kltc} - P_{dk} - P_k^{cal} \tag{4.88}$$

$$\Delta Q_k = -Q_{kltc} - Q_{dk} - Q_k^{cal} \tag{4.89}$$

$$\Delta P_{vR} = -P_{vR} - P_{dvR} - P_{vRltc} \tag{4.90}$$

$$\Delta Q_{vR} = -Q_{vR} - Q_{dvR} - Q_{vRltc} \tag{4.91}$$

$$\Delta P_m = -P_{mltc} - P_{dm} - P_m^{cal} \tag{4.92}$$

$$\Delta Q_m = -Q_{mltc} - Q_{dm} - Q_m^{cal} \tag{4.93}$$

$$\Delta P_{vI} = -P_{vI} - P_{dvI} - P_{vIltc} \tag{4.94}$$

$$\Delta Q_{vI} = -Q_{vI} - Q_{dvI} - Q_{vIltc} \tag{4.95}$$

$$\Delta P_{Rx} = E_{dcRx} I_{Rx} - P_{dcR} \tag{4.96}$$

$$\Delta P_{Ix} = E_{dcIx} I_{Ix} - P_{dcI} \tag{4.97}$$

$$F_{E_{dcR}} = E_{dcR(t-\Delta t)} + 0.5\Delta t \dot{E}_{dcR(t-\Delta t)} - \left(E_{dcR(t)} - 0.5\Delta t \dot{E}_{dcR(t)}\right) \tag{4.98}$$

$$F_{E_{dcI}} = E_{dcI(t-\Delta t)} + 0.5\Delta t \dot{E}_{dcI(t-\Delta t)} - \left(E_{dcI(t)} - 0.5\Delta t \dot{E}_{dcI(t)}\right) \tag{4.99}$$

$$F_{I_{Rx}} = I_{Rx(t-\Delta t)} + 0.5\Delta t \dot{I}_{Rx(t-\Delta t)} - \left(I_{Rx(t)} - 0.5\Delta t \dot{I}_{Rx(t)}\right) \tag{4.100}$$

$$F_{I_{Ix}} = I_{Ix(t-\Delta t)} + 0.5\Delta t \dot{I}_{Ix(t-\Delta t)} - \left(I_{Ix(t)} - 0.5\Delta t \dot{I}_{Ix(t)}\right) \tag{4.101}$$

$$F_{I_{dcIaux}} = I_{dcIaux(t-\Delta t)} + 0.5\Delta t \dot{I}_{dcIaux(t-\Delta t)} - \left(I_{dcIaux(t)} - 0.5\Delta t \dot{I}_{dcIaux(t)}\right) \tag{4.102}$$

$$F_{\gamma_{Raux}} = \gamma_{Raux(t-\Delta t)} + 0.5\Delta t \dot{\gamma}_{Raux(t-\Delta t)} - \left(\gamma_{Raux(t)} - 0.5\Delta t \dot{\gamma}_{Raux(t)}\right) \tag{4.103}$$

$$F_{dm_{aR}} = dm_{aR(t-\Delta t)} + 0.5\Delta t d\dot{m}_{aR(t-\Delta t)} - \left(dm_{aR(t)} - 0.5\Delta t d\dot{m}_{aR(t)}\right) \tag{4.104}$$

$$F_{dm_{aI}} = dm_{aI(t-\Delta t)} + 0.5\Delta t d\dot{m}_{aI(t-\Delta t)} - \left(dm_{aI(t)} - 0.5\Delta t d\dot{m}_{aI(t)}\right) \tag{4.105}$$

$$F_{\phi_I} = \phi_{I(t-\Delta t)} + 0.5\Delta t \dot{\phi}_{I(t-\Delta t)} - \left(\phi_{I(t)} - 0.5\Delta t \dot{\phi}_{I(t)}\right) \tag{4.106}$$

$$F_{\omega_I} = \omega_{I(t-\Delta t)} + 0.5\Delta t \dot{\omega}_{I(t-\Delta t)} - \left(\omega_{I(t)} - 0.5\Delta t \dot{\omega}_{I(t)}\right) \tag{4.107}$$

Notice the reformulation that has taken place in the above set of equations in comparison with the previously developed VSC-HVDC dynamic model, shown in Section 4.2.1. This is to endow the HVDC link with frequency regulation capabilities. Now the model incorporates two differential equations (4.106)-(4.107) that enable the computation of the reference angle and angular speed of the independent AC network connected at the inverter AC terminal. Furthermore, contrary to the customary objective of the power angle controller of the VSC-HVDC link, equation (4.103) represents the DC power controller that acts upon changes in the frequency of the grid connected at the inverter AC terminal. The above set of equations yields the linearised structure given in (4.108) for the VSC-HVDC model with frequency regulation capabilities. Advantageously, this is very similar to that derived for the VSC-HVDC model with power regulation capabilities represented by (4.75). However, it stands out from (4.108) that a full decoupling between the

rectifier and inverter no longer exists. In this particular case, the utilisation of the angular speed measurement by the frequency controller of the rectifier produces a mutual matrix term between both converters; this is matrix $\mathbf{J}_{\mathbf{RI}}$ given in (4.109) which accommodates the derivative of the discretised differential equation of the frequency controller with respect to the actual angular speed of the island network ω_I.

$$\begin{bmatrix} \mathbf{F_R} \\ \mathbf{F_I} \\ \hline \mathbf{F_{dc}} \end{bmatrix}^i = -\left[\begin{array}{cc:c} \begin{bmatrix} \mathbf{J_{RR1}} \\ \mathbf{J_{RR2}} \end{bmatrix} & \begin{bmatrix} \mathbf{0} \\ \mathbf{J_{RI}} \end{bmatrix} & \mathbf{J_{Rdc}} \\ \mathbf{0} & \begin{bmatrix} \mathbf{J_{II1}} \\ \mathbf{J_{II2}} \end{bmatrix} & \mathbf{J_{Idc}} \\ \hdashline \mathbf{J_{dcR}} & \mathbf{0} & \mathbf{J_{dc}} \end{array}\right]^i \begin{bmatrix} \mathbf{\Delta\Phi_R} \\ \mathbf{\Delta\Phi_I} \\ \hline \mathbf{\Delta\Phi_{dc}} \end{bmatrix}^i \tag{4.108}$$

$$\mathbf{J_{RI}} = \begin{bmatrix} 0 & 0 & 0 & 0 & 0 & 0 & \dfrac{\partial F_{\gamma_{Raux}}}{\partial \omega_I} & 0 \\ 0 & 0 & 0 & 0 & 0 & 0 & 0 & 0 \end{bmatrix} \tag{4.109}$$

Some modifications in matrices $\mathbf{J_{RR2}}$, $\mathbf{J_{Rdc}}$, $\mathbf{J_{II1}}$, $\mathbf{J_{II2}}$ and $\mathbf{J_{Idc}}$ take place to be consistent with this control strategy. The new Jacobian entries are shown in equations (4.110)-(4.113).

$$\mathbf{J_{RR2}} = \begin{bmatrix} 0 & 0 & 0 & 0 & \dfrac{\partial F_{\gamma_{Raux}}}{\partial \gamma_{Raux}} & 0 \\ 0 & 0 & 0 & \dfrac{\partial F_{dm_{aR}}}{\partial V_{vR}} & 0 & \dfrac{\partial F_{dm_{aR}}}{\partial dm_{aR}} \end{bmatrix}, \quad \mathbf{J'_{Rdc}} = \begin{bmatrix} 0 & 0 & \dfrac{\partial \Delta P_{vR}}{\partial E_{dcR}} & \dfrac{\partial \Delta Q_{vR}}{\partial E_{dcR}} & 0 & 0 \end{bmatrix}^T \tag{4.110}$$

$$\mathbf{J_{II1}} = \begin{bmatrix} \dfrac{\partial \Delta P_m}{\partial \theta_m} & \dfrac{\partial \Delta P_m}{\partial V_m} & \dfrac{\partial \Delta P_m}{\partial \theta_{vI}} & \dfrac{\partial \Delta P_m}{\partial V_{vI}} & 0 & 0 & 0 & 0 \\ \dfrac{\partial \Delta Q_m}{\partial \theta_m} & \dfrac{\partial \Delta Q_m}{\partial V_m} & \dfrac{\partial \Delta Q_m}{\partial \theta_{vI}} & \dfrac{\partial \Delta Q_m}{\partial V_{vI}} & 0 & 0 & 0 & 0 \\ \dfrac{\partial \Delta P_{vI}}{\partial \theta_m} & \dfrac{\partial \Delta P_{vI}}{\partial V_m} & \dfrac{\partial \Delta P_{vI}}{\partial \theta_{vI}} & \dfrac{\partial \Delta P_{vI}}{\partial V_{vI}} & 0 & \dfrac{\partial \Delta P_{vI}}{\partial dm_{aI}} & 0 & \dfrac{\partial \Delta P_{vI}}{\partial \phi_I} \\ \dfrac{\partial \Delta Q_{vI}}{\partial \theta_m} & \dfrac{\partial \Delta Q_{vI}}{\partial V_m} & \dfrac{\partial \Delta Q_{vI}}{\partial \theta_{vI}} & \dfrac{\partial \Delta Q_{vI}}{\partial V_{vI}} & 0 & \dfrac{\partial \Delta Q_{vI}}{\partial dm_{aI}} & 0 & \dfrac{\partial \Delta Q_{vI}}{\partial \phi_I} \end{bmatrix} \tag{4.111}$$

$$\mathbf{J_{II2}} = \begin{bmatrix} 0 & 0 & 0 & 0 & \dfrac{\partial F_{I_{dcIaux}}}{\partial I_{dcIaux}} & 0 & 0 & 0 \\ 0 & 0 & 0 & \dfrac{\partial F_{dm_{aI}}}{\partial V_{vI}} & 0 & \dfrac{\partial F_{dm_{aI}}}{\partial dm_{aI}} & 0 & 0 \\ 0 & 0 & \dfrac{\partial F_{\omega_I}}{\partial \theta_{vI}} & \dfrac{\partial F_{\omega_I}}{\partial V_{vI}} & 0 & \dfrac{\partial F_{\omega_I}}{\partial dm_{aI}} & \dfrac{\partial F_{\omega_I}}{\partial \omega_I} & \dfrac{\partial F_{\omega_I}}{\partial \phi_I} \\ 0 & 0 & 0 & 0 & 0 & 0 & \dfrac{\partial F_{\phi_I}}{\partial \omega_I} & \dfrac{\partial F_{\phi_I}}{\partial \phi_I} \end{bmatrix} \tag{4.112}$$

$$\mathbf{J'_{Idc}} = \begin{bmatrix} 0 & 0 & \dfrac{\partial \Delta P_{vI}}{\partial E_{dcI}} & \dfrac{\partial \Delta Q_{vI}}{\partial E_{dcI}} & \dfrac{\partial F_{I_{dcIaux}}}{\partial E_{dcI}} & 0 & \dfrac{\partial F_{\omega_I}}{\partial E_{dcI}} & 0 \end{bmatrix}^T \tag{4.113}$$

The modified vectors of mismatches and increments of the VSC-HVDC link model with frequency regulation are shown in (4.114).

$$\begin{aligned} \mathbf{F_I} &= \begin{bmatrix} \Delta P_m & \Delta Q_m & \Delta P_{vI} & \Delta Q_{vI} & F_{I_{dcIaux}} & F_{dm_{aI}} & F_{\omega_I} & F_{\phi_I} \end{bmatrix}^T \\ \mathbf{\Delta\Phi_I} &= \begin{bmatrix} \Delta\theta_m & \Delta V_m & \Delta\theta_{vI} & \Delta V_{vI} & \Delta I_{dcIaux} & \Delta dm_{aI} & \Delta\omega_I & \Delta\phi_I \end{bmatrix}^T \end{aligned} \tag{4.114}$$

4.3 Multi-terminal VSC-HVDC systems for dynamic simulations

Worldwide point-to-point HVDC systems have been so far realised to provide access to remote load points or to facilitate power exchange over very long distances between, for instance, two otherwise independent systems. Due to the fact that only two partners interact in point-to-point VSC-HVDC connections, this hinders the possibility of connecting an additional AC system which may lie within the reach of the DC transmission routing. This limitation has urged companies to make sudden advances in the direction of multi-terminal direct current transmission schemes, multi-terminal VSC-HVDC systems able to adapt easily to the always varying conditions of power networks, facilitating simultaneously the control of the power flowing into or from the DC high power transmission system. Clearly the operation of multi-terminal HVDC systems is more challenging and complex in comparison with former point-to-point connections of power converters; hence, this breakthrough must come with corresponding advances in the arena of modelling and simulation of multi-terminal HVDC systems to aid power system engineers to confront the soon-to-emerge challenges relating to their planning, operation and control.

In a multi-terminal arrangement, balancing the currents of the different converter stations comprising the VSC-based multi-terminal network is one of the main pursued objectives to ensure

a reliable operation not only for the HVDC system itself, but also for the various interconnected networks. Power reallocation and control of the voltage profile on the meshed DC network are also primary functions that must be pursued in a multi-terminal scheme. The control system of each VSC station has to provide a rapid response to recover safely after faults occurring either in the AC system or in the DC system. At least from the conceptual standpoint, it is expected that all benefits gained with the use of two-terminal HVDC systems be inherited to multi-terminal schemes. Also, it is very likely, if not a fact, that the same advantages attained in meshed AC networks, where the power supply to users even during abnormal conditions is ensured, will be also gained in multi-terminal HVDC systems.

At the planning stage of power systems, to carry out holistic assessments of multi-terminal VSC-HVDC systems together with the interconnected AC networks requires suitable VSC models. System-wide dynamic studies of practical networks would benefit from a modular approach, one that enables efficient simulations without jeopardising the accuracy of the results, and at the same time, one that does not exclude the computation of essential state and control variables pertaining to the converter stations. Throughout Chapter 3, particularly in Section 3.5, it was shown that the fundamental VSC station model possesses a high degree of modelling flexibility allowing a straightforward aggregation of a number of VSC stations to give rise to any type of multi-terminal arrangement. The same modular modelling approach is followed for the dynamic regime, one where each VSC unit of the multi-terminal HVDC dynamic model is seen to consist of a power converter, phase reactor, filter capacitor and an interfacing OLTC transformer to connect to the high-voltage AC network, being in the opposite side of the VSC, the DC bus which connects to an arbitrary DC grid, as shown in Figure 4.10 (Castro and Acha, 2016).

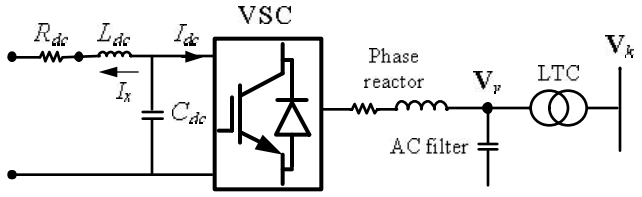

Figure 4.10 Full VSC station with ancillary elements

4.3.1 Three-terminal VSC-HVDC dynamic model

Three types of converters were defined, for the steady-state operating regime, to conform with their specific control strategy and pairing AC network: the slack converter controlling its DC voltage - VSC_{Slack}, the converter controlling its DC power - VSC_{Psch} and the converter feeding into a passive network - VSC_{Pass}. By the same token, the modelling of each one of these converters is

also envisaged in the modelling of VSC-based multi-terminal connections for the dynamic operating regime. To such an end, the basic three-terminal VSC-HVDC system, depicted in Figure 4.11, is initially formulated; this is a VSC-based transmission system that accomodates the aforementioned three types of converters. This system is then expanded quite naturally to build up a model that comprises a number of VSC units which is commensurate with the number of terminals in the HVDC system, suitably accommodated in a unified frame-of-reference aimed at positive-sequence dynamic simulations of power networks (Castro and Acha, 2016).

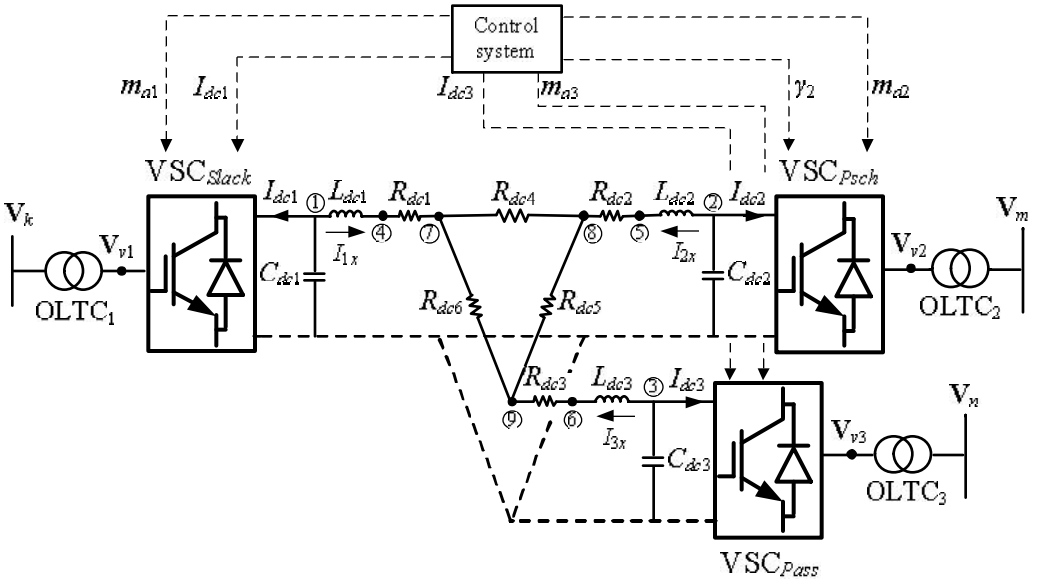

Figure 4.11 Representation of a three-terminal VSC-HVDC link and its control variables

The VSC-based transmission system shown in Figure 4.11 comprises three converters, where for simplicity of representation, the associated phase reactor and AC filter capacitor of each converter have been omitted. Converter 1 is of type VSC_{Slack} whereas converters 2 and 3 are assumed to be of type VSC_{Psch} and VSC_{Pass}, respectively. Each VSC unit may be seen to consist of a power converter, AC phase reactor, AC filter capacitor and an interfacing OLTC transformer to connect to each particular AC network. For simplicity of representation, the associated AC phase reactor and AC filter capacitor of each converter have been omitted in the figure, but their incorporation is quite a straightforward matter. On the opposite side of each VSC there is the DC bus which, in this particular case, connects to a capacitor and smoothing inductor and resistor, forming a delta connection with cables of resistance R_{dc4}, R_{dc5} and R_{dc6}. Notice that in a multi-terminal scheme, any converter can play the role of either a rectifier or inverter according to the actual conditions of power exchange between the converters and the formed DC grid or according to the par-

ticular requirements of the network connected at their corresponding AC terminal. Therefore, for simplicity of developments, the subscripts R and I formerly standing for rectifier and inverter, respectively, have been changed by suitable numbers.

In connection with Figure 4.11, the voltage and current of the capacitors and inductors, respectively, are computed as shown in (4.115)-(4.116).

$$\frac{dE_{dc1}}{dt} = \frac{-I_{dc1} - I_{1x}}{C_{dc1}}, \qquad \frac{dE_{dc2}}{dt} = \frac{-I_{dc2} - I_{2x}}{C_{dc2}}, \qquad \frac{dE_{dc3}}{dt} = \frac{-I_{dc3} - I_{3x}}{C_{dc3}} \tag{4.115}$$

$$\frac{dI_{1x}}{dt} = \frac{E_{dc1} - E_{dc4}}{L_{dc1}}, \qquad \frac{dI_{2x}}{dt} = \frac{E_{dc2} - E_{dc5}}{L_{dc2}}, \qquad \frac{dI_{3x}}{dt} = \frac{E_{dc3} - E_{dc6}}{L_{dc3}} \tag{4.116}$$

In this particular case, the VSC station 1 is charged with the DC voltage control of the three-terminal VSC-based system. This implies that this VSC plays the role of the slack converter for the DC network. Figure 4.12 shows the DC voltage controller for the slack converter VSC_{Slack} whose PI controller is used to process the error between the actual voltage of the converter's DC bus and its nominal one, E_{dc1} and E_{dcnom}, respectively, obtaining new values of its DC current I_{dc1}(Castro and Acha, 2016).

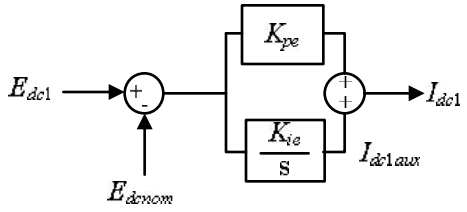

Figure 4.12 DC voltage dynamic controller of the slack converter VSC_{Slack}

Simultaneously, the other two VSC stations are responsible for controlling the power at its corresponding DC bus, but the power control objectives are different from each other. The aim of the converter of type VSC_{Psch} is to achieve a fixed, scheduled DC power transfer. On the contrary, the converter of type VSC_{Pass}, whose main goal is to provide frequency support to the network connected at its AC terminal, regulates the power injection into the passive network as a function of the power deviations in such AC grid. Figure 4.13 shows the control loops for these two converter stations. Notice that the converter of type VSC_{Psch} pursues a power balance at its DC bus by regulating the angular aperture between its phase-shifting angle and its corresponding AC voltage angle whilst the converter of type VSC_{Pass} acts upon variations on the frequency measured at its AC terminal, increasing or decreasing its DC current depending on the actual conditions (Castro and Acha, 2016).

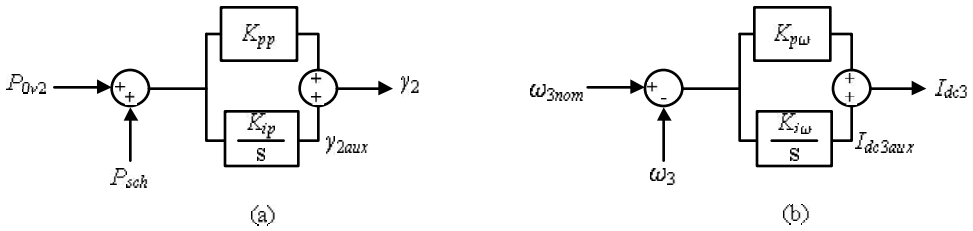

Figure 4.13 (a) DC-power controller of the converter of type VSC_{Psch} and (b) Frequency controller of the converter of type VSC_{Pass}

As it is standard practice in two-terminal HVDC systems, the modulation index of each VSC station is responsible for controlling the voltage magnitude at the corresponding AC terminal. In this particular case, the VSC stations bring about three control loops aimed at controlling the voltage magnitude at each AC terminal of the three-terminal VSC-based transmission system. Each control loop comprises a first-order control block whose aim is also to readjust each corresponding modulation index according to the difference between the scheduled voltage magnitudes and the actual voltage at the nodes where the converters are connected, as shown in Figure 4.14. Notice that each control loop acts autonomously, needing no feedback inputs coming from the rest of the modulation index controllers; this implies that no communication is needed between the converters comprised in the multi-terminal system as far as AC voltage control is concerned.

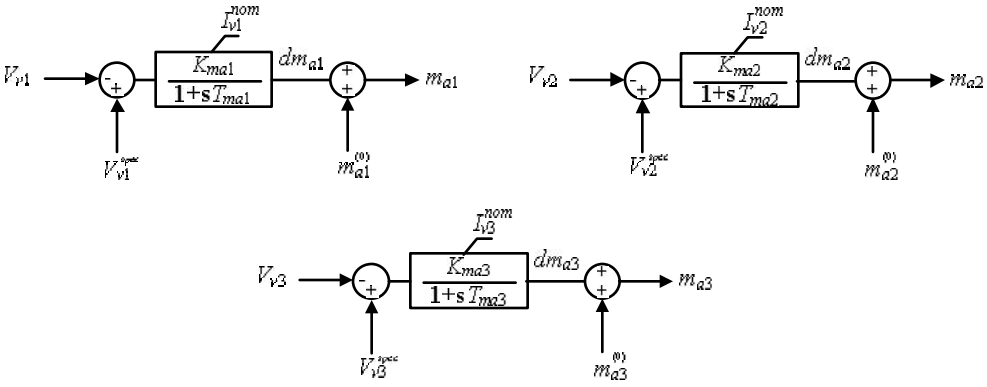

Figure 4.14 Modulation index controllers of the three converter stations making up the three-terminal HVDC system

Clearly, this three terminal HVDC system has increased in terms of complexity, bringing about nine DC buses. Unlike point-to-point HVDC connections where the resistor value corresponding to the DC smoothing inductor can be simply added to the DC cable resistor, in a multi-terminal connection, as the one being addressed in this case, the resistor of each DC smoothing inductor produces an additional node in the DC system. However, its inclusion in the proposed formulation can

be carried out straightforwardly. The calculated power injections at each node of the DC system are computed as shown in (4.117). For practical reasons, this expression only includes the computation of the power injections at the DC buses of the purely resistive network, which is formed from bus 4 to bus 9. Evidently, during steady conditions, the voltage at the DC bus of the three converters equals the voltage at buses 4, 5 and 6, respectively.

$$P_{dcj}^{cal} = E_{dcj}^2 G_{dcjj} + E_{dcj} \sum_{\substack{j=4 \\ m \in j}}^{9} E_{dcm} G_{dcjm} \tag{4.117}$$

Admittedly, the most basic multi-terminal HVDC arrangement, shown in Figure 4.11, encompasses the most representative AC/DC components that may have a significant impact on its dynamics. Nevertheless, if efficient, reliable solutions are pursued for dynamic simulations, the use of a generalised approach, one very similar to that employed in point-to-point HVDC configurations, is essential to carry out simulations of multi-terminal HVDC systems.

The differential equations, shown in (4.118)-(4.131), arise from the voltage and current dynamics of the capacitors and inductors as well as from the controllers of the three-terminal VSC-HVDC link model (Castro and Acha, 2016).

$$F_{E_{dc1}} = E_{dc1(t-\Delta t)} + 0.5\Delta t \dot{E}_{dc1(t-\Delta t)} - \left(E_{dc1(t)} - 0.5\Delta t \dot{E}_{dc1(t)} \right) \tag{4.118}$$

$$F_{E_{dc2}} = E_{dc2(t-\Delta t)} + 0.5\Delta t \dot{E}_{dc2(t-\Delta t)} - \left(E_{dc2(t)} - 0.5\Delta t \dot{E}_{dc2(t)} \right) \tag{4.119}$$

$$F_{E_{dc3}} = E_{dc3(t-\Delta t)} + 0.5\Delta t \dot{E}_{dc3(t-\Delta t)} - \left(E_{dc3(t)} - 0.5\Delta t \dot{E}_{dc3(t)} \right) \tag{4.120}$$

$$F_{I_{1x}} = I_{1x(t-\Delta t)} + 0.5\Delta t \dot{I}_{1x(t-\Delta t)} - \left(I_{1x(t)} - 0.5\Delta t \dot{I}_{1x(t)} \right) \tag{4.121}$$

$$F_{I_{2x}} = I_{2x(t-\Delta t)} + 0.5\Delta t \dot{I}_{2x(t-\Delta t)} - \left(I_{2x(t)} - 0.5\Delta t \dot{I}_{2x(t)} \right) \tag{4.122}$$

$$F_{I_{3x}} = I_{3x(t-\Delta t)} + 0.5\Delta t \dot{I}_{3x(t-\Delta t)} - \left(I_{3x(t)} - 0.5\Delta t \dot{I}_{3x(t)} \right) \tag{4.123}$$

$$F_{I_{dc1aux}} = I_{dc1aux(t-\Delta t)} + 0.5\Delta t \dot{I}_{dc1aux(t-\Delta t)} - \left(I_{dc1aux(t)} - 0.5\Delta t \dot{I}_{dc1aux(t)} \right) \tag{4.124}$$

$$F_{\gamma_{2aux}} = \gamma_{2aux(t-\Delta t)} + 0.5\Delta t \dot{\gamma}_{2aux(t-\Delta t)} - \left(\gamma_{2aux(t)} - 0.5\Delta t \dot{\gamma}_{2aux(t)} \right) \tag{4.125}$$

$$F_{I_{dc3aux}} = I_{dc3aux(t-\Delta t)} + 0.5\Delta t \dot{I}_{dc3aux(t-\Delta t)} - \left(I_{dc3aux(t)} - 0.5\Delta t \dot{I}_{dc3aux(t)} \right) \tag{4.126}$$

$$F_{\phi_3} = \phi_{3(t-\Delta t)} + 0.5\Delta t \dot{\phi}_{3(t-\Delta t)} - \left(\phi_{3(t)} - 0.5\Delta t \dot{\phi}_{3(t)} \right) \tag{4.127}$$

$$F_{\omega_3} = \omega_{3(t-\Delta t)} + 0.5\Delta t \dot{\omega}_{3(t-\Delta t)} - \left(\omega_{3(t)} - 0.5\Delta t \dot{\omega}_{3(t)} \right) \tag{4.128}$$

$$F_{dm_{a1}} = dm_{a1(t-\Delta t)} + 0.5\Delta t d\dot{m}_{a1(t-\Delta t)} - \left(dm_{a1(t)} - 0.5\Delta t d\dot{m}_{a1(t)} \right) \tag{4.129}$$

$$F_{dm_{a2}} = dm_{a2(t-\Delta t)} + 0.5\Delta t d\dot{m}_{a2(t-\Delta t)} - \left(dm_{a2(t)} - 0.5\Delta t d\dot{m}_{a2(t)} \right) \tag{4.130}$$

$$F_{dm_{a3}} = dm_{a3(t-\Delta t)} + 0.5\Delta t\, d\dot{m}_{a3(t-\Delta t)} - \left(dm_{a3(t)} - 0.5\Delta t\, d\dot{m}_{a3(t)} \right) \tag{4.131}$$

The above set of expressions determine the whole dynamics in the three-terminal HVDC system, however, the adopted formulation, which is based on power injections, requires additional AC and DC power balance equations to complete the positive-sequence dynamic model.

The active and reactive power mismatch equations at the AC terminal of each VSC unit are given by (4.132)-(4.143). Notice that, for the sake of completeness, these equations include the power mismatch expressions corresponding to both ends of each converter's OLTC transformer.

$$\Delta P_k = -P_{kltc} - P_{dk} - P_k^{cal} \tag{4.132}$$

$$\Delta Q_k = -Q_{kltc} - Q_{dk} - Q_k^{cal} \tag{4.133}$$

$$\Delta P_{v1} = -P_{v1} - P_{dv1} - P_{v1ltc} \tag{4.134}$$

$$\Delta Q_{v1} = -Q_{v1} - Q_{dv1} - Q_{v1ltc} \tag{4.135}$$

$$\Delta P_m = -P_{mltc} - P_{dm} - P_m^{cal} \tag{4.136}$$

$$\Delta Q_m = -Q_{mltc} - Q_{dm} - Q_m^{cal} \tag{4.137}$$

$$\Delta P_{v2} = -P_{v2} - P_{dv2} - P_{v2ltc} \tag{4.138}$$

$$\Delta Q_{v2} = -Q_{v2} - Q_{dv2} - Q_{v2ltc} \tag{4.139}$$

$$\Delta P_n = -P_{nltc} - P_{dn} - P_n^{cal} \tag{4.140}$$

$$\Delta Q_n = -Q_{nltc} - Q_{dn} - Q_n^{cal} \tag{4.141}$$

$$\Delta P_{v3} = -P_{v3} - P_{dv3} - P_{v3ltc} \tag{4.142}$$

$$\Delta Q_{v3} = -Q_{v3} - Q_{dv3} - Q_{v3ltc} \tag{4.143}$$

In connection with Figure 4.11, the purely resistive network, formed by nodes 7, 8 and 9, produces the mismatch equations (4.147)-(4.149). Furthermore, the coupling between this resistive network and the DC side of the power converters is given at the DC nodes 4, 5, and 6; the power mismatch expressions at these nodes are shown in (4.144)-(4.146).

$$\Delta P_{dc4} = E_{dc4} I_{1x} - P_{dc4}^{cal} \tag{4.144}$$

$$\Delta P_{dc5} = E_{dc5} I_{2x} - P_{dc5}^{cal} \tag{4.145}$$

$$\Delta P_{dc6} = E_{dc6} I_{3x} - P_{dc6}^{cal} \tag{4.146}$$

$$\Delta P_{dc7} = -P_{d7} - P_{dc7}^{cal} \tag{4.147}$$

$$\Delta P_{dc8} = -P_{d8} - P_{dc8}^{cal} \tag{4.148}$$

$$\Delta P_{dc9} = -P_{d9} - P_{dc9}^{cal} \tag{4.149}$$

where the powers P_{d7}, P_{d8} and P_{d9} stand for the powers drawn by DC loads at the nodes that make up the delta arrangement of DC cables, but in this particular scenario they take the value of zero; the power expressions P_{dc4}^{cal} to P_{dc9}^{cal} represent the calculated powers at the corresponding nodes whose calculation is carried out using (4.117). In addition to the above mismatch expressions, the equation shown in (4.150) enables the computation of the power exchange between the AC and DC sides of the slack converters VSC_{Slack}.

$$\Delta P_{dc1} = E_{dc1} I_{dc1} - P_{0v1} \tag{4.150}$$

This last algebraic equation implies that the internal power equilibrium of the slack converter is attained instantaneously, something that does not occur in converters of type VSC_{Psch} and VSC_{Pass}. In these two converters, whose aim is to provide power regulation and frequency support, the internal power equilibrium is reached with a time delay; a time that is imposed by the speed response involved in their corresponding dynamic controllers depicted in Fig. 4.13. Such time delay will cause a momentary energy mismatch, charging or discharging the existing capacitors and inductors of the DC grid. Therefore it can be inferred that the response time of these two controllers will directly impact the magnitude of the DC voltage deviations when the AC/DC system is subjected to disturbances.

The overall three-terminal HVDC model for positive-sequence dynamic simulations is defined by equations (4.118)-(4.150). The linearised form of this model is given by (4.151); the unified frame of reference pursued in this formulation suitably combines the whole set of differential and algebraic equations arising from the AC/DC system formed by the three VSC stations (Castro and Acha, 2016).

$$\begin{bmatrix} \mathbf{F}_{\mathbf{Slack}} \\ \mathbf{F}_{\mathbf{Psch}} \\ \mathbf{F}_{\mathbf{Pass}} \\ \hline \mathbf{F}_{\mathbf{dc}} \end{bmatrix}^{i} = -\left[\begin{array}{ccc:c} \mathbf{J}_{\mathbf{Slack}} & \mathbf{0} & \mathbf{0} & \mathbf{J}_{\mathbf{Sdc}} \\ \mathbf{0} & \mathbf{J}_{\mathbf{Psch}} & \mathbf{0} & \mathbf{J}_{\mathbf{Psdc}} \\ \mathbf{0} & \mathbf{0} & \mathbf{J}_{\mathbf{Pass}} & \mathbf{J}_{\mathbf{Padc}} \\ \hdashline \mathbf{J}_{\mathbf{dcS}} & \mathbf{0} & \mathbf{0} & \mathbf{J}_{\mathbf{dc}} \end{array}\right]^{i} \begin{bmatrix} \mathbf{\Delta\Phi}_{\mathbf{Slack}} \\ \mathbf{\Delta\Phi}_{\mathbf{Psch}} \\ \mathbf{\Delta\Phi}_{\mathbf{Pass}} \\ \hline \mathbf{\Delta\Phi}_{\mathbf{dc}} \end{bmatrix}^{i} \tag{4.151}$$

were the $\mathbf{0}$ entries are zero-padded matrices of suitable orders and all matrix entries are additionally divided for simplicity of presentation and analysis, as shown in (4.152)-(4.153).

$$\mathbf{J}_{\mathbf{Slack}} = \begin{bmatrix} \mathbf{J}'_{\mathbf{Slack}} \\ \mathbf{J}''_{\mathbf{Slack}} \end{bmatrix},\ \mathbf{J}_{\mathbf{Psch}} = \begin{bmatrix} \mathbf{J}'_{\mathbf{Psch}} \\ \mathbf{J}''_{\mathbf{Psch}} \end{bmatrix},\ \mathbf{J}_{\mathbf{Pass}} = \begin{bmatrix} \mathbf{J}'_{\mathbf{Pass}} \\ \mathbf{J}''_{\mathbf{Pass}} \end{bmatrix} \tag{4.152}$$

$$\mathbf{J}_{\mathbf{Sdc}} = \begin{bmatrix} \mathbf{0} & \mathbf{J}'_{\mathbf{Sdc}} & \mathbf{0} \end{bmatrix},\ \mathbf{J}_{\mathbf{Psdc}} = \begin{bmatrix} \mathbf{0} & \mathbf{J}'_{\mathbf{Psdc}} & \mathbf{0} \end{bmatrix},\ \mathbf{J}_{\mathbf{Padc}} = \begin{bmatrix} \mathbf{0} & \mathbf{J}'_{\mathbf{Padc}} & \mathbf{0} \end{bmatrix},\ \mathbf{J}_{\mathbf{dcS}} = \begin{bmatrix} \mathbf{0}\, \mathbf{J}'_{\mathbf{dcS}}\ \mathbf{0} \end{bmatrix}^T \tag{4.153}$$

Matrices $\mathbf{J}'_{\mathbf{Slack}}$, $\mathbf{J}'_{\mathbf{Psch}}$ and $\mathbf{J}'_{\mathbf{Pass}}$ accommodate the derivative terms of the AC power mismatches of the three types of converters with respect to their corresponding AC state variables and control variables, as shown in (4.154)-(4.156). Notice that $\mathbf{J}'_{\mathbf{Pass}}$ also makes provision for the derivatives with respect to the electrical reference variables of the passive network, ϕ_3 and ω_3.

$$\mathbf{J}'_{\mathbf{Slack}} = \begin{bmatrix} \frac{\partial \Delta P_k}{\partial \theta_k} & \frac{\partial \Delta P_k}{\partial V_k} & \frac{\partial \Delta P_k}{\partial \theta_{v1}} & \frac{\partial \Delta P_k}{\partial V_{v1}} & 0 & 0 & 0 \\ \frac{\partial \Delta Q_k}{\partial \theta_k} & \frac{\partial \Delta Q_k}{\partial V_k} & \frac{\partial \Delta Q_k}{\partial \theta_{v1}} & \frac{\partial \Delta Q_k}{\partial V_{v1}} & 0 & 0 & 0 \\ \frac{\partial \Delta P_{v1}}{\partial \theta_k} & \frac{\partial \Delta P_{v1}}{\partial V_k} & \frac{\partial \Delta P_{v1}}{\partial \theta_{v1}} & \frac{\partial \Delta P_{v1}}{\partial V_{v1}} & \frac{\partial \Delta P_{v1}}{\partial \phi_1} & 0 & \frac{\partial \Delta P_{v1}}{\partial dm_{a1}} \\ \frac{\partial \Delta Q_{v1}}{\partial \theta_k} & \frac{\partial \Delta Q_{v1}}{\partial V_k} & \frac{\partial \Delta Q_{v1}}{\partial \theta_{v1}} & \frac{\partial \Delta Q_{v1}}{\partial V_{v1}} & \frac{\partial \Delta Q_{v1}}{\partial \phi_1} & 0 & \frac{\partial \Delta Q_{v1}}{\partial dm_{a1}} \\ 0 & 0 & \frac{\partial \Delta P_{dc1}}{\partial \theta_{v1}} & \frac{\partial \Delta P_{dc1}}{\partial V_{v1}} & \frac{\partial \Delta P_{dc1}}{\partial \phi_1} & 0 & \frac{\partial \Delta P_{dc1}}{\partial dm_{a1}} \end{bmatrix} \tag{4.154}$$

$$\mathbf{J}'_{\mathbf{Psch}} = \begin{bmatrix} \frac{\partial \Delta P_m}{\partial \theta_m} & \frac{\partial \Delta P_m}{\partial V_m} & \frac{\partial \Delta P_m}{\partial \theta_{v2}} & \frac{\partial \Delta P_m}{\partial V_{v2}} & 0 & 0 \\ \frac{\partial \Delta Q_m}{\partial \theta_m} & \frac{\partial \Delta Q_m}{\partial V_m} & \frac{\partial \Delta Q_m}{\partial \theta_{v2}} & \frac{\partial \Delta Q_m}{\partial V_{v2}} & 0 & 0 \\ \frac{\partial \Delta P_{v2}}{\partial \theta_m} & \frac{\partial \Delta P_{v2}}{\partial V_m} & \frac{\partial \Delta P_{v2}}{\partial \theta_{v2}} & \frac{\partial \Delta P_{v2}}{\partial V_{v2}} & 0 & \frac{\partial \Delta P_{v2}}{\partial dm_{a2}} \\ \frac{\partial \Delta Q_{v2}}{\partial \theta_m} & \frac{\partial \Delta Q_{v2}}{\partial V_m} & \frac{\partial \Delta Q_{vR}}{\partial \theta_{v2}} & \frac{\partial \Delta Q_{v2}}{\partial V_{v2}} & 0 & \frac{\partial \Delta Q_{v2}}{\partial dm_{a2}} \end{bmatrix} \tag{4.155}$$

$$\mathbf{J}'_{\mathbf{Pass}} = \begin{bmatrix} \frac{\partial \Delta P_n}{\partial \theta_n} & \frac{\partial \Delta P_n}{\partial V_n} & \frac{\partial \Delta P_n}{\partial \theta_{v3}} & \frac{\partial \Delta P_n}{\partial V_{v3}} & 0 & 0 & 0 & 0 \\ \frac{\partial \Delta Q_n}{\partial \theta_n} & \frac{\partial \Delta Q_n}{\partial V_n} & \frac{\partial \Delta Q_n}{\partial \theta_{v3}} & \frac{\partial \Delta Q_n}{\partial V_{v3}} & 0 & 0 & 0 & 0 \\ \frac{\partial \Delta P_{v3}}{\partial \theta_n} & \frac{\partial \Delta P_{v3}}{\partial V_n} & \frac{\partial \Delta P_{v3}}{\partial \theta_{v3}} & \frac{\partial \Delta P_{v3}}{\partial V_{v3}} & 0 & \frac{\partial \Delta P_{v3}}{\partial dm_{a3}} & 0 & \frac{\partial \Delta P_{v3}}{\partial \phi_3} \\ \frac{\partial \Delta Q_{v3}}{\partial \theta_n} & \frac{\partial \Delta Q_{v3}}{\partial V_n} & \frac{\partial \Delta Q_{v3}}{\partial \theta_{v3}} & \frac{\partial \Delta Q_{v3}}{\partial V_{v3}} & 0 & \frac{\partial \Delta Q_{v3}}{\partial dm_{a3}} & 0 & \frac{\partial \Delta Q_{v3}}{\partial \phi_3} \end{bmatrix} \tag{4.156}$$

The derivative terms of the discretised differential equations arising from the dynamic controllers of the VSC stations making up the three-terminal HVDC system with respect to their corresponding AC state variables and control variables are suitably accommodated in matrices $\mathbf{J}''_{\mathbf{Slack}}$, $\mathbf{J}''_{\mathbf{Psch}}$ and

$\mathbf{J}''_{\mathbf{Pass}}$. They are shown in expanded form in (4.157)-(4.159).

$$\mathbf{J}''_{\mathbf{Slack}} = \begin{bmatrix} 0\ 0\ 0 & 0 & 0 & \dfrac{\partial F_{I_{dc1aux}}}{\partial I_{dc1aux}} & 0 \\ 0\ 0\ 0 & \dfrac{\partial F_{dm_{a1}}}{\partial V_{v1}} & 0 & 0 & \dfrac{\partial F_{dm_{a1}}}{\partial dm_{a1}} \end{bmatrix} \tag{4.157}$$

$$\mathbf{J}''_{\mathbf{Psch}} = \begin{bmatrix} 0\ 0\ 0 & \dfrac{\partial F_{\gamma_{2aux}}}{\partial V_{v2}} & \dfrac{\partial F_{\gamma_{2aux}}}{\partial \gamma_{2aux}} & \dfrac{\partial F_{\gamma_{2aux}}}{\partial dm_{a2}} \\ 0\ 0\ 0 & \dfrac{\partial F_{dm_{a2}}}{\partial V_{v2}} & 0 & \dfrac{\partial F_{dm_{a2}}}{\partial dm_{a2}} \end{bmatrix} \tag{4.158}$$

$$\mathbf{J}''_{\mathbf{Pass}} = \begin{bmatrix} 0\ 0 & 0 & 0 & \dfrac{\partial F_{I_{dc3aux}}}{\partial I_{dc3aux}} & 0 & 0 & 0 \\ 0\ 0 & 0 & \dfrac{\partial F_{dm_{a3}}}{\partial V_{v3}} & 0 & \dfrac{\partial F_{dm_{a3}}}{\partial dm_{a3}} & 0 & 0 \\ 0\ 0 & \dfrac{\partial F_{\omega_3}}{\partial \theta_{v3}} & \dfrac{\partial F_{\omega_3}}{\partial V_{v3}} & 0 & \dfrac{\partial F_{\omega_3}}{\partial dm_{a3}} & \dfrac{\partial F_{\omega_3}}{\partial \omega_3} & \dfrac{\partial F_{\omega_3}}{\partial \phi_3} \\ 0\ 0 & 0 & 0 & 0 & 0 & \dfrac{\partial F_{\phi_3}}{\partial \omega_3} & \dfrac{\partial F_{\phi_3}}{\partial \phi_3} \end{bmatrix} \tag{4.159}$$

The terms arising from deriving both the AC power mismatches and the discretised differential equations of the dynamic controllers of the three VSC stations with respect to each capacitor's DC voltage are located in matrices $\mathbf{J}'_{\mathbf{Sdc}}$, $\mathbf{J}'_{\mathbf{Psdc}}$ and $\mathbf{J}'_{\mathbf{Padc}}$, as shown in (4.160)-(4.162).

$$\mathbf{J}'_{\mathbf{Sdc}} = \begin{bmatrix} 0\ 0 & \dfrac{\partial \Delta P_{v1}}{\partial E_{dc1}} & \dfrac{\partial \Delta Q_{v1}}{\partial E_{dc1}} & \dfrac{\partial F_{I_{dc1aux}}}{\partial E_{dc1}} & 0 \end{bmatrix}^T \tag{4.160}$$

$$\mathbf{J}'_{\mathbf{Psdc}} = \begin{bmatrix} 0\ 0 & \dfrac{\partial \Delta P_{v2}}{\partial E_{dc2}} & \dfrac{\partial \Delta Q_{v2}}{\partial E_{dc2}} & \dfrac{\partial F_{\gamma_{2aux}}}{\partial E_{dc2}} & 0 \end{bmatrix}^T \tag{4.161}$$

$$\mathbf{J}'_{\mathbf{Padc}} = \begin{bmatrix} 0\ 0 & \dfrac{\partial \Delta P_{v3}}{\partial E_{dc3}} & \dfrac{\partial \Delta Q_{v3}}{\partial E_{dc3}} & 0\ 0 & \dfrac{\partial F_{\omega_3}}{\partial E_{dc3}} & 0 \end{bmatrix}^T \tag{4.162}$$

Equation (4.163) shows the vector $\mathbf{J}'_{\mathbf{dcS}}$ that contains the partial derivatives of the discretised differential equation corresponding to the DC voltage of the slack converter's capacitor with respect to its corresponding AC state variables and control variables.

$$\mathbf{J}'_{\mathbf{dcS}} = \begin{bmatrix} 0\ 0 & \dfrac{\partial F_{E_{dc1}}}{\partial \theta_{v1}} & \dfrac{\partial F_{E_{dc1}}}{\partial V_{v1}} & \dfrac{\partial F_{E_{dc1}}}{\partial \phi_1} & 0 & \dfrac{\partial F_{E_{dc1}}}{\partial dm_{a1}} \end{bmatrix} \tag{4.163}$$

Matrix $\mathbf{J}_{\mathbf{dc}}$, shown in (4.164), has been additionally subdivided in several matrix blocks for

simplicity of future developments with a view to multi-terminal schemes. This matrix provides the coupling between the DC cuircuit made up by the delta connection of DC cables and the three VSC stations. This coupling emerges from suitably accommodating the derivatives of the discretised differential equations of inductors current and capacitors voltage together with the nodal power mismatches of the internal DC nodes, 4 to 9, with respect to suitable DC state and control variables, i.e., the set of DC voltages and currents taking part in the dynamics of this three-terminal HVDC system.

$$\mathbf{J}_{\mathbf{dc}} = \left[\begin{array}{cc|c} \mathbf{J}_{\mathbf{dc}1} & \mathbf{J}_{\mathbf{dc}2} & \mathbf{J}_{\mathbf{dc}5} \\ \mathbf{J}_{\mathbf{dc}3} & \mathbf{J}_{\mathbf{dc}4} & \mathbf{0} \\ \hline \mathbf{J}_{\mathbf{dc}6} & \mathbf{0} & \mathbf{J}_{\mathbf{dc}7} \end{array}\right] \tag{4.164}$$

where $\mathbf{J}_{\mathbf{dc}5} = [\mathbf{J}'_{\mathbf{dc}5} \;\; \mathbf{0}]$ and $\mathbf{J}_{\mathbf{dc}6} = [\mathbf{J}'_{\mathbf{dc}6} \;\; \mathbf{0}]^T$. The entries of the Jacobian matrix arising from the DC circuit are given, in explicit form, in (4.165)-(4.167),

$$\mathbf{J}_{\mathbf{dc}1} = \begin{bmatrix} \frac{\partial F_{I_{1x}}}{\partial I_{1x}} & 0 & 0 \\ 0 & \frac{\partial F_{I_{2x}}}{\partial I_{2x}} & 0 \\ 0 & 0 & \frac{\partial F_{I_{3x}}}{\partial I_{3x}} \end{bmatrix}, \; \mathbf{J}_{\mathbf{dc}2} = \begin{bmatrix} \frac{\partial F_{I_{1x}}}{\partial E_{dc1}} & 0 & 0 \\ 0 & \frac{\partial F_{I_{2x}}}{\partial E_{dc2}} & 0 \\ 0 & 0 & \frac{\partial F_{I_{3x}}}{\partial E_{dc3}} \end{bmatrix}, \; \mathbf{J}_{\mathbf{dc}3} = \begin{bmatrix} \frac{\partial F_{E_{dc1}}}{\partial I_{1x}} & 0 & 0 \\ 0 & \frac{\partial F_{E_{dc2}}}{\partial I_{2x}} & 0 \\ 0 & 0 & \frac{\partial F_{E_{dc3}}}{\partial I_{3x}} \end{bmatrix}$$

(4.165)

$$\mathbf{J}_{\mathbf{dc}4} = \begin{bmatrix} \frac{\partial F_{E_{dc1}}}{\partial E_{dc1}} & 0 & 0 \\ 0 & \frac{\partial F_{E_{dc2}}}{\partial E_{dc2}} & 0 \\ 0 & 0 & \frac{\partial F_{E_{dc3}}}{\partial E_{dc3}} \end{bmatrix}, \quad \mathbf{J}'_{\mathbf{dc}5} = \begin{bmatrix} \frac{\partial F_{I_{1x}}}{\partial E_{dc4}} & 0 & 0 \\ 0 & \frac{\partial F_{I_{2x}}}{\partial E_{dc5}} & 0 \\ 0 & 0 & \frac{\partial F_{I_{3x}}}{\partial E_{dc6}} \end{bmatrix}, \quad \mathbf{J}'_{\mathbf{dc}6} = \begin{bmatrix} \frac{\partial \Delta P_{dc4}}{\partial I_{1x}} & 0 & 0 \\ 0 & \frac{\partial \Delta P_{dc5}}{\partial I_{2x}} & 0 \\ 0 & 0 & \frac{\partial \Delta P_{dc6}}{\partial I_{3x}} \end{bmatrix}$$

(4.166)

$$\mathbf{J}_{\mathbf{dc}7} = \begin{bmatrix} \frac{\partial \Delta P_{dc4}}{\partial E_{dc4}} & 0 & 0 & \frac{\partial \Delta P_{dc4}}{\partial E_{dc7}} & 0 & 0 \\ 0 & \frac{\partial \Delta P_{dc5}}{\partial E_{dc5}} & 0 & 0 & \frac{\partial \Delta P_{dc5}}{\partial E_{dc8}} & 0 \\ 0 & 0 & \frac{\partial \Delta P_{dc6}}{\partial E_{dc6}} & 0 & 0 & \frac{\partial \Delta P_{dc6}}{\partial E_{dc9}} \\ \frac{\partial \Delta P_{dc7}}{\partial E_{dc4}} & 0 & 0 & \frac{\partial \Delta P_{dc7}}{\partial E_{dc7}} & \frac{\partial \Delta P_{dc7}}{\partial E_{dc8}} & \frac{\partial \Delta P_{dc7}}{\partial E_{dc9}} \\ 0 & \frac{\partial \Delta P_{dc8}}{\partial E_{dc5}} & 0 & \frac{\partial \Delta P_{dc8}}{\partial E_{dc7}} & \frac{\partial \Delta P_{dc8}}{\partial E_{dc8}} & \frac{\partial \Delta P_{dc8}}{\partial E_{dc9}} \\ 0 & 0 & \frac{\partial \Delta P_{dc9}}{\partial E_{dc6}} & \frac{\partial \Delta P_{dc9}}{\partial E_{dc7}} & \frac{\partial \Delta P_{dc9}}{\partial E_{dc8}} & \frac{\partial \Delta P_{dc9}}{\partial E_{dc9}} \end{bmatrix}. \tag{4.167}$$

Clearly, the diagonal matrices shown in (4.165)-(4.166), whose order corresponds to the number of VSC stations, could be straightforwardly expanded to conform to any kind of multi-terminal arrangement of converters.

The mismatch vectors and increments of the state and control variables for the three VSC units and the DC circuit are shown in (4.168)-(4.169).

$$\begin{aligned}
\mathbf{F}_{\mathbf{Slack}} &= \left[\Delta P_k \;\; \Delta Q_k \;\; \Delta P_{v1} \;\; \Delta Q_{v1} \;\; \Delta P_{dc1} \;\; F_{I_{dc1aux}} \;\; F_{dm_{a1}}\right]^T \\
\mathbf{F}_{\mathbf{Psch}} &= \left[\Delta P_m \;\; \Delta Q_m \;\; \Delta P_{v2} \;\; \Delta Q_{v2} \;\; F_{\gamma_{2aux}} \;\; F_{dm_{a2}}\right]^T \\
\mathbf{F}_{\mathbf{Pass}} &= \left[\Delta P_n \;\; \Delta Q_n \;\; \Delta P_{v3} \;\; \Delta Q_{v3} \;\; F_{I_{dc3aux}} \;\; F_{dm_{a3}} \;\; F_{\omega_3} \;\; F_{\phi_3}\right]^T \\
\mathbf{F}_{\mathbf{dc}} &= \left[F_{I_{1x}} \;\; F_{I_{2x}} \;\; F_{I_{3x}} \;\; F_{E_{dc1}} \;\; F_{E_{dc2}} \;\; F_{E_{dc3}} \;\; \Delta P_{dc4} \;\; \Delta P_{dc5} \;\; \Delta P_{dc6} \;\; \Delta P_{dc7} \;\; \Delta P_{dc8} \;\; \Delta P_{dc9}\right]^T
\end{aligned} \tag{4.168}$$

$$\begin{aligned}
\mathbf{\Delta\Phi}_{\mathbf{Slack}} &= \left[\Delta\theta_k \;\; \Delta V_k \;\; \Delta\theta_{v1} \;\; \Delta V_{v1} \;\; \Delta\phi_1 \;\; \Delta I_{dc1aux} \;\; \Delta dm_{a1}\right]^T \\
\mathbf{\Delta\Phi}_{\mathbf{Psch}} &= \left[\Delta\theta_m \;\; \Delta V_m \;\; \Delta\theta_{v2} \;\; \Delta V_{v2} \;\; \Delta\gamma_{2aux} \;\; \Delta dm_{a2}\right]^T \\
\mathbf{\Delta\Phi}_{\mathbf{Pass}} &= \left[\Delta\theta_n \;\; \Delta V_n \;\; \Delta\theta_{v3} \;\; \Delta V_{v3} \;\; \Delta I_{dc3aux} \;\; \Delta dm_{a3} \;\; \Delta\omega_3 \;\; \Delta\phi_3\right]^T \\
\mathbf{\Delta\Phi}_{\mathbf{dc}} &= \left[\Delta I_{1x} \;\; \Delta I_{2x} \;\; \Delta I_{3x} \;\; \Delta E_{dc1} \;\; \Delta E_{dc2} \;\; \Delta E_{dc3} \;\; \Delta E_{dc4} \;\; \Delta E_{dc5} \;\; \Delta E_{dc6} \;\; \Delta E_{dc7} \;\; \Delta E_{dc8} \;\; \Delta E_{dc9}\right]^T
\end{aligned} \tag{4.169}$$

Notice that the vector $\mathbf{\Delta\Phi}_{\mathbf{dc}}$ not only contains DC voltages as state variables, as it is the case for the three-terminal HVDC steady-state model derived in Section 3.5.1, but also it includes the DC currents of the inductors. The increments of the state variables of both the converters and DC circuit, calculated at iteration i, are used to update the state variables, using (4.170).

$$\begin{aligned}
\mathbf{\Phi}^{i+1}_{\mathbf{Slack}} &= \mathbf{\Phi}^{i}_{\mathbf{Slack}} + \mathbf{\Delta\Phi}^{i}_{\mathbf{Slack}} \\
\mathbf{\Phi}^{i+1}_{\mathbf{Psch}} &= \mathbf{\Phi}^{i}_{\mathbf{Psch}} + \mathbf{\Delta\Phi}^{i}_{\mathbf{Psch}} \\
\mathbf{\Phi}^{i+1}_{\mathbf{Pass}} &= \mathbf{\Phi}^{i}_{\mathbf{Pass}} + \mathbf{\Delta\Phi}^{i}_{\mathbf{Pass}} \\
\mathbf{\Phi}^{i+1}_{\mathbf{dc}} &= \mathbf{\Phi}^{i}_{\mathbf{dc}} + \mathbf{\Delta\Phi}^{i}_{\mathbf{dc}}
\end{aligned} \tag{4.170}$$

4.3.2 Multi-terminal VSC-HVDC dynamic model

The three-terminal HVDC dynamic model synthesised by equation (4.151) demonstrates that the three types of VSCs can be straightforwardly combined in a unified frame of reference. Expanding further such representation, a multi-terminal arrangement of VSCs possessing an arbitrary DC network topology and a number of converter stations can be tailored, as shown in the general expression given by (4.171). Moving towards multi-terminal schemes, expression (4.151) requires

being properly expanded to make provisions for m converter stations of type VSC$_{Slack}$, n converter stations of type VSC$_{Psch}$ and r converter stations of type VSC$_{Pass}$ (Castro and Acha, 2016).

$$\begin{bmatrix} \mathbf{F}_{\mathbf{Slack}1} \\ \vdots \\ \mathbf{F}_{\mathbf{Slack}m} \\ \mathbf{F}_{\mathbf{Psch}1} \\ \vdots \\ \mathbf{F}_{\mathbf{Psch}n} \\ \mathbf{F}_{\mathbf{Pass}1} \\ \vdots \\ \mathbf{F}_{\mathbf{Pass}r} \\ \left[\mathbf{F}_{\mathbf{dc}}\right] \end{bmatrix}^{i} = - \begin{bmatrix} \mathbf{J}_{\mathbf{Slack}1} \cdots \mathbf{0} & \mathbf{0} & \mathbf{0} & \left[\mathbf{J}_{\mathbf{Sdc}}\right] \\ \vdots \ddots \vdots & & & \\ \mathbf{0} \cdots \mathbf{J}_{\mathbf{Slack}m} & & & \\ \hline & \mathbf{J}_{\mathbf{Psch}1} \cdots \mathbf{0} & & \\ \mathbf{0} & \vdots \ddots \vdots & \mathbf{0} & \left[\mathbf{J}_{\mathbf{Psdc}}\right] \\ & \mathbf{0} \cdots \mathbf{J}_{\mathbf{Psch}n} & & \\ \hline & & \mathbf{J}_{\mathbf{Pass}1} \cdots \mathbf{0} & \\ \mathbf{0} & \mathbf{0} & \vdots \ddots \vdots & \left[\mathbf{J}_{\mathbf{Padc}}\right] \\ & & \mathbf{0} \cdots \mathbf{J}_{\mathbf{Pass}r} & \\ \hline \left[\mathbf{J}_{\mathbf{dcS}}\right] & \mathbf{0} & \mathbf{0} & \left[\mathbf{J}_{\mathbf{dc}}\right] \end{bmatrix}^{i} \begin{bmatrix} \Delta\mathbf{\Phi}_{\mathbf{Slack}1} \\ \vdots \\ \Delta\mathbf{\Phi}_{\mathbf{Slack}m} \\ \Delta\mathbf{\Phi}_{\mathbf{Psch}1} \\ \vdots \\ \Delta\mathbf{\Phi}_{\mathbf{Psch}n} \\ \Delta\mathbf{\Phi}_{\mathbf{Pass}1} \\ \vdots \\ \Delta\mathbf{\Phi}_{\mathbf{Pass}r} \\ \left[\Delta\mathbf{\Phi}_{\mathbf{dc}}\right] \end{bmatrix}^{i} \tag{4.171}$$

As implied from this last equation, there will be a number of zero-padded matrices and vectors $\mathbf{0}$. In expression (4.171), the mismatch terms $\mathbf{F}$ and the vectors of state variables increments $\mathbf{\Delta\Phi}$ take the form of (4.168)-(4.169) depending on the type of converter, i.e., VSC$_{Slack}$, VSC$_{Psch}$ or VSC$_{Pass}$. Likewise, matrices $\mathbf{J}$ with subscripts $\mathbf{Slack}$, $\mathbf{Psch}$ and $\mathbf{Pass}$ take the form of (4.152). Caution has to be exercised because the non-zero entries of vectors $\mathbf{J}_{\mathbf{Sdc}}$, $\mathbf{J}_{\mathbf{Psdc}}$, $\mathbf{J}_{\mathbf{Padc}}$ and $\mathbf{J}_{\mathbf{dcS}}$, need to be suitably staggered, something that is well exemplified by the three-terminal case. Preserving the same accommodation of the DC state variables as that of the three-terminal case, the vectors and matrices, which have a location corresponding to any of the DC network variables, $\Delta\mathbf{\Phi}_{\mathbf{dc}}$, have the structure shown in equations (4.172)-(4.175).

$$\left[\mathbf{J}_{\mathbf{Sdc}}\right] = \begin{bmatrix} \mathbf{0} \cdots \mathbf{0} & \mathbf{J}'_{\mathbf{Sdc}1} \cdots \mathbf{0} & \mathbf{0} \cdots \mathbf{0} \\ \vdots \ddots \vdots & \vdots \ddots \vdots & \vdots \ddots \vdots \\ \mathbf{0} \cdots \mathbf{0} & \mathbf{0} \cdots \mathbf{J}'_{\mathbf{Sdc}m} & \mathbf{0} \cdots \mathbf{0} \end{bmatrix} \tag{4.172}$$

$$\left[\mathbf{J}_{\mathbf{Psdc}}\right] = \begin{bmatrix} \mathbf{0} \cdots \mathbf{0} & \mathbf{J}'_{\mathbf{Psdc}1} \cdots \mathbf{0} & \mathbf{0} \cdots \mathbf{0} \\ \vdots \ddots \vdots & \vdots \ddots \vdots & \vdots \ddots \vdots \\ \mathbf{0} \cdots \mathbf{0} & \mathbf{0} \cdots \mathbf{J}'_{\mathbf{Psdc}n} & \mathbf{0} \cdots \mathbf{0} \end{bmatrix} \tag{4.173}$$

$$\left[\mathbf{J}_{\mathbf{Padc}}\right] = \begin{bmatrix} \mathbf{0} \cdots \mathbf{0} & \mathbf{J}'_{\mathbf{Padc}1} \cdots \mathbf{0} & \mathbf{0} \cdots \mathbf{0} \\ \vdots \ddots \vdots & \vdots \ddots \vdots & \vdots \ddots \vdots \\ \mathbf{0} \cdots \mathbf{0} & \mathbf{0} \cdots \mathbf{J}'_{\mathbf{Padc}r} & \mathbf{0} \cdots \mathbf{0} \end{bmatrix} \tag{4.174}$$

$$\left[\mathbf{J}_{\mathbf{dcS}}\right] = \begin{bmatrix} \mathbf{0} \cdots \mathbf{0} & \mathbf{J}'_{\mathbf{dcS}1} \cdots \mathbf{0} & \mathbf{0} \cdots \mathbf{0} \\ \vdots \ddots \vdots & \vdots \ddots \vdots & \vdots \ddots \vdots \\ \mathbf{0} \cdots \mathbf{0} & \mathbf{0} \cdots \mathbf{J}'_{\mathbf{dcS}m} & \mathbf{0} \cdots \mathbf{0} \end{bmatrix}^{T} \tag{4.175}$$

The various entries in (4.172)-(4.175) are vectors with the generic $j\text{–}th$ terms depending on the number and type of converter, with $j = 1,...,m$, $j = 1,...,n$ and $j = 1,...,r$ for converters VSC$_{Slack}$, VSC$_{Psch}$ or VSC$_{Pass}$, respectively. They are shown in equations (4.176)-(4.179).

$$\mathbf{J'_{Sdc}}=\begin{bmatrix}0 & 0 & \dfrac{\partial \Delta P_{vj}}{\partial E_{dcj}} & \dfrac{\partial \Delta Q_{vj}}{\partial E_{dcj}} & \dfrac{\partial F_{I_{dcjaux}}}{\partial E_{dcj}} & 0\end{bmatrix}^T \tag{4.176}$$

$$\mathbf{J'_{Psdc}}=\begin{bmatrix}0 & 0 & \dfrac{\partial \Delta P_{vj}}{\partial E_{dcj}} & \dfrac{\partial \Delta Q_{vj}}{\partial E_{dcj}} & \dfrac{\partial F_{\gamma_{jaux}}}{\partial E_{dcj}} & 0\end{bmatrix}^T \tag{4.177}$$

$$\mathbf{J'_{Padc}}=\begin{bmatrix}0 & 0 & \dfrac{\partial \Delta P_{vj}}{\partial E_{dcj}} & \dfrac{\partial \Delta Q_{vj}}{\partial E_{dcj}} & 0 & 0 & \dfrac{\partial F_{\omega_j}}{\partial E_{dcj}} & 0\end{bmatrix}^T \tag{4.178}$$

$$\mathbf{J'_{dcS}}=\begin{bmatrix}0 & 0 & \dfrac{\partial F_{E_{dcj}}}{\partial \theta_{vj}} & \dfrac{\partial F_{E_{dcj}}}{\partial V_{vj}} & \dfrac{\partial F_{E_{dcj}}}{\partial \phi_j} & 0 & \dfrac{\partial F_{E_{dcj}}}{\partial dm_{aj}}\end{bmatrix} \tag{4.179}$$

The Jacobian matrix of the DC network takes the general form of equation (4.180).

$$[\mathbf{J_{dc}}]=\left[\begin{array}{cc:c}\mathbf{J_{dc1}} & \mathbf{J_{dc2}} & [\mathbf{J_{dc5}}] \\ \mathbf{J_{dc3}} & \mathbf{J_{dc4}} & \mathbf{0} \\ \hdashline [\mathbf{J_{dc6}}] & \mathbf{0} & \mathbf{J_{dc7}}\end{array}\right] \tag{4.180}$$

where $\mathbf{J_{dc5}}=[\mathbf{J'_{dc5}}\ \mathbf{0}]$ and $\mathbf{J_{dc6}}=[\mathbf{J'_{dc6}}\ \mathbf{0}]^T$. The matrices from $\mathbf{J_{dc1}}$ to $\mathbf{J_{dc4}}$, $\mathbf{J'_{dc5}}$ and $\mathbf{J'_{dc6}}$ are diagonal matrices of order $n_{vsc}=m+n+r$, which stands for the total amount of converters making up the multi-terminal system, with $j=1,\ldots,n_{vsc}$ and $k=n_{vsc}+1,\ldots,2n_{vsc}$. Such matrices are presented in an explicit form as shown in equations (4.181)-(4.182).

$$\mathbf{J_{dc1}}=\begin{bmatrix}\dfrac{\partial F_{I_{jx}}}{\partial I_{jx}} & 0 & 0 \\ 0 & \ddots & 0 \\ 0 & 0 & \dfrac{\partial F_{I_{jx}}}{\partial I_{jx}}\end{bmatrix},\ \mathbf{J_{dc2}}=\begin{bmatrix}\dfrac{\partial F_{I_{jx}}}{\partial E_{dcj}} & 0 & 0 \\ 0 & \ddots & 0 \\ 0 & 0 & \dfrac{\partial F_{I_{jx}}}{\partial E_{dcj}}\end{bmatrix},\ \mathbf{J_{dc3}}=\begin{bmatrix}\dfrac{\partial F_{E_{dcj}}}{\partial I_{jx}} & 0 & 0 \\ 0 & \ddots & 0 \\ 0 & 0 & \dfrac{\partial F_{E_{dcj}}}{\partial I_{jx}}\end{bmatrix} \tag{4.181}$$

$$\mathbf{J_{dc4}}=\begin{bmatrix}\dfrac{\partial F_{E_{dcj}}}{\partial E_{dcj}} & 0 & 0 \\ 0 & \ddots & 0 \\ 0 & 0 & \dfrac{\partial F_{E_{dcj}}}{\partial E_{dcj}}\end{bmatrix},\ \mathbf{J'_{dc5}}=\begin{bmatrix}\dfrac{\partial F_{I_{jx}}}{\partial E_{dck}} & 0 & 0 \\ 0 & \ddots & 0 \\ 0 & 0 & \dfrac{\partial F_{I_{jx}}}{\partial E_{dck}}\end{bmatrix},\ \mathbf{J'_{dc6}}=\begin{bmatrix}\dfrac{\partial \Delta P_{dck}}{\partial I_{jx}} & 0 & 0 \\ 0 & \ddots & 0 \\ 0 & 0 & \dfrac{\partial \Delta P_{dck}}{\partial I_{jx}}\end{bmatrix} \tag{4.182}$$

On the other hand, the order of matrix $\mathbf{J_{dc7}}$, shown in (4.183), corresponds to the number of DC nodes n_{dc} minus the number of converters n_{vsc}, with $(j,k)=n_{vsc}+1,\ldots,n_{dc}$.

$$\mathbf{J}_{\mathbf{dc}7}=\begin{bmatrix}\dfrac{\partial\Delta P_{dcj}}{\partial E_{dck}}\cdots\dfrac{\partial\Delta P_{dcj}}{\partial E_{dck}}\\ \vdots\quad\ddots\quad\vdots\\ \dfrac{\partial\Delta P_{dcj}}{\partial E_{dck}}\cdots\dfrac{\partial\Delta P_{dcj}}{\partial E_{dck}}\end{bmatrix} \tag{4.183}$$

The remaining terms, corresponding to the DC side of the multi-terminal HVDC system, with $j=1,\ldots,n_{vsc}$ and $k=n_{vsc}+1,\ldots,n_{dc}$, are:

$$\left[\mathbf{F}_{\mathbf{dc}}\right]=\left[F_{I_{jx}}\cdots F_{I_{jx}}\,|\,F_{E_{dcj}}\cdots F_{E_{dcj}}\,|\,\Delta P_{dck}\cdots\Delta P_{dck}\right]^{T} \tag{4.184}$$

$$\left[\mathbf{\Delta\Phi}_{\mathbf{dc}}\right]=\left[\Delta I_{jx}\cdots\Delta I_{jx}\,|\,\Delta E_{dcj}\cdots\Delta E_{dcj}\,|\,\Delta E_{dck}\cdots\Delta E_{dck}\right]^{T} \tag{4.185}$$

Notice that the generalised form of (4.180) implies that any kind of DC network topology may be straightforwardly handled.

As the adopted approach to modelling multi-terminal schemes is modular, developing new converter models carrying, for instance, different control strategies would not imply extra difficulties in terms of their aggregation into this generalised multi-terminal HVDC link model. During the derivation of the comprehensive multi-terminal HVDC model for dynamic simulations, represented by (4.171), it was assumed that each VSC unit connects to a capacitor and smoothing inductor coupled to a resistor on its DC side, however, a few modifications would take place otherwise. Unlike the steady-state model of the multi-terminal HVDC link, the DC voltage of the slack converter is part of the variables to be computed through the time-domain solution, where at least one slack converter must exist, in the multi-terminal arrangement, to ensure the stability of the voltages throughout the DC network. The calculated power at each node j of the DC network is computed through the expression (4.186). The calculated active and reactive power equations that enable the multi-terminal HVDC system to link with each AC network, at a generic node k, coupled to a particular VSC station are given by (4.187)-(4.188), respectively.

$$P_{dcj}^{cal}=E_{dcj}^{2}G_{dcjj}+E_{dcj}\sum_{\substack{j=n_{vsc}+1\\ m\in j}}^{n_{dc}}E_{dcm}G_{dcjm} \tag{4.186}$$

$$P_{k}^{cal}=V_{k}^{2}G_{kk}+V_{k}\sum_{m\in k}V_{m}\left[G_{km}\cos\left(\theta_{k}-\theta_{m}\right)+B_{km}\sin\left(\theta_{k}-\theta_{m}\right)\right] \tag{4.187}$$

$$Q_{k}^{cal}=-V_{k}^{2}B_{kk}+V_{k}\sum_{m\in k}V_{m}\left[G_{km}\sin\left(\theta_{k}-\theta_{m}\right)-B_{km}\cos\left(\theta_{k}-\theta_{m}\right)\right] \tag{4.188}$$

4.4 Conclusions

This Chapter has presented an RMS-type dynamic modelling framework for various VSC-based devices. The dynamic modelling of the STATCOM, back-to-back and point-to-point HVDC links, and multi-terminal HVDC systems was addressed in this Chapter. These models, as in the case of those developed in Chapter 3 aimed at power-flow studies, are based on power injections where their fundamental power expressions are used as the building platform with which the VSC-based devices are mathematically derived for dynamic simulations of power systems. Indeed, these are all-encompassing models that cater for the steady-state and dynamic simulations of AC/DC networks. The AC systems may be quite general in nature, in terms of their size, degree of operational complexity and type of electrical power equipment contained in these AC networks, as long as they are represented by either positive-sequence or *dq* models, depending on whether they are static equipment or rotating machinery.

Owing to the modular manner in which the basic VSC unit is dynamically modelled, the STATCOM, the two-terminal and multi-terminal VSC-HVDC systems may be directly represented by carrying out minor modifications that affect the control strategies of each particular power electronics device. A case in point is the frequency control loop of the VSC-HVDC link providing frequency support to low-inertia networks which uses, quite effectively, the regulation of the angular aperture that exists between the internal phase-shifting angle of the rectifier and the voltage angle at its AC terminal. This is amenable to power flow regulation in the DC link and, hence, to frequency control in the supported AC network, where the inverter acts as a virtual synchronous generator, playing the role of the reference for all the other nodes in the low-inertia AC network. On the other hand, the dynamic model of multi-terminal schemes, with any number of VSC units and an arbitrary DC network topology, may be comprehensively carried using the three types of VSC dynamic models derived to conform to each paring AC sub-network, i.e., the slack converter, the power-scheduled converter and the passive converter, whose main dynamic features consist of controlling its DC voltage, its DC power and the electrical frequency, respectively.

In general terms, a unified dynamic solution of AC power systems and VSC-based equipment has been introduced in this Chapter. It yields great flexibility, enabling not only the estimation of the fundamental dynamics of the STATCOM, back-to-back and point-to-point HVDC links, and multi-terminal HVDC systems, but also efficient numerical solutions are attained owing to the Newton-Raphson method which solves simultaneously the algebraic and discretised differential equations arising from the whole AC/DC network at each time step.

5 Case studies

In this Chapter, the steady-state and dynamic performaces of the various VSC-based devices developed in the two previous Chapters are investigated. The models coded in software are suitable for carrying out power-flow studies as well as for conducting time-domain simulations of power systems. The results obtained from the introduced VSC-HVDC models, including that of the multi-terminal scheme, are compared against switching-based models using the widely-used EMT-type package Simulink, confirming the suitability of the proposed models to capture the most relevant phenomena occurring when subjected to perturbations, in both the AC and DC sides, with sufficient accuracy. Furthermore, the STATCOM and point-to-point HVDC link are both tested using the New England test system (Chow, 1982) which comprises 39 buses and ten synchronous generators. More notably, this Chapter presents a representative case study of a six-terminal VSC-HVDC system forming a DC ring which is meant to signify a stage of development of the undersea power grid in the North Sea (Vrana et al., 2010; Hertem and Ghandhari, 2010; Orths et al., 2012).

The models of the STATCOM, back-to-back, point-to-point and multi-terminal VSC-HVDC links were implemented according to the procedures shown in Chapters 3 and 4, using a unified frame of reference for conducting both steady-state and dynamic analyses. The software implementation was carried out in Matlab code and its simulation environment was used to run all the cases presented in this thesis.

5.1 Power systems simulations including STATCOMs

5.1.1 New England 39-bus network, 2 STATCOMs

The New England test system, shown in Figure 5.1, is a power network widely used in academic circles. This is a thirty nine-bus network containing ten synchronous generators, thirty four transmission lines, twelve transformers and nineteen loads. This system has been slighly modified

to incorporate two STATCOMs at nodes 5 and 27 where large voltage fluctuations are expected following a disturbance at any of the main corridors of the electrical network. In steady-state, the generator 10 which is connected to node 39 is considered to be the slack generator, whilst the rest are assumed to be PV generators. Generators 1 to 5 are driven by a hydro turbine whilst generators 6 to 10 are driven by steam turbines for the dynamic operating regime, but all synchronous generators are represented by their transient model. Table 5.1 shows the parameters of the STATCOMs given on their own base, S_{nom} = 100 MVA. It is worth remarking that for the purpose of the dynamic simulations, the tap of the OLTC transformers is kept constant. The reason for this assumption lies on the fact that the time response of the servomotor that imposes small variations on the tap changer is much slower than the time response afforded by the controller that drives the modulation ratio of the VSCs.

Table 5.1 Parameters of the STATCOMs

Bus	S_{nom} (MVA)	E_{dc} (p.u)	G_0 (p.u)	R (p.u)	X (p.u)	K_{pe}	K_{ie}	K_{pp}	K_{ip}	K_{ma}	T_{ma}	X_{ltc} (p.u)
5	100.0	1.00	2e-3	2e-3	0.01	0.20	7.50	0.001	0.15	7.5	0.02	0.05
27	100.0	1.00	2e-3	2e-3	0.01	0.20	7.50	0.001	0.15	7.5	0.02	0.05

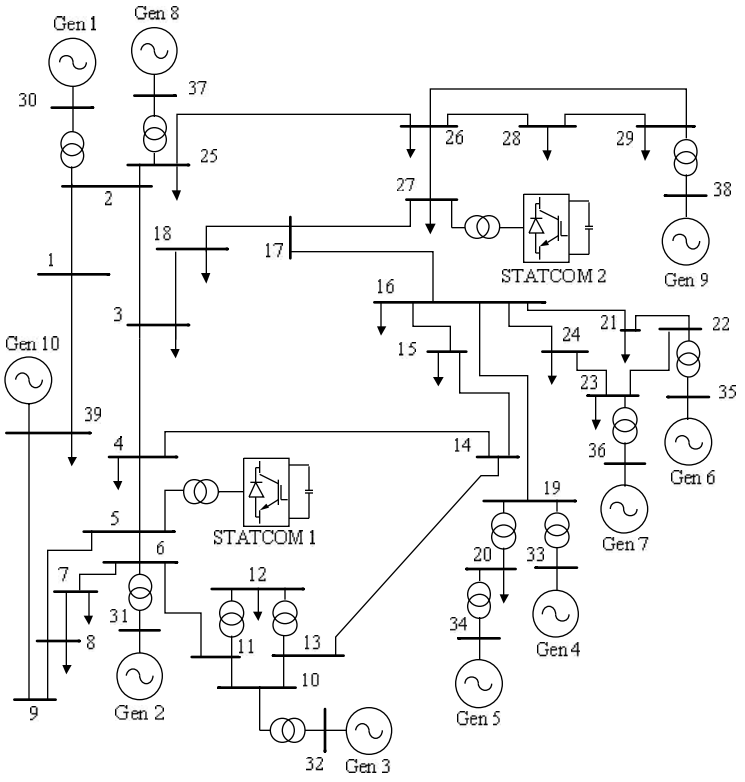

Figure 5.1 New England test system with two embedded STATCOMs

Steady-state results of the embedded STATCOMs

Table 5.2 presents a summary of the steady-state power flow results, from which it is noticed that the STATCOMs inject 12.258 MVAr and 35.646 MVAr into nodes 5 and 27 in order to uphold their target voltage at 1.01 p.u and 1.04 p.u, respectively. In connection with the derivation of the steady-state model of the STATCOM presented in Section 3.3, its reactive power generation is computed as $Q_g = -Q_{dtc}$. In steady-state conditions, the total power losses incurred by the STATCOMs stand at 0.0125 MW and 0.1142 MW. The reason for such a difference lies on the total current magnitude flowing through each VSC which are: 0.1120 p.u and 0.3380 p.u, respectively. It should be beared in mind that the switching losses are fucntions of the existing operating conditions, i.e., the losses are scaled by the quadratic ratio of the actual terminal current magnitude to the nominal current of the equipment which in this example is 1 p.u for both VSCs. In this case, the STATCOM 2 carries a higher current and, therefore, has higher internal losses.

Table 5.2 STATCOM results as furnished by the power-flow solution

STATCOM	Q_g (MVAr)	m_a	ϕ (deg)	B_{eq} (p.u.)	OLTC tap	P_{loss} (MW)
1	12.258	0.8311	1.6759	0.1100	1.0060	0.0125
2	35.646	0.8685	2.2568	0.3177	1.0165	0.1142

Dynamic analysis of the power system incorporating two STATCOMs

Once the steady-state power-flow solution has been obtained, the calculation of the initial values of the control variables with which the dynamic simulation will be carried out is a simple task. Their values are shown in Table 5.3.

Table 5.3 Initial values of the STATCOM variables for the dynamic simulation

STATCOM	E_{dc} (p.u)	I_{dcaux} (p.u)	γ_{aux} (rad)	dm_a
1	1.00	0.0	0.2286e-3	0.0
2	1.00	0.0	0.7078e-3	0.0

Notice that the following relationships hold for the steady-state regime: $I_{dc} = I_{dcaux}$, $\gamma = \gamma_{aux}$ and $m_a = m_a^{(0)}$. The network is subjected to a disturbance where the transmission lines connecting buses 2-25, 2-3 and 3-4 (which are transmitting in steady-state approximately 230 MW, 380 MW and 75 MW, respectively) are tripped at t = 0.1 s. The simulation runs for 5 s with a time step of 1

ms. As a result of such a drastic change in the network topology, a rearrangement of power flows takes place in several transmission lines of the system together with changes in the powers drawn by the loads (owing to their voltage dependency). All this produces variations in the power flows which are accompanied by changes in the angular speed of the synchronous generators, as seen from Figure 5.2 to Figure 5.4. Also, such power fluctuations cause significant voltage oscillations in several nodes of the power system, as shown in Figure 5.5. It should be mentioned that this is a representative performance of what the rest of the nodes in the power network experience after the perturbation.

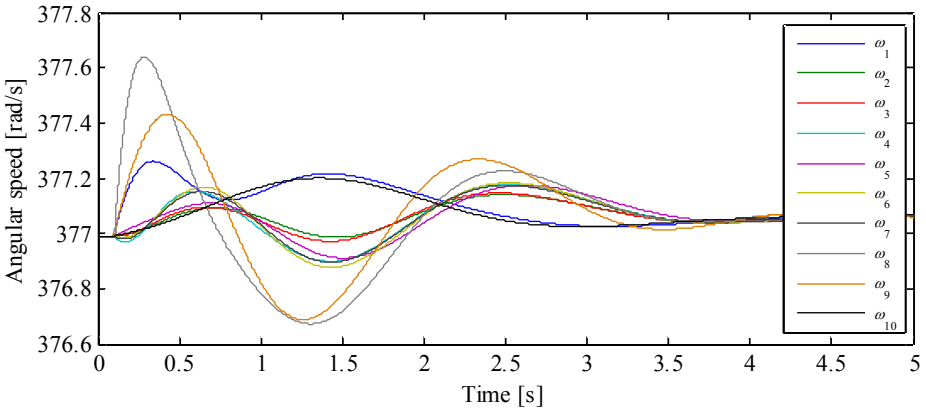

Figure 5.2 Angular speed of the synchronous generators

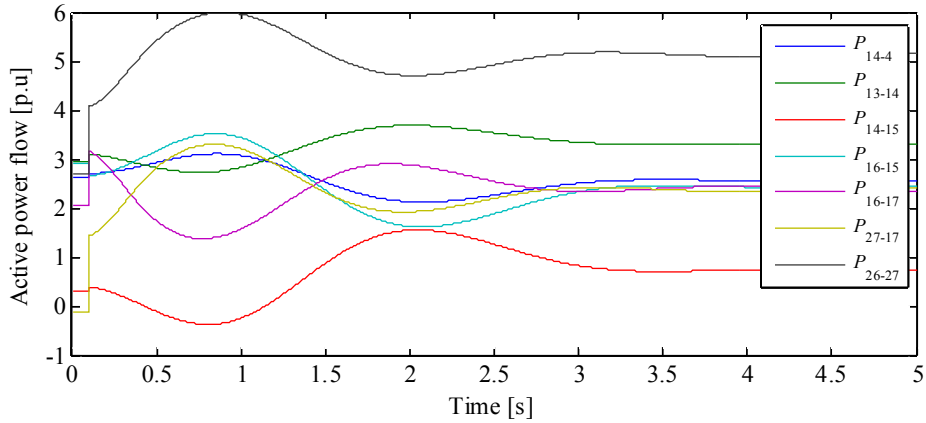

Figure 5.3 Active power flow behaviour in some transmission lines

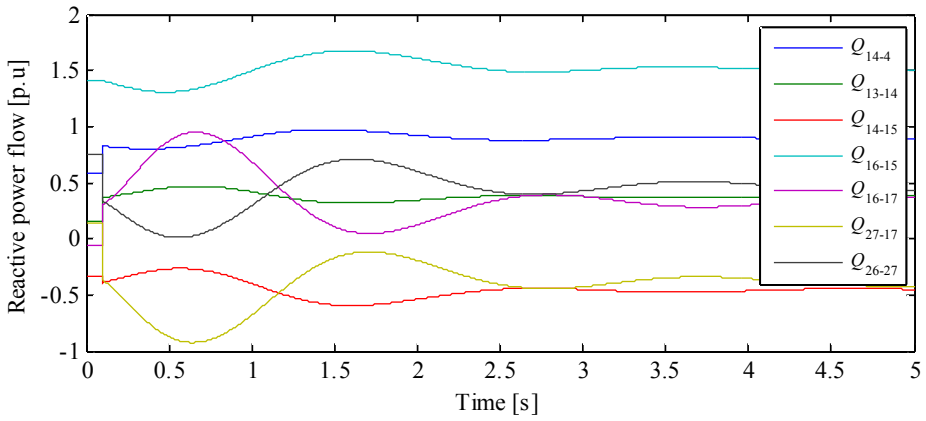

Figure 5.4 Reactive power flow behaviour in some transmission lines

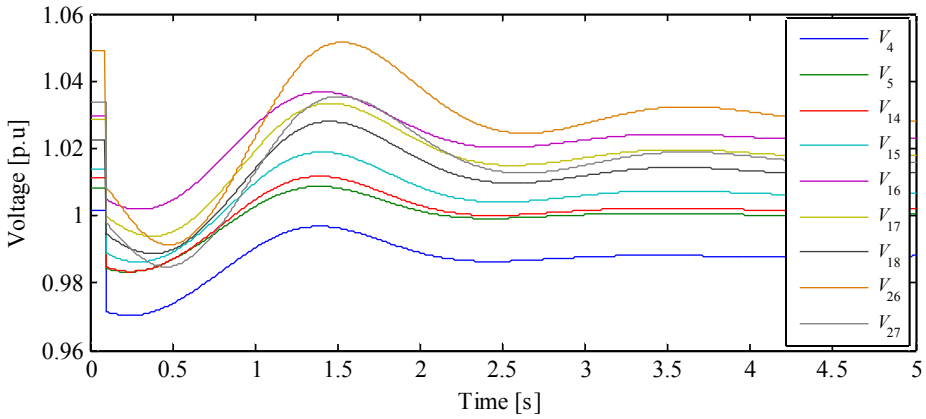

Figure 5.5 Voltage performance at different nodes of the network

Due to the very rapid reactive power provision afforded by the STATCOMs, as shown in Figure 5.6, where during the transient period reaches a peak value of approximately 46 MVAr and 98 MVAr, respectively, are observed. The nodal voltage at the AC terminal of the converters V_v (low-voltage side of the OLTC transformer), undergoes little change and is fittingly controlled, as seen in Figure 5.7. Undoubtedly, the STATCOMs assists not only the AC voltage of the converters, but also the neighbouring nodes throughout the transient period, as shown in Figure 5.8, in the sense that the network voltages are stabilised much faster compared to Fig. 5.5. This feature makes the STATCOM a very attractive choice to install in weak nodes of the power network since this power electronic device improves the voltage performance very effectively.

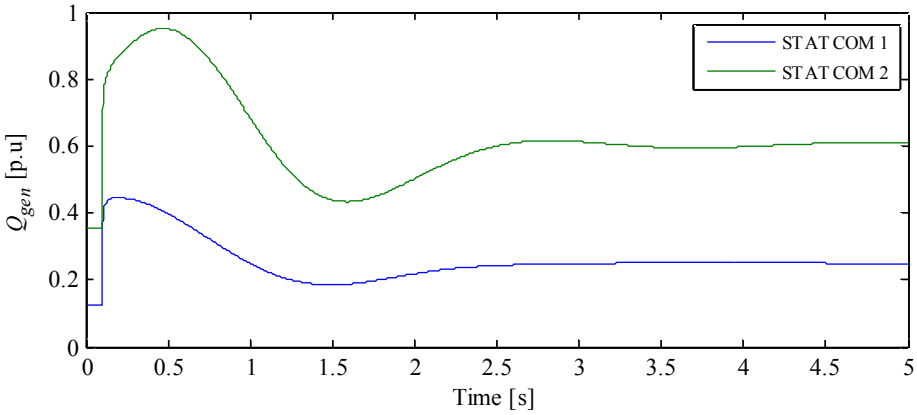

Figure 5.6 Reactive power generated by the STATCOMs

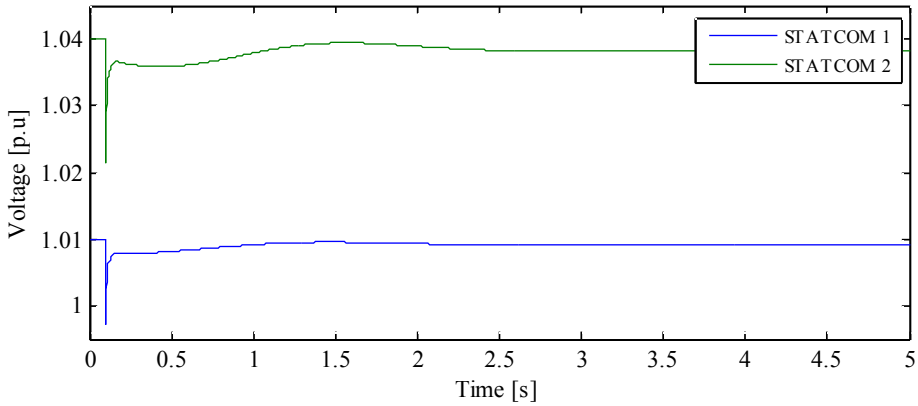

Figure 5.7 Voltage performance at the AC nodes of the VSCs

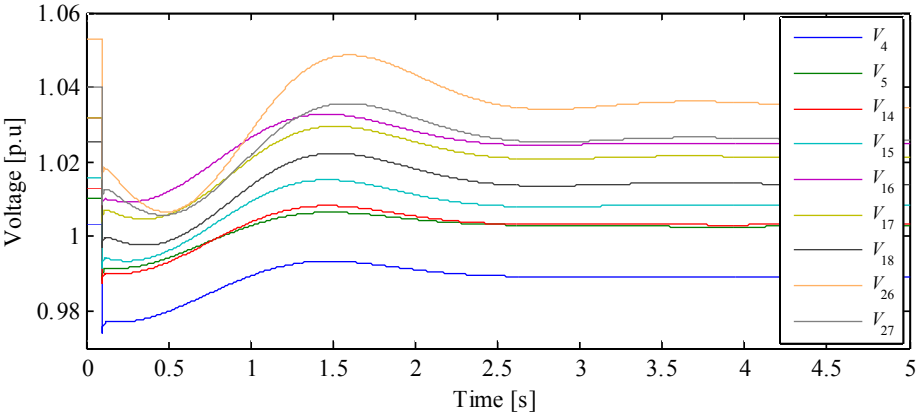

Figure 5.8 Voltage performance at several nodes of the network including two STATCOMs

Following the disturbance, abrupt changes occur in the terminal current of the VSCs; as a result of this abnormal situation, the power balance on the DC side of the VSCs is disrupted, inducing variations on the DC voltage, as shown in Figure 5.9. This forces the DC voltage controller to respond by modulating the DC current, as seen in Figure 5.10. It is seen that both control variables stabilise just after a few seconds of the occurrence of the perturbation. It should be remarked that, as expected, the DC current returns to be zero once the VSCs and the whole network reach a new equilibrium point. This behaviour fully agrees with the fact that the current of the DC capacitor must be zero at steady-state.

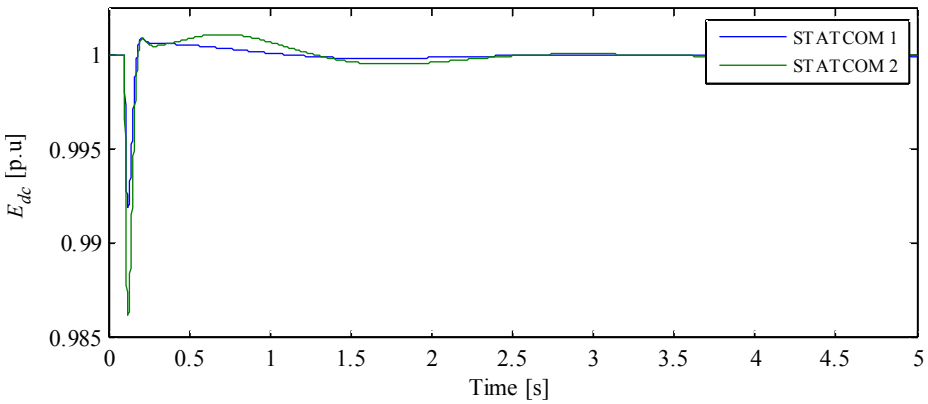

Figure 5.9 STATCOMs DC-bus voltages

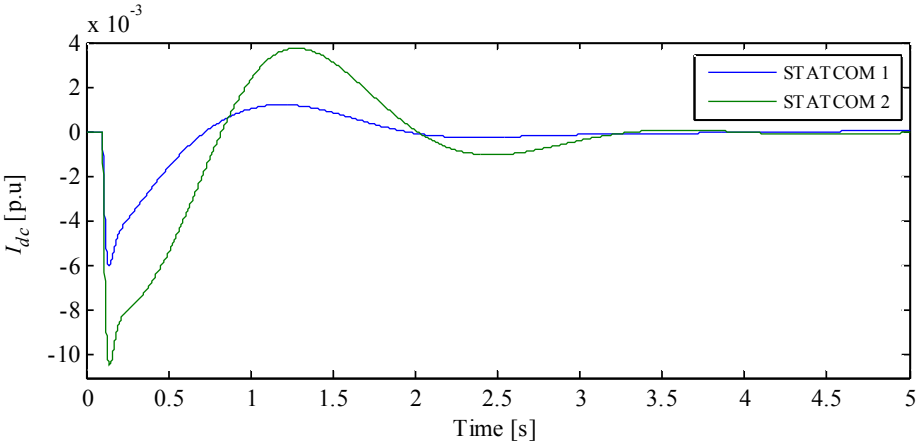

Figure 5.10 STATCOMs DC current

The performance of the angle used in the DC power controller γ , is shown in Figure 5.11. The reason for the increase in γ can be explained by recalling that this angle represents the angular aperture between the phase-shifting angle ϕ and the terminal voltage angle θ_v . As expected, the more current passes through the electronic switches the more power losses are incurred by the

VSCs. In general, when rises of the terminal current take place, the power losses are amplified, as shown in Figure 5.12; the angle controller, therefore, adjusts during the transient period with the aim of re-establishing the power balance on the DC side of the converters. Notice that the power losses of the STATCOM 2 reach almost 1% during the transient period and those of the STATCOM 1 reach approximately 0.2%.

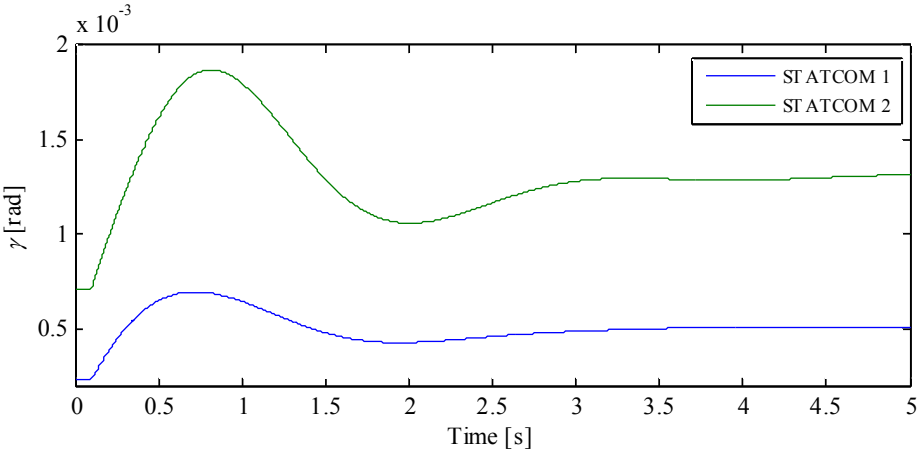

Figure 5.11 Dynamic performance of the angle γ of the VSCs

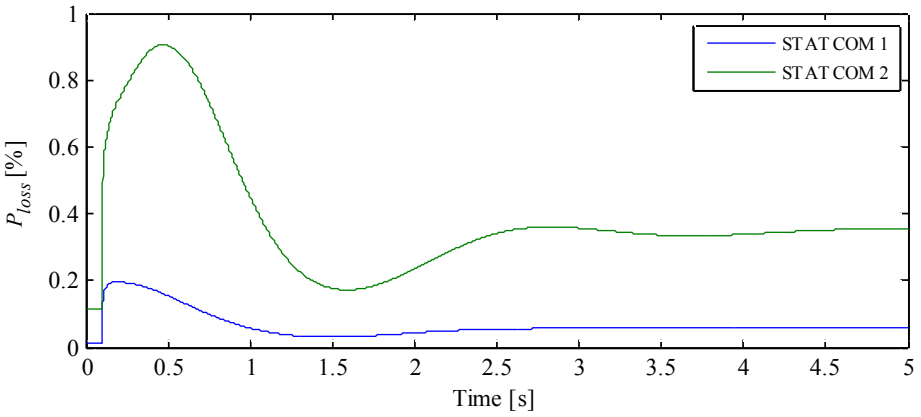

Figure 5.12 Total active power losses incurred by the STATCOMs

Likewise, the modulation index control of the STATCOMs starts to exert voltage regulation just after the disturbance has occurred, as depicted in Figure 5.13. Its behaviour is governed by equation (4.9) from which it can be inferred that when the terminal voltage V_v is smaller than V_{v0}, the derivative of the modulation index with respect to time is positive. This explains the increments in the modulation ratio of both STATCOMs just after the disturbance. Notice that for a very short period of time, the modulation index corresponding to STATCOM 2 suffers a rapid increase, reaching

a value of 0.943. After the transient event has passed, it quickly settles down at a new steady-state value of 0.884.

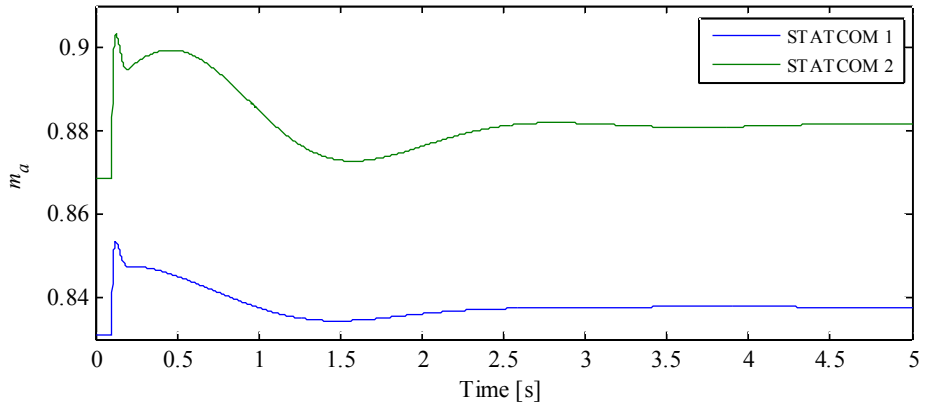

Figure 5.13 Dynamic behaviour of the modulation index of the STATCOMs

The state variables of STATCOM 2 are more sensitive to the disturbance since this device is located closer to the transmission line that connects buses 17 and 18, which becomes the only path available to supply the loads connected at nodes 3 and 18.

Parametric analysis – impact of resizing the capacitors of the STATCOMs

A parametric analysis would permit assessment of the impact of, for instance, the size of the capacitors on the dynamics of both the internal variables of the STATCOMs and their reactive power injection into the grid. With this goal in mind, it is of interest to reproduce the same disturbance conditions for the test system but now altering the inertia of the capacitors to be: (i) 5 ms, (ii) 10 ms, and (ii) 20ms. The dynamic performance of the DC voltage and modulation ratio is shown in Figure 5.14 and Figure 5.15, respectively. Significant differences are seen when the electrostatic energy stored in the capacitors increase. It is noticed that the DC voltage dip is smaller with increases of the capacitor's inertia, but accompanied by a DC voltage overshoot, which is rapidly damped out. The reactive power generated by the STATCOM, for different values of the capacitor's inertia, is presented in Figure 5.16. For the purpose of this parametric analysis, the values of the gains of the STATCOM control loops have not been altered.

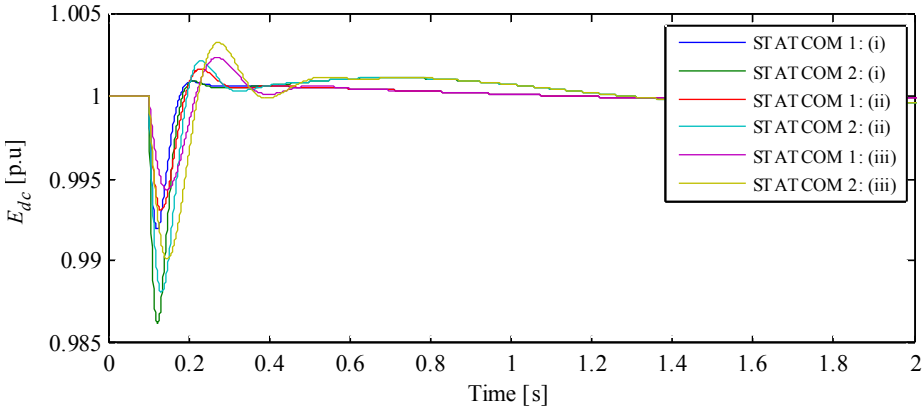

Figure 5.14 Performance of the DC voltages for different ratings of the capacitors

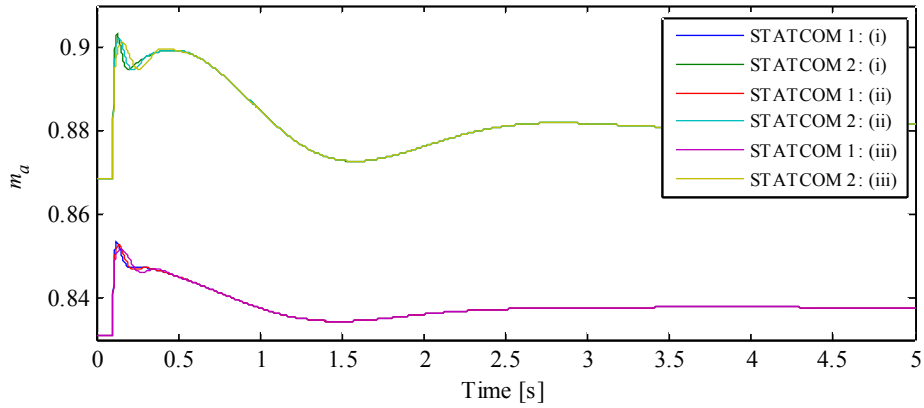

Figure 5.15 Performance of the modulation ratio for different ratings of the capacitors

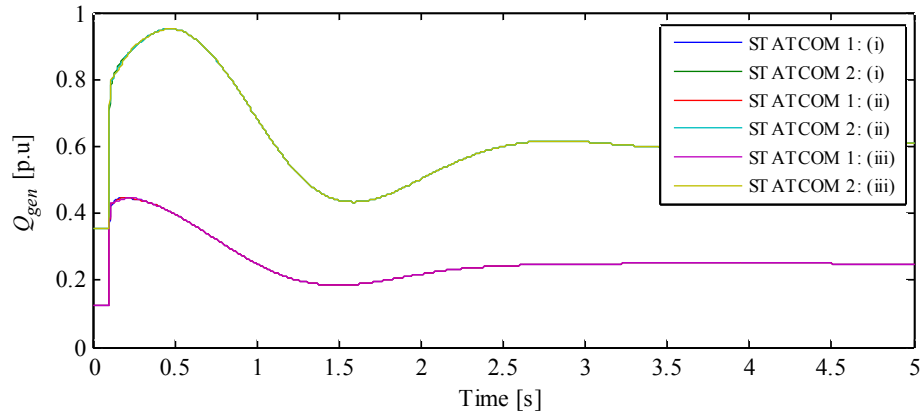

Figure 5.16 Reactive power generation for different ratings of the capacitors

5.2 Point-to-point VSC-HVDC-upgraded power systems

5.2.1 Validation of the VSC-HVDC model for power regulation

The validity of the response of the VSC-HVDC link model is demonstrated by carrying out a comparison against the widely-used EMT-type simulation software Simulink. It should be mentioned that both types of simulation tools enable dynamic assessments of electrical power networks but they take a fundamentally different solution approach. Simulink represents every component of the power grid by means of RLC circuits and their corresponding differential equations require discretisation at relatively small time steps, in the order of micro-seconds, to ensure a stable numerical solution. On the contrary, the solution of the RMS-type model introduced in this thesis (Section 3.4.1) requires only one phase of the network, i.e., the positive-sequence network and uses fundamental-frequency phasors of voltages and currents as opposed to the three-phase representation of the network and instantaneous waveforms of voltages and currents used in EMT tools such as Simulink. The VSC-HVDC model comparison is carried out using the simple power system shown in Figure 5.17 which comprises two independent AC networks (2000 MVA, 230 kV, 50 Hz) and whose interconnection is carried out through a VSC-HVDC link rated at 200 MVA and ±100 kV DC with a DC cable length of 75 km.

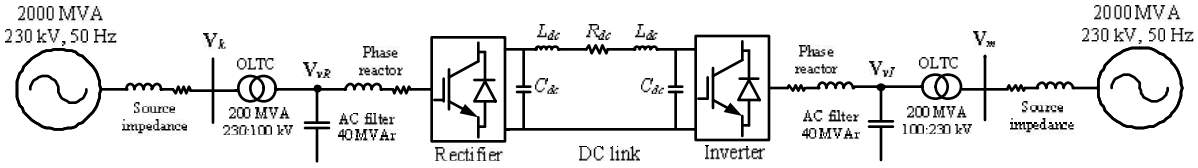

Figure 5.17 Test system used to validate the proposed VSC-HVDC model

Both converter stations comprise of a step-down transformer, AC filters, converter reactor, DC capacitors and DC filters, and fixed off-nominal taps positions. The model of the power system including the VSC-HVDC link together with its parameters can be found in the section of 'demos' in Simulink under the title: VSC-Based HVDC Transmission System (Detailed Model). The parameters of the developed VSC-HVDC model are shown in Table 5.4. To ensure a reliable numerical solution, the EMT-type simulation package discretises the power system and the control system with a sampling time of 7.4074 μs and 74.074 μs, respectively, whereas for the RMS-type model described in Section 3.4.1, an integration time step of 1 ms is used. Initially the rectifier station is set to control the active power transmission at P_{sch} = 200 MW (2 p.u.), the inverter is responsible for controlling the DC voltage at E_{dcInom} = 200 kV. The rectifier and inverter stations are set to comply with a fixed reactive power command of 0 p.u. and -0.1 p.u., respectively. In order to

reach the steady-state equilibrium point in Simulink, the simulation is run up to t = 1 s. At this point, the active power transmission is reduced from 200 MW to 100 MW, that is, a -50% step is applied to the reference scheduled DC power. Furthermore, at t = 3 s, a step change of -5% is applied to the reference DC voltage of the inverter, i.e., the DC voltage is decreased from 1 p.u to 0.95 p.u.

Table 5.4 Parameters of the VSC-HVDC link

S_{nom} (p.u)	P_{sch} (p.u)	R_{dc} (p.u)	E_{dcI} (p.u)	G_{0I} , G_{0R} (p.u)	R_I , R_R (p.u)
2.0	2.0	0.02135	1.00	4e-3	0.0
X_I , X_R (p.u)	R_{fI} , R_{fR} (p.u)	X_{fI} , X_{fR} (p.u)	B_{fI} , B_{fR} (p.u)	R_{ltc} (p.u)	X_{ltc} (p.u)
0.0	7.5e-4	0.075	0.40	2.5e-3	0.075
H_c , H_i (s)	K_{pe}	K_{ie}	K_{pp} , K_{ip}	K_{maR} , K_{maI}	T_{maR} , T_{maI}
14e-3, 14e-3	0.60	35.0	0.0, 5.0	25.0	0.02

The DC voltages corresponding to cases where step changes in the reference DC power and DC voltage are applied are shown in Figure 5.18. As expected, some differences may be seen in these results, owing to the two very different solution techniques employed. The dynamic performance of the DC voltages of the RMS-type model follows well the dynamic pattern obtained by the switching-based HVDC model in Simulink. The difference between the two solution approaches at the start of the simulation (0.5 s of the simulation), a fact that is explained by the very different manner in which both power system simulations are initialised; the proposed RMS model of the VSC-HVDC system uses accurate starting conditions furnished by a power-flow solution whereas the Simulink model starts from its customary zero initial condition, i.e., the currents and voltages of the inductors and capacitors, respectively, are set to zero at t = 0 s. From the physical vantage, this is akin to assuming that the system was in a de-energised state and it is energised at a time 0+. Conversely, the RMS solution assumes that the system together with the VSC-HVDC are operating under normal steady-state conditions.

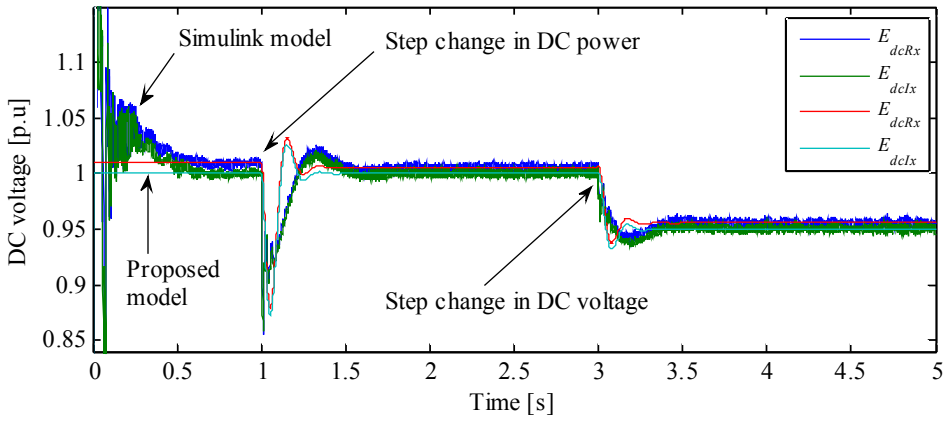

Figure 5.18 DC voltage performance for the proposed and Simulink models

Similar conclusions can be drawn when analysing the dynamic response of the DC power following the application of the step changes in DC power and DC voltage, as shown in Figure 5.19. As for the change in the DC power reference, it can be seen that the power stabilises in no more than 0.5 seconds; this shows the quick response and robustness afforded by the dynamic controls of the VSC-HVDC link even in the event of a drastic change in the DC power transmission. On the other hand, the step change in the DC voltage reference causes momentary power flow oscillations in the DC link which are also damped out quite rapidly.

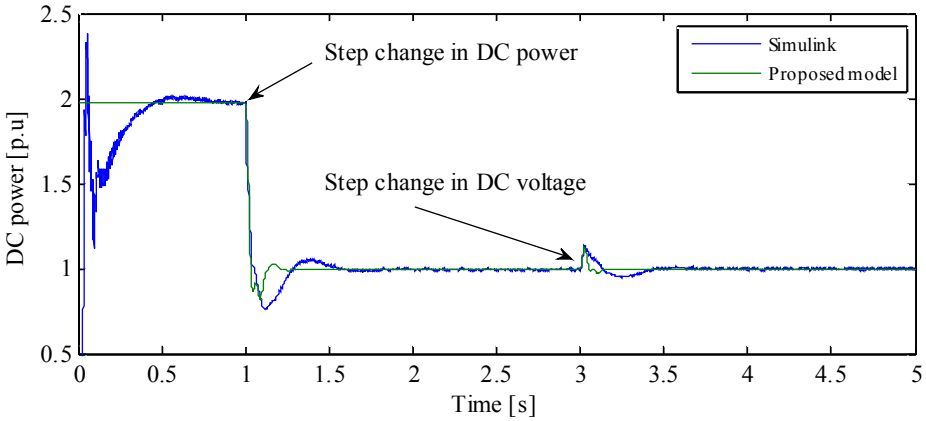

Figure 5.19 DC power performance for the proposed and Simulink models

Admittedly, the performance of the proposed VSC-HVDC link model represents a good approximation compared to that of the Simulink model. To validate this statement, the definition of root-mean-square error (RMSE) is used to assess the dynamic performances of the DC voltages and the DC power, shown in Fig. 5.18 and Fig. 5.19, respectively. The following errors are calculated:

$$RMSE_{E_{dcRx}} = \sqrt{\frac{1}{n}\sum_{t=1}^{t=5}\left(E^{s}_{dcRx} - E^{p}_{dcRx}\right)^2} = 0.0254; \quad RMSE_{E_{dcIx}} = \sqrt{\frac{1}{n}\sum_{t=1}^{t=5}\left(E^{s}_{dcIx} - E^{p}_{dcIx}\right)^2} = 0.0278; \quad RMSE_{P_{dc}} = \sqrt{\frac{1}{n}\sum_{t=1}^{t=5}\left(P^{s}_{dc} - P^{p}_{dc}\right)^2} = 0.0413$$

where n is the number of points compared in time, between 1 and 5 seconds of simulation; the superscripts s and p stand for Simulink model and proposed model, respectively. As observed from the estimated indices, the root-mean-square errors are relatively small. This indicates that the deviations between the two different approaches are relatively small during the dynamic simulation, being the DC power the parameter incurring a larger deviation, i.e., $RMSE_{Pdc}$ = 0.0413 p.u.

The dynamic behaviour of the modulation indices of the converters are depicted in Figure 5.20. The step change in the DC power reference yields a very abrupt variation in the modulation indices; the dynamic performance of the modulation indices as calculated by both Simulink and the

proposed RMS-type VSC-HVDC model, follow the same trend although an exact match was not expected. After the first disturbance, a steady-state error of 0.87% and 1.67% is obtained for the modulation indices of the rectifier and inverter, respectively. Similarly, once the oscillations due to the step change in the reference DC voltage have been damped out, the differences in the modulation indices stand at 0.07% and 1.16%, respectively. These variations in the modulation indices may be explained by the very different modelling and solution approaches employed.

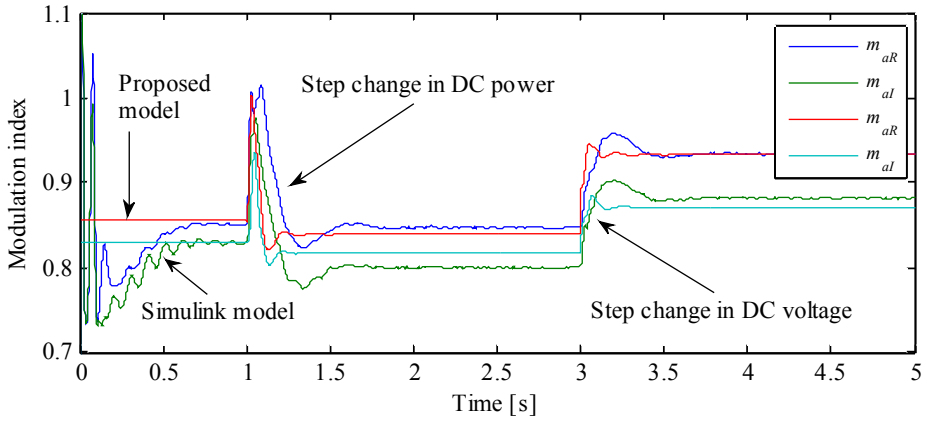

Figure 5.20 Modulation indices performance for the proposed and Simulink models

For the sake of comparison, Table 5.5 shows the VSC-HVDC results as obtained by the proposed model and the Simulink model at different points in time during the simulation. Table 5.5 also shows the computing times required to simulate the test system using both the RMS-type VSC-HVDC model and the EMT-type simulation tool Simulink, with the former model being approximately 9 times faster than the EMT simulation. The very significant saving in terms of cumputing time, without jeopardising the accuracy of the results, makes the developed VSC-HVDC link model a suitable option to use in cases of power system simulations; particularly in studies that require long simulation times such as those involving synchronous generators' frequency variations and long-term voltage stability issues.

Table 5.5 VSC-HVDC variables for the proposed model and Simulink model

Time	Proposed model					Simulink model				
	E_{dcR}	E_{dcI}	m_{aR}	m_{aI}	$-P_{dcI}$	E_{dcR}	E_{dcI}	m_{aR}	m_{aI}	$-P_{dcI}$
t = 1⁻ s	1.0105	1.0000	0.8553	0.8296	1.9791	1.0007	0.9968	0.8499	0.8301	1.9795
t = 3⁻ s	1.0053	1.0000	0.8389	0.8172	0.9947	1.0044	0.9996	0.8476	0.8005	0.9954
t = 5 s	0.9556	0.9500	0.9329	0.8711	0.9942	0.9554	0.9494	0.9336	0.8827	0.9909
	Computing time: 19.76 seconds					Computing time: 180.39 seconds				

5.2.2 New England 39-bus network, 1 embedded VSC-HVDC link

The New England test system is modified, as shown in Figure 5.21, to incorporate a VSC-HVDC link with the parameters shown in Table 5.6. This system is used to show the dynamic performance of the VSC-based transmission link when the network is subjected to disturbance. The rest of the parameters correspond to those of the original case. The transmission line connecting nodes 4 and 14 is replaced by a VSC-HVDC link. The DC cable resistance is assumed to be 0.24% on the converters' base: S_{nom} = 300 MVA, resulting in the same resistance value as that of the replaced transmission line for the system's base: 0.08%.

Table 5.6 Parameters of the embedded VSC-HVDC link

S_{nom} (p.u)	P_{sch} (p.u)	R_{dc} (p.u)	E_{dcI} (p.u)	G_{0I} , G_{0R} (p.u)	R_I , R_R (p.u)
3.0	1.0	0.0008	1.00	6e-3	6.66e-4
X_I , X_R (p.u)	R_{fI} , R_{fR} (p.u)	X_{fI} , X_{fR} (p.u)	B_{fI} , B_{fR} (p.u)	R_{ltc} (p.u)	X_{ltc} (p.u)
3.33e-3	0.0	0.02	0.30	0.0	0.01667
H_c , H_i (s)	K_{pe}	K_{ie}	K_{pp} , K_{ip}	K_{maR} , K_{maI}	T_{maR} , T_{maI}
15e-3, 15e-3	0.05	1.00	0.002,0.075	25.0	0.02

The rectifier and inverter stations exert voltage control at their respective AC terminals at V_{vR} = 1.01 p.u and V_{vI} = 1.03 p.u, respectively. For the steady-state conditions, the high-voltage side of the OLTC transformers, which correspond to nodes 4 and 14, are held fixed at the same voltage level as those for the converters' terminals, V_{vR} and V_{vI}; under these conditions, the taps of the OLTCs are computed through the steady-state power flow algorithm and these are kept constant during the dynamic solution. In addition to providing reactive power control, the VSC-HVDC link performs power regulation at the DC bus of the rectifier station at P_{sch} = 100 MW, which implies that the active power is drawn from node 4 and injected to node 14.

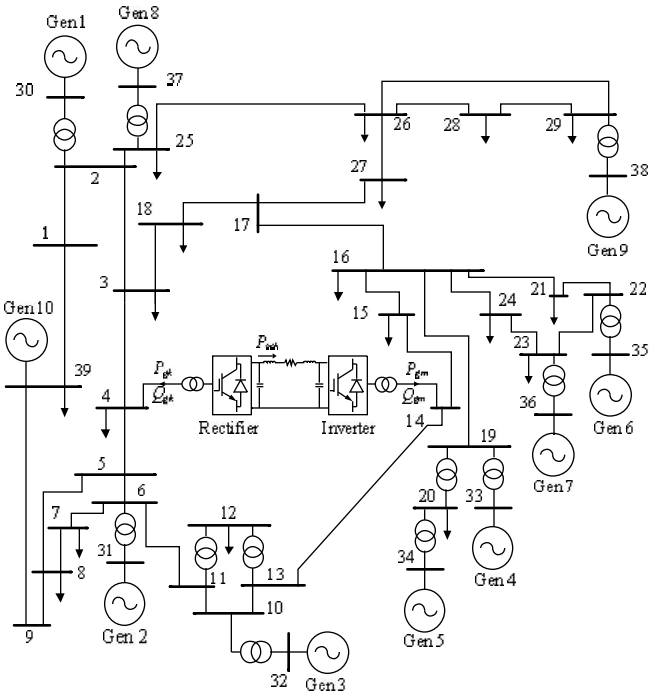

Figure 5.21 New England test system with embedded VSC-HVDC link

During steady-state conditions, the rectifier station delivers 153.291 MVAr to the network so as to uphold its target voltage magnitude with a modulation index of 0.8484, whereas the inverter station operates with a modulation index of 0.8412, injecting 27.3 MVAr to the grid. In the case of the power flowing through the HVDC system, the active power entering the rectifier station stands at 100.869 MW and the active power leaving the inverter station takes a value of 99.667 MW. It is clear that the difference between these two powers is the total power loss incurred by the HVDC system, including the power loss in the DC cable. Taking as a reference the nominal apparent power of each converter, the total power losses stand at 0.4% of which 0.29% corresponds to the rectifier station and 0.104% to the inverter station whilst the power loss produced by Joule's effect in the DC cable stands at 0.006%, recalling that its magnitude is dependent on the length of the DC transmission line. Table 5.7 shows the main VSC-HVDC results as given by the steady-state power-flow solution with which the dynamic simulation is started.

Table 5.7 VSC-HVDC results given by the power-flow solution

Converter	P_{gk} , P_{gm} (MW)	Q_{gk} , Q_{gm} (MVAr)	E_{dc} (p.u.)	m_a	ϕ (deg)	B_{eq} (p.u.)	OLTCs tap	P_{loss} (MW)
Rectifier	-100.869	153.291	1.0002	0.8484	-3.7380	1.2433	1.0252	0.8697
Inverter	99.667	27.300	1.0000	0.8412	7.9373	-0.0062	1.0044	0.3124

Using the information of Table 5.7, it is a starighforward matter to proceed with the calculation of the initial values for the control variables taking part in the dynamics of the VSC-HVDC link, as shown in Table 5.8; these values of the state variables are employed to initialise the dynamic simulation where the modified test network is assumed to undergo the same disturbance as that of the original network, that is, the transmission lines connecting nodes 25-2, 2-3 and 3-4 are tripped at t=0.1 s.

Table 5.8 Initial values of the STATCOM variables for the dynamic simulation

E_{dcI} (p.u)	I_{dclaux} (p.u)	γ_{Raux} (rad)	dm_{aR}	dm_{aI}
1.000	0.4999	0.0232	0.0	0.0

Figure 5.22 shows the voltage magnitudes at several nodes following the change in the topology of the power network. During the transient period, the target voltage set point is achieved very quickly by the action of the AC-bus voltage controllers that regulate the modulation indices of the converters, as shown in Figure 5.23. The prompt action of both controllers leads to a rapid reactive power injection at both converters' AC terminal, as seen in Figure 5.24, resulting in a very effective damping of the voltage oscillations, enabling a smooth voltage recovery throughout the grid.

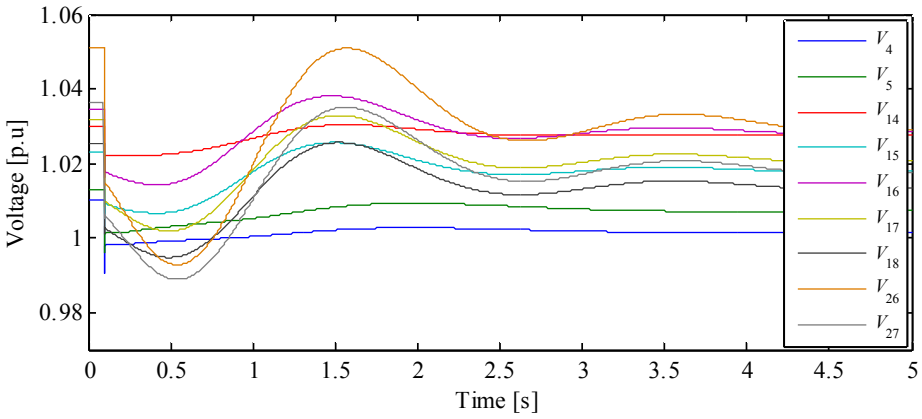

Figure 5.22 Voltage performance at different nodes of the network

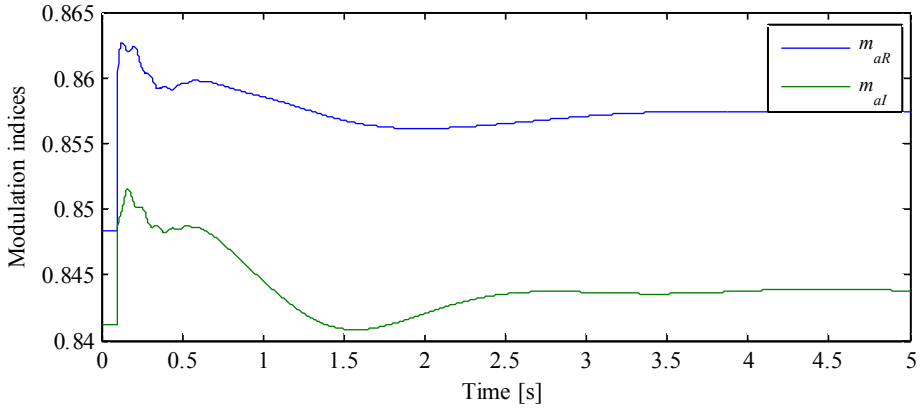

Figure 5.23 Dynamic behaviour of the modulation indices

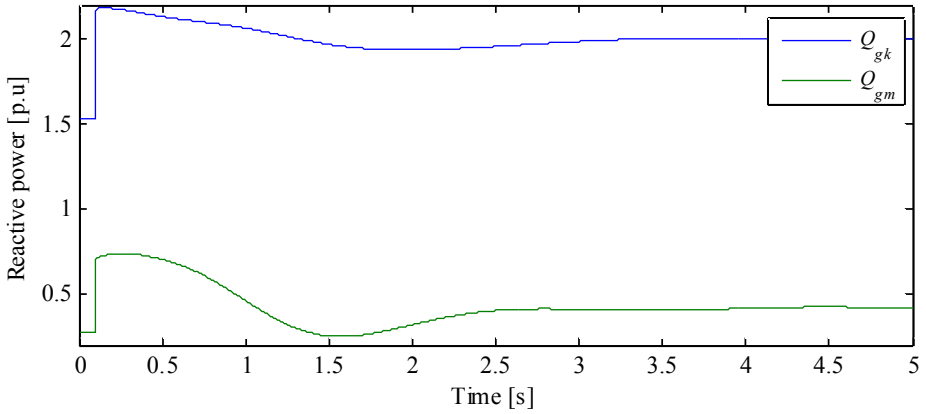

Figure 5.24 Reactive power generated by the VSCs of the HVDC link

The disturbance occurs in the AC system breaks the power balance in the DC link and the voltage sags that take place at both converters' AC terminal reduce the power being transferred through the DC link. Accordingly, the current of the rectifier I_{dcR} drops abruptly from 0.4999 p.u. to 0.4849 p.u., as illustrated by the blue line in Figure 5.25. A momentary mismatch between both converters DC currents is then produced because the DC current cannot be instantly re-established due to the time constants involved in the current controller of the inverter station; as a result, DC voltage oscillations take place, as shown in Figure 5.26. Nevertheless, once this controller takes action in response to the DC voltage variations, the current I_{dcI} starts following the DC current of the rectifier I_{dcR} to compensate for the voltage drop, as shown in Figure 5.25. This enables a speedy recovery of the DC link voltages. It should be remarked that given that the cable resistance is relatively small in this case, so is the voltage drop along the DC transmission line.

Notice the differences that exist between the performance of the voltages E_{dcR}, E_{dcI} and the voltages E_{dcRx}, E_{dcIx}; the voltage oscillations of E_{dcRx} and E_{dcIx} are smoother due to the damping effect of the DC inductors.

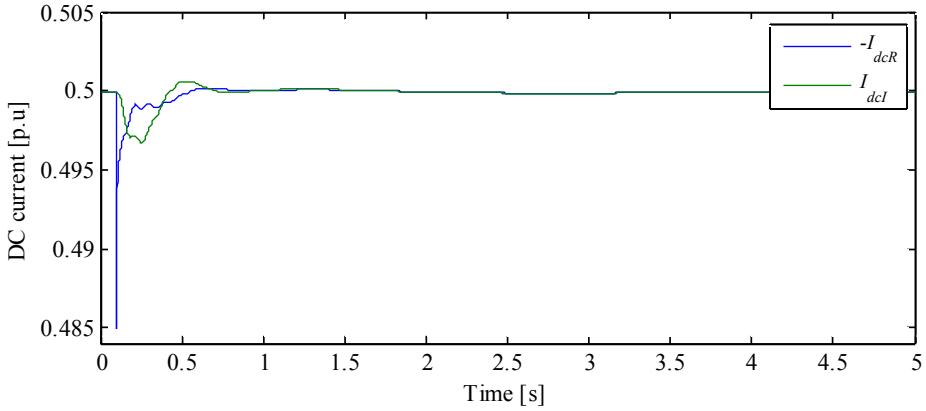

Figure 5.25 DC current behaviour of the rectifier and inverter

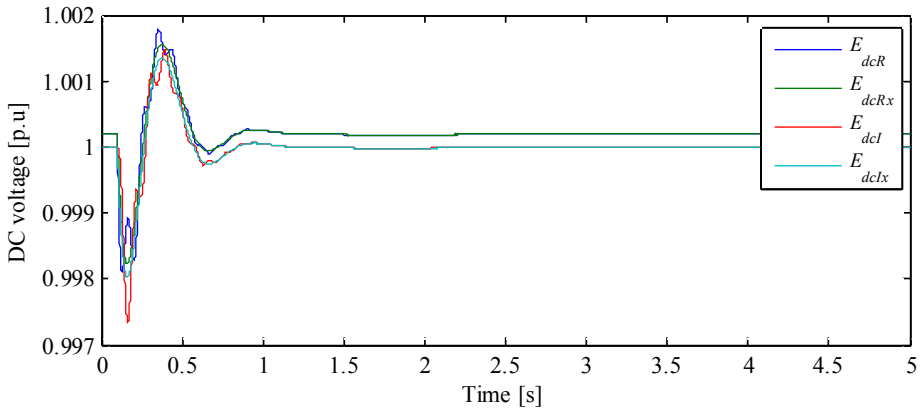

Figure 5.26 DC voltage behaviour of the VSC-HVDC system

The simulation results for the active powers and the DC power transfer through the HVDC link, following the disconnection of the transmission lines, are illustrated in Figure 5.27. The blue line represents the active power entering to the high-voltage side of the OLTC transformer coupled to the rectifier station whereas the green line is the active power leaving the high-voltage side of the OLTC transformer coupled to the inverter station. The difference between both powers represents the total power losses incurred by the VSC-HVDC link, including those incurred by the DC link. The DC power transfer P_{dcR} is also shown in the same graph. Since the voltage and current controls have been proven to operate quite efficiently, as illustrated in Figure 5.25 and Figure 5.26, then a fast power recovery is achieved in spite of the relatively severe disturbance occurred in the power network. Given that the power flowing from the rectifier towards the inverter station has been

brought back to its initial target power transfer of P_{sch} = 1.0 p.u., the deviation of the power angle γ_R experiences a marginal increase, as can be seen in Figure 5.28. This is to agree with the new steady-state conditions where different currents and, therefore, active power losses are incurred. Figure 5.28 also shows the performance of the phase-shifting angles for the rectifier and inverter converters. As expected, such angles follow the same pattern as those obtained for the voltage angles of the network at the nodes where the VSC-HVDC system is connected.

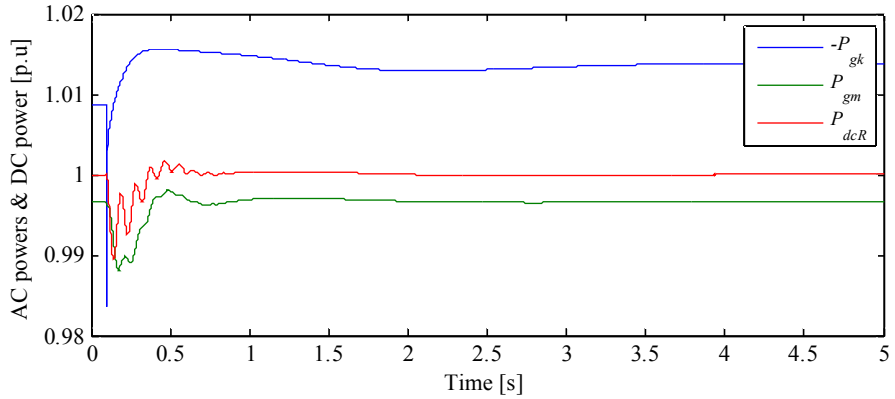

Figure 5.27 AC active powers and DC power behaviour of the HVDC link

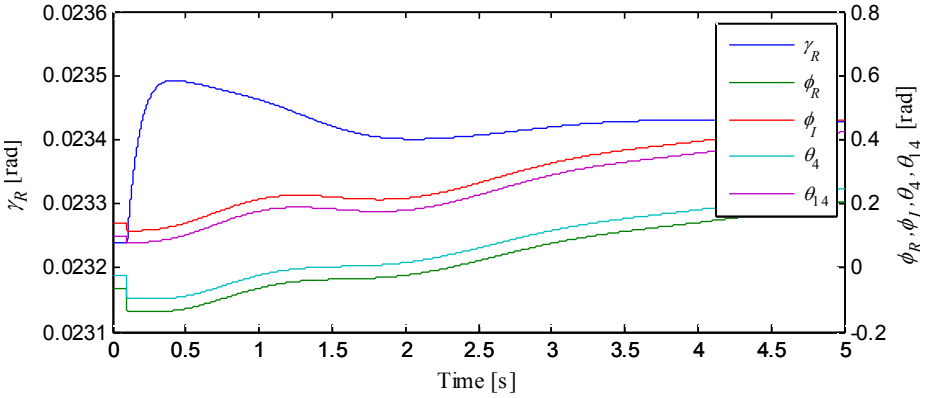

Figure 5.28 Dynamic performance of the various angles involved in the HVDC link

5.2.3 Validation of the VSC-HVDC model providing frequency regulation

The dynamic response of the VSC-HVDC link model with frequency regulation capabilities is compared against a model assembled in the widely-used Simulink environment which uses an EMT-type model. The VSC-HVDC model comparison is carried out using a simple electrical network comprising two independent AC networks which are interconnected through a VSC-HVDC link. The system shown in Figure 5.17 is employed to carry out the validation test. The parameters of the HVDC link are given in Table 5.9. A similar frequency control loop to the one derived in Section 4.2.2 is implemented in the Simulink model to endow it with frequency regulation

capabilities. It should be stated that the two interconnected AC networks possess an idealised, programmable three-phase voltage source each with time-varying parameters permitting the variation of amplitude, phase, frequency and harmonics. From the power system simulation standpoint, they are modelled as swing generators with nominal voltage and frequency of 230 kV and 50 Hz, respectively.

Table 5.9 Parameters of the VSC-HVDC link with frequency regulation capabilities

S_{nom} (p.u)	P_{sch} (p.u)	R_{dc} (p.u)	E_{dcI} (p.u)	G_{0I} , G_{0R} (p.u)	R_I , R_R (p.u)
2.0	0.2	0.02135	1.00	4e-3	0.0
X_I , X_R (p.u)	R_{fI} , R_{fR} (p.u)	X_{fI} , X_{fR} (p.u)	B_{fI} , B_{fR} (p.u)	R_{ltc} (p.u)	X_{ltc} (p.u)
0.0	7.5e-4	0.075	0.40	2.5e-3	0.075
H_c , H_t (s)	K_{pe}	K_{ie}	$K_{p\omega}$, $K_{i\omega}$	K_{maR} , K_{maI}	T_{maR} , T_{maI}
14e-3, 14e-3	2.50	10.0	0.5e-3, 38e-3	25.0	0.02

The initial DC power setpoint of the rectifier station is 20 MW (0.2 p.u.) whilst the inverter is set to control the DC voltage at E_{dcInom} = 1 p.u. The simulation in Simulink is run up to t = 1.0 s in order to reach the steady-state. To assess the dynamic response of the HVDC link in the face of critical frequency deviations, a sudden frequency drop is imposed by the ideal voltage source connected at the AC terminal of the inverter, as shown in Figure 5.29, something expected to occur in low-inertia networks. Figure 5.29 also depicts the dynamic performance of the DC power transfer for both solution approaches; as expected, some differences exist but it is clear that the dynamic response of the proposed RMS-type HVDC model follows well the pattern obtained by the switching-based HVDC model simulated in Simulink.

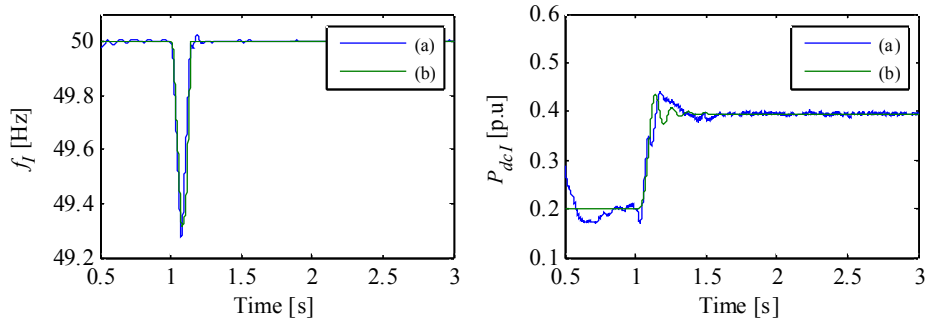

Figure 5.29 Dynamic behaviour of the frequency at the inverter's AC terminal and DC power: (a) Simulink model; (b) Proposed model

The abrupt frequency drop seen by the inverter station is rapidly taken care of by the frequency control loop of the HVDC link. This regulator quickly increases the amount of power drawn from the utility grid connected at the rectifier's terminal. The momentary excess of energy in the DC link gives rise to voltage swells in both E_{dcRx} and E_{dcIx}, as seen in Figure 5.30. However the DC voltage

controller operates very effectively to damp out the oscillations after only a few milliseconds. The dynamic performance of the modulation indices, as obtained with both Simulink and the proposed HVDC link model with frequency regulation capabilities, are shown in Figure 5.30. Both responses follow the same trend, although an exact match was not expected, owing to the very different modelling approaches used in this comparison.

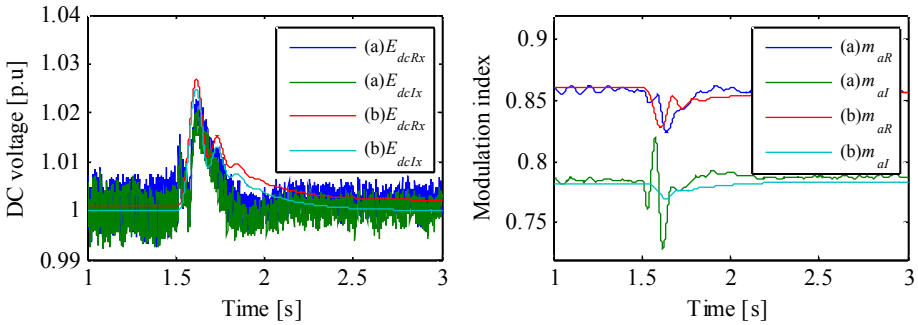

Figure 5.30 Dynamic performance of the DC voltages and modulation indices: (a) Simulink model; (b) Proposed model

The computing times required to simulate the test system using the RMS-type VSC-HVDC model and the EMT-type model are 16.51 s and 160.42 s, respectively. Both solutions agree quite well with each other but the developed RMS-type model outperforms the switching-based model available in Simulink by 10 times, in terms of computing speed. This is mainly due to two reasons: (i) the RMS-type model uses an integration time step of 1 ms whereas a sample time of 7.4074 μs is needed for the EMT-type model in order to ensure a reliable numerical solution, and (ii) the RMS-type model requires only the positive sequence representation of the network whereas a three-phase representation is used in the EMT-type model. Thus the scope of the model introduced in this research work broadens, for instance, when the target is the simulation of larger, more practical networks.

5.2.4 VSC-HVDC link feeding into low-inertia AC networks

Figure 5.31 shows the schematic representation of a 10 MVA VSC-HVDC system interconnecting two independent AC networks operating at 60 HZ, but with very different characteristics. The main utility grid (strong AC network) is represented by the Thevenin equivalent of a large power system with a total demand of 60 GW operating with a lagging power factor of 0.95 which is coupled to a reactive tie of value X_s =0.06 p.u. The low-inertia AC grid (weak network) consists of a 1 MW hydrogenerator, a 2 MW wind turbine and a 7 MVA constant load with a lagging power factor of 0.95.

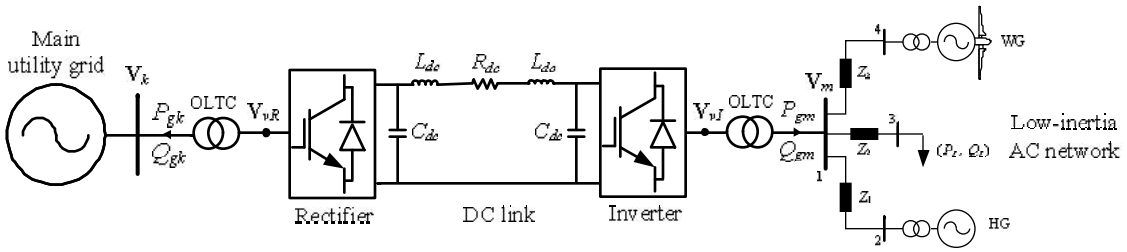

Figure 5.31 VSC-HVDC link feeding into a low-inertia network

The hydrogenerator's synchronous machine is represented by a two-axis model with an inertia constant of 1 ms, resulting in a network with very low inertia. The parameters of the VSC-HVDC and the low-inertia network on a 100 MVA base are given in Table 5.10. The distribution lines parameters are $Z_1 = Z_2 = Z_3$ =0.1+j0.15 p.u.

Table 5.10 Parameters of the VSC-HVDC link feeding into a low-inertia network

S_{nom} (p.u)	R_{dc} (p.u)	E_{dcI} (p.u)	G_{0I} , G_{0R} (p.u)	R_I , R_R (p.u)	X_I , X_R (p.u)
0.1	5.00	1.00	2e-4	0.00	0.10
R_{fI} , R_{fR} (p.u)	X_{fI} , X_{fR} (p.u)	B_{fI} , B_{fR} (p.u)	R_{ltc} (p.u)	X_{ltc} (p.u)	H_c , H_i (s)
0.02	0.60	0.10	0.0	0.50	7e-4,7e-3
K_{pe}	K_{ie}	$K_{p\omega}$	$K_{i\omega}$	K_{maR} , K_{maI}	T_{maR} , T_{maI}
0.05	1.00	15e-4	30e-4	2.50	0.02

The rectifier and inverter stations are set to exert voltage control at their respective AC nodes at 1 p.u. and 1.025 p.u., respectively. From the results furnished by the power-flow solution, it is noticed that to meet the power equilibrium at the weak network, 3.9175 MW are imported from the main utility grid using the DC link. The power injected by the inverter station, which stands at 3.7030 MW, accounts for the power losses incurred in the low-inertia AC network: $P_{gm} + P_g - P_d$ =52.95 kW. The inverter plays the role of a slack generator from the power-flow solution standpoint where the hydrogenerator is treated as *PV* node with the reference angle provided by the inverter which stands at zero, as shown in Table 5.11. During steady-state operation, the power losses incurred by the rectifier and inverter converters are 16.5 kW and 24.4 kW, respectively, whereas the DC link power loss stands at 173.7 kW.

Table 5.11 VSC-HVDC results given by the power-flow solution

Converter	P_{gk} , P_{gm} (MW)	Q_{gk} , Q_{gm} (MVAr)	E_{dc} (p.u.)	m_a	ϕ (deg)	B_{eq} (p.u.)	OLTCs tap
Rectifier	-3.9175	0.1020	1.0466	0.7803	-2.8295	0.0018	1.0007
Inverter	3.7030	3.4375	1.0000	0.8570	0	0.0329	1.0165

To show that the VSC-HVDC link is able to assist low-inertia networks with frequency support, the load is increased by 5% at t = 0.5 s. Two cases are considered, when the HVDC link is set to provide frequency support and when it is not. As a result of the momentary power imbalances, a rearrangement of power flows takes place causing both voltage variations and frequency deviations in the low-inertia network, as shown in Figure 5.32 and Figure 5.33, respectively.

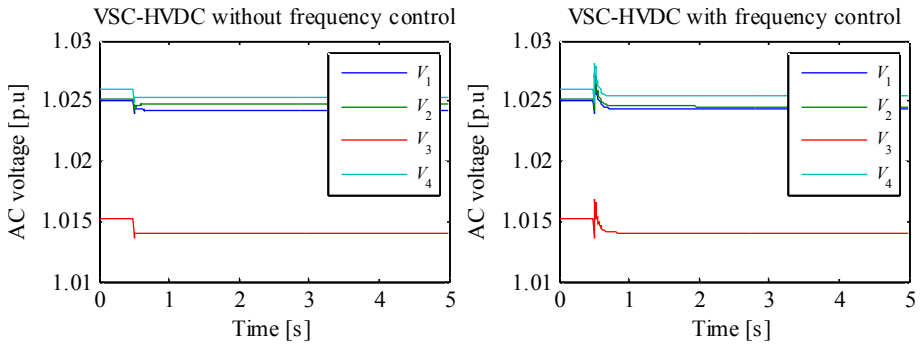

Figure 5.32 Voltage behaviour in the low-inertia network

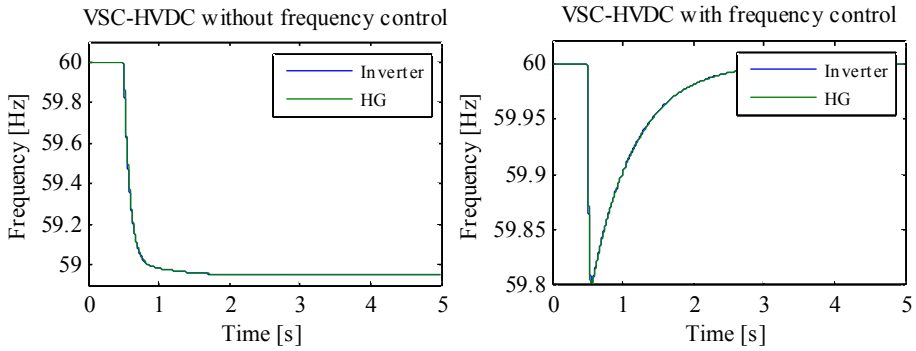

Figure 5.33 Frequency behaviour in the low-inertia network

The simulated event leads to temporary frequency deviations of approximately 1 Hz when the VSC-HVDC does not provide frequency support, given the low inertia of the network, as seen from Figure 5.33. However, when frequency control is carried out via the power converters, the frequency only drops to about 59.8 Hz. It is clear that the amount of power injected P_{gm} to the low-inertia network via the inverter converter helps to mitigate the temporary power imbalances brought about

by the load increase. Figure 5.34 shows the dynamic performance of the powers involved in the VSC-HVDC link. As expected, when the converters do not support the frequency in the low-inertia network, the powers P_{gk} and P_{dcR} are practically constant and there is a short-duration power peak in P_{gm}.

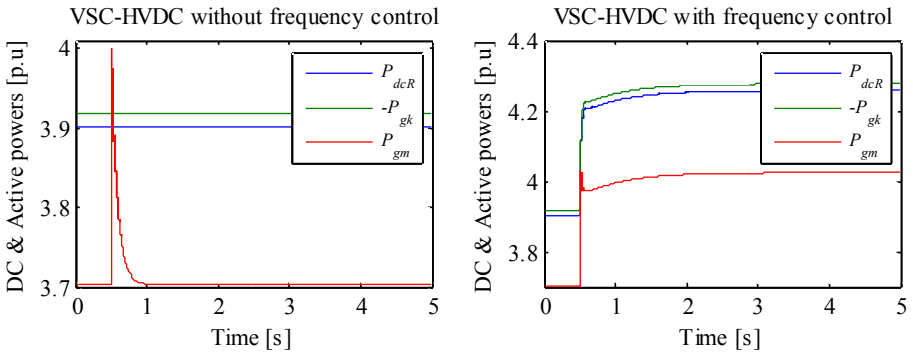

Figure 5.34 Dynamic performance of the AC and DC powers of the HVDC link

As shown in Figure 5.33, the frequency is successfully controlled just after 3 s of the occurrence of the perturbation. This is due to the quick response of both the rectifier and inverter which regulate the angular aperture γ_R and the DC current I_{dcI}, respectively, as shown in Figure 5.35. It should be stressed that although γ_R controls the power being drawn from the main utility grid to provide frequency regulation to the low-inertia AC network, the DC current I_{dcI}, which is responsible for controlling the DC voltage, impacts directly the performance of the DC power P_{dcR}. By examining the performance of DC voltages shown in Figure 5.36, it is observed that the controller takes less time to bring E_{dcI} back to its nominal value than the time required to lead the frequency in the low-inertia network back to its rated value, as shown in Figure 5.33.

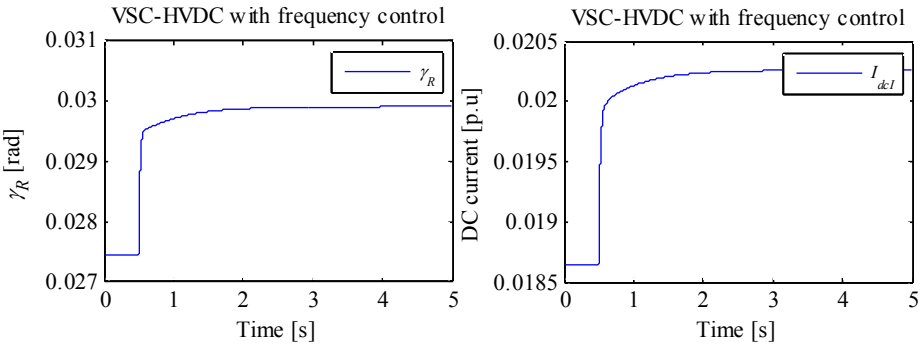

Figure 5.35 Dynamic performance of γ_R and I_{dcI}

On the other hand, small voltage oscillations appear in the low-inertia AC network as a result of the power imbalance, as shown in Figure 5.32. During the transient period, the voltage set point is achieved in a very quick fashion by the action of the AC-bus voltage controllers, that is, the modulation indices, as seen in Figure 5.36. As expected, these controllers are very effective in damping the voltage oscillations, ensuring a smooth voltage recovery throughout the low-inertia network.

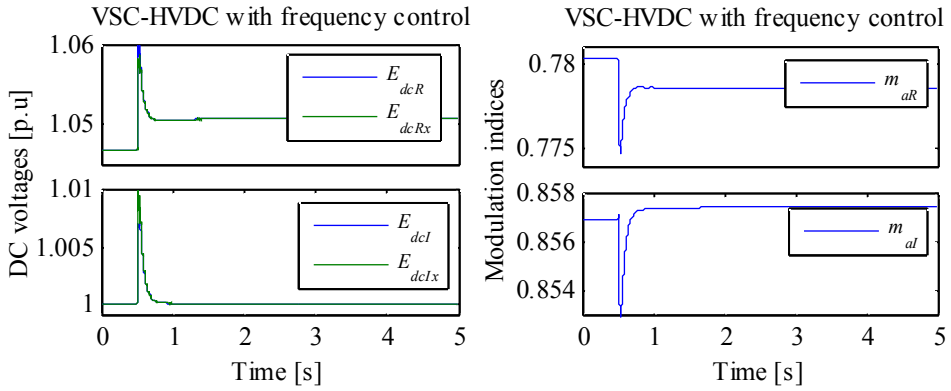

Figure 5.36 Dynamic performance of the DC voltages and modulation indices

Parametric analysis of the frequency control loop gains of the VSC-HVDC link

The VSC-HVDC model developed in this research work is capable of providing frequency regulation to networks with near-zero inertia as it would be the case of a system fitted with only one small hydrogenerator, one wind generator and a fixed load. However, in cases such as the one considered above, the value of the gains corresponding to the HVDC frequency controller plays a key role in determining the frequency behaviour in the low-inertia AC network. To illustrate this, a load increase of 5% occurring at *t*= 0.5 s is assessed for different values of gains in the frequency controller, as shown in Table 5.12.

Table 5.12 Different gain values for the frequency controller

	Scenarios					
Gains	(i)	(ii)	(iii)	(iv)	(v)	(vi)
$k_{p\omega}$	1e-4	15e-4	30e-4	15e-4	15e-4	15e-4
$k_{i\omega}$	25e-4	25e-4	25e-4	10e-4	30e-4	50e-4

Figure 5.37 shows the dynamic performance of the frequency in the low-inertia network for different values of the frequency control loop gains, $k_{p\omega}$ and $k_{i\omega}$. In cases (i) to (iii), the proportional gain $k_{p\omega}$ is increased whilst the integral gain $k_{i\omega}$ is kept constant; it stands out that the frequency

f_1 improves in terms of what would be called the inertial response of the low-inertia network, with the frequency deviation, just after the disturbance, narrowing from 0.56 Hz to 0.12 Hz. On the other hand, for cases (iv) to (vi), $k_{p\omega}$ is kept constant whilst $k_{i\omega}$ increases gradually. This results in improvement in what is termed the primary frequency response given that a faster frequency recovery is achieved when increasing $k_{i\omega}$. Notice that for the simulated cases, the smaller the frequency deviations the bigger the DC voltage offsets, as can be appreciated from Figure 5.37. This is due to the fact that the required power to bring back the frequency to its nominal value is injected faster to the network causing relatively larger overvoltages in the DC link.

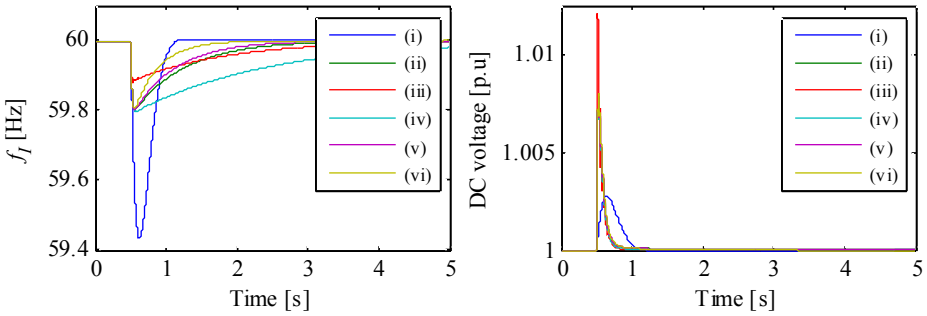

Figure 5.37 Frequency in the low-inertia network and DC voltage of the inverter for different gains of the frequency control loop

5.3 Multi-terminal VSC-HVDC-upgraded power systems

5.3.1 Validation of the multi-terminal VSC-HVDC dynamic model

The three-terminal VSC-HVDC system, shown in Figure 5.38, is used to carry out a comparison of the developed RMS-type model against an EMT-type model assembled in the simulation package Simulink. With no loss of generality, the AC sub-networks connected to VSC_{Slack} and VSC_{Psch} are represented by equivalent networks (2000 MVA, 230 kV, 50 Hz), whereas the passive network fed by VSC_{Pass} is represented by a 50 MW load. Each VSC comprising this multi-terminal HVDC system is rated at 200 MVA, ±100 kV DC. The resistance of the DC cables, R_{dc4}, R_{dc5} and R_{dc6}, carries a value of 1.39×10^{-2} Ω/km, with each cable having a length of 75 km, 100 km and 150 km, respectively. The rest of the parameters, given on a 100 MVA base, are shown in Table 5.13.

Table 5.13 Parameters of the three-terminal VSC-HVDC link

Parameters of each VSC	S_{nom} (p.u)	G_0 (p.u)	R (p.u)	X (p.u)	R_f (p.u)
	2.0	4e-3	0.0	0.0	7.5e-4
	X_f (p.u)	B_f (p.u)	R_{ltc} (p.u)	X_{ltc} (p.u)	H_c , H_i (s)
	0.075	0.40	2.5e-3	0.075	14e-3, 14e-3
Gains	K_{pe} , K_{ie}	K_{pp} , K_{ip}	$K_{p\omega}$, $K_{i\omega}$	K_{maR} , K_{maI}	T_{maR} , T_{maI}
VSC_{Slack}	1.5, 15	---	---	50.0	0.20
VSC_{Psch}	–-	0.0, 5.0	---	50.0	0.20
VSC_{Pass}	–-	---	0.025, 0.25	50.0	0.20

Initially the slack converter VSC_{Slack} controls its DC voltage at E_{dcnom} = 1 p.u., the converter VSC_{Psch} controls its DC power at P_{sch} = 150 MW and the converter VSC_{Pass} feeds the 50 MW load, with the three converters controlling the reactive power flow to a null value, i.e., $Q_v^{ref}=0$. The simulation in Simulink is run up to t = 1.5 s to reach the steady-state conditions. In order to put the converters through their paces at what they are responsible for, the following step changes in parameters are applied: (i) a 50 MW reduction of the scheduled power of the converter VSC_{Psch} is applied at t = 1.5 s, and (ii) the load fed by the converter VSC_{Pass} is increased by 40% (20 MW) at t = 3 s.

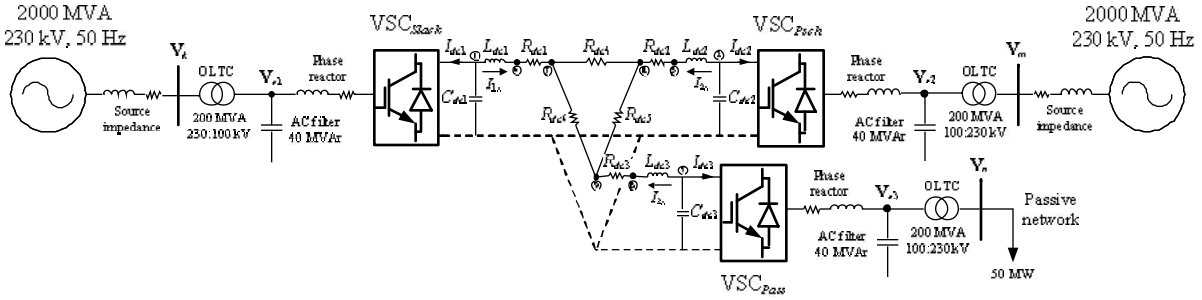

Figure 5.38 Three-terminal VSC-HVDC link used to carry out the validation test

As expected, both disturbances cause voltage variations in the DC network, as shown in Figure 5.39, but the slack converter fittingly controls the voltage at its corresponding DC bus, benefiting also the voltages at the DC bus of the converters VSC_{Psch} and VSC_{Pass}. It is noticed that the pattern of the dynamic response of the developed RMS-type multi-terminal VSC-HVDC model follows quite well the obtained using the EMT-type model simulated in Simulink.

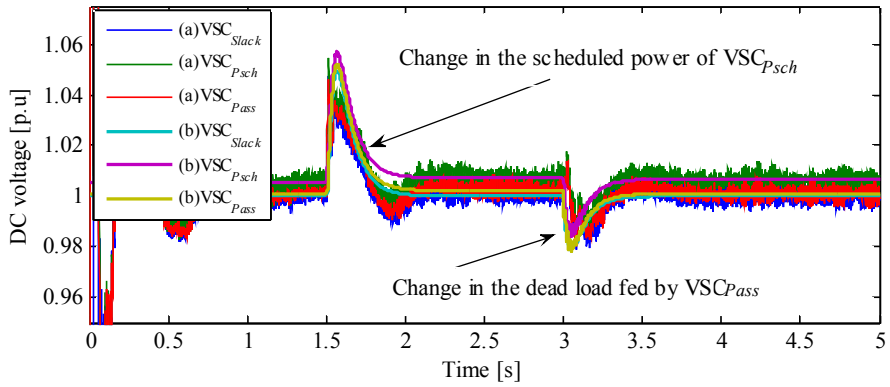

Figure 5.39 DC voltages of the VSCs comprising the three-terminal VSC-HVDC link. (a) Simulink model; (b) Developed model

As expected, the power reduction of 50 MW in P_{sch} of the converter VSC$_{Psch}$ produce larger DC voltage offsets than those experienced by the power increase of 20 MW in the load fed by the converter VSC$_{Pass}$. These DC voltage deviations affect the DC power performance of the three converters, as seen from Figure 5.40. It is noticed that some momentary power peaks computed by the Simulink model during the applied step changes are not captured by the calculations carried out by the developed RMS-type model. This is an expected situation due to the two very different solution approaches and models. However, the rest of the DC power responses follow the same trend reasonably well.

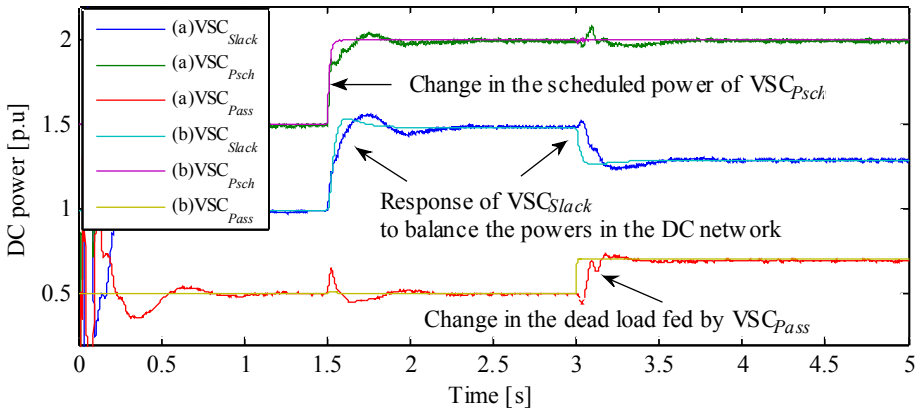

Figure 5.40 DC power behaviour at the DC bus of the three VSCs. (a) Simulink model, (b) Developed model

The conclusions drawn from the dynamic behaviour of the DC voltages and DC powers may be directly applied to the dynamic response of the modulation indices, shown in Figure 5.41. The most noticeable differences appear by the time the change in load fed by the converter VSC$_{Pass}$ is im-

posed, i.e., the oscillations of the modulation index of VSC_{Pass} are slightly greater than those obtained by the same converter of the RMS-type multi-terminal VSC-HVDC link. Notwithstanding this fact, the overall dynamic responses between the two multi-terminal VSC-HVDC models are comparable. Furthermore, the developed multi-terminal VSC-HVDC model, together with its solution approach, outperforms by more than 8 times the EMT-type model, in terms of computing time, since 1.04 min and 8.5 min were required to solve the three-terminal VSC-HVDC system, respectively.

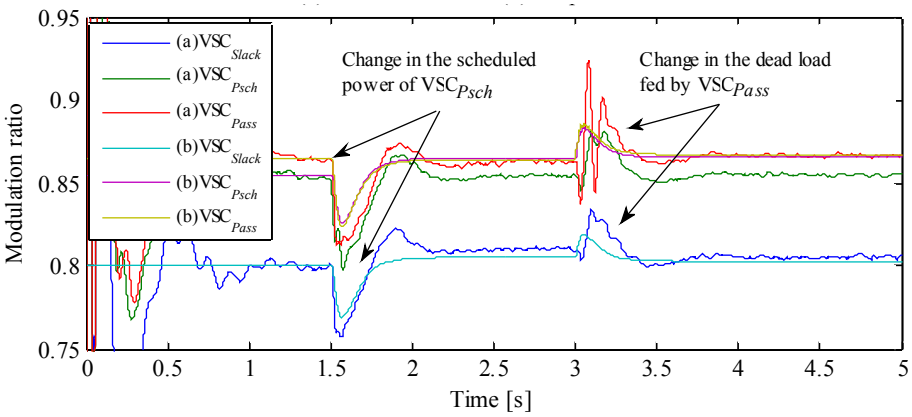

Figure 5.41 Modulation ratio of the three VSCs. (a) Simulink model; (b) Developed model

5.3.2 Multi-terminal VSC-HVDC link with a DC ring

The six-terminal VSC-HVDC network, shown in Figure 5.42, is used to illustrate the suitability of the new multi-terminal VSC-HVDC model for power system dynamic simulations. It is meant to signify a stage of development of the undersea power grid in the North Sea (Vrana et al., 2010; Hertem and Ghandhari, 2010; Orths et al., 2012). The AC networks 1, 3 and 5 are taken to represent the UK Grid, the NORDEL Grid and the UCTE Grid with total power demands of 60 GW, 30 GW and 450 GW, respectively. For the purpose of this illustrative test case and with no loss of generality for the frame-of-reference presented in this work, these AC power networks are represented by their Thevenin equivalents coupled to reactive ties. The equivalent is determined as shown in (5.1) where a power factor pf =0.95 is selected.

$$R_{th} + \mathrm{j}X_{th} = \left[P\left(1 + \mathrm{j}\tan\left(\cos^{-1}\left(pf\right)\right)\right)\right]^{-1} \tag{5.1}$$

The network AC_2 represents the in-feed point of the Valhall oil platform which lies 294-km away from the Norwegian coast with a power demand of 78 MW. The buses of networks AC_4 and AC_6

represent the collector points of the wind parks at the German Bight and Dogger Bank. The former is a wind park that lies 100 km off the German coast and comprises 80 5-MW wind turbines, being 400 MW its total power injection. The latter lies 100 km off the east coast of England where permission has been granted for a 7.2 GW of wind generation development; for the purpose of this test case a power injection of 400 MW is assumed.

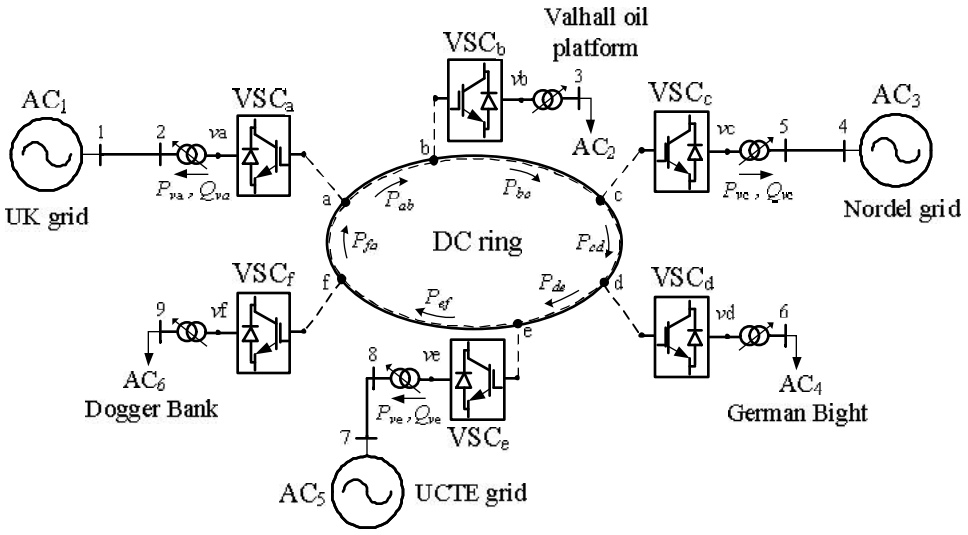

Figure 5.42 Schematic representation of a multi-terminal VSC-HVDC link with a DC ring

Table 5.13 gives the parameters in per-unit values of the VSCs, DC ring cables, Thevenin equivalents and the reactive ties for systems AC_1, AC_3 and AC_5. The 1600 km length submarine cables comprising the DC ring are taken to be rated at ±160 kV with a resistance value of 0.02 Ω/km. The nominal power of each converter is 500 MVA.

Table 5.14 Parameters of the VSCs, AC_1, AC_3, AC_5 and DC networks

VSCs and OLTCs				
G_0 (p.u)	$R + \mathrm{j}X$ (p.u)	B_f (p.u)	$R_f + \mathrm{j}X_f$ (p.u)	X_{ltc} (p.u)
0.01	1e-4+ j0.001	j0.20	0.0015+j0.15	0.006+j0.06
AC Networks				
Network	V_{th} (p.u)	R_{th} (p.u)	X_{th} (p.u)	Tie line (p.u)
AC_1	1.00	1.504e-3	4.943e-4	X_s = 0.06
AC_3	1.00	3.0e-3	9.887e-4	X_s = 0.06
AC_5	1.00	2.005e-4	6.591e-5	X_s = 0.06

Length (km) and resistance of the DC ring sections (p.u)						
	a-b	b-c	c-d	d-e	e-f	f-a
Length	300	300	250	200	300	250
R_{dc}	0.0058	0.0058	0.0048	0.0039	0.0058	0.0048

The VSC_a is selected to be a converter of type VSC_{Slack} providing voltage regulation at its DC bus at E_{dcnom} = 1 p.u. The stations VSC_c and VSC_e are modelled as converters of type VSC_{Psch} and set to draw each 250 MW from the DC ring. The stations VSC_b, VSC_d and VSC_f are modelled as converters of type VSC_{Pass}. The OLTC transformers are set to uphold the voltage magnitude at their high-voltage buses at 1.05 p.u. and 1 p.u. for (VSC_a, VSC_c, VSC_e) and (VSC_b, VSC_d, VSC_f), respectively.

The power flow simulation results are provided in Tables 5.14, 5.15 and 5.16. As expected, the convergence to tolerances of 10^{-6} and 10^{-12} were reached in 4 and 5 iterations, respectively, this being the hallmark of a true unified iterative solution using the power flow Newton-Raphson method. Table 5.14 gives the values of the state variables of the VSCs. Power is injected into the DC ring through converters VSC_d and VSC_f and their respective DC voltages are higher than the reference voltage provided by VSC_a. The angle φ of the converters VSC_b, VSC_d and VSC_f have been kept at zero since these converters provide the angular references for networks AC_2, AC_4 and AC_6. As shown in Table 5.15, the voltage phase angles at these nodes are displaced by -1.4316° and 7.3180°, respectively. There is a marked difference between the modulation indices of the group of converters (VSC_a, VSC_c, VSC_e) and the group of converters (VSC_b, VSC_d, VSC_f), owing to the different voltages selected for each group.

Table 5.15 State variables solution for each VSC

	VSC no/type	E_{dc} (p.u.)	m_a	φ (deg)	OLTCs tap	P_{loss} (MW)
a	VSC_{Slack}	1.0000	0.8567	11.3806	1.0127	0.7641
b	VSC_{Pass}	0.9998	0.7927	0.0000	1.0009	0.3029
c	VSC_{Psch}	0.9998	0.8573	13.4952	1.0129	1.0699
d	VSC_{Pass}	1.0005	0.8012	0.0000	0.9963	3.1377
e	VSC_{Psch}	1.0002	0.8600	13.4811	1.0143	1.0684
f	VSC_{Pass}	1.0006	0.8011	0.0000	0.9963	3.1383
Convergence: ε=10^{-6} takes 4 iterations and ε=10^{-12} takes 5 iterations						

The power loss incurred by each VSC is also reported in Table 5.14. Converters VSC_d and VSC_f are the stations that incur more power loss whereas VSC_b is the unit that incurs less power loss since this converter is the one that draws less power from the DC ring. The nodal voltages, active and reactive powers injected at each AC network terminals are reported in Table 5.15. It should be noticed that more than 90 MVAr are injected through the OLTC transformers of VSC_a, VSC_c, VSC_e to uphold the target values of 1.05 p.u. at AC_1, AC_2 and AC_3, respectively. Given that VSC_c and VSC_e are set to draw each 250 MW from the DC ring, the remaining amount of power that flows through VSC_a towards AC_1 stands at 212.2746 MW.

Table 5.16 Voltages and injected powers at the AC networks

Network	V (p.u.)	θ (deg)	P_{inj} (MW)	Q_{inj} (MVAr)
AC_1	1.05	6.8625	209.7336	94.0067
AC_2	1.00	-1.9359	78.0000	0.0000
AC_3	1.05	8.1370	248.1699	91.2079
AC_4	1.00	9.7335	-400.000	0.0000
AC_5	1.05	8.1492	248.1436	104.2285
AC_6	1.00	9.7335	-400.000	0.0000

The scheduled power control of a converter VSC_{Psch} is applied at its DC bus; hence, the power delivered at its AC terminal is expected to be smaller than its corresponding scheduled power owing to the losses incurred in the converter. In this test case, the powers delivered to AC_3 and AC_5 stand at 248.7249 MW and 248.6736 MW, respectively. Also it should be noticed that the power injected at AC_4 and AC_6 carry a negative sign which correctly account for the fact that the powers generated by the wind parks are being injected into the DC ring. The opposite occurs for the case of the oil platform which draws power from the DC grid at the AC_2 network's terminals.

The power flows in the DC ring are listed in Table 5.16. It is noticed that the ring sectors that are the most heavily loaded are the cables connected between nodes c-d and f-a, with each carrying approximately 269 MW and 272 MW, respectively. Conversely, the cable sections of the DC ring that carry less power are the sections a-b and b-c since they link to converter VSC_b which, in turns, is the converter that draws less power from the DC ring. The total power loss in the DC ring stands at 2.19 MW.

Table 5.17 Power flows in the DC ring

DC cables		P_{dc} (MW)		P_{loss}
		(send – rec)	(rec – send)	(MW)
a	b	59.0374	-59.0272	0.0101
b	c	-19.3486	19.3497	0.0010
c	d	-269.3497	269.5239	0.1741
d	e	125.4183	-125.3877	0.0306
e	f	-124.6122	124.6572	0.0450
f	a	270.2843	-270.1092	0.1751

The DC transmission line that connects the nodes d and e, which carries 126 MW at steady-state, trips at t = 0.5 s. This disturbance causes the DC ring to open, converting it into a lengthwise DC grid. In order to redistribute the power flows in the longitudinal DC network, the DC voltages are readjusted as shown in Figure 5.43. The DC voltage of the slack converter is fittingly controlled and so are the rest of the DC voltages. Accordingly, the power imbalances throughout the DC grid are mitigated promptly in no more than a few miliseconds, as shown in Figure 5.43.

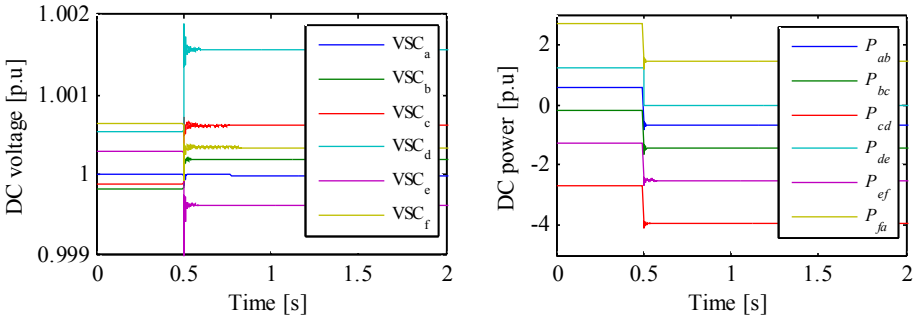

Figure 5.43 Converter's DC voltage and power flows in the DC grid

The dynamic behaviour of the modulation ratio of the converters is shown in Figure 5.44, where it is noticed that only a small readjustment took place after the disconnection of the DC transmission line. This is so to conform to the post-disturbance voltages obtained in the longitudinal DC network. The frequency of the passive networks fed by the converters VSC_b, VSC_d and VSC_f are also reported in Figure 5.44. It stands out that the disturbance in the DC grid does not impose severe affectations on the operation of the island AC networks being fed by the corresponding converters.

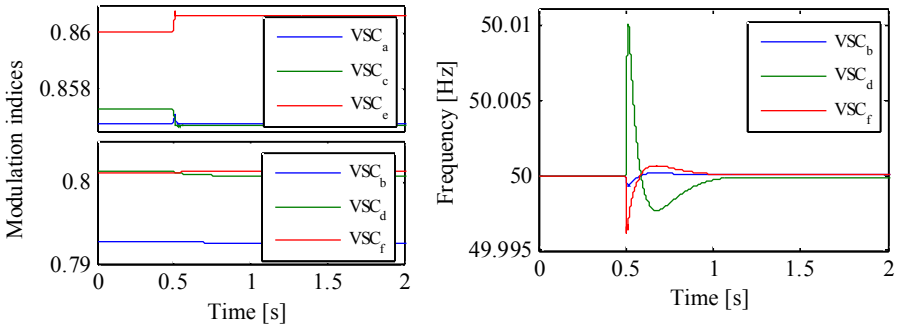

Figure 5.44 Modulation ratio of the VSCs and frequency of the passive networks fed by VSC_b, VSC_d, VSC_f.

5.4 Conclusions

Various case studies of the developed steady-state and dynamic models of the STATCOM, point-to-point and multi-terminal VSC-HVDC links have been presented in this Chapter. The dynamic response of the STATCOM and point-to-point HVDC link has been comprehensively investigated using a test network widely-used in academic circles such as the New England test system which comprises 39 nodes. Furthermore, the model of the point-to-point HVDC link itself has been compared, in terms of the dynamic behaviour of its main state variables, against an EMT-type, switch-

ing-based model for two different applications; one where the VSC-HVDC link is used to maintain a scheduled DC power transfer and the other where the VSC-HVDC link is providing frequency support to low-inertia AC networks. In both cases, it was corroborated that the models are suitable for conducting both steady-state and dynamic simulations since the state variables' dynamic response of the developed models and those of the EMT-type models agree well with each other. The conclusions drawn from these validation tests were very much the same when a comparison of a three-terminal VSC-HVDC system using the developed modelling framework was carried out against an EMT-type model assembled in Simulink. However, it was also revealed that very significant time reductions are obtained when using the proposed RMS-type models developed in this research work. Undoubtedly, both situations are the result of the comprehensive VSC models together with their suitable control strategies and the adopted phasorial approach together with the unified frame-of-reference which is the computing engine that permits an efficient numerical solution of the models.

6 General conclusions and future research work

6.1 General conclusions

The research work reported in this thesis advances current knowledge in the modelling of the STATCOM, back-to-back and point-to-point VSC-HVDC links and multi-terminal VSC-HVDC systems aimed at power flows and time-domain, dynamic simulations of electrical power systems. The starting point is the development of a comprehensive model of the VSC, this being the basic building block with which the STATCOM, two-terminal and multi-terminal VSC-HVDC links are assembled. These models are useful to carry out steady-state and dynamic simulations of AC/DC networks, with the AC networks represented by their positive-sequence equivalents, using phasorial information.

From the outset, the emphasis of the research work was placed on the realisation of a VSC model which would capture the essential steady-state and dynamic characteristics of the actual equipment. This required a fundamentally different modelling approach to the classical VSC representation which uses an idealised controllable voltage source (or current source) and quite clearly, do not possess an explicit DC node. To circumvent this problem, the VSC model put forward in this research uses a compound phase-shifting transformer and an equivalent shunt admittance with which key control properties of PWM-based converters may be linked. The phase-shifting transformer decouples, angle-wise, the circuits connected at both ends of the ideal complex transformer in such a way that a notional DC side and AC side of the converter model are created. The equivalent shunt admittance is responsible for the VAR absorption/generation process of the converter to provide, for instance, voltage control during steady-state operation. This two-port circuit of the VSC, with its DC and AC sides explicitly available, results in a flexible building block which underpins, in quite a natural manner, the back-to-back, point-to-point and multi-terminal VSC-HVDC systems for cases of both, steady-state and dynamic operating regimes. This has resulted in a number of key improvements in the VSC's representation: (i) the switching and conduction losses are included in

the model in quite a natural manner; (ii) the tap magnitude of the phase-shifting transformer is directly associated to the amplitude modulation index of the converter; (iii) the DC bus of the converter may be directly connected to, say, another VSC, back-to-back, or by using the model of a DC cable giving rise to a point-to-point VSC-HVDC configuration; (iv) in fact, any number of these converter models may be interlinked with ease at their DC buses, to constitute a multi-terminal VSC-HVDC scheme. Moreover, the VSC model was made more realistic by adding an AC phase reactor, an AC filter capacitor and an interfacing OLTC transformer on its AC side and, on its DC side, a shunt capacitor and a series smoothing inductor with its resistive part included. The full model of the VSC unit and, by extension, its derived formulations, yields a realistic representation of this equipment even though they are lumped-type models. Their steady-state and dynamic responses compare well with the responses of the more-detailed, switching-based models available in EMT-type simulation programs such as Simulink.

A great deal of research effort was paid to the modelling of the back-to-back and point-to-point VSC-HVDC links, to incorporate realistic control mechanisms. Each one of these two-terminal VSC-HVDC models was endowed with four degrees of freedom, a feature that conforms well with actual installations, i.e., simultaneous voltage control on the two AC terminals, DC bus voltage regulation and regulation of the transmitted power through the DC link. The VSC-HVDC link was modelled bearing in mind the standard HVDC application of transmitting a scheduled DC power transfer, the steady-state and dynamic operating regimes were considered. This was followed by adapting the model to encompass the particular application when the VSC-HVDC link feeds into passive, near-zero inertia AC networks; the aim was to provide frequency support to weak AC networks and, accordingly, power flows and dynamic simulations were considered. It should be brought to attention that its effective participation in frequency regulation was possible owing to the frequency control scheme in use, which is based on the regulation of the angular aperture that exists between the internal phase-shifting angle of the rectifier and the voltage angle at its AC terminal. This was amenable to power flow regulation in the DC link and, hence, to frequency control in the supported AC network, where it was shown that the inverter acts as a virtual synchronous generator, with its AC bus playing the role of the reference node for all the other nodes in the low-inertia AC network. The control scheme was comprehensively investigated using a wide range of gains of the frequency controller, demonstrating its great effectiveness owing to the fast speed of response of the rectifier station of the VSC-HVDC link, which is in the range of a few milliseconds.

These developments were taken as springboard to tackle the most challenging topic of multi-terminal VSC-HVDC systems, where a generalised frame-of-reference has emerged that greatly improves on existing multi-terminal VSC-HVDC models. The proposed frame-of-reference to carry out steady-state and dynamic solutions of multi-terminal VSC-HVDC systems uses a modular building block which represents the fundamental-frequency operation of a VSC unit. The dynamic frame-of-reference is fitted with three different VSC dynamic models (control strategies) applicable

to each pairing AC sub-network, namely, the slack converter whose aim is to control its DC voltage, the scheduled-power converter which injects a scheduled amount of power and the passive converter which is connected to an AC network with no frequency control equipment. The model of the multi-terminal VSC-HVDC system was tested using a three-terminal scheme and a six-terminal scheme. The former was used to carry out a comprehensive comparison against an EMT-type model exhibiting similar characteristics, to demonstrate that the RMS-type model resembles to switching-based models in terms of the accuracy of its internal variables' responses for the steady-state and dynamic operating regimes. The larger multi-terminal VSC-HVDC system has demonstrated the principle that this new framework is suitable for solving AC/DC power systems where a single or multiple perturbations at any of the AC networks or at the DC network may occur.

Concerning the numerical solution of these models, the Newton-Raphson method was used as the computing engine with which the whole set of algebraic and discretised differential equations were solved, for efficient iterative solutions of the steady-state and operating regimes. The modelling approach used to encompass the STATCOM, back-to-back and point-to-point HVDC links and multi-terminal HVDC systems was a unified framework; one that suitably accommodates and solves, in a simultaneous manner, all the equations resulting from the VSC-based devices together with the AC sub-networks. The flow chart presented in Chapter 3, Fig. 3.8, summarizes the adopted modelling approach for the RMS-type models of the STATCOM and VSC-HVDC models for both variants steady-state and dynamic operating regimes. In general terms and using case studies, it has been demonstrated that the new framework enables the comprehensive assessment of the main operational variables of the VSC-FACTS and VSC-HVDC equipment as well as the study of the impact of these equipment on the AC and DC networks.

6.2 Future research work

The applicability of the STATCOM, back-to-back, point-to-point and multi-terminal VSC-HVDC models put forward in this research work, has been demonstrated in terms of power-flow studies and time-domain, dynamic simulations of power systems. It should be expected that given the high modularity exhibited by these models, they would be extended to enable their implementation into other power system analysis tools. For instance:

i. Economic dispatch (ED) and optimal power flows (OPF) are two interrelated tools used to allocate the optimal amount of power that each dispatchable generating unit supplies to the network to ensure minimum generation costs bearing in mind physical and operational constraints. It is envisaged that the conventional ED and OPF algorithms would need upgrading in order to incorporate VSC-HVDC models of the two-terminal and multi-terminal kinds. This would enable

the study of energy transactions between different AC systems interlinked in an asynchronous manner.

ii. State estimation of power networks is an application tool that enables the reconstruction of the state of the whole system, at a given point in time, using partial information coming from in situ measurement devices. This tool employs positive-sequence, power flow-type models of synchronous generators, wind generators, induction machines, transmission lines, FACTS devices, etc., to carry out the corresponding state estimations of the power system. In this context, the steady-state models of the STATCOM and VSC-HVDC systems put forward in this research work could be used directly to carry out state estimation of AC/DC power networks. Hence, it is envisaged that the weighted least square method (WLS) could be used, as an initial approach, to carry out state estimation of AC/DC power systems which would represent a valuable tool aimed at preserving the stability of the whole system.

iii. The controllability of active power carries high priority in the daily operation of an electrical network; its impact on electrical frequency is direct. Hence, the models of the two-terminal and multi-terminal VSC-HVDC links could be upgraded to investigate if it is feasible to connect at any point of the DC network a battery energy storage system. Such a hybrid system has the potential to provide frequency support to AC networks with embedded VSC-based equipment.

iv. The overall steady-state and dynamic models of the STATCOM and VSC-HVDC systems are based on power injections (as opposed to current injections), and their solution is carried out, together with the rest of the power system, using a unified frame-of-reference and Newton's method. The Jacobian matrix is readily available at any point in time and this opens a window of applications for the all-important power systems studies of eigenvalue tracking, dynamic sensitivity analysis and evaluation of dynamic stability indices. This may be of particular interest to power systems analysts concerned with the security and reliability of the electrical network.

References

ABB review special report, special report – 60 years of HVDC (2014). ABB technology Ltd Zurich/Switzerland 2014.
URL:
https://library.e.abb.com/public/aff841e25d8986b5c1257d380045703f/140818%20ABB%20SR%2060%20years%20of%20HVDC_72dpi.pdf.

Acha E., Fuerte-Esquivel C.R., Ambriz-Perez H. and Angeles-Camacho C. (2005). *FACTS modeling and simulation in power networks*, John Wiley & Sons.

Acha E. and Castro L.M. (2016a). A Generalized Frame of Reference for the Incorporation of Multi-Terminal VSC-HVDC Systems in Power Flow Solutions, *Electric Power Systems Research* 136: 415-424.

Acha, E. and Castro, L.M. (2016b). "Power Flow Solutions of AC/DC Micro-grid Structures". Accepted for publication in the 19th PSCC, Genoa, Italy, on 19-24 June 2016.

Acha E. and Kazemtabrizi B. (2013). A New STATCOM Model for Power Flows Using the Newton-Raphson Method, *IEEE Transactions on Power Systems* 28(3): 2455-2465.

Acha E., Kazemtabrizi B. and Castro L.M. (2013). A New VSC-HVDC Model for Power Flows Using the Newton-Raphson Method, *IEEE Transactions on Power Systems* 28(3): 2602-2612.

Adam G.P., Ahmed K.H., Finney S.J. and Williams B.W. (2013). Generalized Modeling of DC Grid for Stability Studies, *4th International Conference Power Engineering, Energy and Electric Drives (POWERENG)*, Istanbul, pp. 1168-1174.

Baradar M., and Ghandhari M. (2013). A Multi-Option Unified Power Flow Approach for Hybrid AC/DC Grids Incorporating Multi-Terminal VSC-HVDC, *IEEE Transactions on Power Systems* 28 (3): 2376-2383.

Barrios-Martinez E., Angeles-Camacho C., Acha E. and Olguin-Becerril M.A. (2009). Dynamic Phase-domain Modelling and Simulation of STATCOM in Large-scale Power Systems, *IEEE Power Tech Conference 2009*, Bucharest, pp. 1-9.

Bauer J.F., Wissen M., Gutt T., Biermann J., Schäffer C., Schmidt G. and Pfirsch F. (2014). New 4.5 kV IGBT and Diode Chip Set for HVDC Transmission Applications, *Power Conversion and Intelligent Motion (PCIM) Europe 2014*, Berlin, pp. 60-67.

Beccuti G., Papafotiou G. and Harnerfors L. (2014). Multivariable optimal control of HVDC transmission links with network parameter estimation for weak grids, *IEEE Transactions on Control Systems* 22: 676-689.

Beerten J., Cole S. and Belmans R. (2010). A Sequential AC/DC Power Flow Algorithm for Networks Containing Multi-terminal VSC HVDC Systems, *IEEE PES Winter Meeting 2010*, USA, pp. 1-7.

Callavik E.M., Lundberg P., Bahrman M.P. and Rosenqvist R.P. (2012). HVDC technologies for the future onshore and offshore grid*, Cigré F-75008*: 1-6.

Cañizares C.A. (2000). Power flow *and* transient stability models *of* FACTS controllers *for* voltage *and* angle stability studies*", IEEE PES Winter Meeting 2*: 1447-1454.

Castro L.M., Acha E. and Fuerte-Esquivel C.R. (2013). A New STATCOM Model for Dynamic Power System Simulations, *IEEE Transactions on Power Systems* 28(3): 3145-3154.

Castro L.M. and Acha E. (2015a). A novel VSC-HVDC Link Model for Dynamic Power System Simulations, *Electric Power Systems Research* 126: 111-120.

Castro L.M. and Acha E. (2015b). On the Provision of Frequency Regulation in Low Inertia AC Grids Using HVDC Systems, *IEEE Transactions on Smart Grid* 7(6): 2680-2690.

Castro L.M. and Acha E. (2016). A Unified Modeling Approach of Multi-Terminal VSC-HVDC Links for Dynamic Simulations of Large-Scale Power Systems, *IEEE Transactions on Power Systems* 31(6): 5051-5060.

Chen Q., Tang G. and Wang X. (2005). AC-DC Power Flow Algorithm for Multi-Terminal VSC-HVDC Systems, *Electric Power Automation Equipment* 25 (6).

Chaudhuri N.R., Majumder R., Chaudhuri B. and Pan J. (2011). Stability Analysis of VSC MTDC Grids Connected to Multimachine AC Systems, *IEEE Transactions on Power Delivery* 26 (4): 2274-2784.

Chiniforoosh S., Jatskevich J., Yazdani A., Sood V., Dinavahi V., Martinez J.A. and Ramirez A. (2010). Definitions and applications of dynamic average models for analysis of power systems, *IEEE Transactions on Power Delivery* 25: 2655-2669.

Chung I.Y., Liu W., Cartes D.A., Collins E.G. and Moon S. (2010). Control methods of inverter-interfaced distributed generators in a microgrid system, *IEEE Transactions on Industrial Applications* 46: 1078-1088.

Cole A., Beerten J. and Belmans R. (2010). Generalized Dynamic VSC MTDC Model for Power system stability Studies, *IEEE Transactions on Power Systems* 25 (3): 1655-1662.

Cole S. and Belmans R. (2008). Modelling of VSC HVDC using coupled current injectors, *IEEE PES General Meeting - Conversion and Delivery of Electrical Energy in the 21st Century*, pp. 1-8.

Cole S. and Belmans R. (2011). A proposal for standard VSC HVDC dynamic models in power system stability studies, *Electric Power Systems Research* 81: 967-973.

Cole S., Karoui K., Vrana T.K., Fosso O.B., Curis J.B, Denis A.M. and Liu C.C. (2011). A European Supergrid: Present State and Future Challenges, *17th Power Systems Computation Conference (PSCC) 2011*, Stockholm.

Dodds S., Railing B., Akman K., Jacobson B., Worzyk T. and Nilsson B. (2010). HVDC VSC (HVDC light) transmission - operating experiences*, Cigré B4-203 2010*: 1-9.

Eghtedarpour N. and Farjah E. (2014). Power control and management in a hybrid AC/DC microgrid, *IEEE Transactions on Smart Grid* 5: 1494-1505.

Faisal S.F., Rahim A.H.M.A. and Bakhashwain J.M. (2007). A Robust STATCOM Controller for a Multi-Machine Power System Using Particle Swarm Optimization and Loop-Shaping, *International Journal of Electrical, Computer and Systems Engineering*: 64-70.

Fuerte-Esquivel C.R. and Acha E. (1997). A Newton-type algorithm for the control of power flow in electrical power networks, *IEEE Transactions on Power Systems* 12: 1474–1480.

Gilje S.*,* Hyttinen M. and Westman B. (2009). Valhall re-development project, power from shore*, Cigré SC B4 2009*, pp. 1-10.

Gomis-Bellmunt O., Liang J., Ekanayake J, King R. and Jenkins N. (2011). Topologies of Multiterminal HVDC-VSC Transmission for Large Offshore Wind Farms, *Electric Power Systems Research* 81: 271-281.

Gong X. (2012). A 3.3 kV IGBT Module and Application in Modular Multilevel Converter for HVDC, *IEEE International symposium on Industrial Electronics ISIE 2012*, Hongzhou, pp. 1944-1949.

Guo C. and Zhao C. (2010).Supply of an entirely passive AC network through a double-infeed HVDC system, *IEEE Transactions on Power Electronics* 24: 2835-2841.

Hertem D. V. and Ghandhari M. (2010). Multi-terminal VSC-HVDC for the European Supergrid: obstacles, *Renewable and Sustainable Energy Reviews* 14: 3156-3163.

Hingorani N.G. and Gyugyi L. (1999). *Understanding FACTS: Concepts and Technology of Flexible AC Transmission Systems,* Wiley-IEEE Press.

Jabbari M., Shahgholian G., Mahdavian M., Attarpour E. and Leilaeyoun A. (2011). Modeling and Dynamic Analysis of a STATCOM for System Damping Enhancement, *IEEE International Symposium on Industrial Electronics*, pp. 1087-1092.

Jacobson B. and Asplund G. (2006). City Infeed with HVDC Light® and Extruded Cables, *16th Conference of the Electric Power Supply Industry*, Mumbai, India.

Kjaer S.B., Pedersen J.K. and Blaabjerg F. (2005). A Review of Single-Phase Grid-Connected Inverters for Photovoltaic Modules", *IEEE Transactions on Industrial Applications* 41 (5): 1292-1306.

Larsson T., Edris A., Kidd D. and Aboytes F. (2001). Eagle Pass Back-to-Back Tie: a Dual Purpose Application of Voltage Source Converter technology, *IEEE Power Engineering Society 3*: 1686-1691.

Latorre H.F., Ghandhari M. and Söder L. (2008). Active and reactive power control of a VSC-HVDC, *Electric Power Systems Research 78*: 1756-1763.

Li X., Yuan Z., Fu J., Wang Y, Liu T., and Zhu Z. (2014). Nanao multi-terminal VSC-HVDC project for integrating large-scale wind generation, *IEEE PES General Meeting 2014*, National Harbor MD, USA, pp. 1-5.

Mahdavian M. and Shahgholian G. (2011). Effect of STATCOM on Enhancing Power System Dynamic Stability, *8th IEEE International Conference on Electrical Engineering, Computer, Telecommunications and Information Technology (ECTI-CON),* pp. 780-783.

Moustafa M.M.Z. and Filizadeh S. (2012). A VSC-HVDC model with reduced computational intensity, *IEEE PES General Meeting*, USA, pp. 1-6.

Nnachi A.F., Munda J.L., Nicolae D.V. and Mabwe A.M. (2013). Stability improvement of a HVDC transmission link between weak AC systems by multi-terminal scheme, IEEE Conference AFRICON 2013.

Orths A., Hiorns A., Van Houtert R., Fidher L. and Fourment C. (2012). The European North Seas Countries' Offshore Grid Initiative – The Way Forward, *IEEE PES General Meeting*, USA, pp. 1-8.

Peralta J., Saad H., Dennetiere S. and Mahseredjian J. (2012). Dynamic Performance of Average-Value Models for Multi-terminal VSC-HVDC Systems, *IEEE PES General Meeting 2012*, USA, pp. 1-8.

Petersonn A. and Edris A. (2001). Dynamic Performance of the Eagle Pass back-to-back HVDC Light Tie, *7th International Conference on AC-DC Power Transmission*, London, pp. 220-225.

Robinson J., Jovcic D. and Joos G. (2010). Analysis and Design of an Offshore Wind Farm Using a MV DC Grid, *IEEE Transactions on Power Delivery* 25 (4): 2164-2173.

Rocabert J., Luna A., Blaabjerg F. and Rodriguez P. (2012). Control of power converters in AC microgrids", *IEEE Transactions on Power Electronics 27: 4734-4749.*

Ronström L., Hoffstein M.L., Pajo R. and Lahtinen M. (2007). The Estlink HVDC Light Transmission Systems, *CIGRE Regional Meeting - Security and Reliability of Electric Power Systems* , Tallin, pp. 1-7.

Ruihua S., Chao Z., Ruomei L., and Xiaoxin Z. (2005). VSCs based HVDC and its control strategy, *IEEE PES T&D Conference and Exhibition*, pp. 1-6.

Sao C.K. and Lehn P.W., (2008). Control and power management of converter fed microgrids, *IEEE Transactions on Power Syst*ems 23: 1088-1098.

Schauder C., Gernhardt M., Stacey E., Lemak T., Gyugyi L., Cease T.W. and Edris A. (1997). Operation of ±100 MVAR TVA STATCOM, *IEEE Transactions on Power Delivery* 12: 1805-1811.

Shahgholian G., Mahdavian M., Etesami A., Moalem S. and Jabbari M. (2011). Improvement of Dynamic Behavior and System Stability by Using STATCOM, *IEEE International Symposium on Industrial Electronics*, pp. 1057-1062.

Shen L., Wang W. and Barnes M. (2014). The Influence of MTDC control on DC Power Flow and AC System Dynamic Responses, *IEEE PES General Meeting 2014*, National Harbor MD, USA, pp. 1-5.

Smed T., Andersson G., Sheble G.B. and Grigsby L.L. (1991). A new approach to AC/DC power flow, *IEEE Transactions on Power Systems* 6: 1238–1244.

Stagg, G.W. and El-Abiad, A.H. (1968). *Computer Methods in Power System Analysis*, McGraw-Hill.

Stendius L. and Jones P. (2006). The challenges of offshore power system construction - bringing power successfully to Troll A, one of the worlds largest oil and gas platform, *8th IEE International Conference on AC and DC Power Transmission*, pp. 75–78.

Teeuwsen S.P. (2009). Simplified dynamic model of a voltage-sourced converter with modular multilevel converter design, *IEEE PES Power Systems Conference and Exposition PSCE*, pp.1-6.

Trötscher T., Korpås M. and Tande J.O. (2009). Optimal Design of Subsea grid for Off-Shore Wind Farms and Transnational Power Exchange, *EWEC2009 Scientific proceedings: European Wind Energy Conference & Exhibition*, pp. 163-167.

Van der Meer A.A., Gibescu M., Van der Miejden M.A.M.M., Kling W.L. and Ferreira J.A. (2015). Advanced Hybrid Transient Stability and EMT simulation for VSC-HVDC Systems, *IEEE Trans. on Power Delivery* 30 (3): 1057-1066.

Vrana T.K., Torres-Olguin R.E., Liu B. and Haileselassie T.M. (2010). The North Sea Super Grid – A Technical Perspective, *9th IET International Conference on AC and DC Power Transmission*, pp. 1-5.

Wang K. and Crow M.L. (2011). Power System Voltage Regulation via STATCOM Internal Nonlinear Control*, IEEE Transactions on Power Systems* 26: 1252-1262.

Wang W. and Barnes M. (2014). Power Flow Algorithms for Multi-Terminal VSC-HVDC with Droop Control, *IEEE Transactions on Power systems* 29 (4): 1721-1730.

Watson N.R. and Arrillaga J (2007). Incorporation of VSC Transmission in Power-Flow Simulations, *8th International Power Engineering Conference*, Singapore, 3-6 Dec, pp. 619-624.

Yao M. and Cai X. (2015). Preliminary study on voltage level standardization of DC grid based on VSC-HVDC technology in China, *IEEE PowerTech Eindhoven 2015*, pp. 1-4.

Ye F., Wei Z.N. and Sun G.Q. (2011). Improved Power Flow Algorithm Incorporating Multi-Terminal VSC-HVDC, *ICMST2011 Advanced Materials Research* 383-390: 2188-2194.

Zhang L., Harnefors L. and Nee H.P. (2011). Modeling and control of VSC-HVDC links connected to island systems, *IEEE Transactions on Power Systems 26: 783-793.*

Zhang X.P. (2004). Multiterminal Voltage-Sourced Converter-Based HVDC Models for Power Flow Analysis, *IEEE Transactions on Power Systems* 19: 1877-1884.

Tampereen teknillinen yliopisto
PL 527
33101 Tampere

Tampere University of Technology
P.O.B. 527
FI-33101 Tampere, Finland

ISBN 978-952-15-3866-7
ISSN 1459-2045